

AD-A085 726

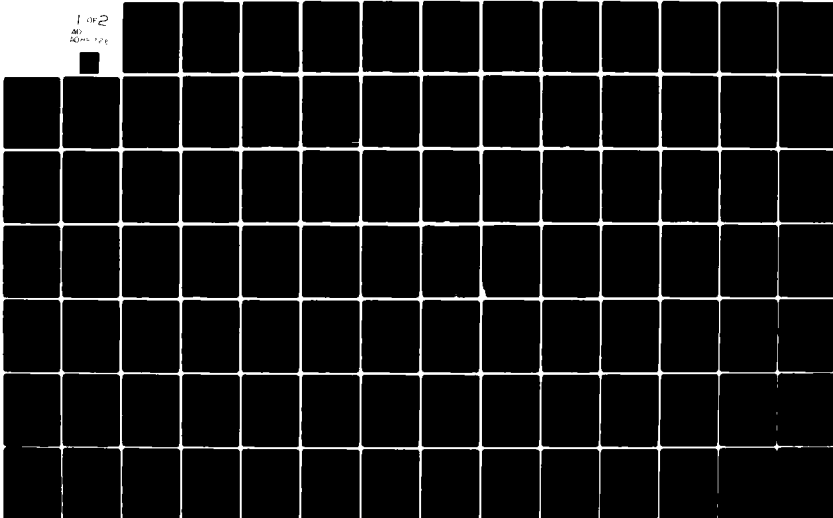
CIVIL SYSTEMS INC ALBUQUERQUE NM F/G 18/3
MISERS BLUFF PHASE I SINGLE BURST EXPERIMENTS. GROUND SHOCK ANA--ETC(U)
MAR 78 J L BRATTON, J S PHILLIPS DNA001-77-C-0301

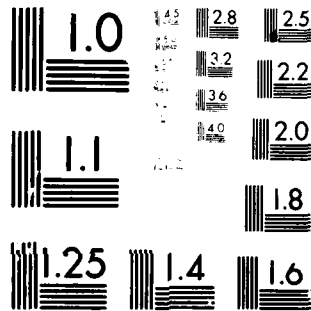
UNCLASSIFIED

DNA-5004Z

NL

1 of 2
AD-A085 726





MICROCOPY RESOLUTION TEST CHART
NATIONAL BUREAU OF STANDARDS-1963-A

ADA 085726

LEVEL III

AD-E 300 799

BS 12

DNA 5004Z

MISERS BLUFF PHASE I SINGLE BURST EXPERIMENTS

Ground Shock Analysis

James S. Phillips
Jimmie L. Bratton
Civil Systems, Inc.
2201 San Pedro, N.E., Bldg. 3, Suite 214
Albuquerque, New Mexico 87110

17 March 1978

Interim Report for Period 1 October 1977-1 January 1978

CONTRACT No. DNA 001-77-C-0301

APPROVED FOR PUBLIC RELEASE;
DISTRIBUTION UNLIMITED.

THIS WORK SPONSORED BY THE DEFENSE NUCLEAR AGENCY
UNDER RDT&E RMSS CODE B344077462 H35KAXSX35510 H2590D.

DDC FILE COPY

Prepared for
Director
DEFENSE NUCLEAR AGENCY
Washington, D. C. 20305

DTIC ELECTED
S JUN 20 1980 D
D

80 5 19 222

Destroy this report when it is no longer needed. Do not return to sender.

PLEASE NOTIFY THE DEFENSE NUCLEAR AGENCY,
ATTN: STTI, WASHINGTON, D.C. 20305, IF
YOUR ADDRESS IS INCORRECT, IF YOU WISH TO
BE DELETED FROM THE DISTRIBUTION LIST, OR
IF THE ADDRESSEE IS NO LONGER EMPLOYED BY
YOUR ORGANIZATION.



UNCLASSIFIED

SECURITY CLASSIFICATION OF THIS PAGE (When Data Entered)

REPORT DOCUMENTATION PAGE		READ INSTRUCTIONS BEFORE COMPLETING FORM
1. REPORT NUMBER DNA 5004Z	2. GOVT ACCESSION NO. AD-A085 726	3. RECIPIENT'S CATALOG NUMBER
4. TITLE (and Subtitle) MISERS BLUFF PHASE I SINGLE BURST EXPERIMENTS Ground Shock Analysis		5. TYPE OF REPORT & PERIOD COVERED Interim Report for Period 1 Oct 77-1 Jan 78
		6. PERFORMING ORG. REPORT NUMBER
7. AUTHOR(s) Jimmie L. Bratton James S. Phillips		8. CONTRACT OR GRANT NUMBER(s) DNA 001-77-C-0301
9. PERFORMING ORGANIZATION NAME AND ADDRESS Civil Systems, Inc. 2201 San Pedro, N.E., Bldg. 3, Suite 214 Albuquerque, New Mexico 87110		10. PROGRAM ELEMENT, PROJECT, TASK AREA & WORK UNIT NUMBERS Subtask H35KAXSX355-10
11. CONTROLLING OFFICE NAME AND ADDRESS Director Defense Nuclear Agency Washington, D.C. 20305		12. REPORT DATE 17 March 1978
		13. NUMBER OF PAGES 186
14. MONITORING AGENCY NAME & ADDRESS (if different from Controlling Office)		15. SECURITY CLASS (of this report) UNCLASSIFIED
		15a. DECLASSIFICATION/DOWNGRADING SCHEDULE
16. DISTRIBUTION STATEMENT (of this Report) Approved for public release; distribution unlimited.		
17. DISTRIBUTION STATEMENT (of the abstract entered in Block 20, if different from Report)		
18. SUPPLEMENTARY NOTES This work sponsored by the Defense Nuclear Agency under RDT&E RMSS Code B344077462 H35KAXSX35510 H2590D.		
19. KEY WORDS (Continue on reverse side if necessary and identify by block number) Misers Bluff Prediction Methods High Explosive Test Wave Propagation Ground Shock Data Data Analysis		
20. ABSTRACT (Continue on reverse side if necessary and identify by block number) The single burst events of Misers Bluff Phase I provided the basic data for use in evaluation of the superposition principles in predicting the ground shock effects of multiburst experiments. In addition, it provided an opportunity for evaluating the current empirical procedures for predicting the ground shock effects of high explosive experiments. Evaluation of the single burst empirical predictions and the superposition principle as a part of the multiburst experiments of Phase I will allow an evaluation of		

DD FORM 1473
1 JAN 73

EDITION OF 1 NOV 65 IS OBSOLETE

UNCLASSIFIED

SECURITY CLASSIFICATION OF THIS PAGE (When Data Entered)

394871

UNCLASSIFIED

SECURITY CLASSIFICATION OF THIS PAGE(When Data Entered)

20. ABSTRACT (Continued)

the uncertainties one might expect in making empirical predictions of a multiburst weapons effect environment.

The current state-of-the-art in empirical ground shock predictions of high explosive experiments are discussed and utilized in the pretest predictions for each of the 5 single burst experiments discussed in this report. The apparent deficiencies and the problems associated with use of the nuclear weapons effects predictions procedures for high explosive experiments are discussed in some detail.

The phenomenology associated with these experiments is discussed and related to the waveforms observed in various experiments. This understanding of the single burst phenomenology will provide the basis for understanding the small yield multiburst experiments also conducted as a part of Phase I of the Misers Bluff program. The predictions are then compared with the measurements on a component by component basis. Conclusions regarding the validity of the prediction procedures are drawn.

Accession For	
NTIS GRA&I	<input checked="" type="checkbox"/>
DDC TAB	<input type="checkbox"/>
Unannounced	<input type="checkbox"/>
Justification	<input type="checkbox"/>
By _____	
Distribution/	
Availability Codes	
Dist.	Avail and/or special
A	

UNCLASSIFIED

SECURITY CLASSIFICATION OF THIS PAGE(When Data Entered)

PREFACE

This Report was prepared by SAI/CSI, Albuquerque, New Mexico, under Contract DNA001-77-C-0301. This research was performed under Program Element T62710H, Project H35KAXS, Task Area X355, Work Unit 10, and was funded by the Defense Nuclear Agency. The Technical Monitor was Dr. George W. Ullrich, DNA.

Inclusive dates of Research were October 1977 through January 1978.

PERTINENT CONVERSION FACTORS - SI TO U. S. CUSTOMARY UNITS OF MEASUREMENT

<u>PARAMETERS</u>	<u>TO CONVERT FROM</u>	<u>TO</u>	<u>MULTIPLY BY</u>
Length	Meters (m)	Feet	3.281
Velocity	Meters/Second (mps)	Feet/Second	3.281
Unit Weight	Grams/Cubic Centimeter (gm/cc)	Pounds/Cubic Foot	62.427
Yield	Terra Joules (TJ)	Kilotons	2.391×10^{-1}
Volume	Cubic Meters (m ³)	Cubic Feet	35.315
Cratering Efficiency	Cubic Meters/Terra Joule (m ³ /TJ)	Cubic Feet/Ton	6.770
Pressure	Mega Pascals (Mpa)	Pounds/Square Inch	145
Impulse	Mega Pascals-Sec (Mpa-sec)	Pounds/Square Inch-Sec	145

TABLE OF CONTENTS

	<u>Page</u>
List of Illustrations	6
List of Tables	13
1. Introduction	15
2. Experimental Plan	18
2.1 General	18
2.2 Geology	18
2.2.1 General Description	18
2.2.2 Seismic Properties	18
2.2.3 Material Properties	23
2.3 Instrumentation Plan	23
3. Prediction Methods	33
3.1 General	33
3.2 Predictions	33
3.2.1 Airblast	33
3.2.2 TOA Contours	36
3.2.3 Ground Motion	40
a) Air Slap Component	43
b) Oscillatory Component	43
c) Crater Related Component	50
d) Waveform Superposition	53
4. Discussion of Data	56
4.1 Explanation of Phenomenology	56
4.2 Airblast Results	67
4.3 Ground Motion	77
4.3.1 General	77
4.3.2 Air Slap Component of Ground Motion	77
a) Definition	77
b) Discussion of Data	77
1. Surface Tangent Configuration	77
2. Half Buried Configuration	85
3. Tangent Below Configuration	94
4. Height of Burst Comparison	97

TABLE OF CONTENTS (continued)

	<u>Page</u>
4.3.3 Oscillatory Component of Ground Motion	97
a) Definition	97
b) Discussion of Data	102
1. Surface Tangent Configuration	102
2. Half Buried Configuration . .	105
3. Tangent Below Configuration .	113
4. Height of Burst Comparison . .	118
5. Periods of Oscillatory Motion	122
4.3.4 Crater Related Ground Motion	122
a) Introduction	122
b) Crater	131
c) Crater Related Displacements . . .	133
1. Half Buried and Tangent Below Configurations	133
2. Surface Tangent Configuration	133
d) Crater Related Particle Velocity .	140
4.4 Waveforms	144
4.4.1 Comparison of Measured Predicted Wave- forms	144
a) Surface Tangent Configuration . .	144
b) Half Buried Configuration	150
c) Tangent Below Configuration . . .	154
4.4.2 Event-to-Event Waveform Comparisons for the Half Buried Configurations	154
4.5 Comparison of Integrated Accelerometers and Velocity Gages	160
4.6 Stress Measurements	160
4.7 Transverse Measurements	168
5. Summary, Conclusions, and Recommendations	172
5.1 Summary	172
5.1.1 Data Scatter	172

TABLE OF CONTENTS (continued)

	<u>Page</u>
5.1.2 Height of Burst	173
5.1.3 Evaluation of Empirical Prediction Procedures	174
5.1.4 Phenomenology	176
5.2 Conclusions	176
5.3 Recommendations	177

LIST OF ILLUSTRATIONS

<u>Figure</u>		<u>Page</u>
1	Misers Bluff Phase I Test Bed Location	19
2	Misers Bluff Phase I Test Bed Plan	20
3	P-wave Velocity Profile Interpreted from Crosshole, Uphole and Surface Refraction Seismic Data	22
4	S-wave Velocity Profile Interpreted from Crosshole Seismic Data	24
5	Simplified Seismic Profile of Misers Bluff Phase I Test Bed	25
6	Moisture Content Data Measured for Single Burst Events	26
7	Gage Layout for Event 1 - Half Buried Configuration .	27
8	Gage Layout for Event 2 - Surface Tangent Configuration	28
9	Gage Layout for Event 3 - Half Buried Configuration .	29
10	Gage Layout for Event 5 - Tangent Below Configuration	30
11	Gage Layout for Event 7 - Half Buried Configuration .	31
12	Prediction Curves of Overpressure and Impulse for Surface Tangent and the Half Buried Configurations	34
13	Predicted Curve of Duration for the Surface Tangent and Half Buried Configurations	35
14	Arrival Time of Airblast for Surface Tangent and Half Buried Configurations	37
15	Predicted Time of Arrival Contours of Airblast Induced Motion	38
16	Continuation of Predicted Time of Arrival Contours of Airblast Induced Motion for Ranges Greater than 50 Meters	39
17	Predicted Time of Arrival Contours of Direct Induced Motion	41
18	Continuation of Predicted Time of Arrival Contours of Direct Induced Motion for Ranges Greater than 50 Meters	42
19	Prediction Curves of Airblast Induced Acceleration for the Half Buried Configuration	44
20	Prediction Curves of Airblast Induced Velocity for the Half Buried Configuration	45
21	Prediction Curves of Airblast Induced Displacement for the Half Buried Configuration	46

LIST OF ILLUSTRATIONS (continued)

<u>Figure</u>		<u>Page</u>
22	Prediction Curves of Oscillatory Component for the Half Buried Configuration	48
23	Comparison of Prediction Procedures for the Oscillatory Component of Ground Motion at the 36.6 Meter Range .	49
24	Cratering Efficiencies for TNT Surface Bursts	51
25	Height of Burst Effects in the Near Surface Region . .	52
26	Prediction of Crater Related Motion for the Half Buried Configuration	54
27	Components of the Predicted Vertical Waveform at the 18.3 Meter Range for the Half Buried Configuration .	55
28	Vertical Velocity Waveforms at the .46 m Depth-MBI-2 .	57
29	Vertical Velocity Waveforms at the .46 m Depth-MBI-2 .	58
30	Shock Spectra for Vertical Velocity Waveforms at the .46 m Depth; MBI-2	61
31	Horizontal Velocity Waveforms at the .46 m Depth-MBI-2	63
32	Horizontal Velocity Waveforms at the .46 m Depth-MBI-2	64
33	Shock Spectra for Horizontal Velocity Waveforms at the .46 m Depth MBI-2	65
34	Overpressure and Impulse Data Compared with Predictions for the Surface Tangent Configuration	68
35	Overpressure and Impulse Data Compared with Predictions for the Half Buried Configuration	69
36	Overpressure and Impulse Data from Other Half Buried Experiments Scaled to the 2.09×10^{-3} TJ Yield . . .	71
37	Misers Bluff Data and Predictions Compared with Other Experiments - Half Buried Configuration	72
38	Overpressure and Impulse Data Compared with Predictions for the Tangent Below Configuration	73
39	Height of Burst Effect on Overpressure and Impulse . .	75
40	Height of Burst Effect on Arrival Times	76
41	Definition of Air Slap Component of Vertical Motion R=18.3 m; Z=.46 m	78

LIST OF ILLUSTRATIONS (continued)

<u>Figure</u>		<u>Page</u>
42	Definition of Air Slap Component of Horizontal Motion R=18.3 m; Z=.46 m	79
43	Comparison of Measured and Predicted Peak Values of Airblast Induced Acceleration for the Top 1.52 m of the Test Bed-MBI-2	80
44	Comparison of Measured and Predicted Peak Values of Airblast Induced Velocity for the Top 1.52 m of the Test Bed-MBI-2	81
45	Comparison of Measured and Predicted Peak Values of Airblast Induced Acceleration Below the 1.52 m Depth-MBI-2	82
46	Comparison of Measured and Predicted Peak Values of Airblast Induced Velocity Below the 1.52 m Depth- MBI-2	83
47	Comparison of Measured and Predicted Peak Values of Airblast Induced Acceleration for MBI-1	86
48	Comparison of Measured Peak Values of Airblast Induced Acceleration from MBI-1 and MBI-3	88
49	Comparison of Measured and Predicted Peak Values of Airblast Induced Acceleration for MBI-7	89
50	Comparison of Measured and Predicted Peak Values of Airblast Induced Velocity for MBI-1	90
51	Comparison of Measured and Predicted Peak Values of Airblast Induced Velocity from MBI-1 and MBI-3	92
52	Comparison of Measured and Predicted Peak Values of Airblast Induced Velocity for MBI-7	93
53	Comparison of Measured and Predicted Peak Values of Airblast Induced Acceleration for MBI-5	95
54	Comparison of Measured and Predicted Peak Values of Airblast Induced Velocity for MBI-5	96
55	Height of Burst Comparison of Airblast Induced Velocities at the .46 m Depth	98
56	Height of Burst Comparison of Airblast Induced Velocities at the 3.05 m Depth	99
57	Definition of Oscillatory Component of Vertical Motion .	100
58	Definition of Oscillatory Component of Horizontal Motion	101

LIST OF ILLUSTRATIONS (continued)

<u>Figure</u>		<u>Page</u>
59	Comparison of Predicted and Measured Zero-to-Peak Values of the Oscillatory Component at the .46 m Depth for the Surface Tangent Configuration-MBI-2 . . .	103
60	Peak-to-Peak Values of the Oscillatory Component at the .46 m Depth for the Surface Tangent Configuration MBI-2	104
61	Peak-to-Peak Values of the Oscillatory Component at Greater Depths for the Surface Tangent Configuration-MBI-2	106
62	Arrival Time of the Oscillatory Component for the Surface Tangent Configuration-MBI-2	107
63	Comparison of Predicted and Measured Zero-to-Peak Values of the Oscillatory Component at the .46 m Depth for the Half Buried Configuration-MBI-1 and MBI-3	108
64	Peak-to-Peak Values of the Oscillatory Component at the .46 m Depth for the Half Buried Configuration MBI-1 and MBI-3	110
65	Peak-to-Peak Values of the Oscillatory Component at Greater Depths for the Half Buried Configuration MBI-1 and MBI-3	111
66	Peak-to-Peak Values of the Oscillatory Component for Half Buried Configuration - MBI-7	112
67	Oscillatory Component for MBI-1 Compared with Oscillatory Component from MBI-7	114
68	Arrival Time of the Oscillatory Component for the Half Buried Configuration	115
69	Comparison of Predicted and Measured Zero-to-Peak Values of the Oscillatory Component at the .46 m Depth for the Tangent Below Configuration-MBI-5 . . .	116
70	Peak-to-Peak Values of the Oscillatory Component at the .46 m Depth for the Tangent Below Configuration MBI-5	117
71	Peak-to-Peak Values of the Oscillatory Component at Greater Depths for the Tangent Below Configuration MBI-5	119
72	Arrival Time of the Oscillatory Component for the Tangent Below Configuration-MBI-5	120

LIST OF ILLUSTRATIONS (continued)

<u>Figure</u>		<u>Page</u>
73	Height of Burst Comparison for the Oscillatory Component at .46m Depth	121
74	Periods of Oscillatory Motion for Vertical Velocity MBI-2 and MBI-7	123
75	Periods of Oscillatory Motion for Vertical Velocity MBI-3 and MBI-7	124
76	Periods of Oscillatory Motion for Vertical Velocity MBI-5	125
77	Periods of Oscillatory Motion for Vertical Velocity at the .46m Depth for all Events	126
78	Periods of Oscillatory Motion for Horizontal Velocity MBI-2 and MBI-1	127
79	Periods of Oscillatory Motion for Horizontal Velocity MBI-3 and MBI-7	128
80	Periods of Oscillatory Motion for Horizontal Velocity MBI-5	129
81	Periods of Oscillatory Motion for Horizontal Velocity at the .46m Depth for all Events	130
82	Crater Volume Scaled Displacements for Region 1	134
83	Crater Volume Scaled Displacements for Region 2	135
84	Crater Volume Scaled Displacements for Region 3	136
85	Crater Volume Scaled Displacements from Event 2, Surface Tangent Configuration - Region 1	137
86	Crater Volume Scaled Displacements from Event 2, Surface Tangent Configuration - Region 2	138
87	Crater Volume Scaled Displacements from Event 2, Surface Tangent Configuration - Region 3	139
88	Crater Volume Scaled Velocities for Region 1	141
89	Crater Volume Scaled Velocities for Region 2	142
90	Crater Volume Scaled Velocities for Region 3	143
91	Comparison of Measured and Predicted Vertical Wave- forms at the 10.68m Range and .46m Depth - MBI-2	145

LIST OF ILLUSTRATIONS (continued)

<u>Figure</u>		<u>Page</u>
92	Comparison of Measured & Predicted Horizontal Waveforms at the 10.68m Range and the .46m Depth - MBI-2	147
93	Comparison of Measured and Predicted Vertical Waveforms at the 21.35m Range and 0.46m Depth	148
94	Comparison of Measured and Predicted Horizontal Waveforms at the 21.35m Range and .46m Depth	149
95	Comparison of Measured and Predicted Vertical Velocity Waveforms at the 18.3m Range and .46m Depth - MBI-1	151
96	Comparison of Measured and Predicted Horizontal Waveforms at the 18.3m Range and .46m Depth - MBI-1 . .	152
97	Comparison of Measured and Predicted Vertical Waveforms at the 36.6m Range and .46m Depth - MBI-1	153
98	Comparison of Measured and Predicted Horizontal Waveforms at the 36.6m Range & the .46m Depth - MBI-1 .	155
99	Comparison of Measured and Predicted Vertical Waveforms at the 36.6m Range and .46m Depth - MBI-5 . .	156
100	Comparison of Measured and Predicted Horizontal Waveforms at the 36.6m Range and .46m Depth - MBI-5 . .	157
101	Event-to-Event Vertical Waveforms Comparison for the Half Buried Configuration	158
102	Event-to-Event Horizontal Waveform Comparison for the Half Buried Configuration	159
103	Comparison of Velocity Gage Waveforms and Integrated Accelerometer Waveforms MBI-1	161
104	Comparison of Velocity Gage Waveforms and Integrated Accelerometer Waveforms MBI-1	162
105	Comparison of Velocity Gage Waveforms and Integrated Accelerometer Waveforms for MBI-2	163
106	Comparison of Velocity Gage Waveforms and Integrated Accelerometer Waveforms MBI-2	164
107	Comparison of Peak Values from Integrated Accelerometers and Velocity Gages	165

LIST OF ILLUSTRATIONS (continued)

<u>Figure</u>		<u>Page</u>
108	Vertical Stress Waveforms at R=18.3m and Z=1.5m for the Three Configurations	166
109	Horizontal Stress Waveforms at the 18.3m Range and the 1.5m Depth for the Three Configurations	167
110	Vertical Stress Data from Phase I Single Burst Experi- ments	169
111	Horizontal Stress Data from Phase I Single Burst Experi- ments (1.53m Depth)	170
112	Tangential Data from the Three Configurations	171

LIST OF TABLES

<u>Table</u>	<u>Title</u>	<u>Page</u>
1	Objectives of the Single Burst Events	17
2	Misers Bluff Phase I Test Program	21
3	Crater Predictions vs Data for Phase I Single Burst Events	132
4	Summary of Prediction Evaluation	175

1.

INTRODUCTION

The Multiple Aim Point Basing concept for the proposed MX weapon system derives its survivability by creating more targets than can be attacked one-on-one. The current estimates of the deployment pattern for the MX system places neighboring aim points from 1220 meters to 1830 meters apart for a "baseline" threat. For most geologic conditions this distance corresponds to a ground motion environment within the "transition" or "plateau" region (Reference 1). In this region there is little or no attenuation of ground motion with range, so that peak amplitudes of motion are relatively insensitive to distance from the source. Preliminary estimates of the effect of this multiburst phenomenon, assuming the superposition principle to be valid, indicated that unattacked elements of the system may be subjected to a greater ground motion environment than that which results for a single burst at the design miss distance (Reference 2).

Currently no generally accepted method exists for predicting ground motions from multiple bursts. An evaluation of the superposition assumption performed by the Data Analysis Working Group (DAWG) prior to Misers Bluff and using the very limited available data indicated that superposition of the effects of a single burst is not a satisfactory estimate of the multiburst effects. In general, superposition under-estimated the period of oscillatory ground motion and under-(however occasionally over-) estimated the peak amplitudes (Reference 2).

The Misers Bluff test program was designed to provide an experimental data base upon which a method of predicting ground motions from multiple bursts could be developed. The program consisted of a series of single burst and multiburst experiments in two phases. Phase I was a series of small-scale experiments upon which a waveform synthesis procedure for predicting HE multiburst effects in a layered geology would be developed. Phase II will be a test of the procedures at higher yields and for a different geology. The Phase II site was selected to be as representative as possible of a miniature MX siting area (valley). The single burst experiments of Phase

I are the subject of this interim report. Table 1 summarizes the objectives of these experiments.

The experimental plan and site properties are discussed in Section 2. Prediction procedures for the single burst events are presented in Section 3. The test data and comparison with predictions is contained in Section 4. Conclusions and evaluations are discussed in Section 5.

The Phase I multiburst experiments and development of a waveform synthesis model will be reported in a companion report. The waveform synthesis model is a procedure for predicting the ground shock waveforms from an arbitrary number of bursts spaced arbitrarily in time and location.

Table 1. OBJECTIVES OF THE SINGLE BURST EXPERIMENTS

<u>Event</u>	<u>Objective</u>
MBI-1	Provide single burst data for multiburst waveform synthesis
MBI-2	Identify depth of burst phenomena differences in oscillatory ground motion region; provide data for scaling comparisons with Pre-Dice Throw 100 ton event; provide single burst data for multi-burst waveform synthesis
MBI-3	Repeat of MBI-1 to obtain data on reproducibility and emphasize definitions of motions in the plateau region
MBI-5	Identify depth of burst phenomena differences in oscillatory ground motion region
MBI-7	Provide data on scaling between 2.09×10^{-3} TJ and 5.35×10^{-4} TJ.

2.

EXPERIMENTAL PLAN

2.1 GENERAL

The test bed for Phase I of Misers Bluff was located at the Queen 15 site on the White Sands Missile Range (WSMR), New Mexico, approximately 1200 meters east of the Pre-Dice Throw (PDT) II test bed (Figure 1). The locations of the various ground zeroes are shown in Figure 2.

The Queen 15 site was chosen for the Phase I experiments because of the availability of both site geologic data and ground shock data from the Pre-Dice Throw experiments and because the Pre-Dice Throw data indicate data variation at this site is not large.

Phase I consisted of eight experiments, five of which were single burst events. The configurations and dates of these events are shown in Table 2.

2.2 GEOLOGY

2.2.1 General Description

The test site is characterized by 2.1 meters of brown silty clay overlying a soft, gray clay that extends to a depth of 5 to 6 meters. Below this lies a fine-to-coarse silty sand, with gravel, that extends to the 11 to 12 meter depth. Alternating layers of clay, sand, and silt lie below the sand to a depth of 131 meters. The ground water table is about 2.1 to 2.4 meters below the ground surface (Reference 3).

2.2.2 Seismic Properties

Due to the close proximity of the Misers Bluff site to the Pre-Dice Throw site no seismic survey was conducted. Therefore, the seismic properties were considered to be the same as the PDT site.

Seismic tests performed for the PDT events included crosshole, uphole, and surface refraction. P-wave and s-wave velocity profiles interpreted from the results of these tests are shown in Figures 3

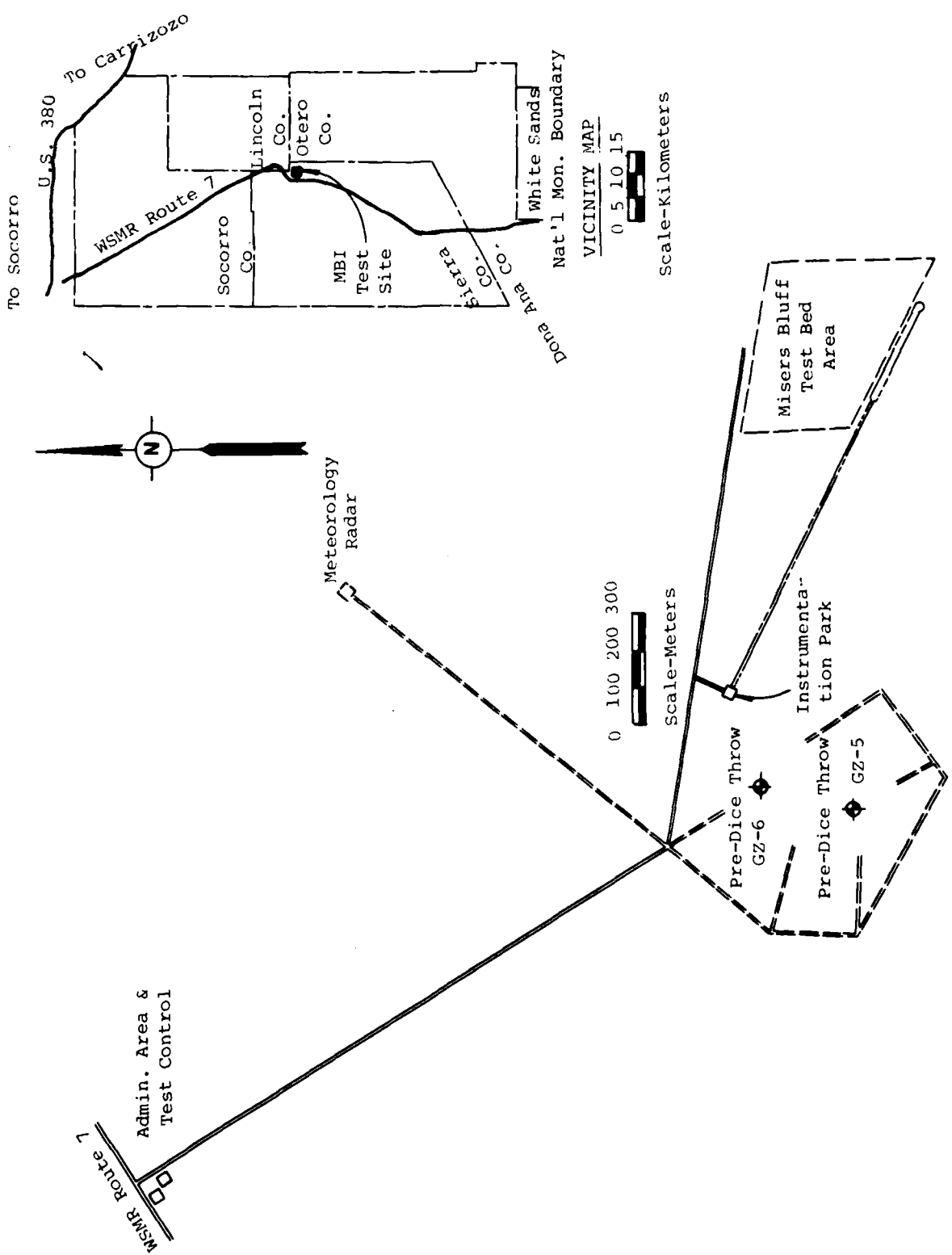
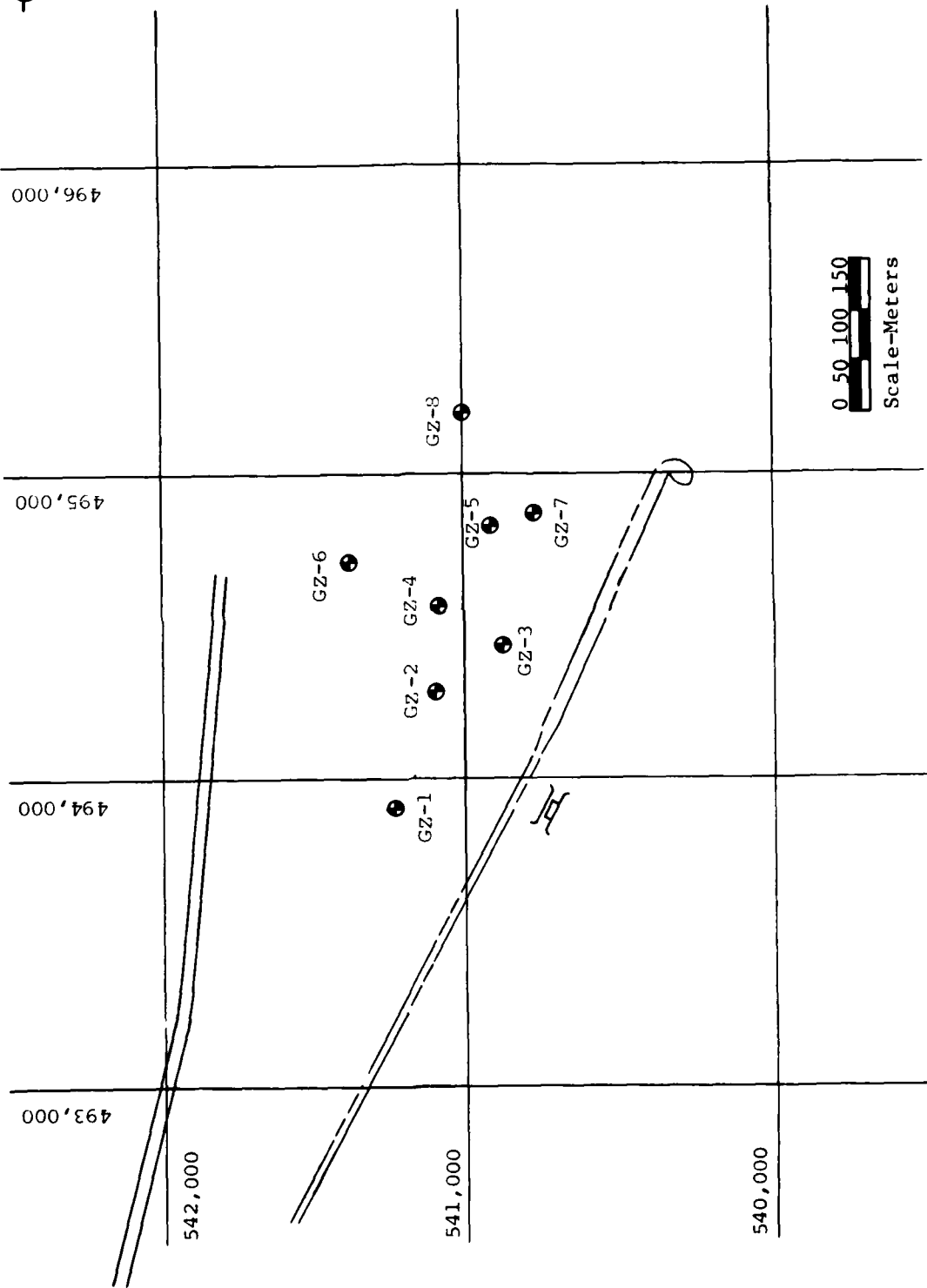


Figure 1. Misers Bluff Phase I Test Bed Location



0 50 100 150
Scale-Meters

Figure 2. Misers Bluff Phase I Test Bed Plan

TABLE 2. MISERS BLUFF PHASE I TEST PROGRAM

EVENT	NO. OF CHARGES	YIELD/CHARGE	CHARGE CONFIGURATION	DATE
MBI-1	1	2.09×10^{-3} TJ (1000 lb)	Half Buried \ominus	2 August 1977
MBI-2	1	2.09×10^{-3} TJ (1000 lb)	Surface Tangent \underline{Q}	15 August 1977
MBI-3	1	2.09×10^{-3} TJ (1000 lb)	Half Buried \ominus	23 August 1977
MBI-4	6	2.09×10^{-3} TJ (1000 lb)	Surface Tangent \underline{Q}	7 September 1977
MBI-5	1	2.09×10^{-3} TJ (1000 lb)	Tangent Below \overline{O}	20 September 1977
MBI-6	6	2.09×10^{-3} TJ (1000 lb)	Half Buried \ominus	13 October 1977
MBI-7	1	5.35×10^{-4} TJ (256 lb)	Half Buried \ominus	25 October 1977
MBI-8	24	2.09×10^{-3} TJ (1000 lb)	Surface Tangent \underline{Q}	7 December 1977

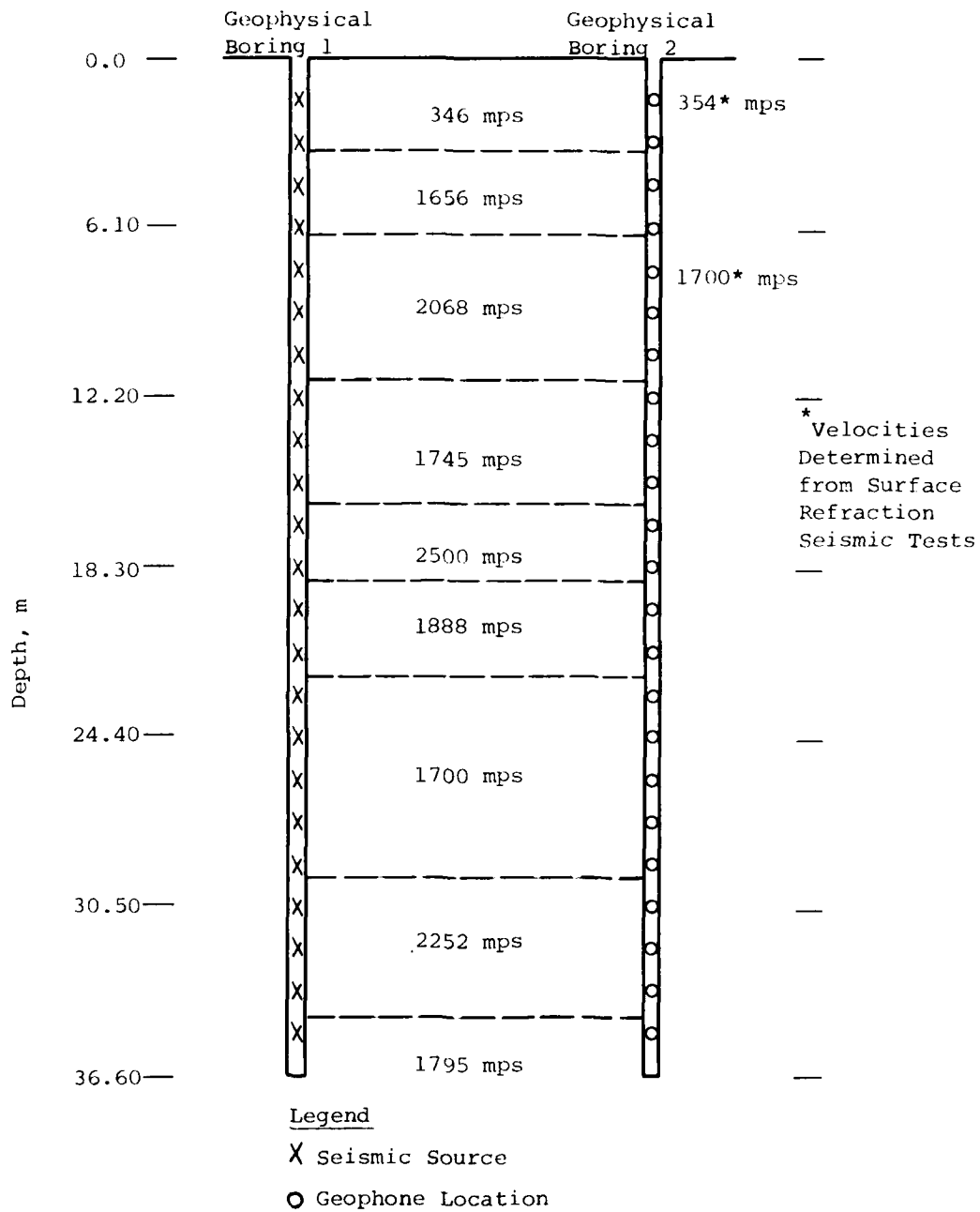


Figure 3. P-wave Velocity Profile Interpreted from Crosshole, Uphole and Surface Refraction Seismic Data (from Reference 3)

and 4. A detailed discussion of these tests is presented in Reference 3. These profiles indicate numerous seismic reversals, however, the changes in velocity are not large. These high velocity layers probably represent zones of increased cementation or greater percentages of gravel (and, therefore, higher densities). Neither of these conditions is typically uniform in the horizontal direction, therefore the simplified profile shown in Figure 5 was used for prediction and preliminary analysis purposes.

2.2.3 Material Properties

The material properties for Misers Bluff were also assumed to be the same as those determined for PDT. The material property tests run for PDT were routine classification and index tests, water content, specific gravity, density, undrained static and dynamic uniaxial strain and isotropic compression, and static and dynamic triaxial shear tests. The results of these tests are presented in detail in Reference 4.

During the Misers Bluff program water content measurements were made for the near surface soils and are presented in Figure 6. This was done since seasonal variations in rainfall and weather conditions may lead to changes in near surface conditions which could be important to near surface ground motion data.

In addition, two Cylindrical In-Situ Tests (CIST 15 and 16) were conducted at the PDT site. These data are presented in Reference 5. These data were also used in developing the simplified profile shown in Figure 5.

2.3 INSTRUMENTATION PLAN

Instrumentation layouts for the single burst events are presented in Figures 7 through 11. Instruments used in these events were Endevco Accelerometers, Sandia DX and Bell and Howell velocity gages, Kulite air pressure gages, and WES SE stress gages. The capabilities and limitations of these gages are discussed in Reference 6.

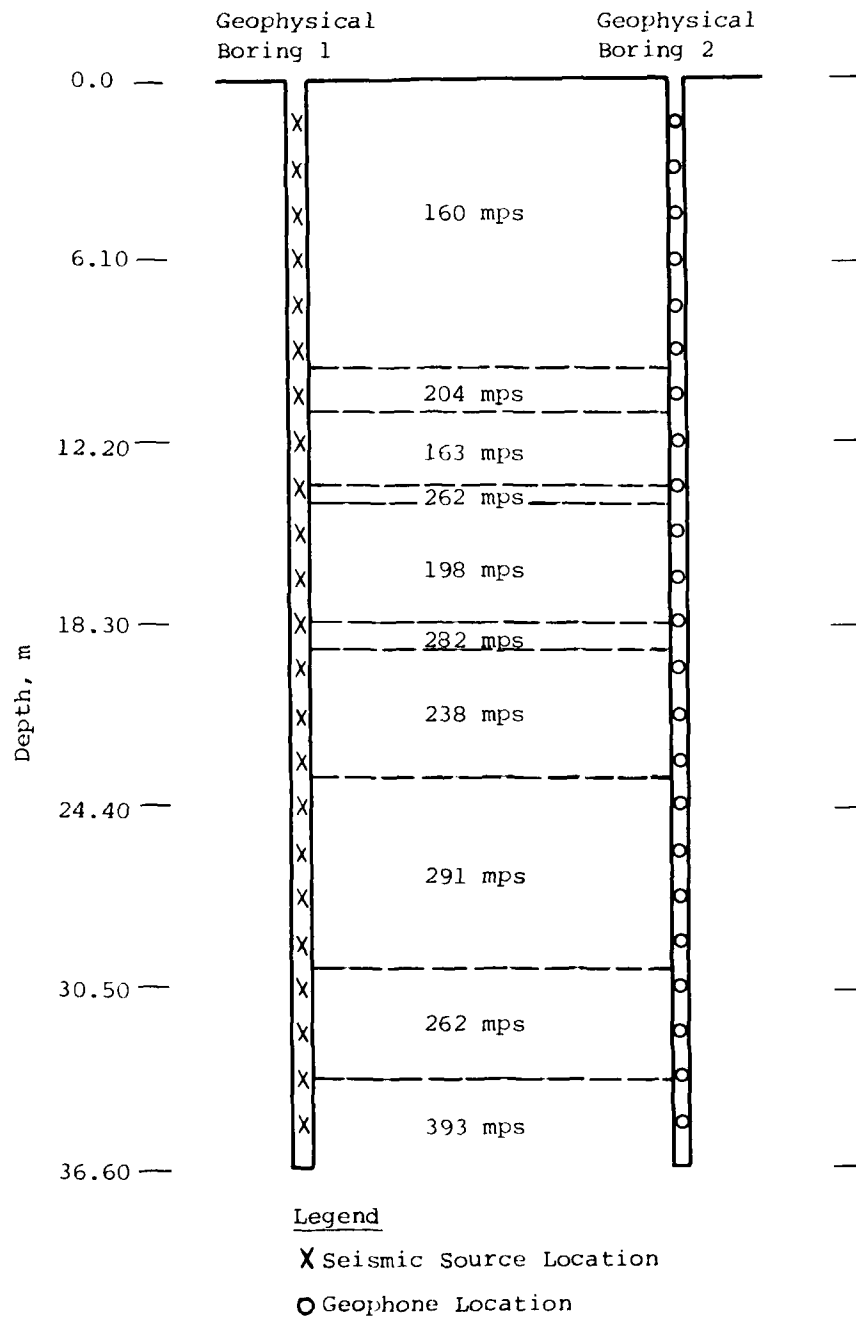


Figure 4. S-wave Velocity Profile Interpreted from Crosshole Seismic Data (from Reference 3)

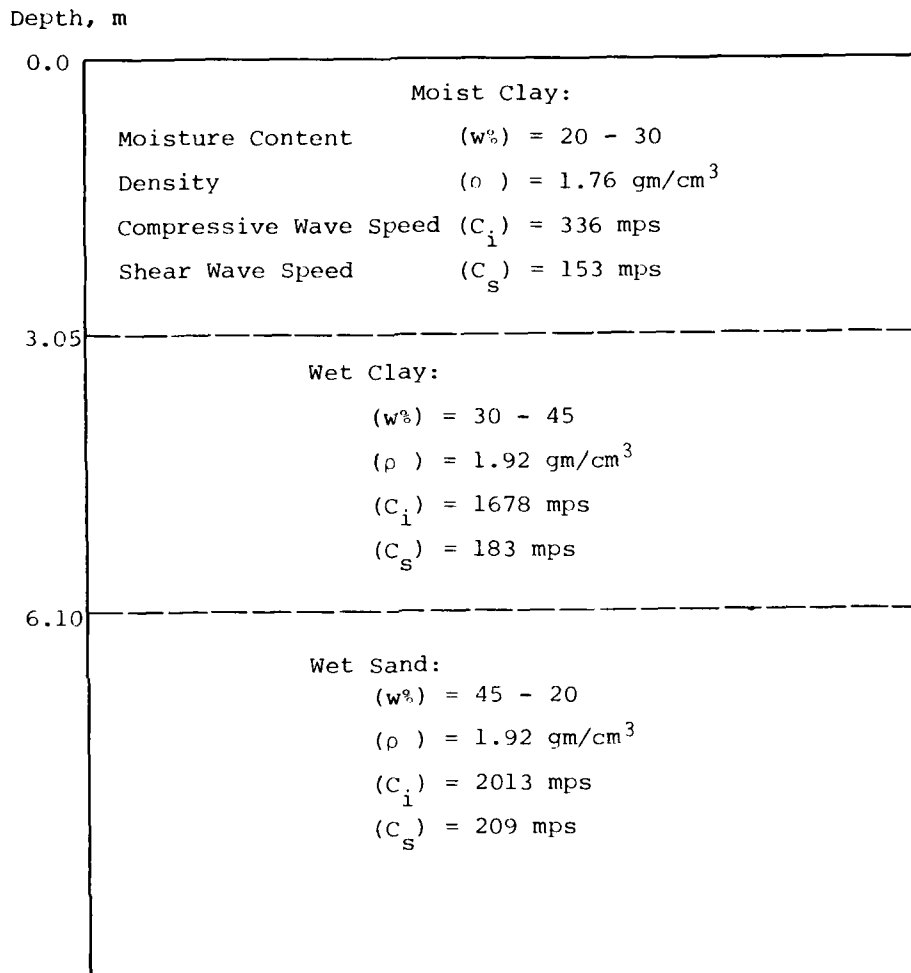


Figure 5. Simplified Seismic Profile of Misers Bluff Phase I Test Bed (Reference 3)

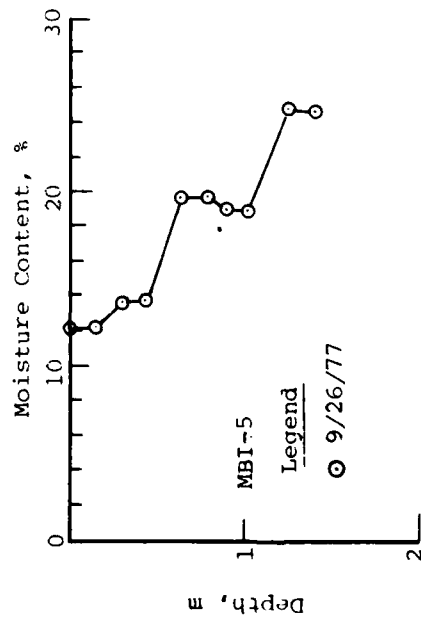
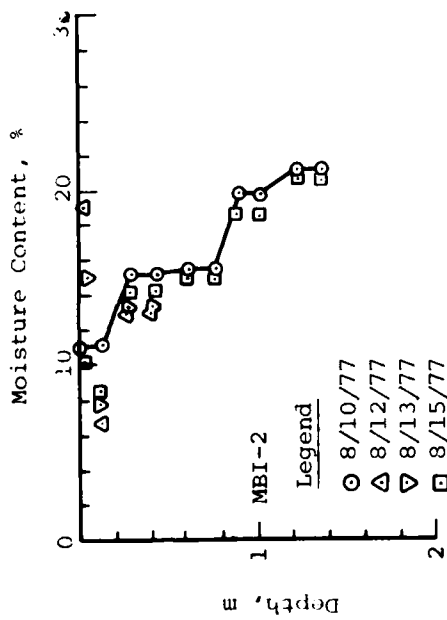
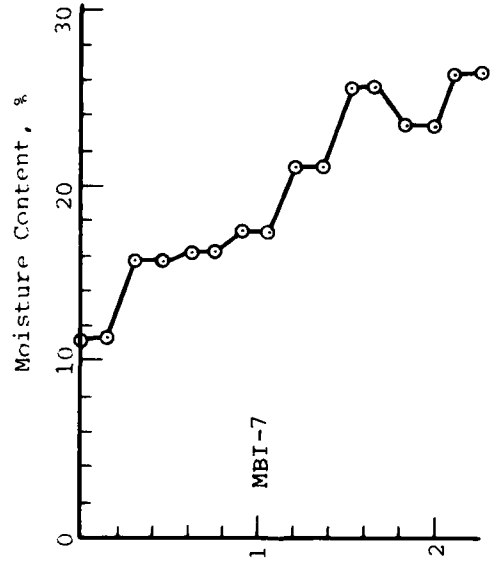
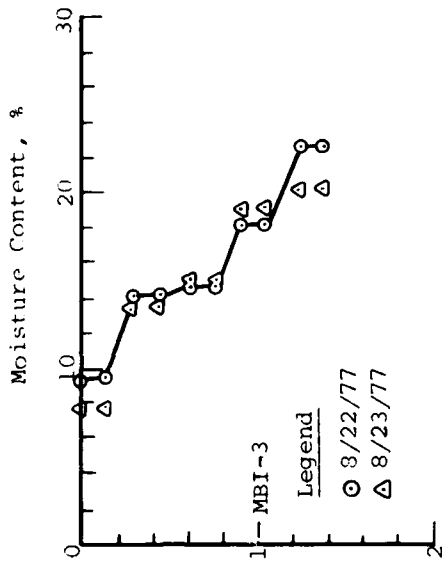


Figure 6. Moisture Content Data Measured for Single Burst Events

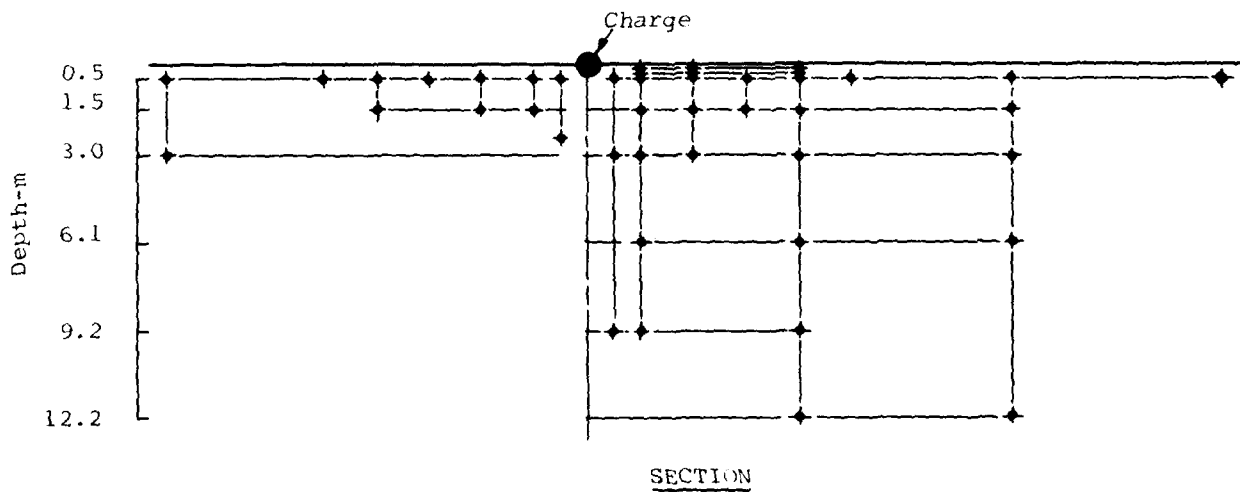
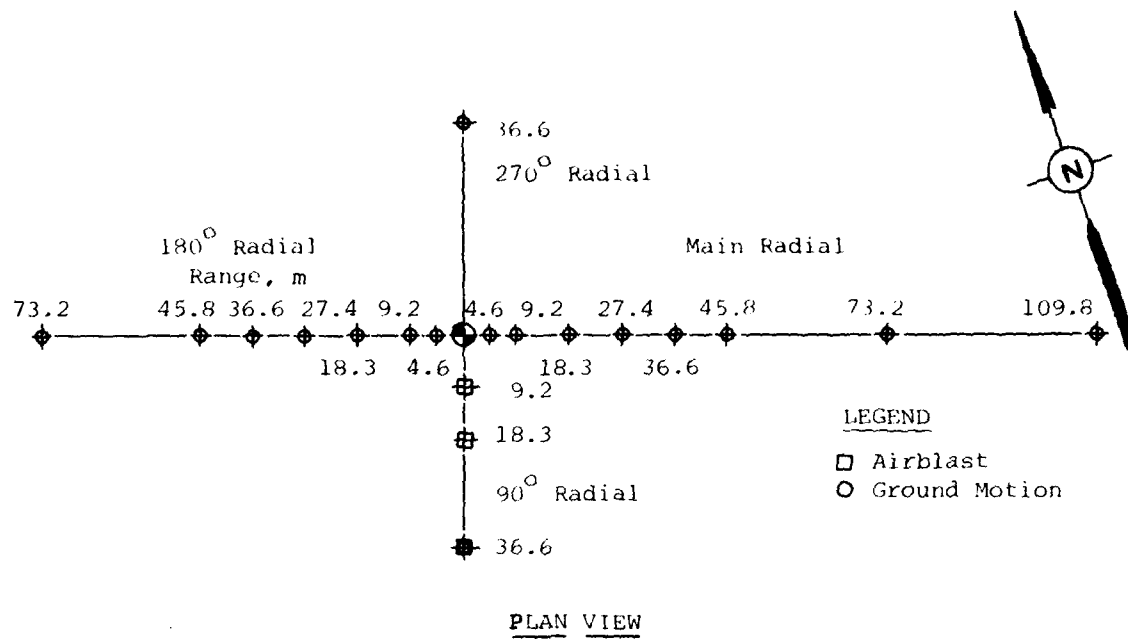


Figure 7. Gage Layout for Event 1 - Half Buried Configuration

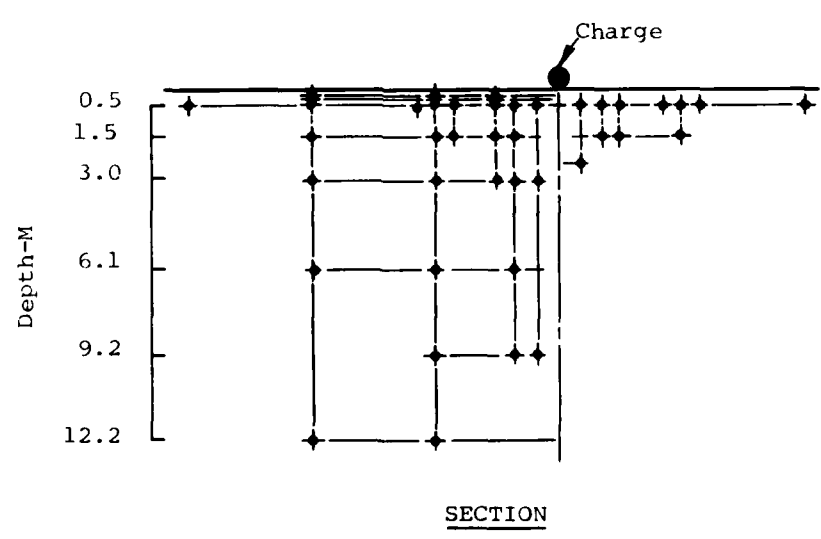
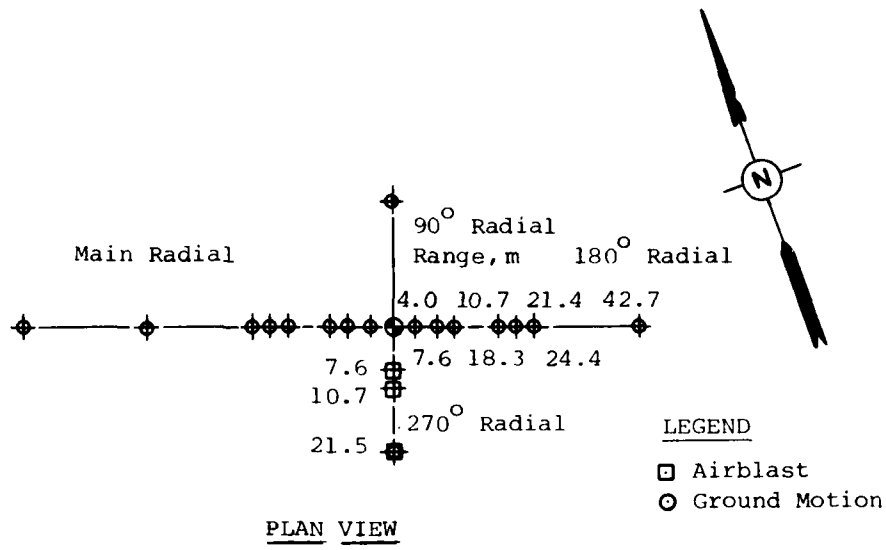


Figure 8. Gage Layout for Event 2 - Surface Tangent Configuration

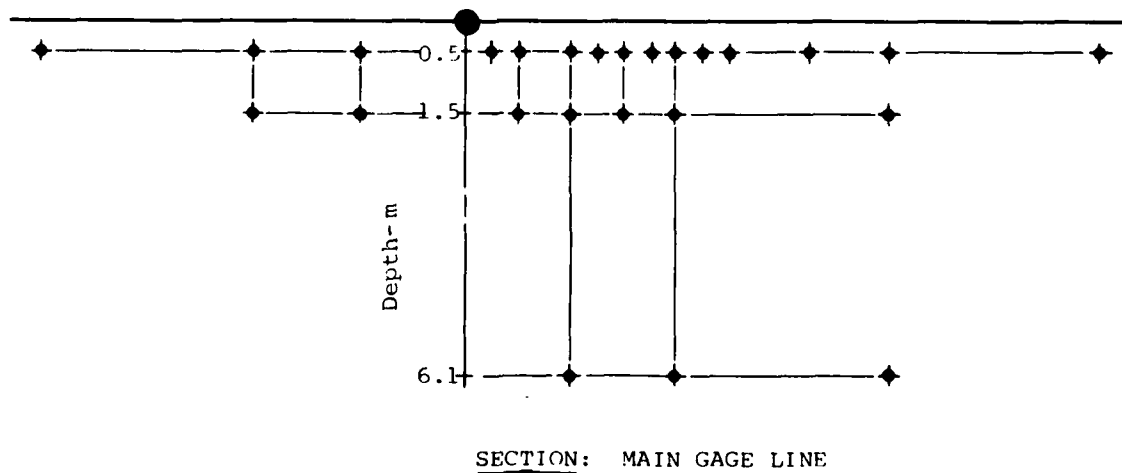
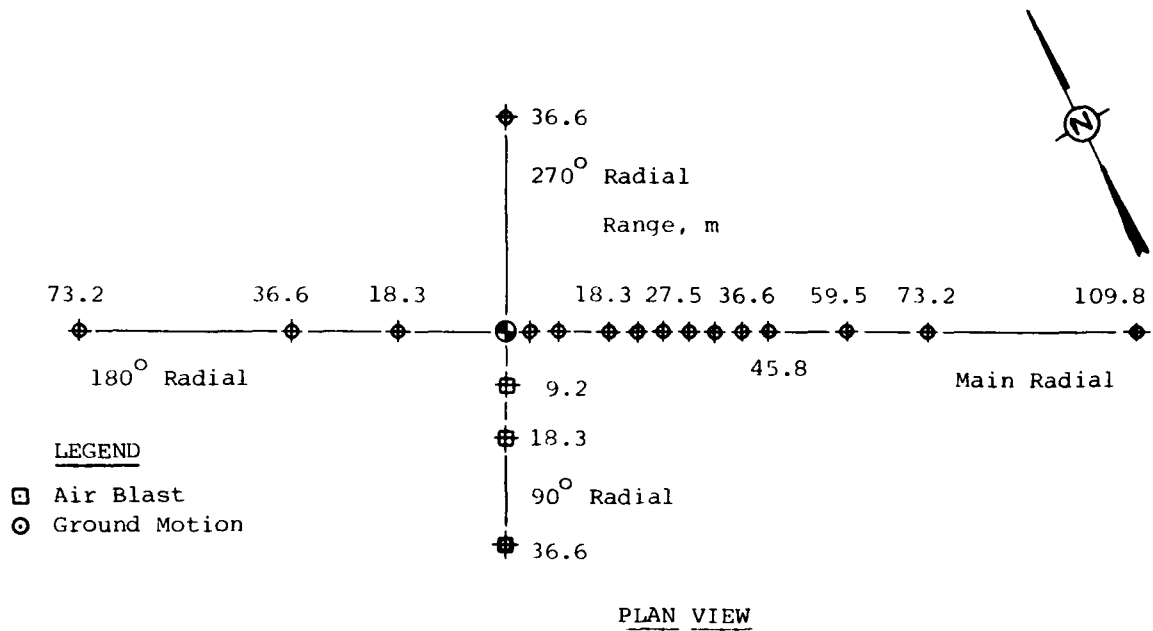
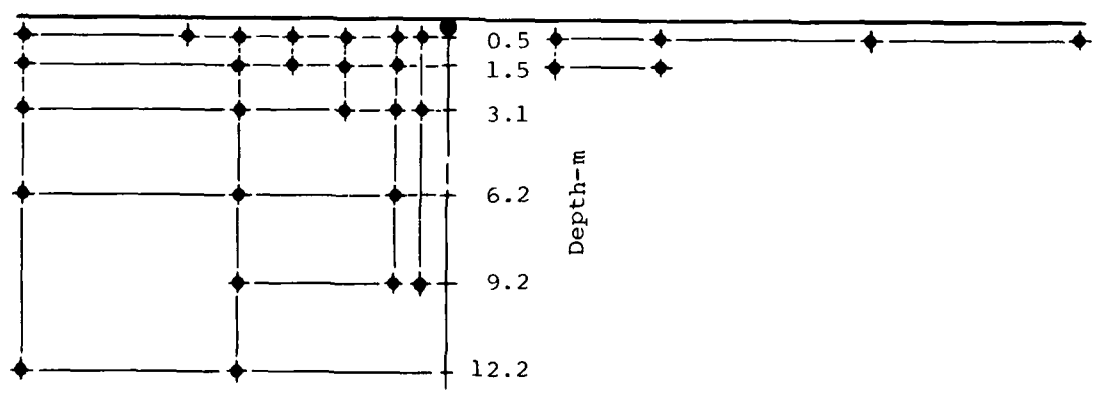
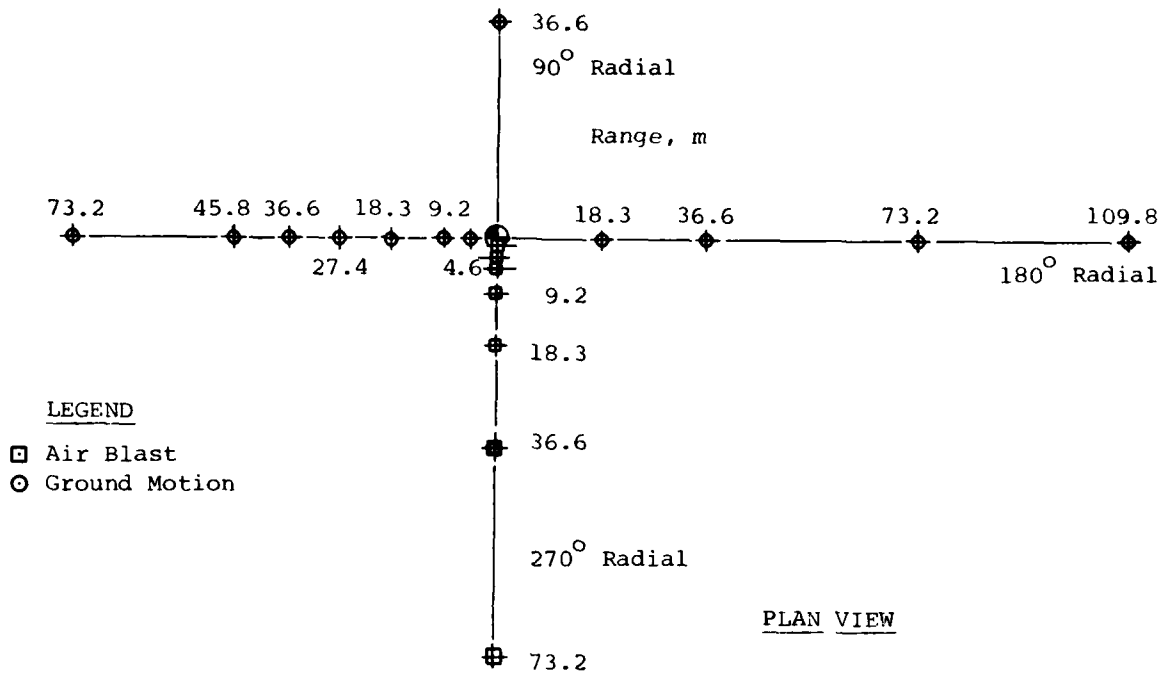


Figure 9. Gage Layout for Event 3 - Half Buried Configuration.



SECTION: MAIN GAGE LINE

Figure 10. Gage Layout for Event 5 - Tangent Below Configuration

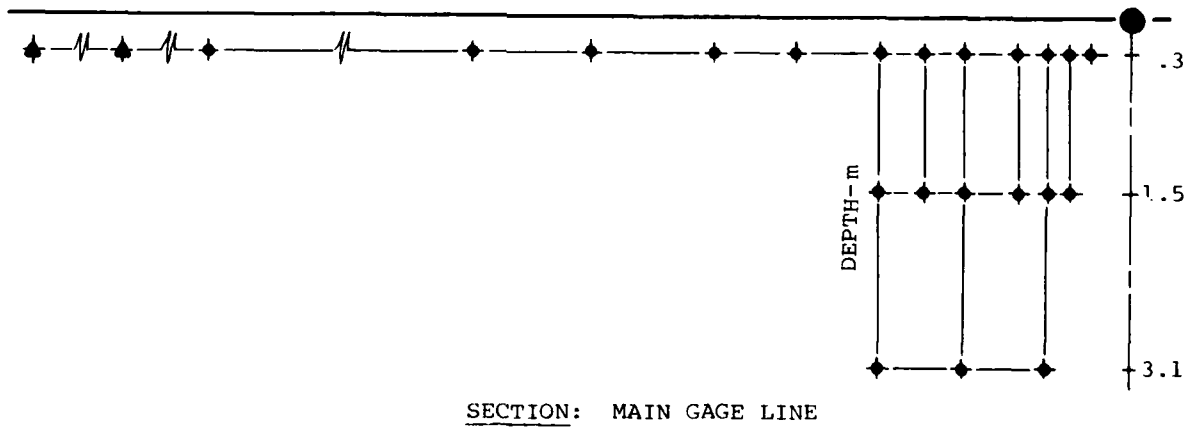
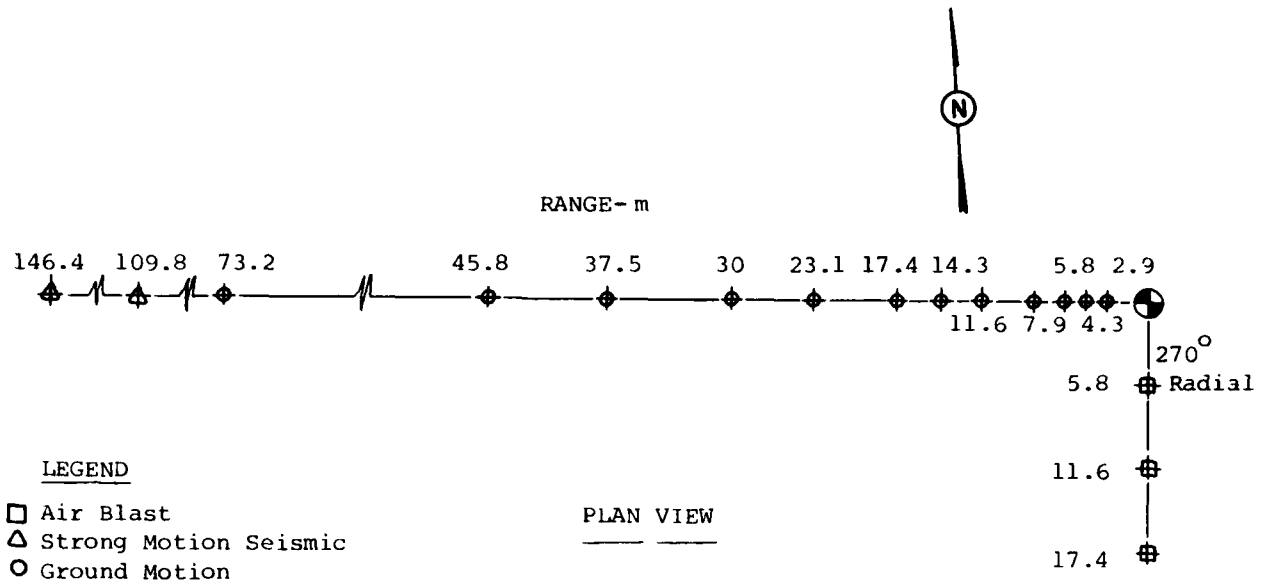


Figure 11. Gage Layout for Event 7 - Half Buried Configuration

Initial data reduction for this series was performed by the U. S. Army Engineer Waterways Experiment Station, Vicksburg, Mississippi. They provided corrected data plots at scales of 1 in = 200 msec to 1 second with amplitude scales automatically selected by the plot program. WES then provided corrected data plots to the AFWL who made additional plots with expanded time and amplitude scales. Shock spectra and Fourier spectra were also provided by WES on selected records.

3.

PREDICTION METHODS

3.1 GENERAL

No standard procedure is available for predicting the ground shock from high explosive detonations. The procedures which we have used, are based on prediction procedures developed for nuclear events of much greater yields. The "usual" procedure for the prediction of HE events is to modify (sometimes scale) the results of a "similar" yield event in a "similar" geology based primarily on the judgement of the experimenter. The major disadvantages of this scaling procedure are that a great deal of judgement is required, therefore, only experienced practitioners can make predictions, and comparison of test data and predictions after the event cannot be generalized to assess the status of our predictive capability. For these reasons we have chosen to follow a set procedure wherever possible, even though the procedures were intended for predictions of large yield nuclear events. When this was not possible we have chosen an objective approach which can be generalized and have documented the procedure so that it may be applied in future prediction efforts.

In general, these same procedures were followed in the Pre-Dice Throw predictions (Reference 7).

3.2 PREDICTIONS

3.2.1 Airblast

The airblast environment is a major input to the ground shock predictions and is well understood. Cube root scaling of both high explosive and nuclear airblast phenomenon has been shown to be valid. The predictions of airblast were made with standard procedures and will be discussed only briefly.

The parameters associated with the airblast environment are shown in Figures 12 and 13. Predictions for the half buried charge configuration were scaled from Reference 8 and checked against the Middle Gust data (Reference 9). Predictions for the surface tangent

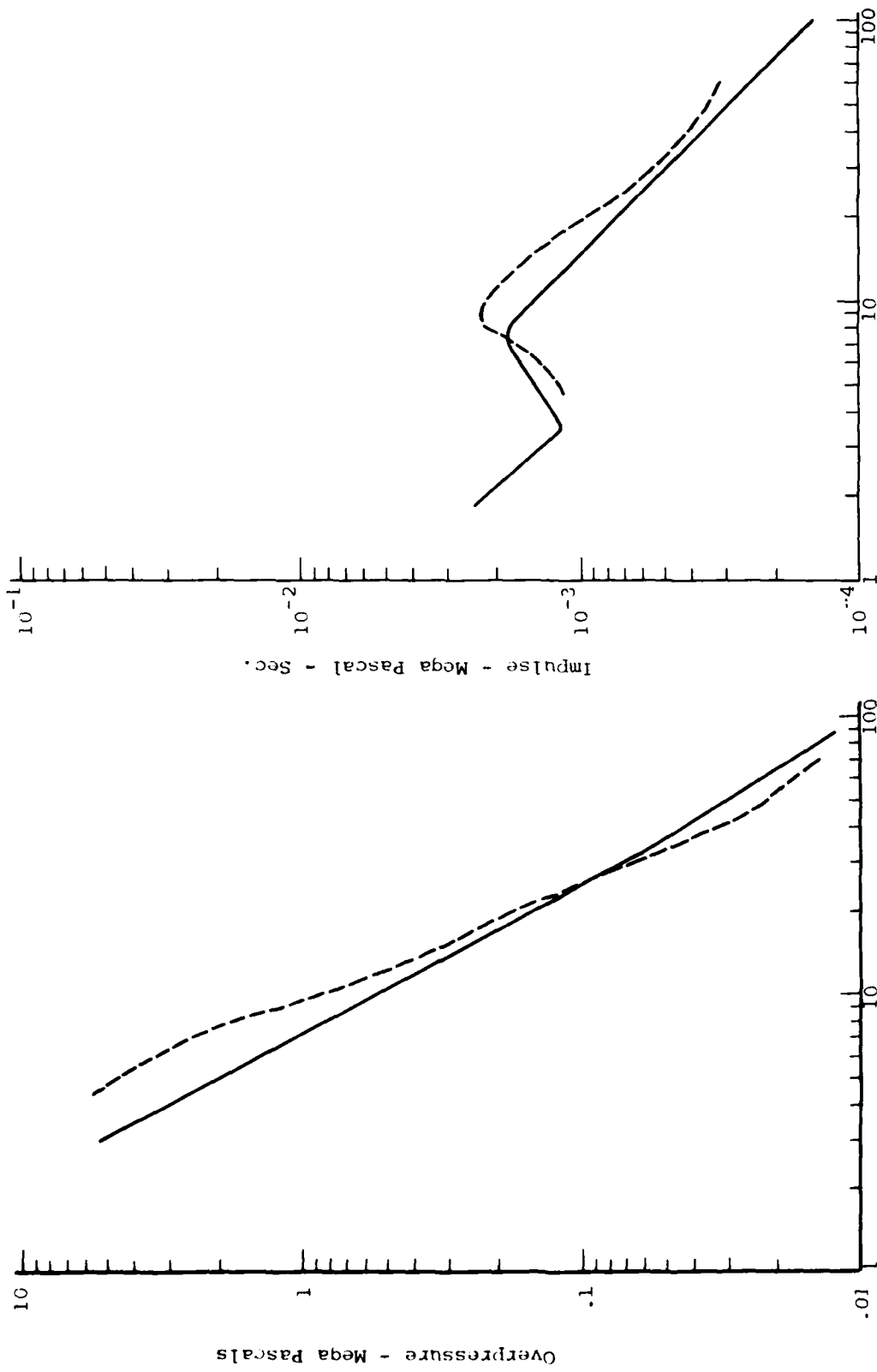


Figure 12. Prediction Curves of Overpressure and Impulse for Surface Tangent and the Half Buried Configurations.

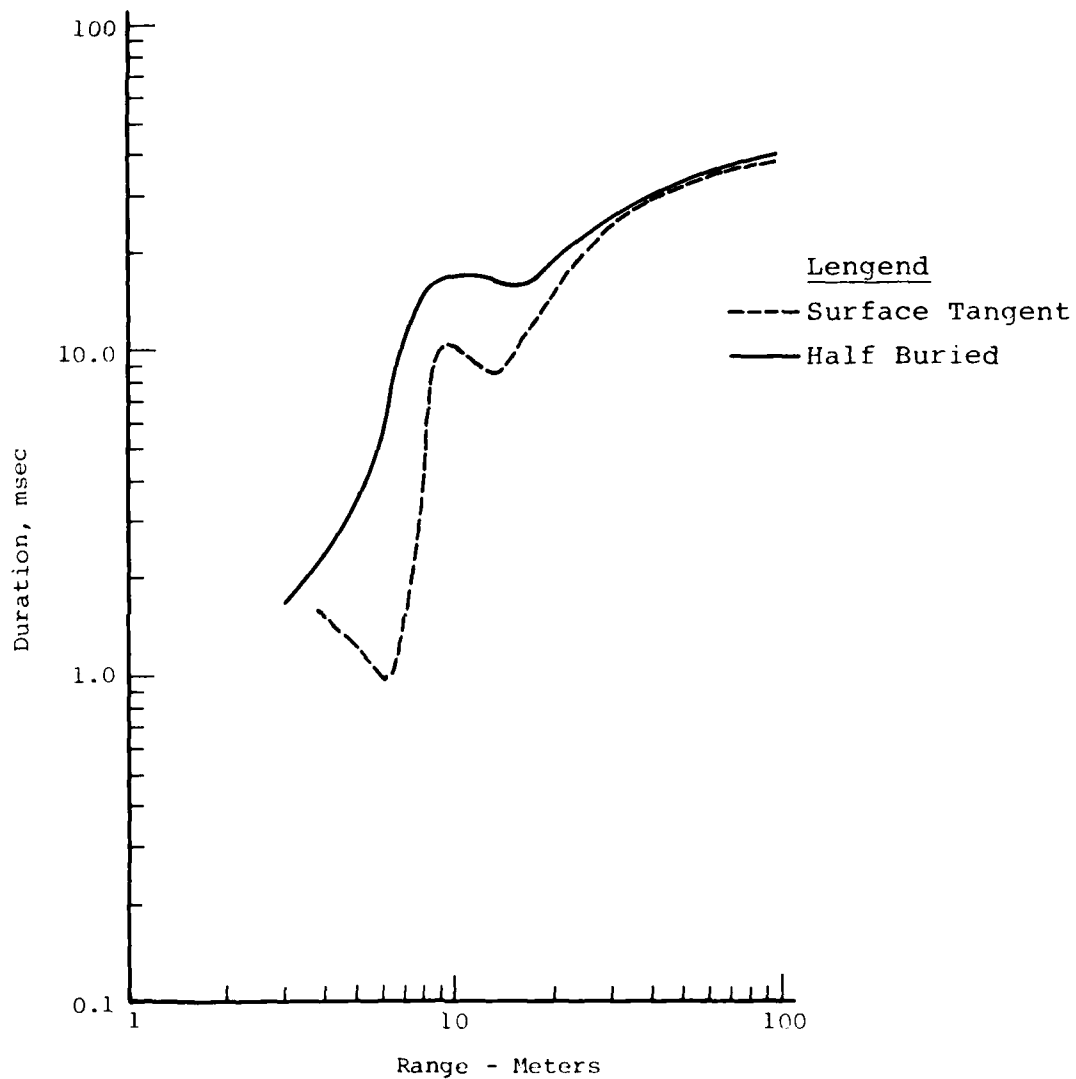


Figure 13. Predicted Curves of Duration for the Surface Tangent and Half Buried Configurations.

configuration were scaled from Middle Gust and other data. Airblast time of arrival plots are shown on Figure 14.

3.2.2 TOA Contours

The ground shock predictions which will be discussed in the following sections involve the superposition of the air slap, outrunning and crater related effects. In order to properly time phase these effects, it is necessary to predict the arrival time of each effect as a function of both range and depth. The procedures for predicting these time of arrival contours are the same as recommended in Reference 10 for the nuclear case. The airblast-related time of arrival contours are shown in Figures 15 and 16. These contours represent the first arriving compressional wave and are based on the airblast time of arrival (Figure 16), the seismic profile (Figure 5), and the theory of elastic wave propagation. The outrunning effect of the higher velocity layers is clearly evident. The 16 msec contour illustrates the phenomenon fairly well. At 16 msec the airblast is at a range of 20.6 meters. The contour from the surface to a depth of 2 meters is controlled by the local airblast p-wave and results in what is commonly called the air slap motions. Between the 2 meter depth and the saturated layer at 3 meters, the first arriving signal is a compressional head wave which was generated by the upstream airblast energy traveling through the second layer. From the 3 to 4.5 meter depth, the first arrival is a p-wave from upstream which has traveled through the second layer. At the 4.5 meter depth and down to the layer interface at 6 meters a p-head wave is again the first arrival. The head wave was generated by the upstream airblast energy traveling in the layer below 6 meters.

The motion associated with p-waves is normal to the wave fronts, so at the 20 meter range and above 6 meter depth the initial motion will change rapidly with depth. Below 6 meters, initial motion will be down.

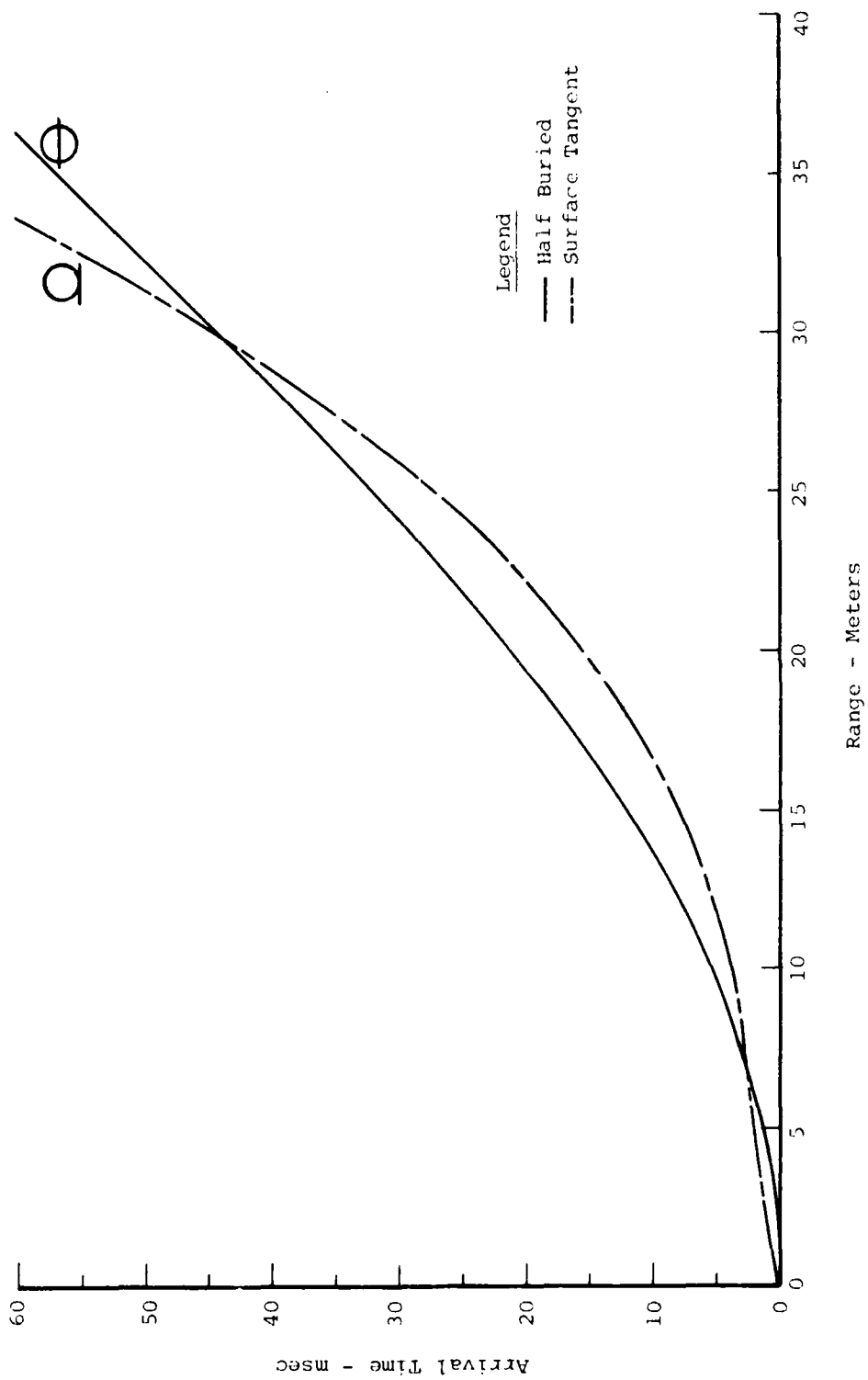
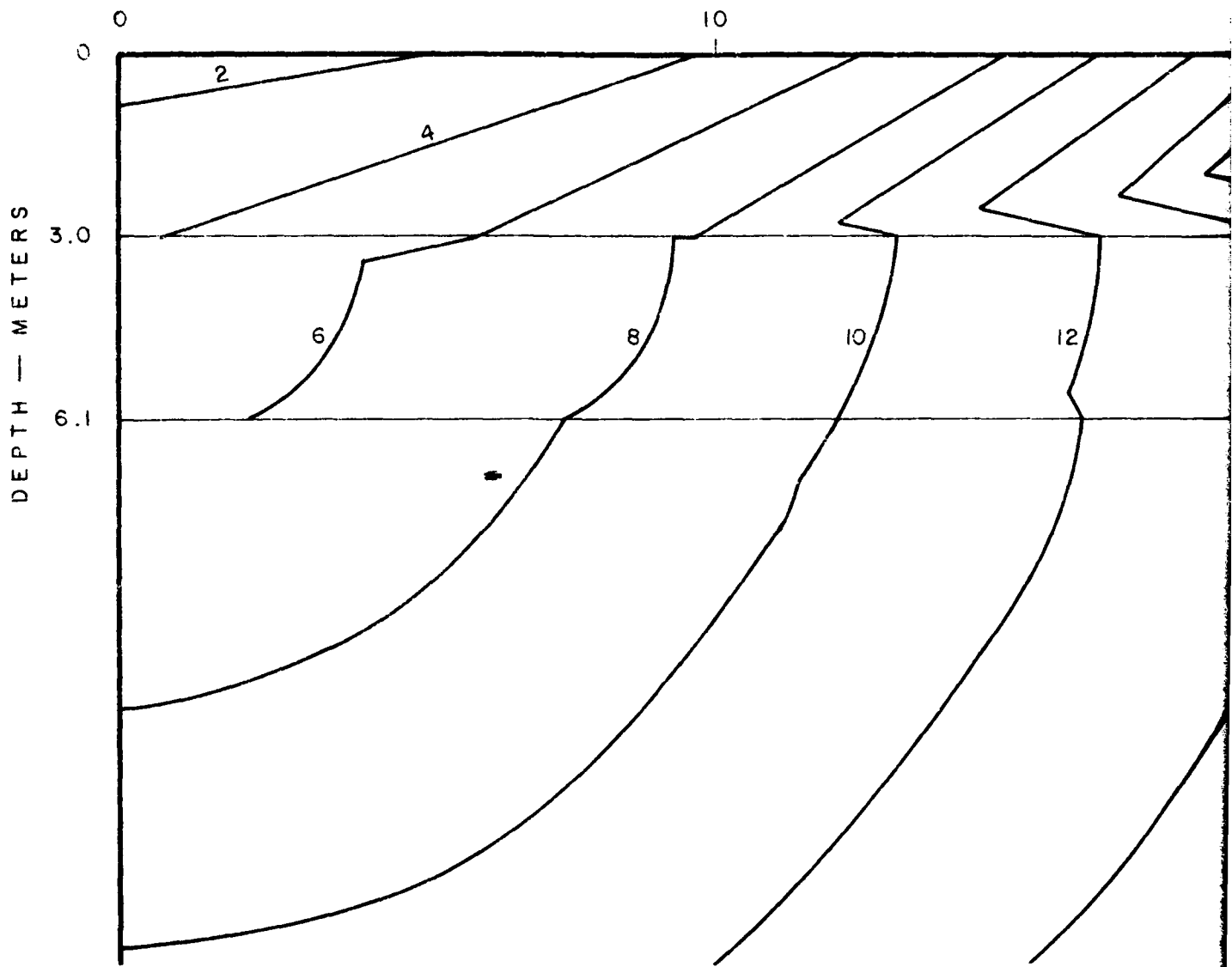


Figure 14. Arrival Time of Airblast for Surface Tangent and Half Buried Configurations



RANGE — METERS

20

30

40

14

16

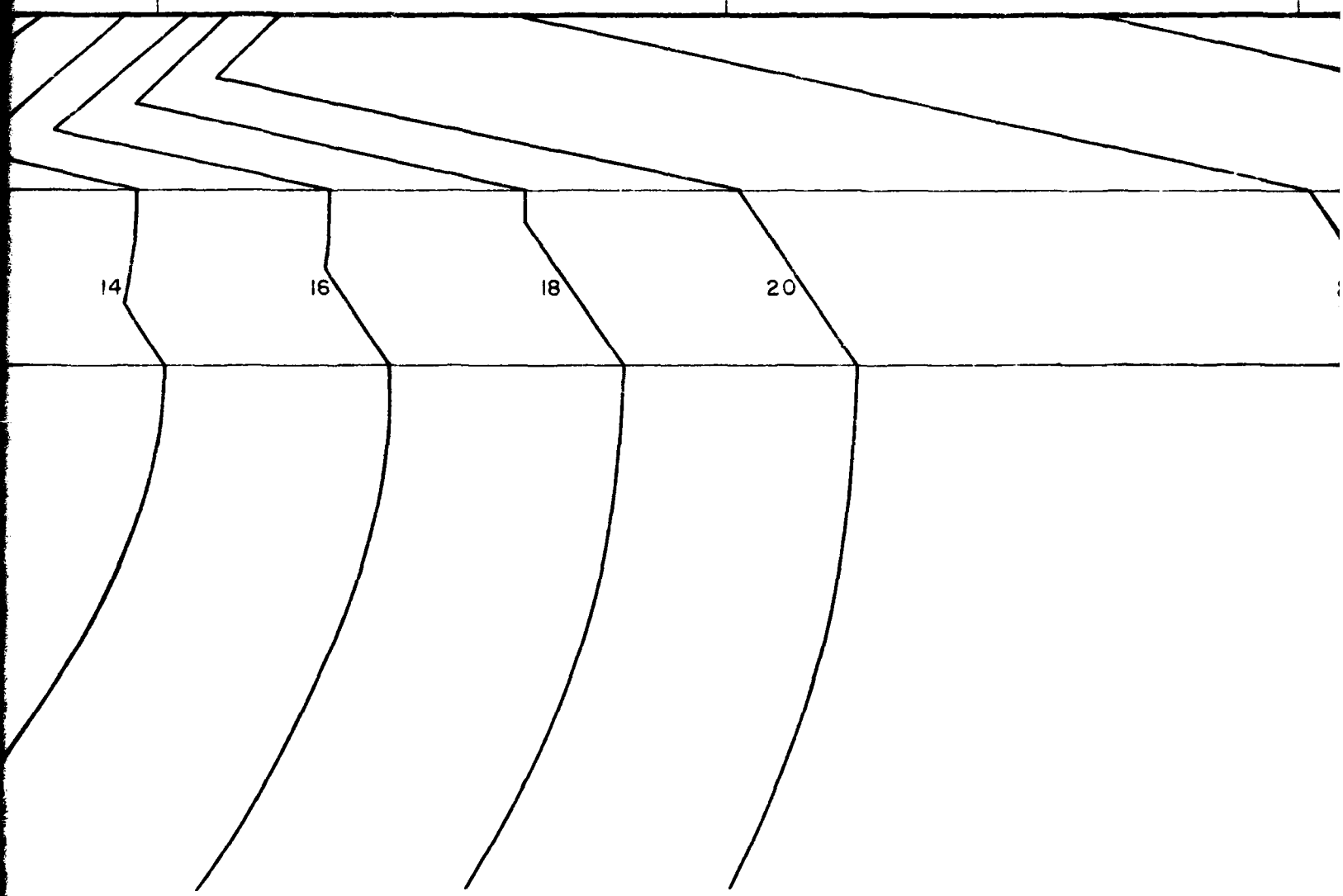
18

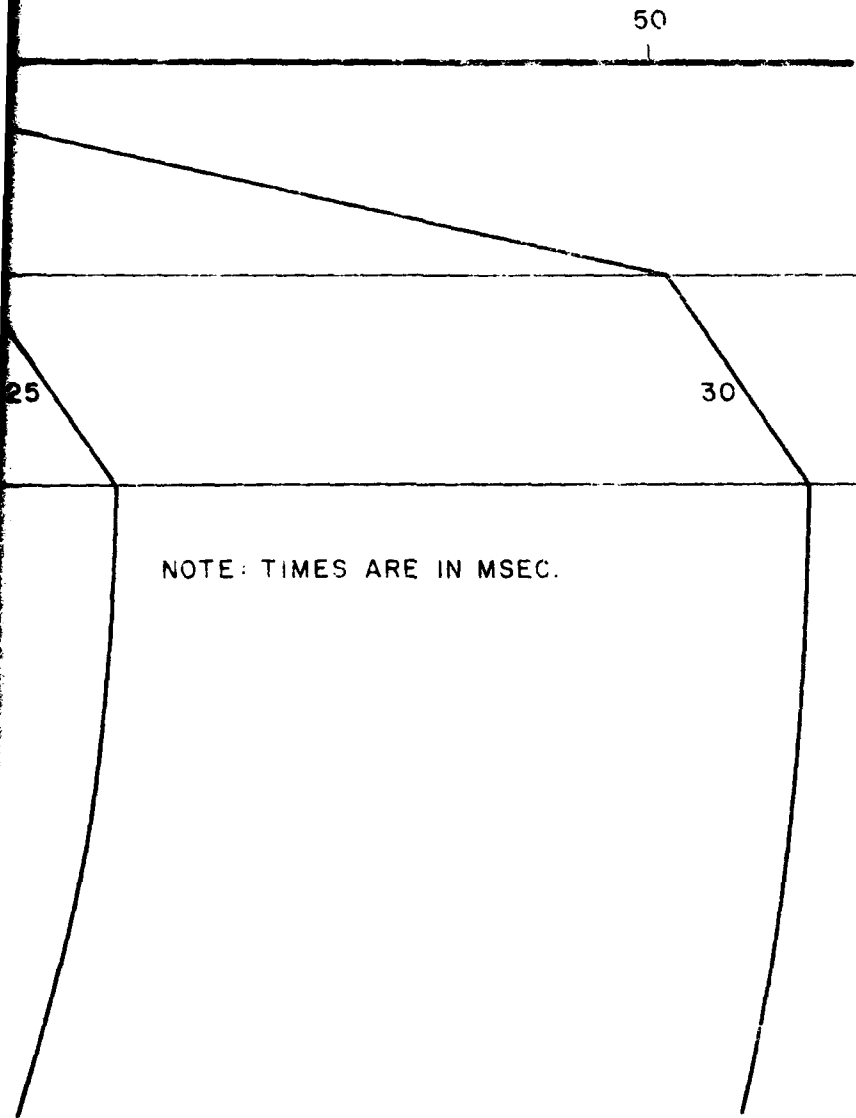
20

Figure

2

1





15: Predicted Time of Arrival Contours of Airblast Induced Motion

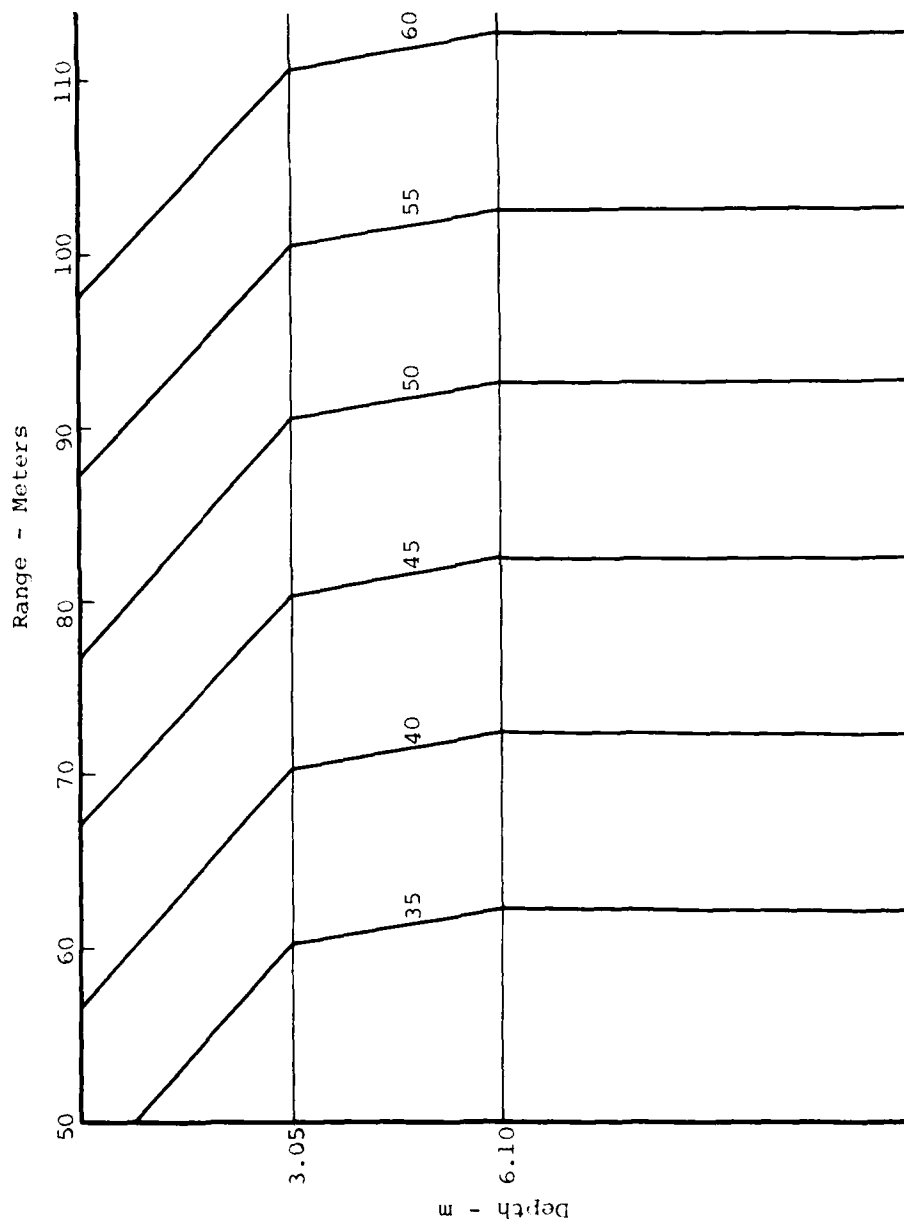


Figure 16. Continuation of Predicted Time of Arrival Contours of Airblast Induced Motion at Ranges Greater than 50 Meters

The outrunning range is defined as the range where the first motion at the ground surface is upward. This occurs at about 24.4 meters and is associated with the wave traveling through the third layer.

Similar arrival time plots for the direct induced signals are shown in Figures 17 and 18. The major differences between this and the airblast induced motions are close to the origin and associated with the point source nature of the direct induced motions. Outrunning occurs in the same manner as for the airblast induced motions and after that occurs, the contours are essentially identical. However, the direct induced waves lag slightly behind the airblast induced wave because they must travel the entire distance through the ground. The only downward motion in the upper two layers occurs at closer than 6 meters from the origin. Beyond this range the direct induced signal will either terminate the downward air slap motion or enhance the upward reflected signal.

These time of arrival contours will be used later in combining the various components of motion to produce predicted waveforms. The almost simultaneous arrival of the upstream airblast and directed induced in the superseismic region will make it impossible to separate the effects of the direct induced energy from the effects of the direct induced energy from the effects of the upstream coupled airblast energy.

3.2.3 Ground Motion

For the purpose of ground motion predictions, the procedure recommended in Reference 10 was used in that the ground shock was assumed to be composed of three components. The first component, air slap, is motion that is directly attributable to the overhead airblast. The crater related (or direct induced) component is motion that is due to the ground stresses and motions caused by the initial stress wave that results from the energy coupled at the burst point. The prediction procedure used crater volume

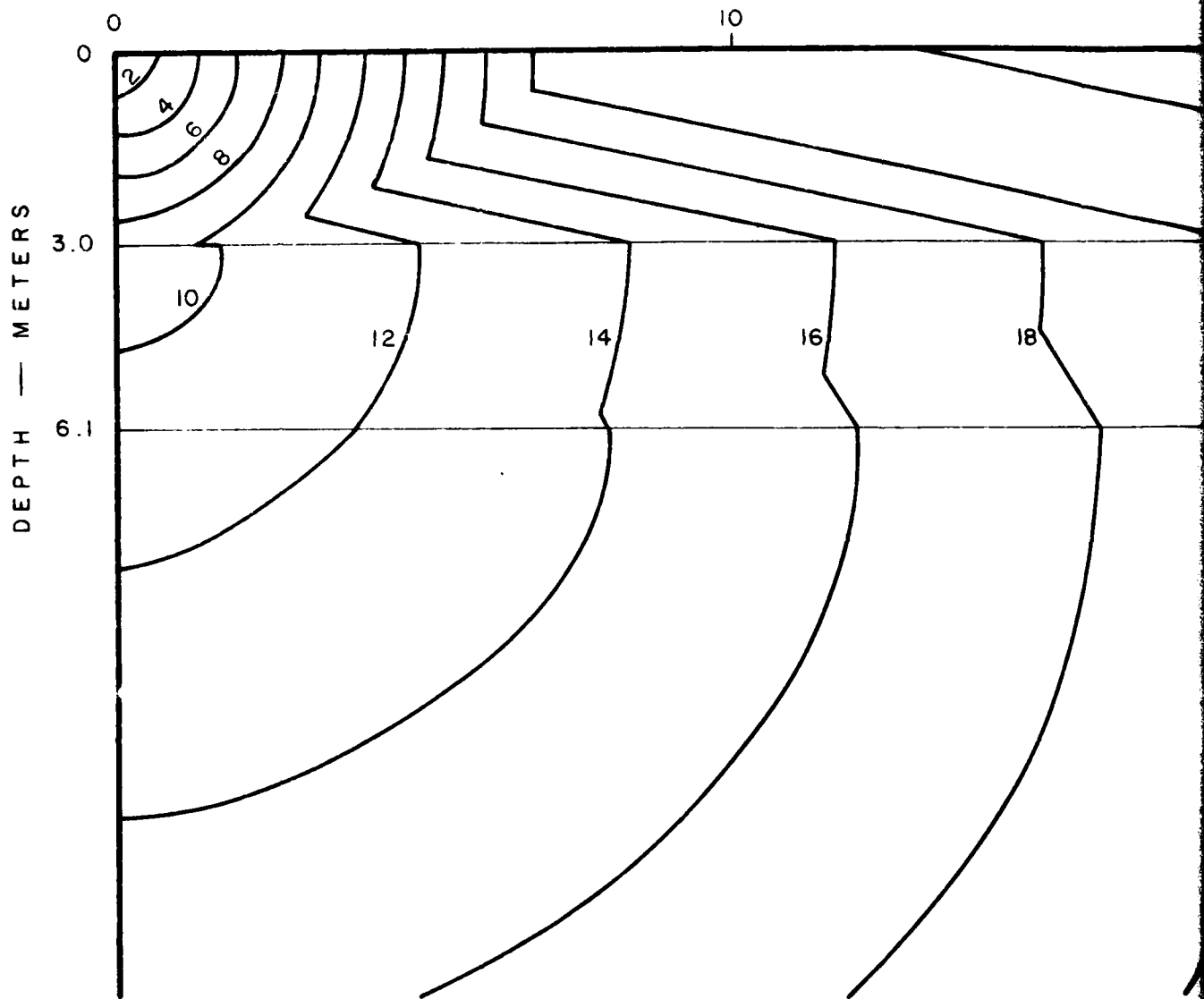


Figure 17: Predicted Time of Arrival Contours of Direct Induced Motion

RANGE — METERS

20

30

40

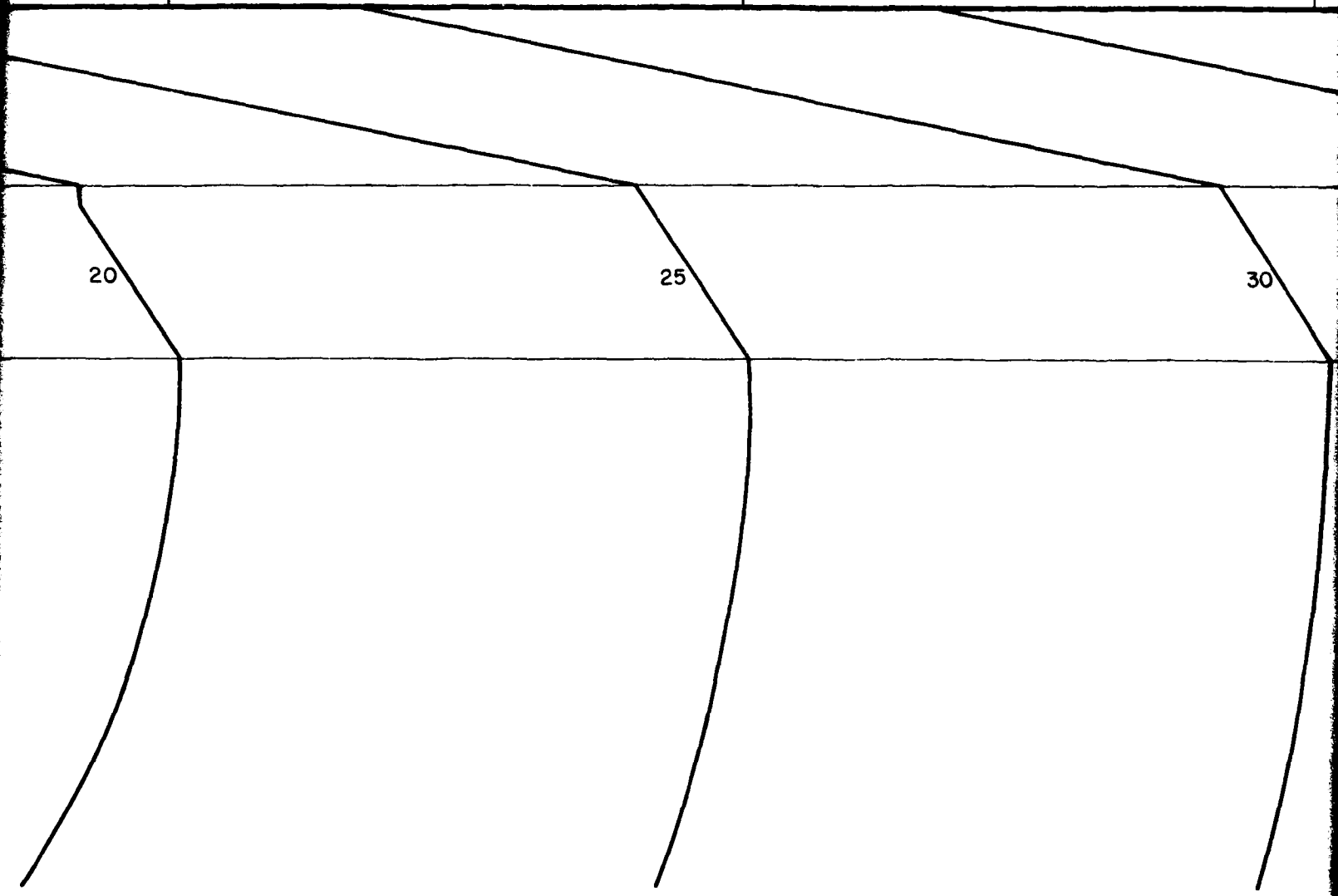
20

25

30

1

2



40

50

35

NOTE: TIMES ARE IN MSEC.

W

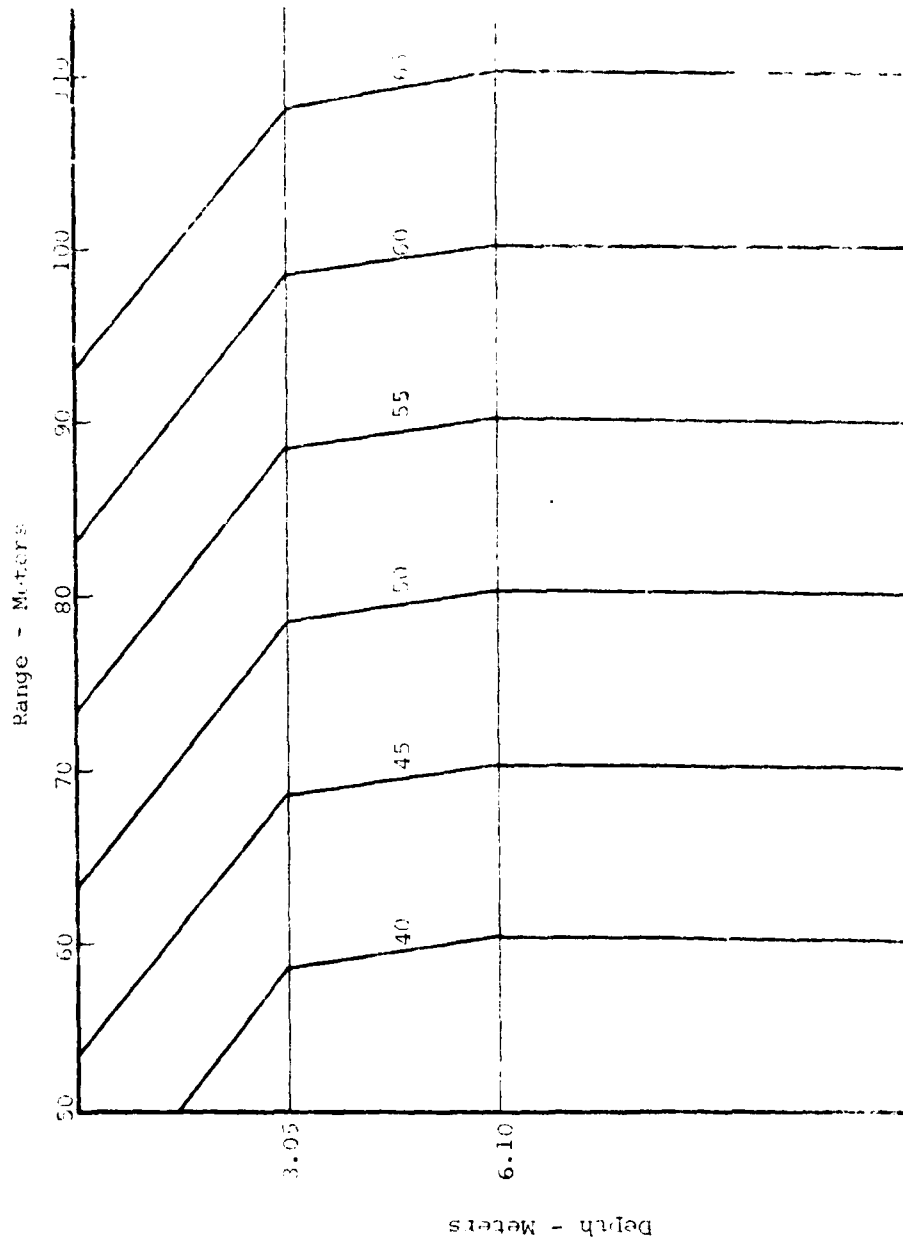


Figure 18. Continuation of Predicted time of arrival contours for induced motion at Ranges Greater than 50 Meters

scaling and does not differentiate between upstream airblast and crater related motions, therefore the upstream airblast effects are not predicted independently. The final component is the oscillatory component which included the initial head waves and the surface waves and becomes the dominant feature of motion in the outrunning region. The peak values and waveforms for each component were predicted independently and the results superimposed to develop the composite waveforms.

In the following sections the prediction curves presented will be for the half buried configuration. These are shown here for illustrative purposes, and the reader is referred to Section 4 in which the prediction curves for the other configurations are compared with the data.

a Air Slap Component. The air slap component of ground motion is the best understood of all ground motion phenomena, therefore, predictions of the vertical component are possible with relatively high confidence. The horizontal component is related to the relative velocity of the airblast and near surface layers as well as the shear properties of these near surface materials. Much less success has been achieved in predictions of this component.

Procedures for predicting the vertical component of the air slap motion include one- and two-dimensional finite difference calculations and the AFDM empirical procedure. The AFDM procedure (Reference 10) was used in predicting the events reported herein.

Examples of the peak accelerations, velocities and displacements predicted by AFDM for Event 1 are shown in Figures 19 through 21. The most significant result shown in these figures is the rapid attenuation of both acceleration and velocity with depth.

b Oscillatory Component. Predictions of the oscillatory component of motion has received considerably less attention and predictions of it are less certain. Therefore, two techniques were utilized in predicting this component. The procedures contained in

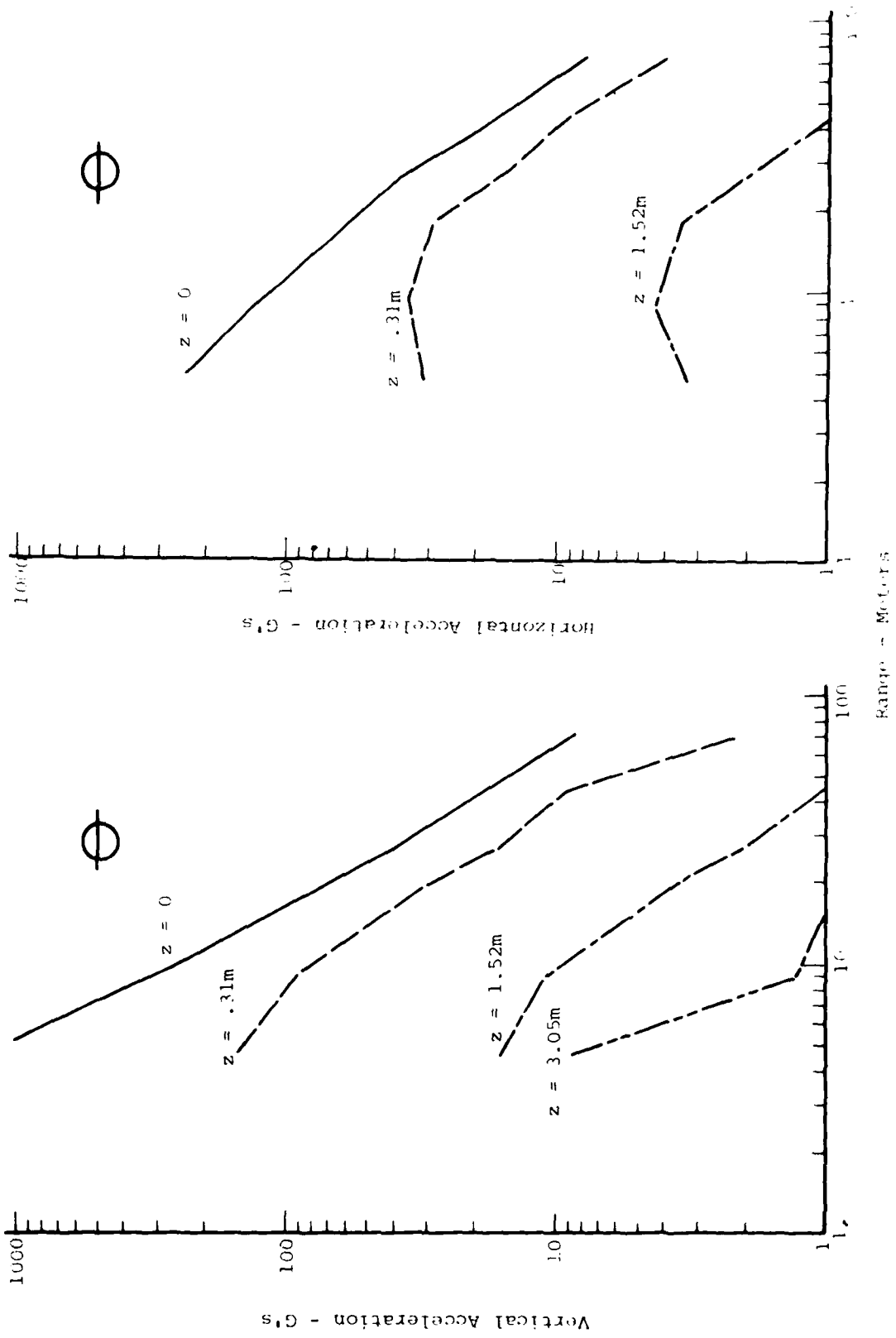


Figure 19. Prediction Curves of Airblast Induced Acceleration for the Half Buried Configuration

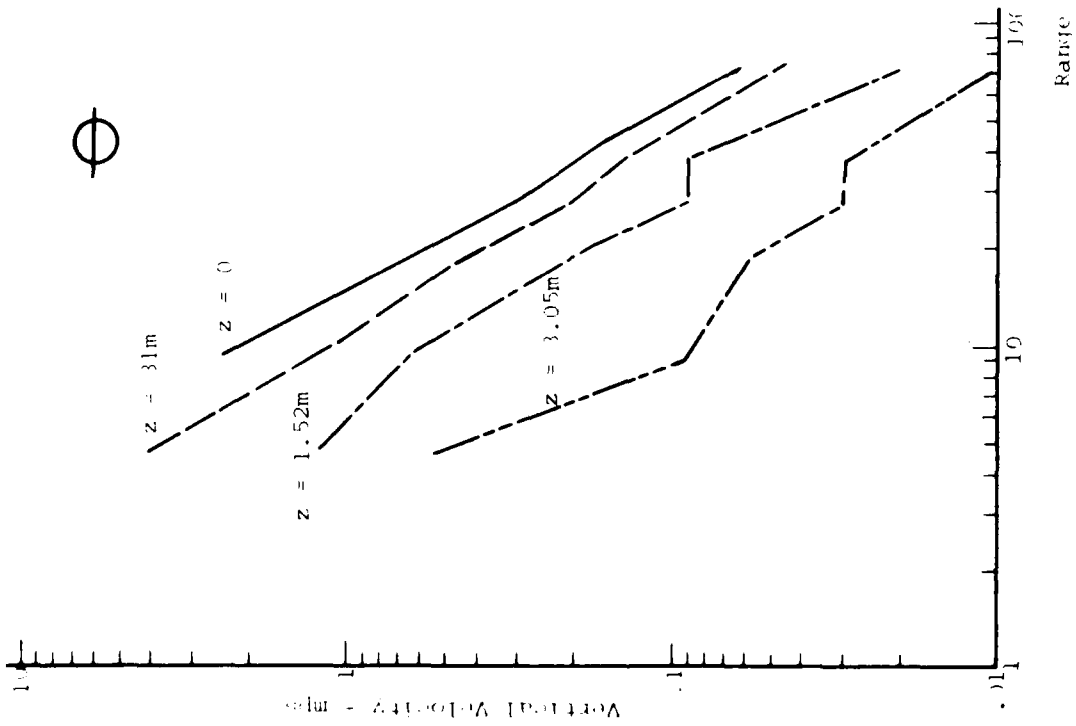
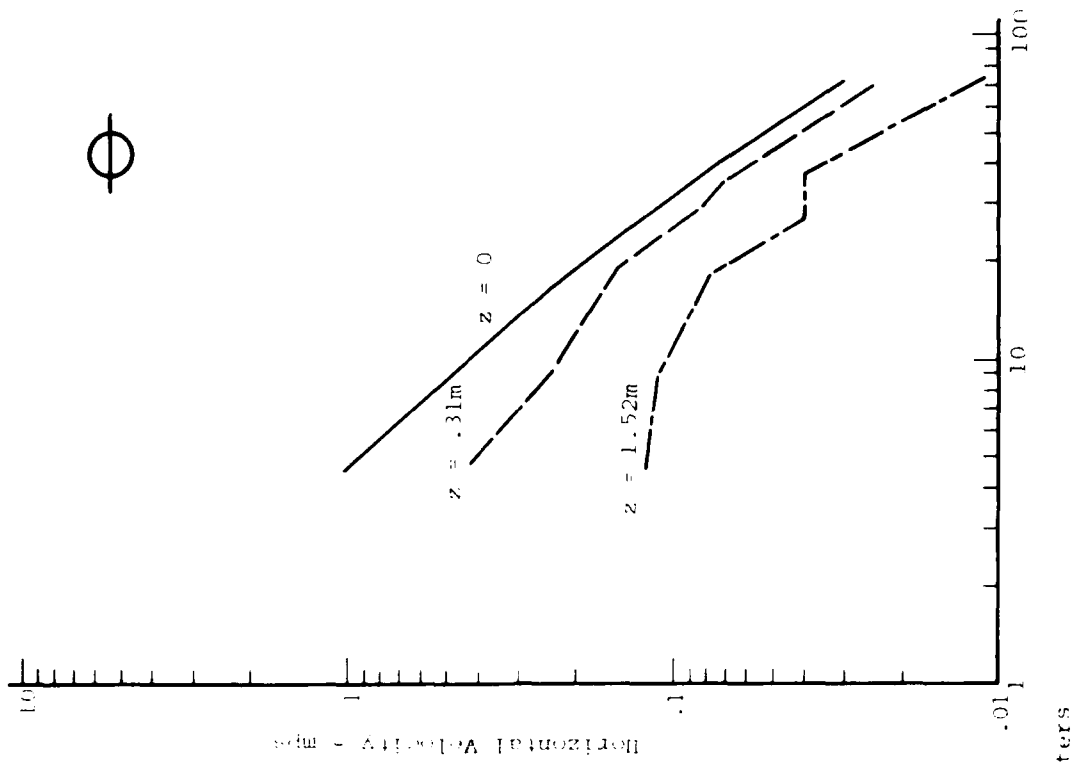


Figure 20. Prediction Curves of Airblast Induced Velocity for the Half Buried Configuration

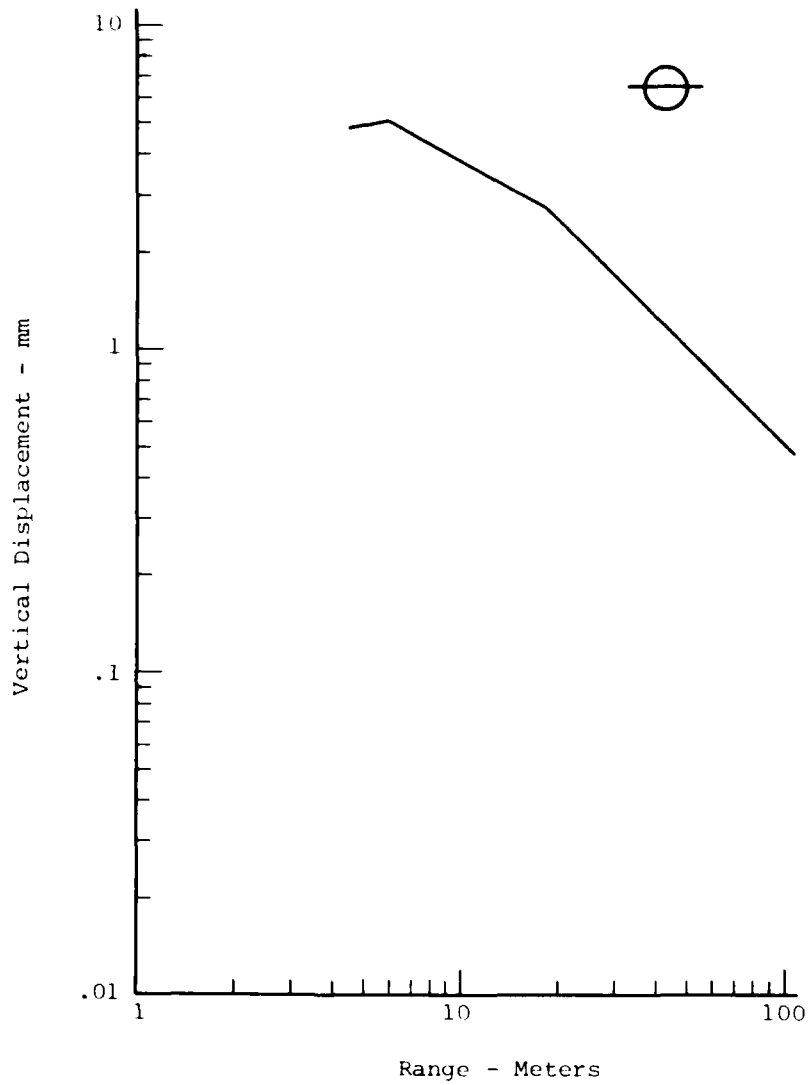


Figure 21. Prediction Curve of Airblast Induced Surface Displacement for the Half Buried Configuration

the AFDM were developed from an analysis of nuclear data whereas those developed by Higgins in Reference 11 were based on analysis of high explosive data. Both procedures involve cube root of the yield scaling for vertical motions. The AFDM presents a single waveform for all ranges whereas Reference 11 recommends three different waveforms for different scaled ranges and recommends that the ranges be scaled by the cube root of the crater volume. It also recommends different waveforms for vertical and horizontal motions.

Predictions of peak velocities were made using both procedures and are compared in Figure 22. Reference 11 does not predict displacements directly, however, this can be obtained by integration of the velocity time histories.

Fairly significant differences in predicted vertical amplitudes are evident in the plots of both the peaks and waveforms. (Figures 22 and 23). This discrepancy was not expected and led us to evaluate the procedures carefully. Both techniques suffer in regard to prediction of low yield HE events in that no such data was included in the development of the procedures. However, the Reference 11 analysis is based on HE data where the Reference 10 analysis is based on nuclear data. In addition, only Nevada Test Site data from noncratering burst was used in developing the Reference 10 procedure. As a result the decision was made to use Reference 11 since it was based on HE shots in geologies more like the Misers Bluff site.

A second major discrepancy was observed in the predicted horizontal motion periods. Representative waveform comparisons are shown in Figure 23. The development of the period scaling relationship in Reference 11 did not include a very large range in yields and the horizontal component was based only on crater volume. After examination of Middle Gust (2.09×10^{-3} terrajoules) and Mole (5.35×10^{-4} terrajoules) data, and the vertical period predicted by both procedures, it was decided that a horizontal period of 100 msec would be used in predicting waveforms.

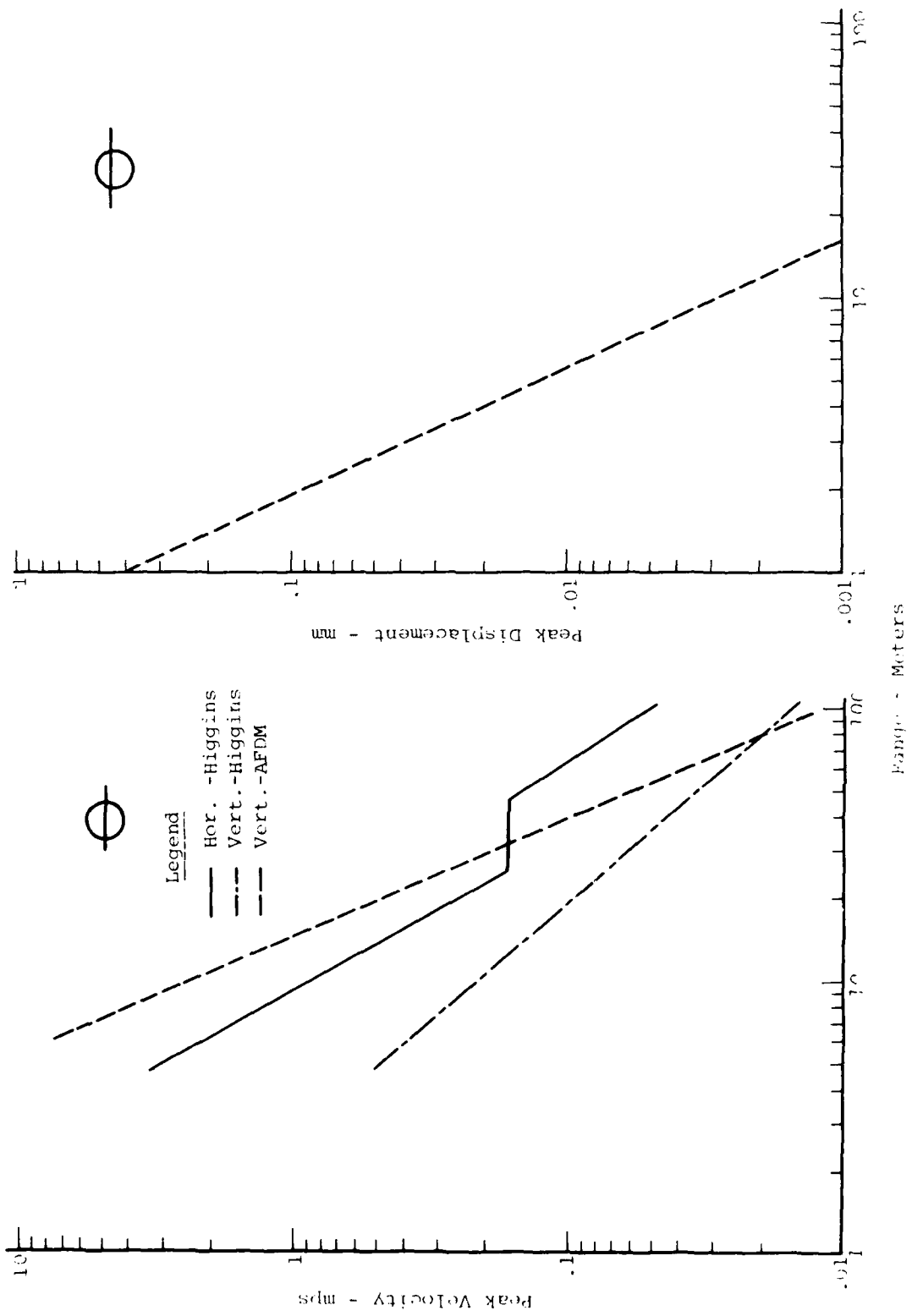


Figure 22. Prediction Curves of Oscillatory Component for the Half Buried Configuration.

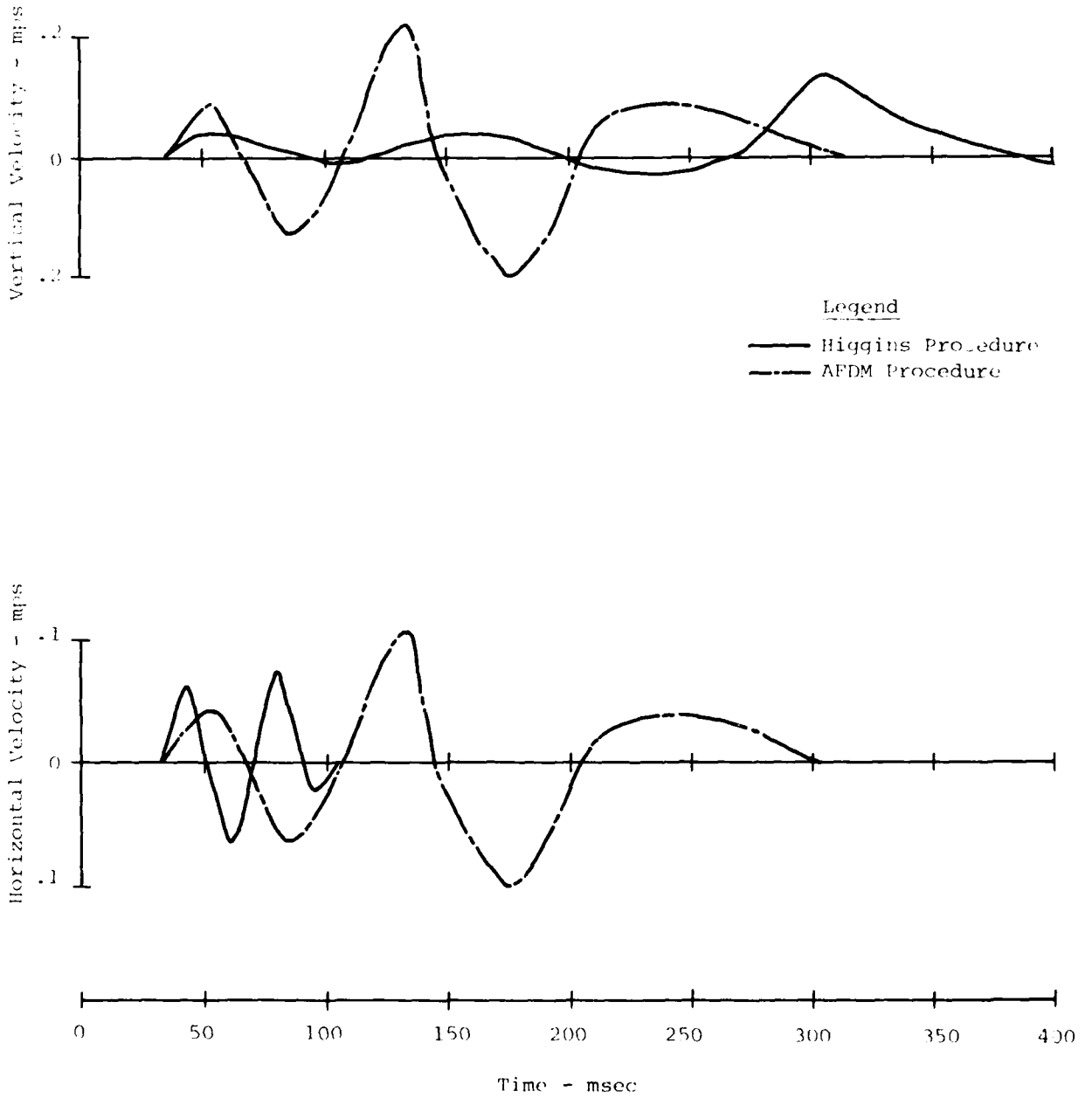


Figure 23. Comparison of Prediction Procedures for the Oscillatory Component of Ground Motion at the 36.6m Range.

The prediction of the horizontal oscillatory component period certainly deserves more study. At the present time it appears that the AFDM procedure should be used in predicting nuclear events.

c Crater Related Component. The prediction of crater related motions require estimates of the apparent crater volume. This was predicted using Figures 24 and 25 from the AFDM for determining cratering efficiency and the effect of height of burst. The value chosen for cratering efficiency requires a great deal of judgement and experience in the classification of subsurface materials into the ground groups shown in Figure 26. A consensus judgement with personnel at the AFWL was that the material influencing the crater would be a marginal "wet clay" (toward the lower bound) and the estimated cratering efficiency would be $16,280 \text{ m}^3/\text{TJ}$ for the half buried charge configuration (Reference 12). A cratering efficiency of $5425 \text{ m}^3/\text{TJ}$ was then determined for the surface tangent configuration. In determining these cratering efficiencies it was assumed that the saturated material below the water table would not effect the craters. This was checked using the AFDM procedure for layered sites and found to be valid. For the tangent below configuration (Event 5) the effect of the saturated material below the water table was taken into account and a cratering efficiency of $32,560 \text{ m}^3/\text{TJ}$ was determined.

The near surface peak particle velocity, displacement and waveforms were all calculated using AFDM equations based on cube root of the crater volume scaling. Attenuation of particle velocity and displacement with depth was predicted using the same method as was used in Reference 7. Although this procedure is not included in the AFDM, it is generally agreed to be good practice. The AFDM equations were used for depths of less than one-tenth of the cube root of the apparent crater volume ($0.1 V_a^{1/3}$). The attenuation prediction presented in Reference 7 is based on Middle Gust analysis (Reference 13) and recommends that the depths be grouped into those $< 0.1 V_a^{1/3}$, those

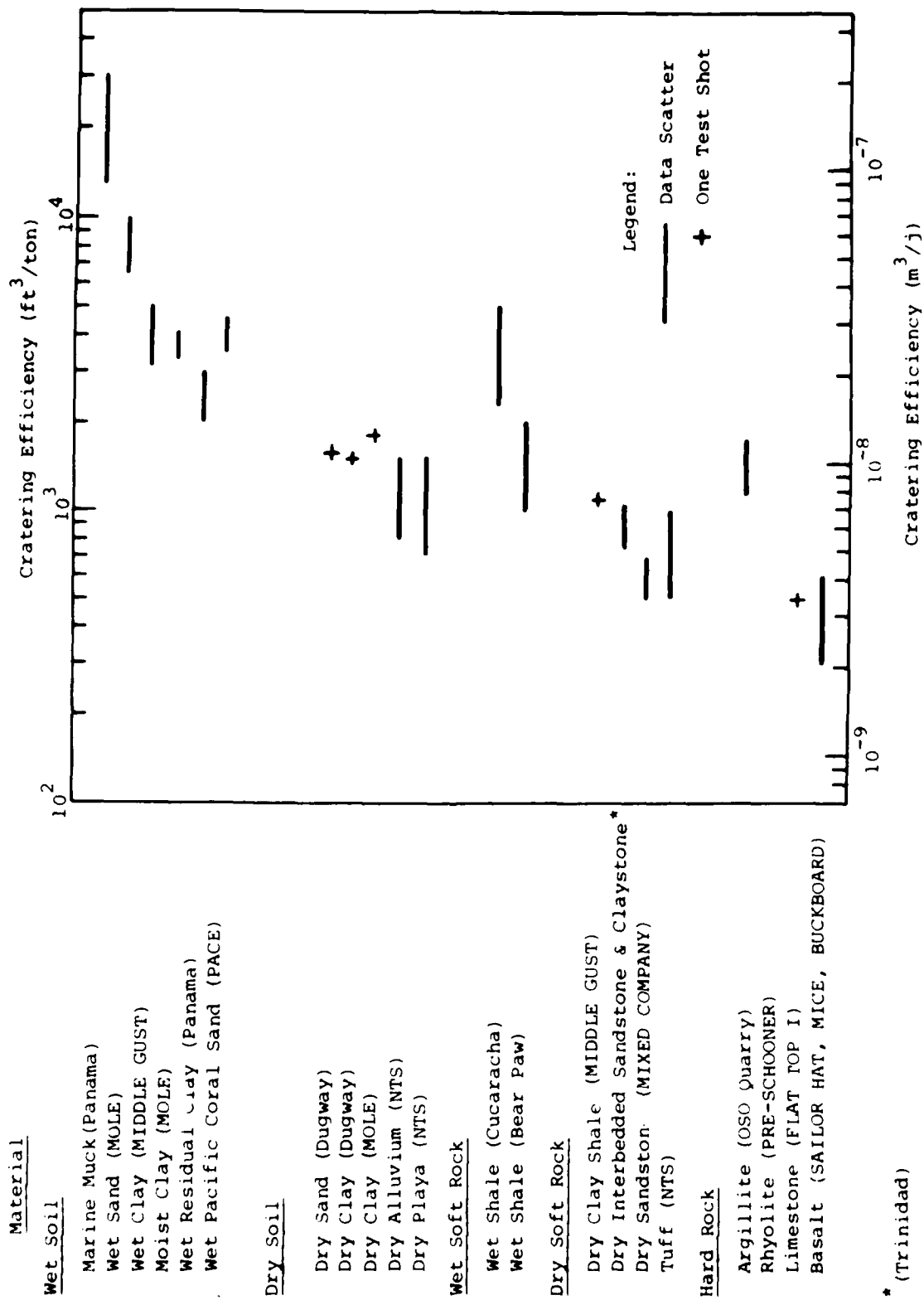


Figure 24. Cratering Efficiencies for TNT Surface Bursts (Ref. 10)

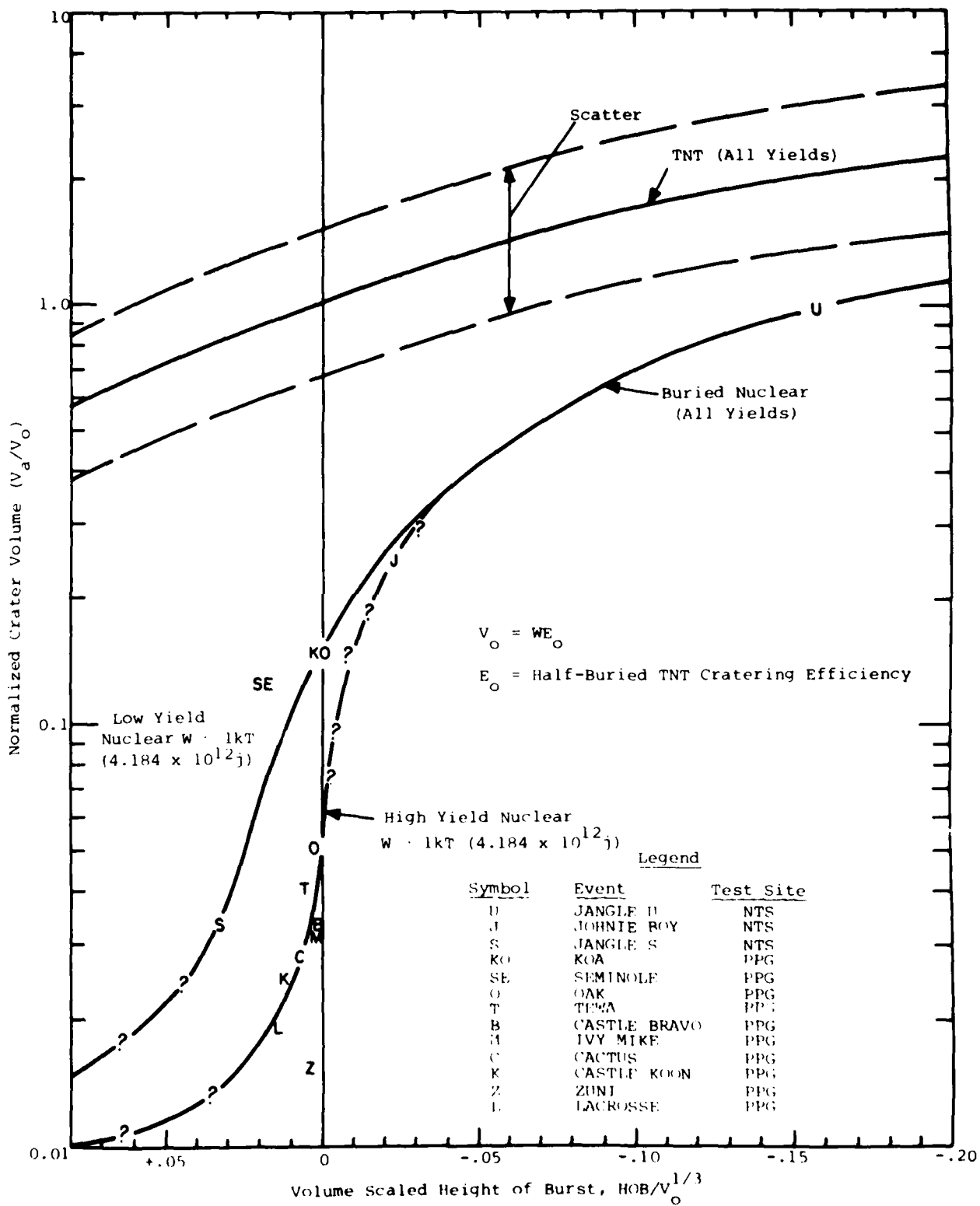


Figure 25. Height of Burst Effects in the Near Surface Region (Ref. 10)

between $0.1 v_a^{1/3}$ and $0.5 v_a^{1/3}$ and those $> 0.5 v_a^{1/3}$. The peak displacements for these depth increments are predicted by replacing the 0.1 coefficient in the prediction equation

$$d = 0.1 \frac{v_a^{4/3}}{R^3}$$

with values of 0.06 and 0.009 for the greater depths.

Predicted amplitudes for the crater related component of motion are shown in Figure 26.

d Waveform Superposition. Representative vertical particle velocity waveforms using the procedures discussed above are shown in Figure 27. Each waveform component begins at the time predicted from the arrival time contours. Although the crater related waveform is shown it was not included in the composite waveform. Study of the oscillatory component predicted using Higgins' technique indicated that these waveforms contained the effects of the crater related motion. At ranges closer to ground zero, however, the crater related motion dominates the motion. At those locations the oscillatory component has not developed and was not included in the composite waveforms. This same approach was used in making the horizontal predictions. After the waveforms for the various components of ground motion were developed, they were then superimposed to form the composite waveform shown.

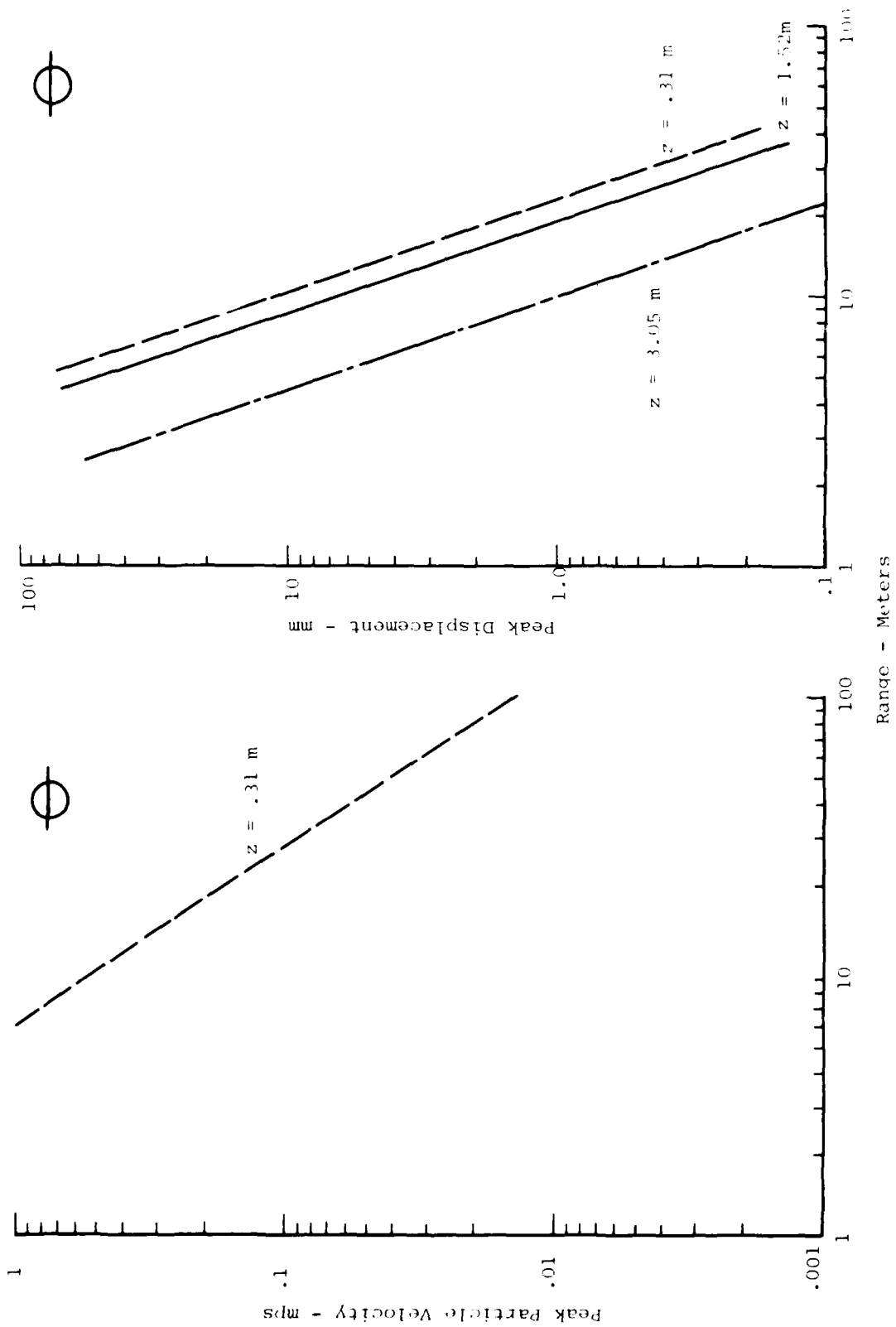


Figure 26. Prediction of Crater Related Motion for the Half Buried Configuration.

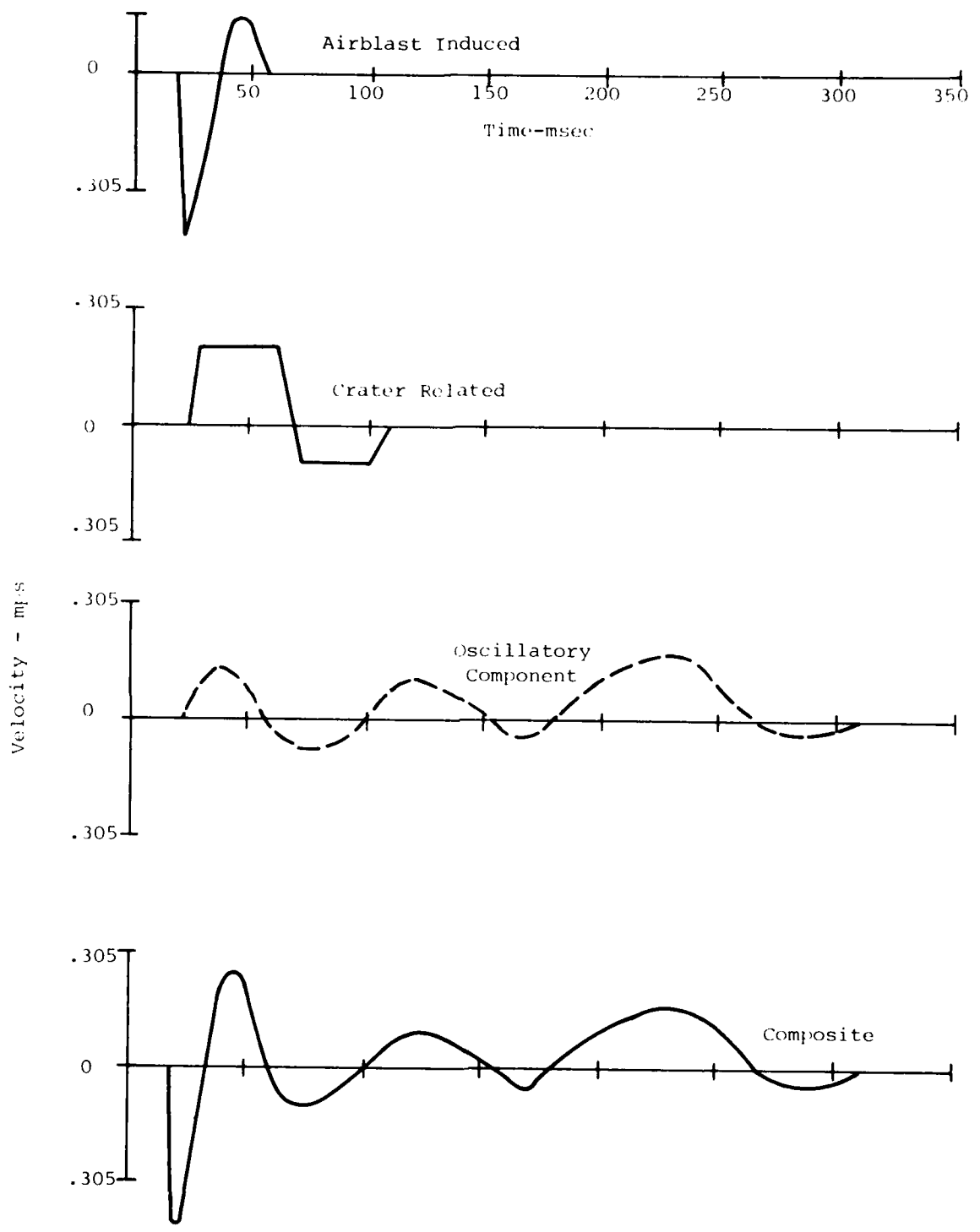


Figure 27. Components of the Predicted Vertical Waveform at the 18.3 Meter Range for the Half Buried Configuration.

4.

DISCUSSION OF DATA

4.1 EXPLANATION OF PHENOMENOLOGY

The primary purpose of the single burst program was to establish a data base for evaluation of the applicability of superposition and for the development of the waveform synthesis model. To do this it is necessary to have an understanding of the physics of the single burst events. Such an understanding is also required in evaluating the empirical prediction procedures discussed in the previous section, since it involves superimposing dependent predictions of various components of motion predicted in different ways.

The near surface (0.46 m) vertical particle velocity records for MBI-2 are shown in Figures 28 and 29. This was a surface tangent experiment. These vertical waveforms may be classified into three distinct types. Near ground zero and to a range of about 11 meters the waveforms are of the classical superseismic type with strong crater related effects. Between the ranges of about 18.3 m and 24.4 m the waveforms represent a transitional character where the crater related effects are becoming insignificant and the oscillatory component is beginning to develop. Beyond 24.4 m, classical outrunning waveforms are exhibited with the air slap superimposed during the first half cycle of outrunning ground motion.

The first arrival at the three close-in gages is the air-blast induced particle velocity. This is followed almost immediately by the large upward pulse associated with the crater related effects. Calculations indicate, however, that the air slap downward particle velocity reached its peak before the arrival of the upward crater related pulse. The crater related pulse is long in duration with respect to the air slap pulse and goes through about one full cycle of motion. The upward particle velocity is approximately equal to the downward air slap related values. The very rapid attenuation of the upward crater related pulse can be seen by comparison of the data recorded at the 4, 7.63, 10.7 meter ranges.

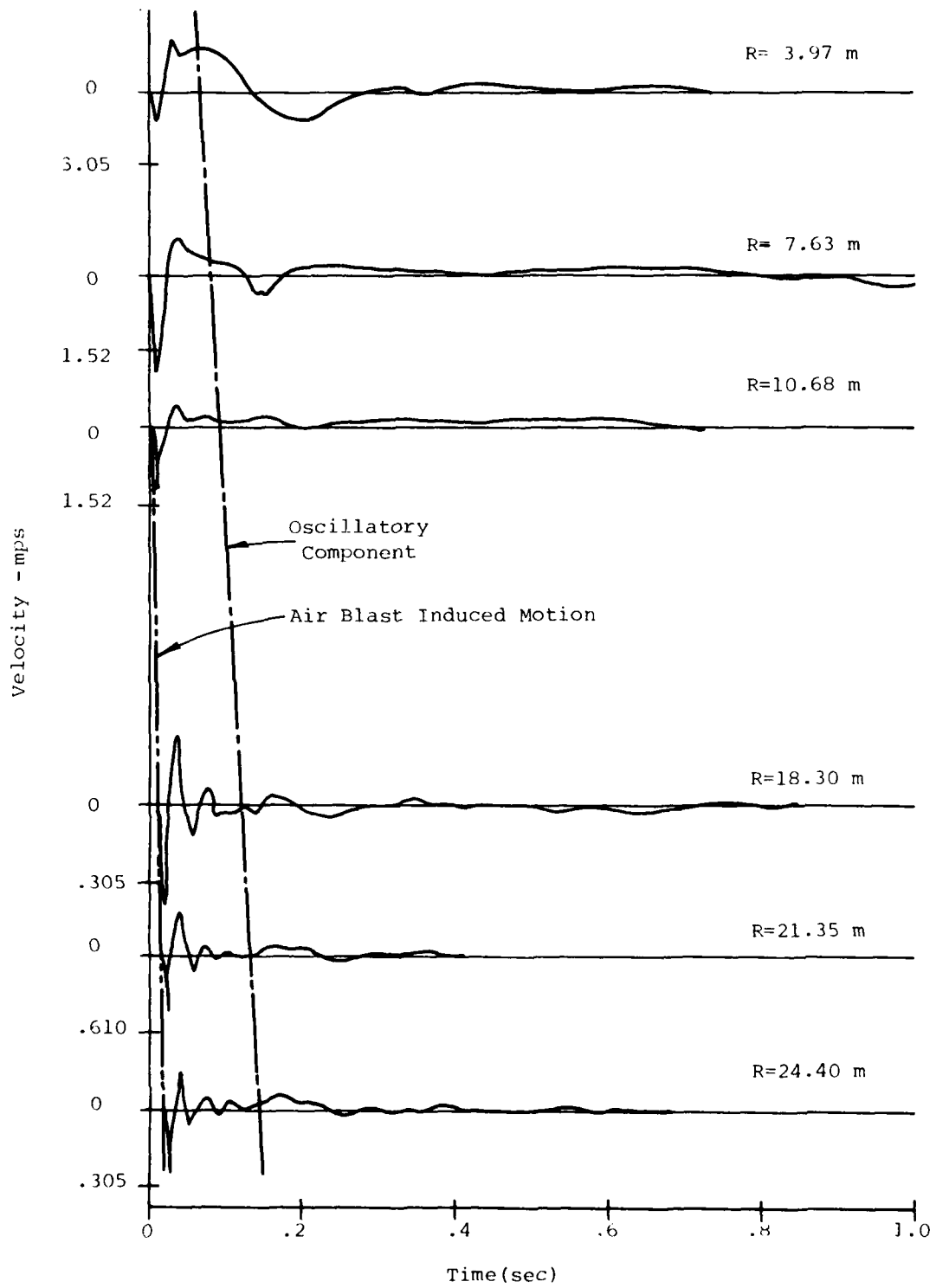


Figure 28. Vertical Velocity Waveforms at the .46 m Depth - MBI-2.

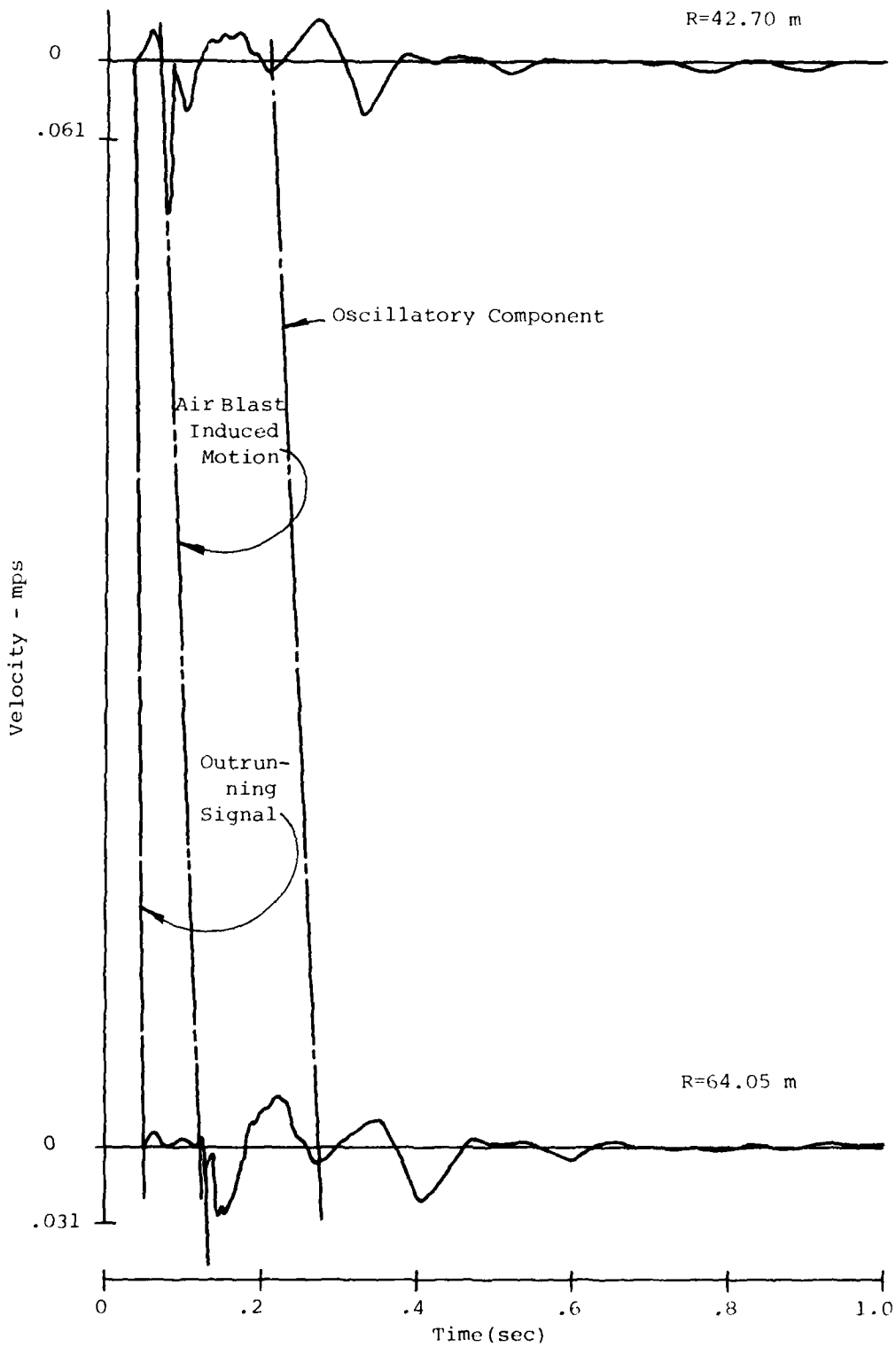


Figure 29. Vertical Velocity Waveforms at the .46 m Depth - MBI-2.

The second group of waveforms represent the transition from the predominance of the crater related effects to development of the oscillatory components. The initial arrival is still associated with the air slap motion, however, examination of additional data indicate that outrunning begins at the 0.46 m depth just beyond the 24.4 meter range. This is also shown by the projection of the arrival time of the outrunning signal and the air slap signals at the 24.4 meter range. The duration of the upward pulse of these records is much shorter than for those closer in, although the amplitudes are still approximately the same as the airblast induced particle velocity. Wave propagation analysis and examination of the deeper records indicates that this upward peak is a combination of the recovery from the air slap, the reflection of the airblast induced motions from the water table (3.05 meter depth) and the arrival of the crater related signal. At the 24.4 range the outrunning signal arrives at the 0.46 m depth at about 29 msec, the reflection off the saturated layer at about 41 msec and the crater related motion arrives at 62 msec. The oscillatory nature of the waveform can be seen to be developing at later times, however, the amplitudes are low with respect to the early time peaks.

The waveforms at 42.7 and 64.05 meter ranges are generally of a classical outrunning nature with the air slap motions superimposed (Figure 29). The initial motion at the 42.7 meter range is associated with the P-headwave generated by the outrunning signal in the saturated layer. When the air slap arrives it creates the high frequency downward spike which has a duration of approximately 10 msec. This produces a frequency of about 100 Hz. As this dies away, the outrunning waveform continues through a negative peak. At approximately 205 msec the low frequency groundroll arrives resulting in the peak upward motion. Only about one full cycle of the oscillatory component is evident in this waveform. The frequency of the oscillatory component is about 9 Hz. The arrival time of this low frequency groundroll is very evident in the two further out stations. The propagation velocity of about 305 meters per second is representative of the shear wave velocity of the deep

materials at the site. This wave has been traced back through the intermediate range waveforms and extrapolated back to the close-in data. It is obvious from Figure 28 that the arrival is consistent at the intermediate ranges and the wave is not evident at the closer in ranges. Analysis of these data indicate that this signal is a surface-type wave and is influenced by the top 116 to 122 meters of the profile. This depth estimate is based on an approximate dispersion curve analysis assuming shear wave velocities below 36.6 meters.

The shock spectra calculated for the vertical waveforms are shown in Figure 30. These spectra also illustrate the three regions discussed above.

In the first region the spectra are rather flat in the velocity regime, but there are two rather distinct peaks. The first peak occurs at a frequency of about 6 Hz. This peak is created by the crater related signal seen in the waveform. The rapid attenuation of this peak with range is also seen in the spectra. The second peak is much broader and covers a frequency range of 20 Hz to 200 Hz. This peak tends to reach its maximum at about 120 Hz and represents the air slap component.

The second region shown on Figure 30 is quite different from the first region. The spectra here are basically single peaked. The maximum amplitude occurs at about 30 Hz. This is the frequency of the downward air slap and the rebound. The crater related peak is still evident at these ranges, but at a much reduced amplitude.

The spectra in the third region on Figure 30 returns to the two peaked nature. Unlike the double peaked spectra in the first region, these spectra contain very distinct peaks. The first peak occurs at about 9 Hz, which is about 50% greater than the crater related frequency indicating that the related phenomenon are different. This 9 Hz signal represents the oscillatory component in the waveform.

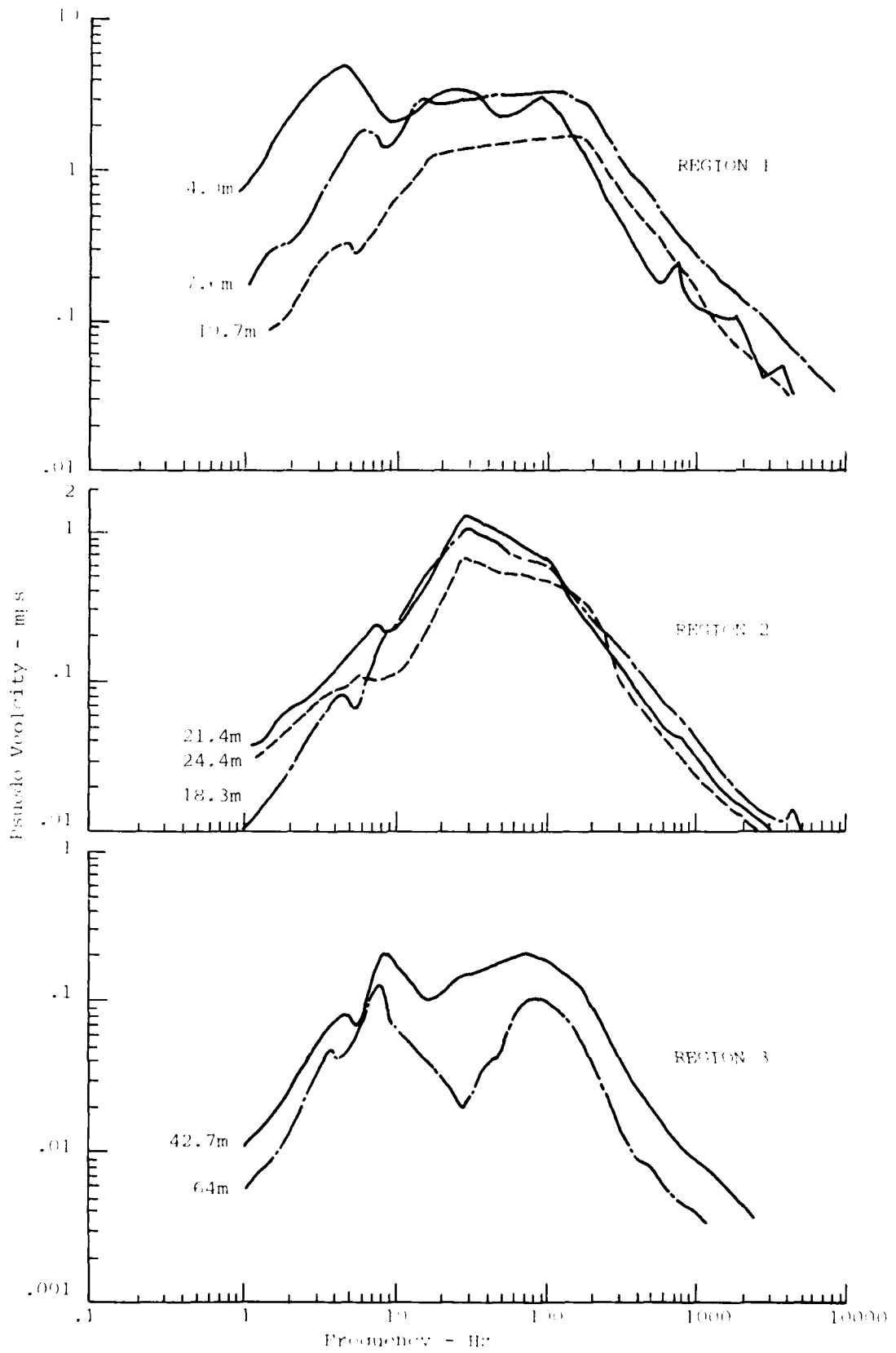


Figure 30. Shock spectra for Vertical Velocity Waveforms at the 0.46m depth; MBI-2.

The second peak occurs at about 100 Hz and represents the air slap component in the waveform.

The horizontal particle velocity waveforms at the same ranges are shown in Figures 31 and 32. The same phenomenological explanation is applicable to these waveforms with one exception. The shear wave associated with the air slap motion is quite distinct, particularly at the intermediate and outrunning ranges. This airblast induced shear wave has little effect on vertical records; however, the inward motion associated with it is stronger than the outward particle velocity associated with the compressional-wave and results in an abrupt reversal of the horizontal motion.

The shock spectra calculated for the horizontal waveforms are shown in Figure 33. These spectra also fall into the three distinct regions.

The first region is dominated by the crater related signal. As the range is increased within this region, the spectra begins to develop a second peak. Again the rapid attenuation of the low frequency crater related signal can be seen. The dominant low frequency in these spectra is about 6 Hz to 9 Hz. The air slap component has a frequency of around 200 Hz, significantly greater than in the vertical records, which result of the clipping by the airblast shear wave.

The spectrum from the second region shown in Figure 33 is made up of three peaks of approximately the same magnitude. This particular waveform (refer to Figure 31) appears to have more oscillations after the air slap and airblast induced shear wave. These oscillations produce the 40 Hz peak. The air slap is the cause of the spectrum peak at 200 Hz. The low frequency peak is due to the developing surface wave. When compared to the oscillatory components from other spectra, this frequency is somewhat lower. This may, in part, be due to a baseline problem in this waveform, or to the interaction of the crater related and surface wave effects.

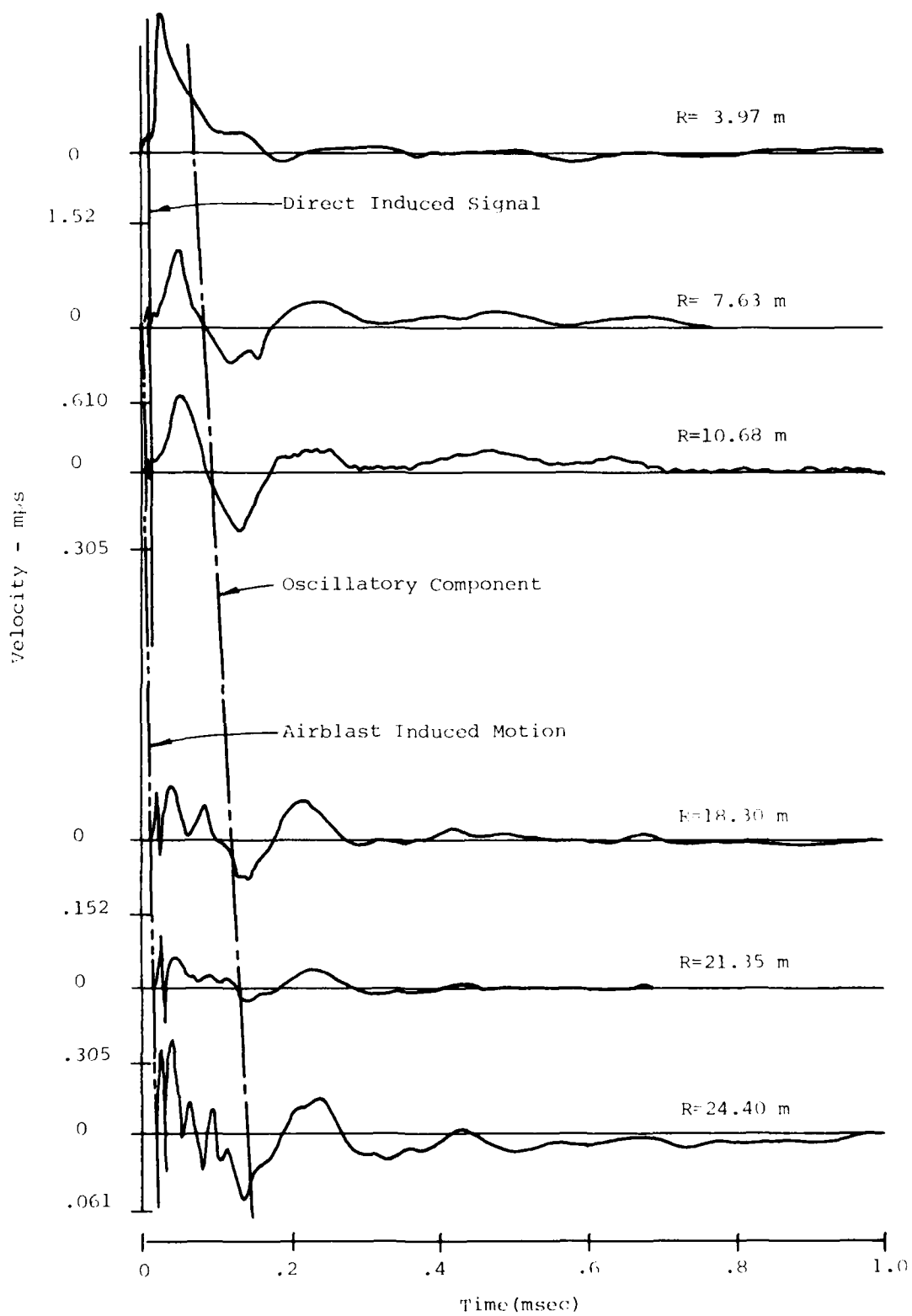


Figure 31. Horizontal Velocity Waveforms at the .46 m Depth -MBI-2.

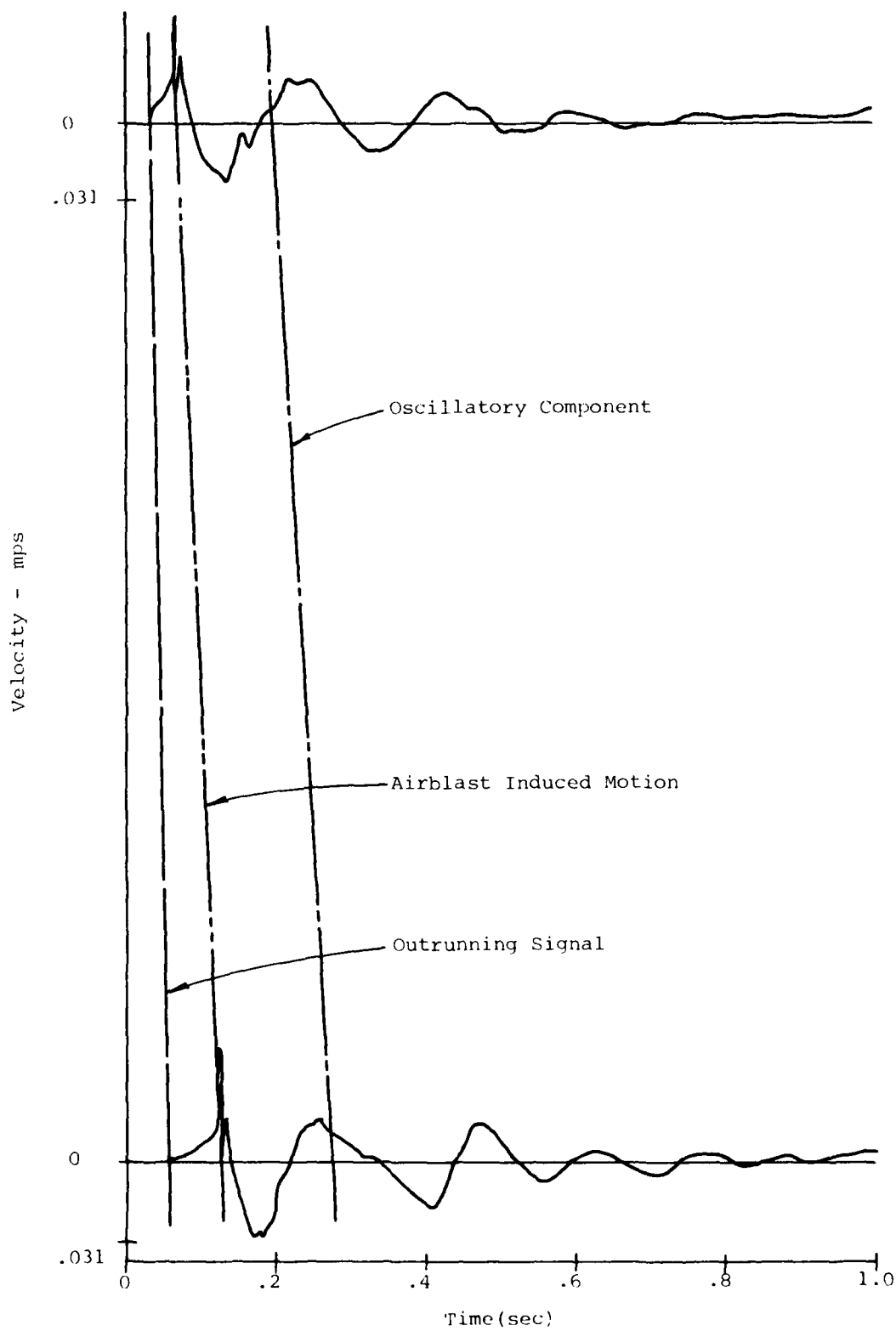


Figure 32. Horizontal Velocity Waveforms at the .46 m Depth - MBI-2.

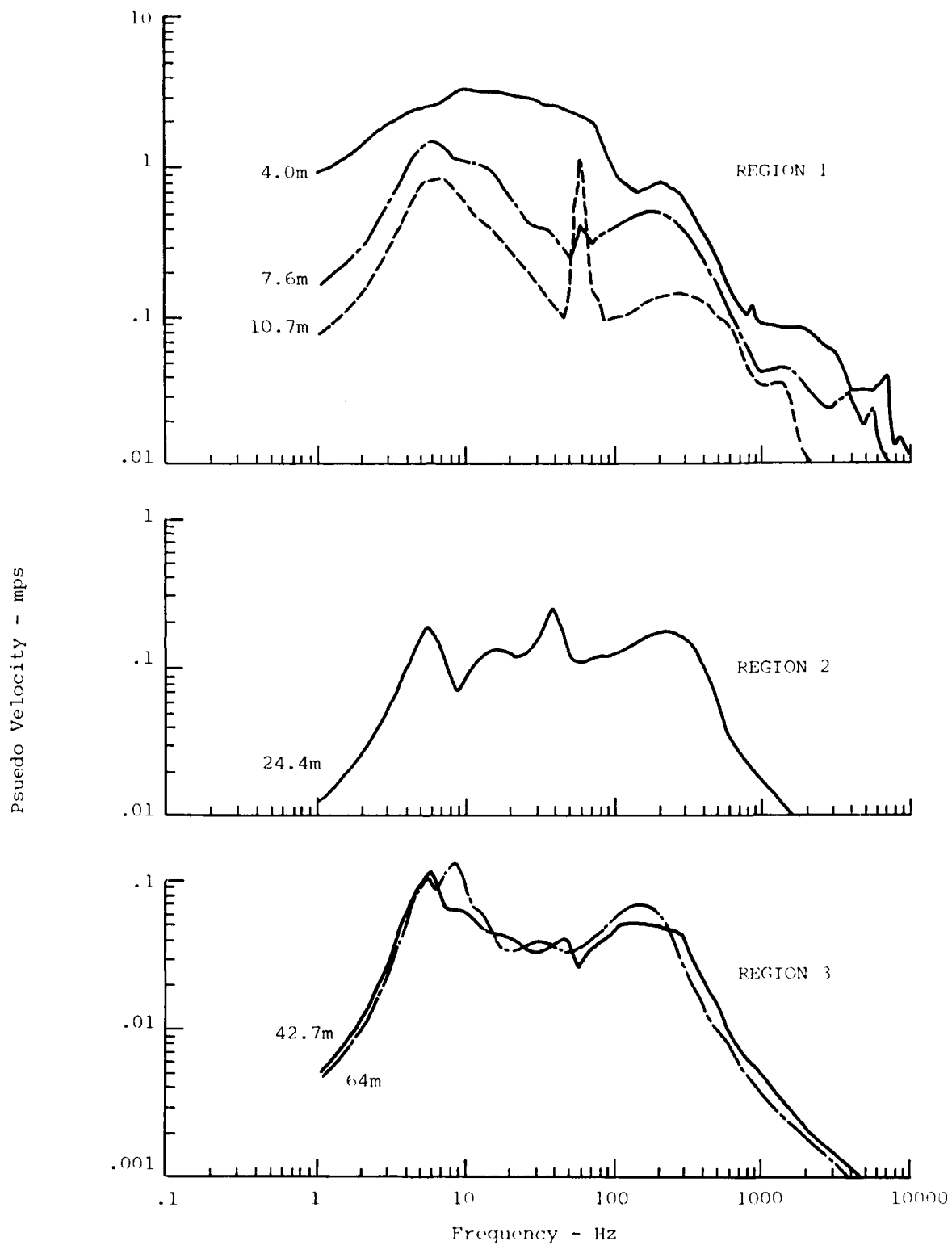


Figure 33. Shock Spectra for Horizontal Velocity Waveforms at the 0.46m depth; MBI-2.

The spectra from the third region are double peaked and similar in nature to the vertical spectra for this region, but with somewhat lower frequencies.

The separate signals seen in the waveforms are related primarily to different portions of the subsurface geology. The air slap motions are most predominate near the ground surface and are controlled by the soft top layer (unsaturated silty clay). The interface between this layer and the saturated clay, at a depth of about 3 meters, also plays an important role in the air slap motions. The reflection from this interface is large and clips the vertical motion in the top layer. Because the impedance of the saturated layer is high, the transmitted wave is small. The reflected shear wave associated with the air slap motions is quite evident in the horizontal motions and would not be expected since the shear moduli of the top 2 layers are almost identical.

The crater related signal is also primarily controlled by the top layer. No reflection of this signal from the saturated layer is evident, probably because of the strong shear associated with the signal.

The outrunning signal at the instrumented ranges is controlled by the saturated layer. This is evident from the arrival times, the shocked nature of the wave front and the high frequency content of the first arrivals. The first cycle of low frequency motion is fairly constant in amplitude and duration as a result of the continual feeding of airblast energy into the saturated layer.

The signal which has been designated the oscillatory component (or ground roll) in this analysis has, in previous studies, been considered a portion of the outrunning signal. In outrunning waveforms such as are presented in References 1 and 2, the peak motions occur after 1-1/2 cycles of motion and are created by what we have referred to here as the oscillatory component. We have separated this out as

a separate signal in our analysis because we believe it is a surface wave which is being superimposed on the outrunning (body) waves. We are referring to surface wave here in the classical geophysical definition. Its development and propagation are controlled by the shear properties of the site and at large ranges, very deep layers have a significant influence on its behavior. In MBI-2 almost 122 meters of material was influencing this wave at the larger ranges. Projection of the arrival times of this signal to ground zero indicates that it was not initiated until about 55 msec after detonation.

The predominant motion at the 21.35 meter range, which is the key range for the superposition predictions of the multiburst experiment, is the air slap related downward motion and the combination of rebound, reflection, crater related and outrunning effects resulting in an upward peak of fairly high frequency. The oscillatory components at this range is relatively small with respect to the initial peaks.

4.2 AIRBLAST RESULTS

Figures 34 through 40 present peak values of airblast overpressure, impulse, and time of arrival for the single burst experiments of Phase I.

Of the three configurations, the surface tangent experiment (MBI-2) was the most successfully predicted for airblast parameters. This is shown graphically in Figure 34. In general, data points fall within the published accuracy of ± 20 percent for airblast predictions.

Figure 35 presents quite a different story for the half buried experiments (MBI-1, MBI-3 and MBI-7). Peak overpressures are about 20 percent or more below the predicted values. Peak impulse values are generally well below the lower bound of the 20 percent accuracy band. Even though the predicted peaks were too high, attenuation rates were well predicted for all ranges of interest. Attenuation of impulse was well predicted between the 9.15 m and 18.30 m ranges, but the data show almost no attenuation beyond 18.30 m.

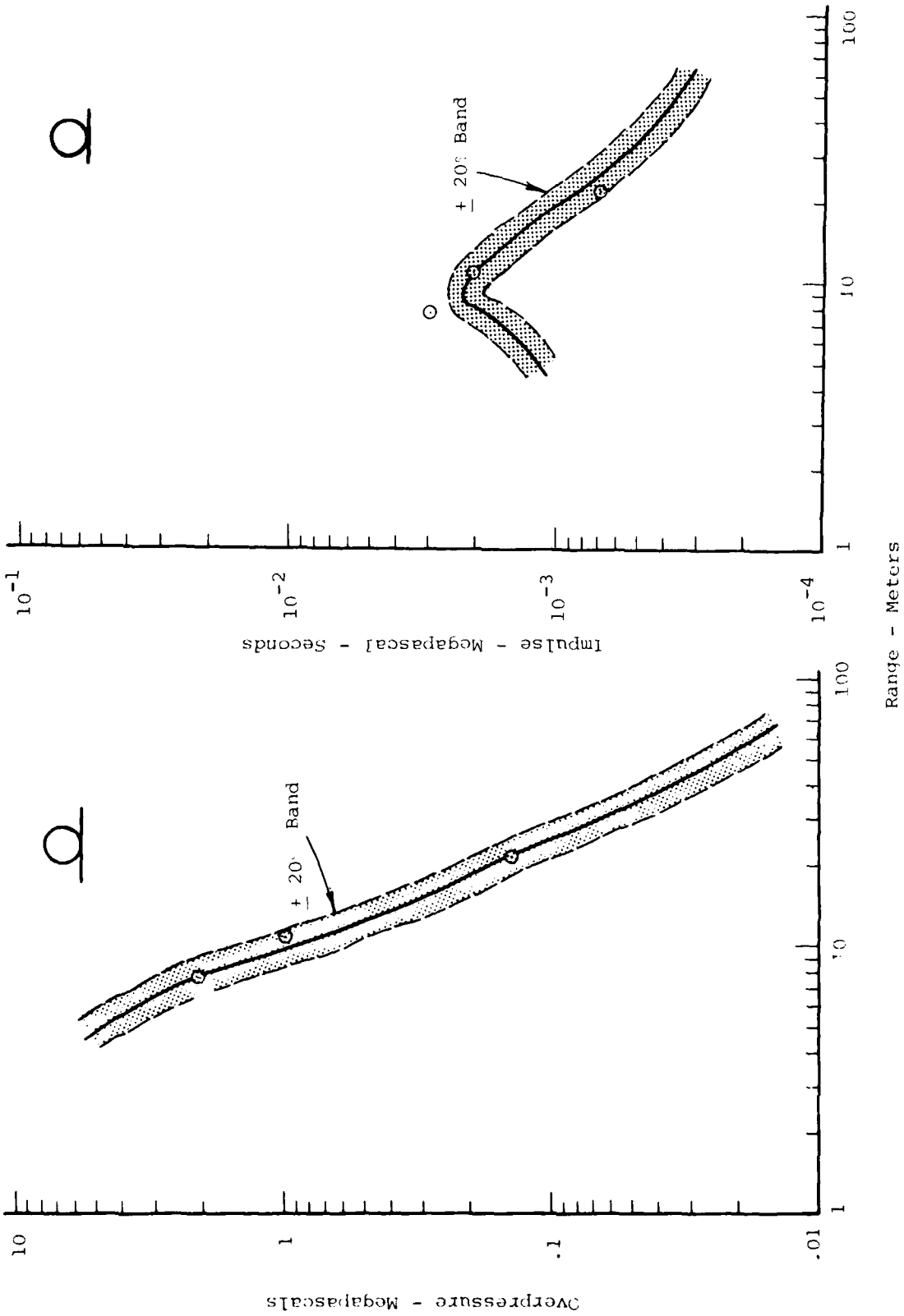


Figure J4. Overpressure and Impulse Data Compared with Predictions for the Surface Tangent Configuration.

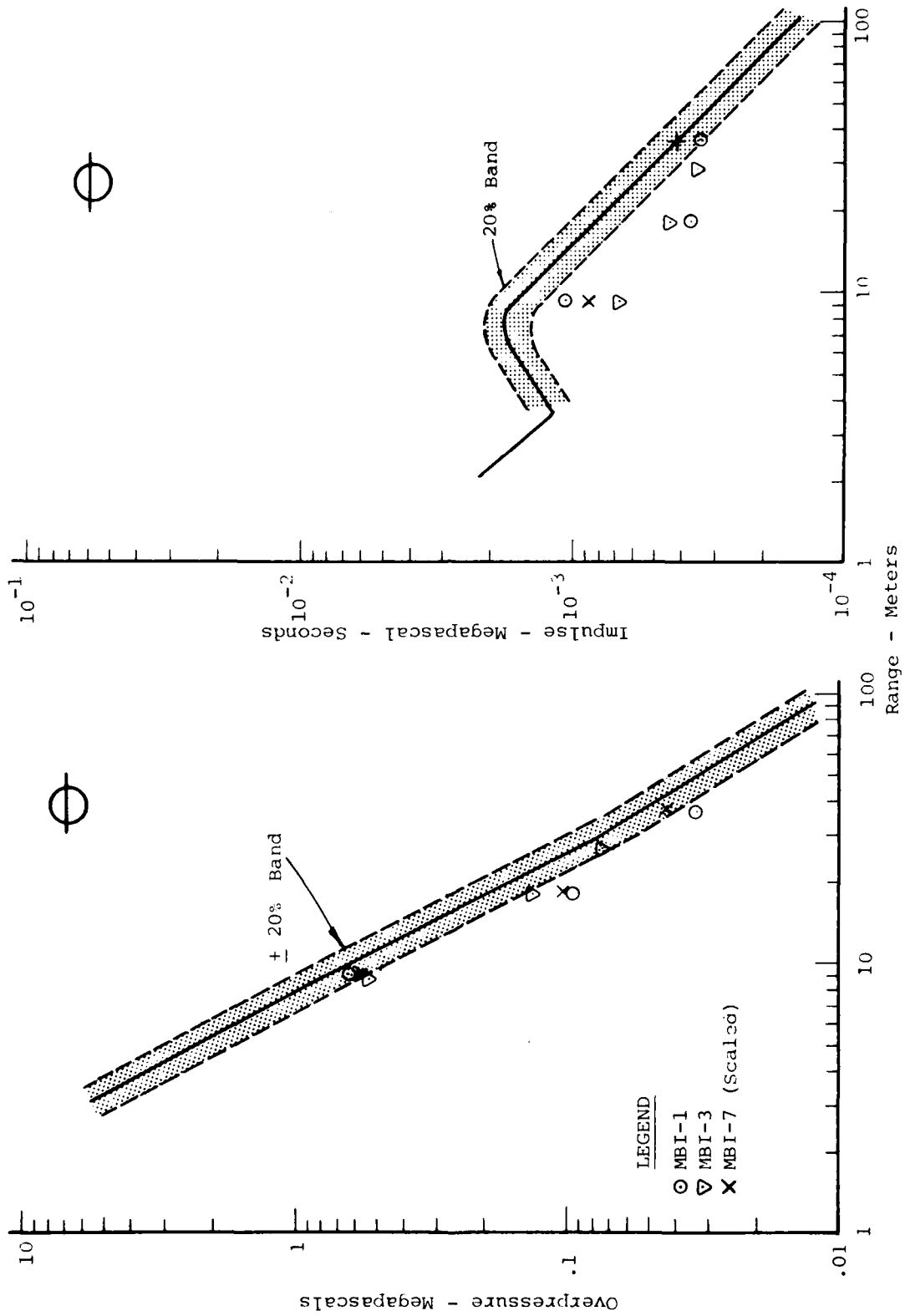


Figure 35. Overpressure and Impulse Data Compared with Predictions for the Half Buried Configuration.

Due to the disparity of the data and the predictions, a synthesis of previous data of the same configuration was performed (References 9, 14 and 15). The results of this exercise are shown in Figure 36. As can be seen the data scatter is large and much greater than 20 percent. These scatter bands have been superimposed on the Misers Bluff data in Figure 37. This indicates, that at least for the half buried configuration, airblast is not as well understood as was thought. Another interesting point is that the Misers Bluff data generally occupies the lower half of the data scatter band developed from previous experiments. A review of Figure 36 shows that other experiments of similar yields to Misers Bluff fall in the same general region, while the large yield experiments occupy the upper half of the scatter band.

Reproducibility from the three half buried configuration experiments was good. Events 1 and 3 were of the same yield and peak values were generally the same. Event 7 was a smaller yield and when scaled to 2.09×10^{-3} terrajoules also agreed very well. In general, the peak values from all these experiments were within normal data scatter (see Figure 37).

Figure 38 presents the overpressure and impulse curves for the tangent below experiment (MBI-5). Predictions for this particular configuration were difficult, as the data base is quite limited. For the pretest predictions a rough estimate for overpressure was achieved by using the free air curves produced by John Keefer of BRL. beyond the 7.63 meter range. The pretest predictions for impulse were the same as the half buried experiment. As would be expected, the pretest predictions were quite high when compared with the data at the close in and intermediate ranges. For comparison purposes, the equation given in Reference 16 to scale surface bursts to buried bursts was used to produce the dashed curves on the figure. The equation was applied to the half buried airblast prediction curve

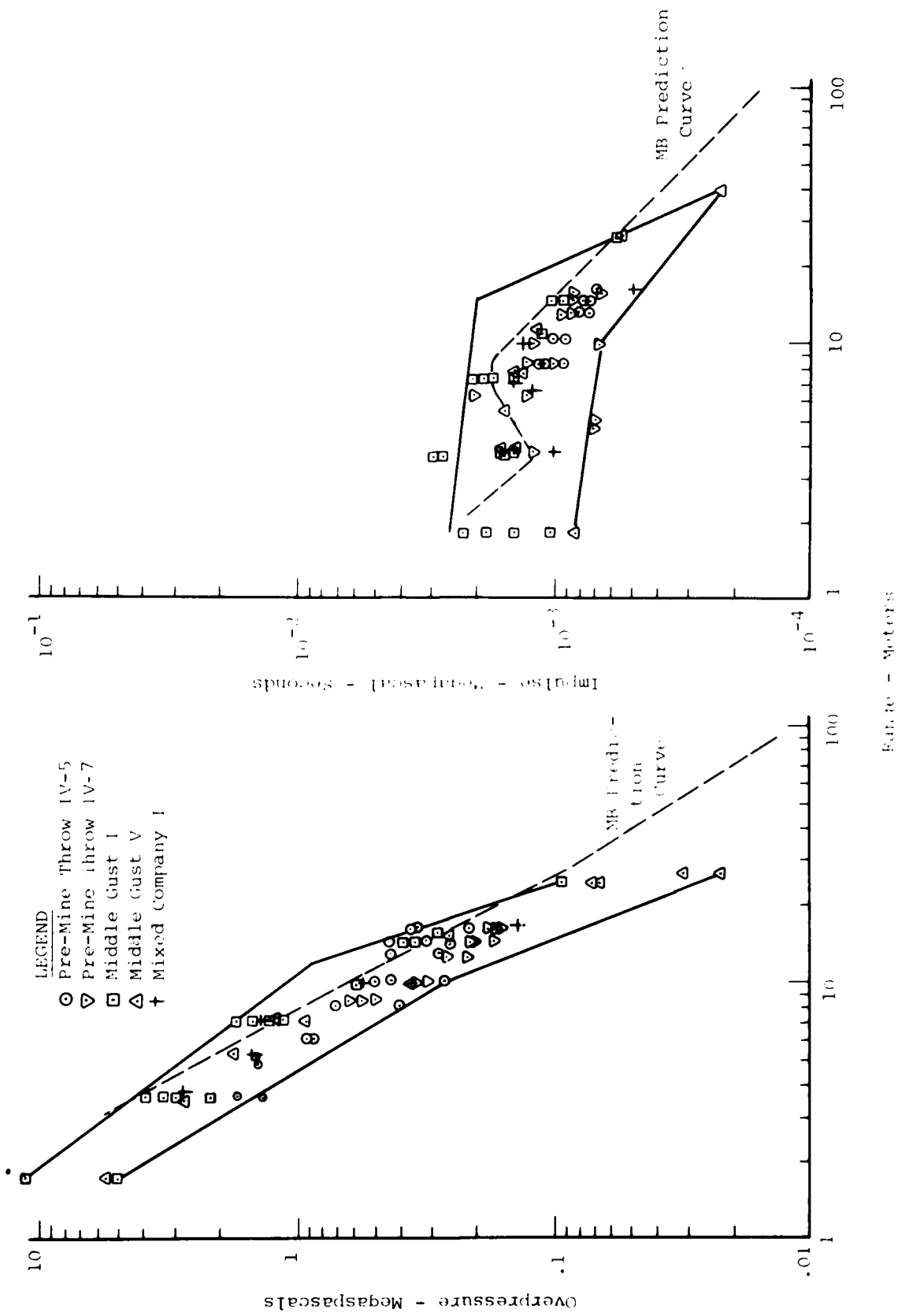


Figure 36. Overpressure and Impulse Data from Other Half Buried Experiments Scaled to 2.09×10^{-3} Terrajoule Yield (1000 lb).

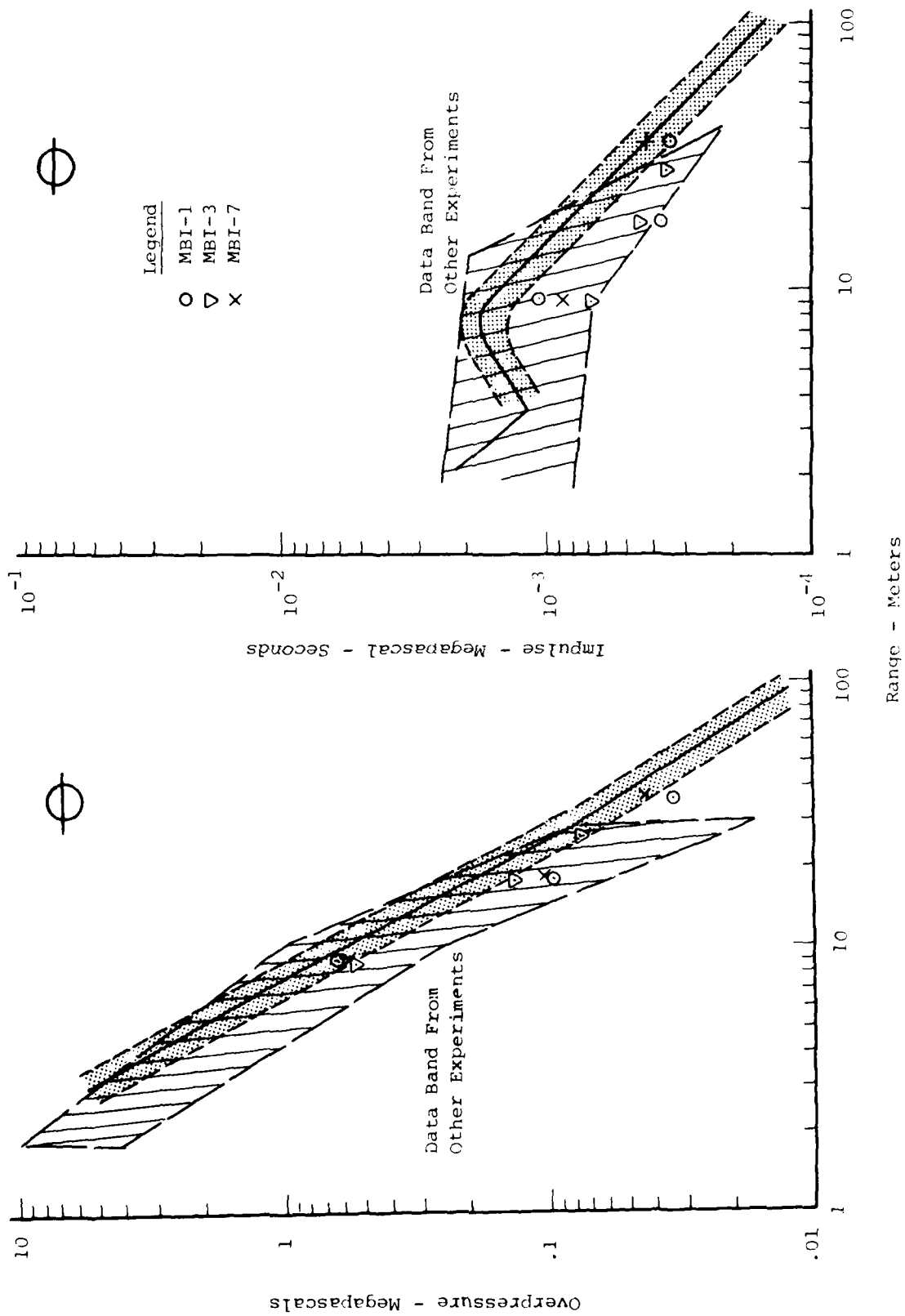


Figure 37. Misers Bluff Data and Predictions Compared with Other Experiments - Half Buried Configuration.

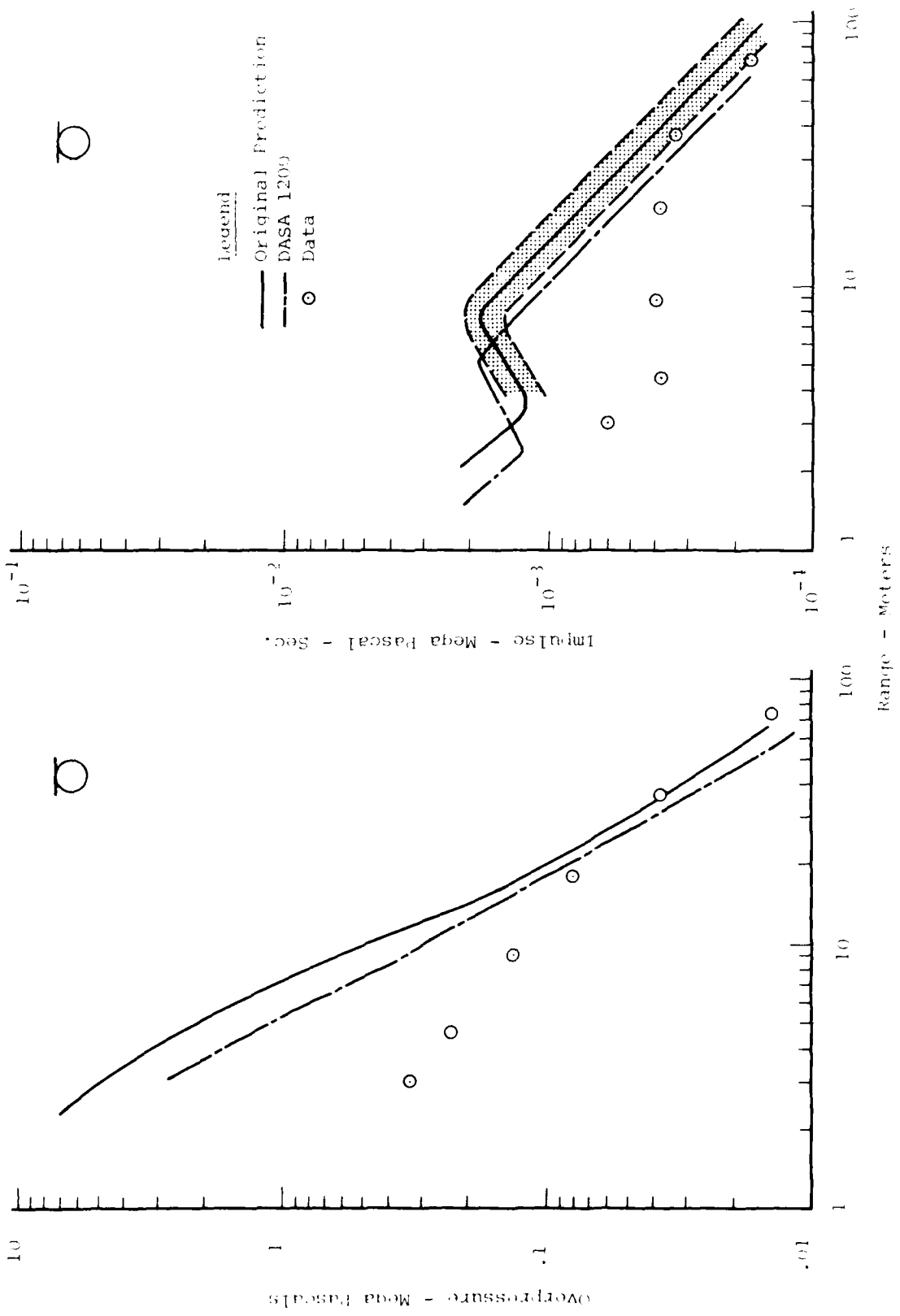


Figure 38. Overpressure and Impulse Data Compared with Predictions for the Tangent Below Configuration.

(shown in Figure 35). As can be seen, this improved the prediction slightly, but it is still somewhat above the data at the close in ranges. Both predictions improve with range, and beyond about 0.1 MPa agree reasonably well with the data.

The effect of height of burst on overpressure, impulse and time of arrival is shown in Figure 39 and 40. Overpressure peaks were as expected, with the highest values produced by the surface tangent experiment. The half buried experiments produced the next highest peaks, with the tangent below experiment, producing the lowest values. Attenuation of overpressure was the same for both the surface tangent and half buried experiments between the 9.15 m range and the 21.35 m range. Attenuation of overpressure for the tangent below experiment was much slower between these ranges. At the 36.6 m range all of the configurations produced approximately the same results. Although data at ranges greater than 36.6 m is scarce, it is expected that data from all three configurations would converge at these large ranges.

Peak impulse exhibited much the same behavior as overpressure. Attenuation rates for the surface tangent and the half buried experiments were the same between the 9.15 m and 18.3 m ranges, with the tangent below experiment exhibiting this same attenuation rate at ranges between 3.05 m and 4.58 m. Impulse on the tangent below experiment was generally constant between 4.58 m and 36.6 m. The half buried experiment exhibited the same behavior between 18.3 m and 36.6 m. The attenuation range for the surface tangent experiment appears to be constant for all ranges of interest.

For both overpressure and impulse the height of burst affects the close and intermediate ranges, while all data tends to converge at the greater ranges.

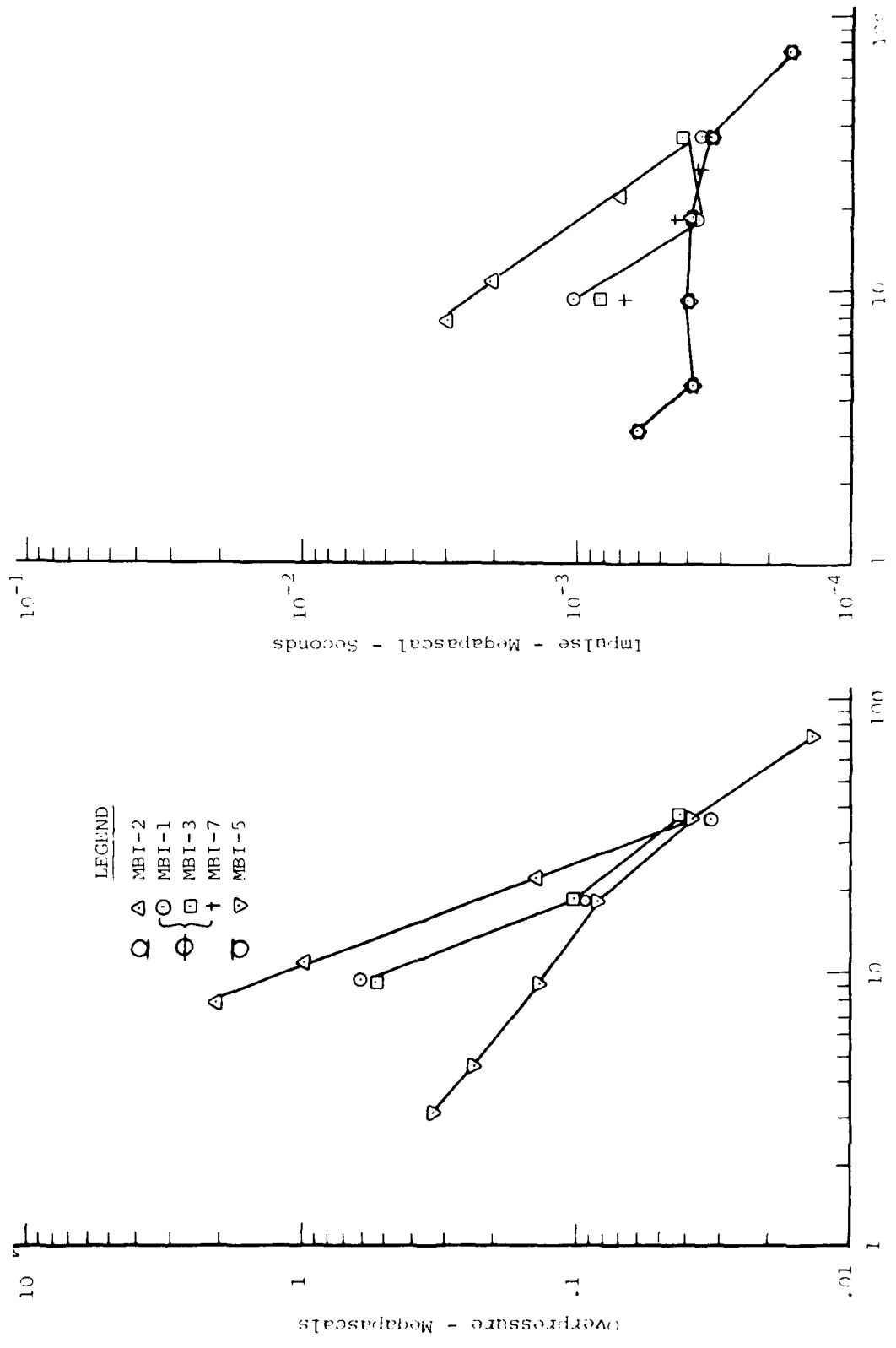


Figure 39. Height of Burst Effect on Overpressure and Impulse.

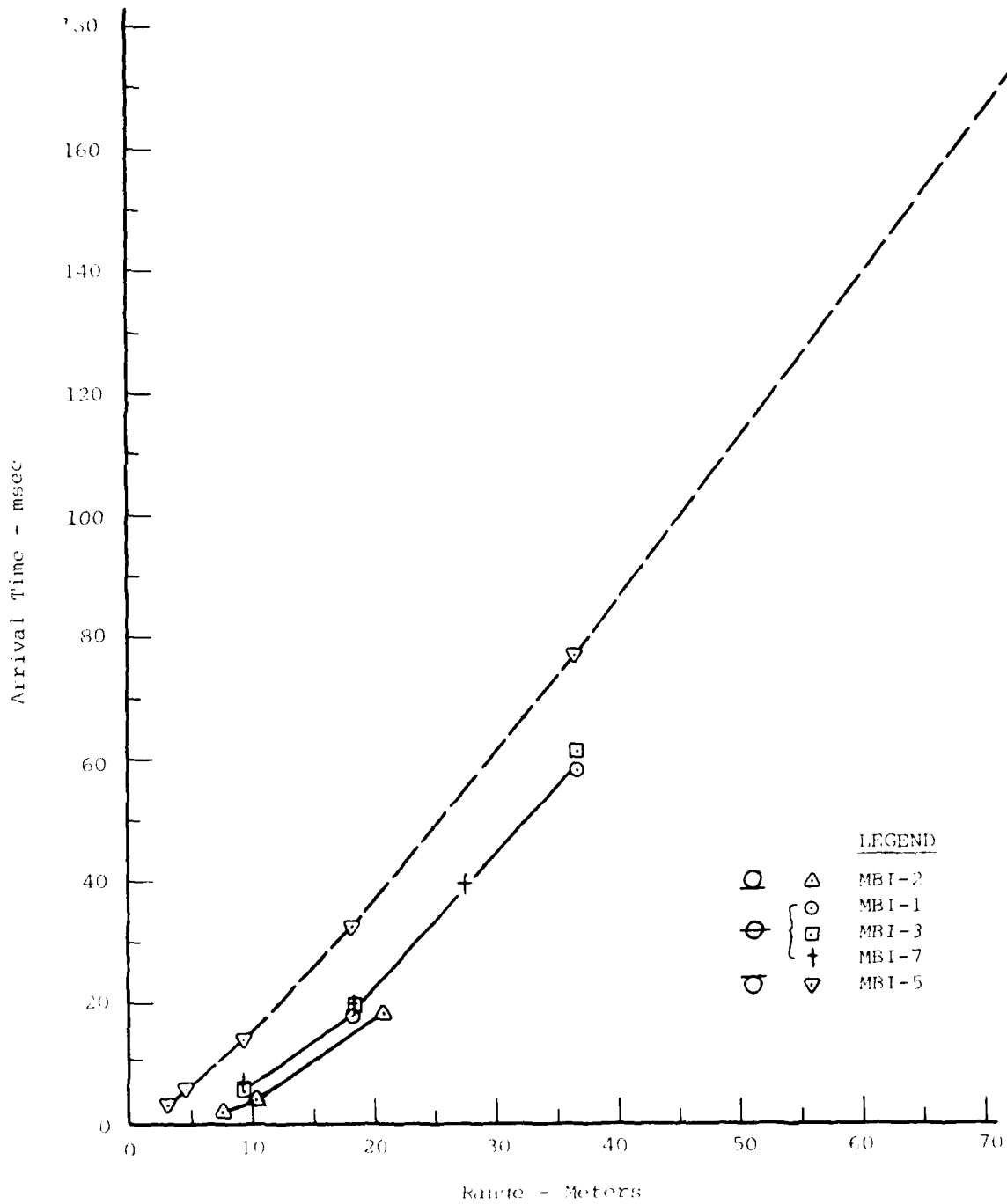


Figure 40. Height of Burst Effect on Arrival Times.

Figure 40 shows the time of arrival of the airblast vs range. As would be expected, the time of arrival curves are similar but shifted with the surface tangent arriving first.

4.3 GROUND MOTION

4.3.1 General

Dissection of the waveforms is necessary in order to evaluate the prediction procedures and the superposition assumption discussed in previous sections. It is impossible to do this, however. What we have tried to do in the following sections is to isolate those peaks which we believe are due primarily to a single effect and compare those to the predicted values. The measured and predicted waveforms will then be compared to make a general evaluation of the remainder of the signals and the superposition assumption.

4.3.2 Air Slap Component of Ground Motion

a Definition. The air slap component of ground motion is that portion of the waveform that is directly attributable to the overhead airblast. Figures 41 and 42 illustrate the component graphically for vertical and horizontal motions of the three different burst configurations. Initial motion is always down and out as a result of the induced p-wave. This is followed by a shear wave which imparts down and inward motion. The strength of this shear wave is strongly dependent on the material properties of the near surface layers.

Only the initial portion of the air slap component will be discussed in this section because, as discussed previously, at many locations other signals arrive shortly after the peak and it is not possible to separate the effects.

b Discussion of Data.

1 Surface Tangent Configuration. Peak values of the air slap component recorded in the surface tangent experiment (MBI-2) are presented in Figures 43 through 46. Included on these figures are the empirical pre-test predictions.

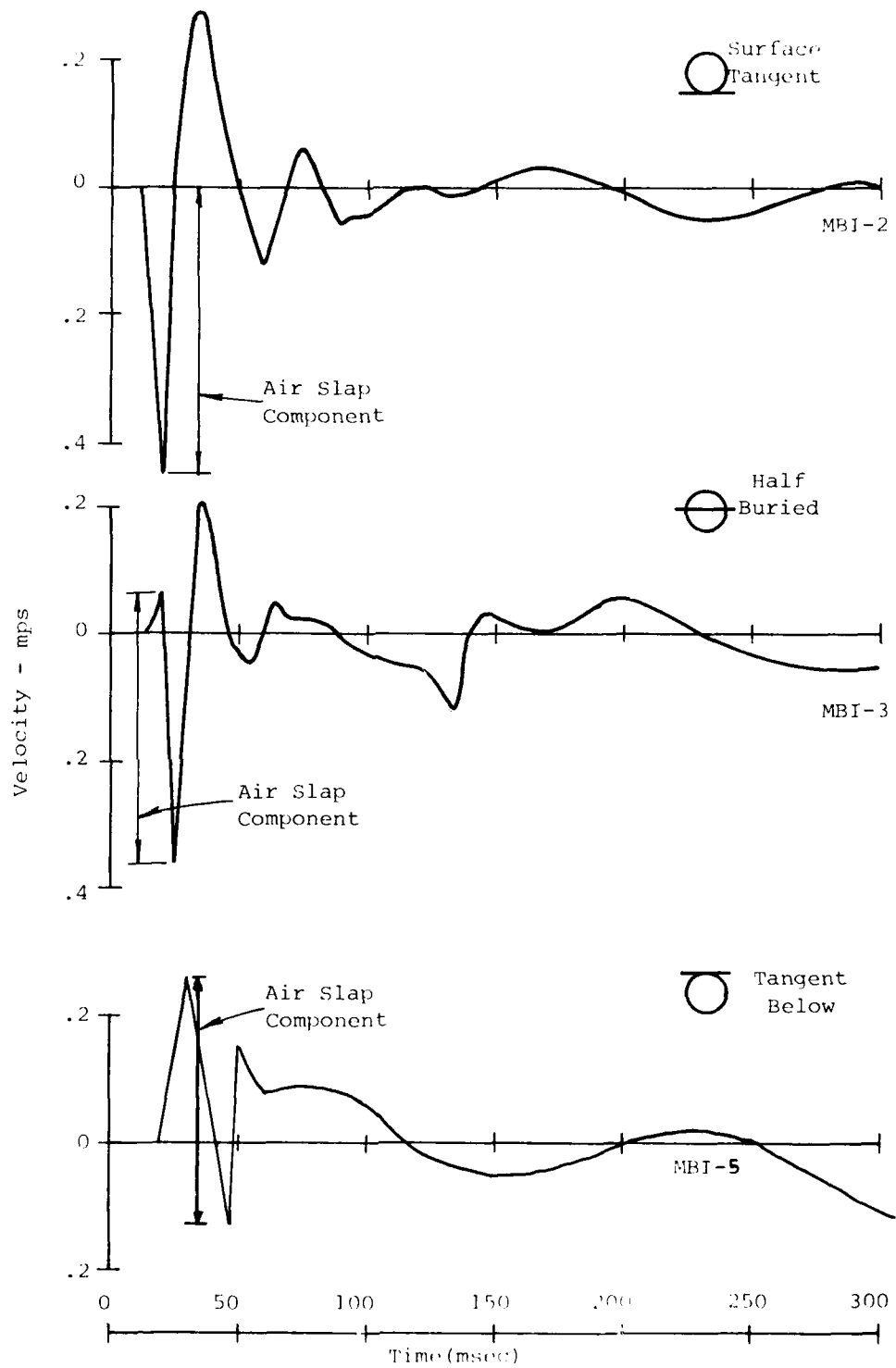


Figure 41. Definition of Airslap Component of Vertical Motion
 $R = 18.3 \text{ m}$, $Z = .46 \text{ m}$.

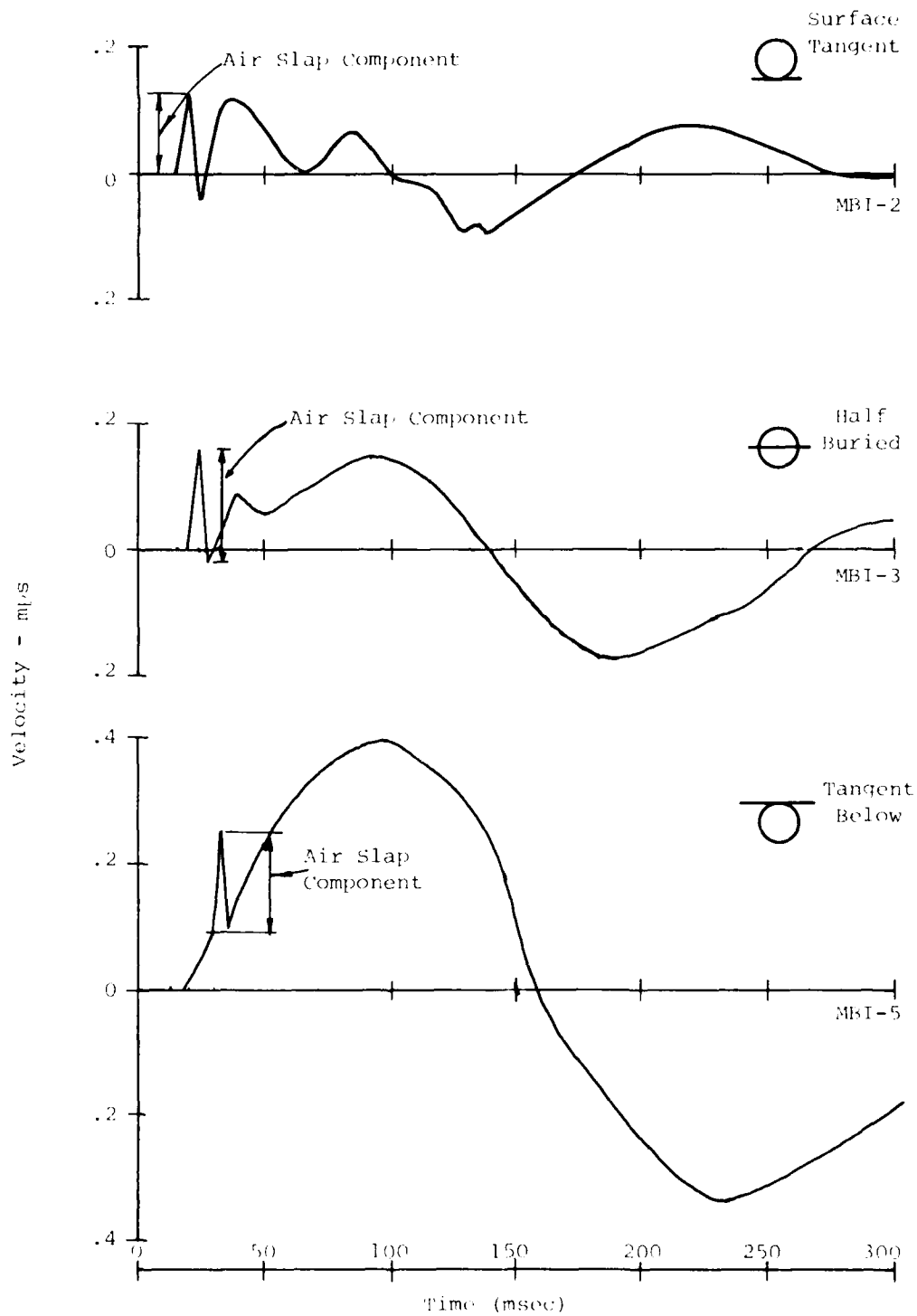


Figure 42. Definition of Airslap Component of Horizontal Motion, $R = 18.3 \text{ m}$, $Z = .46 \text{ m}$.

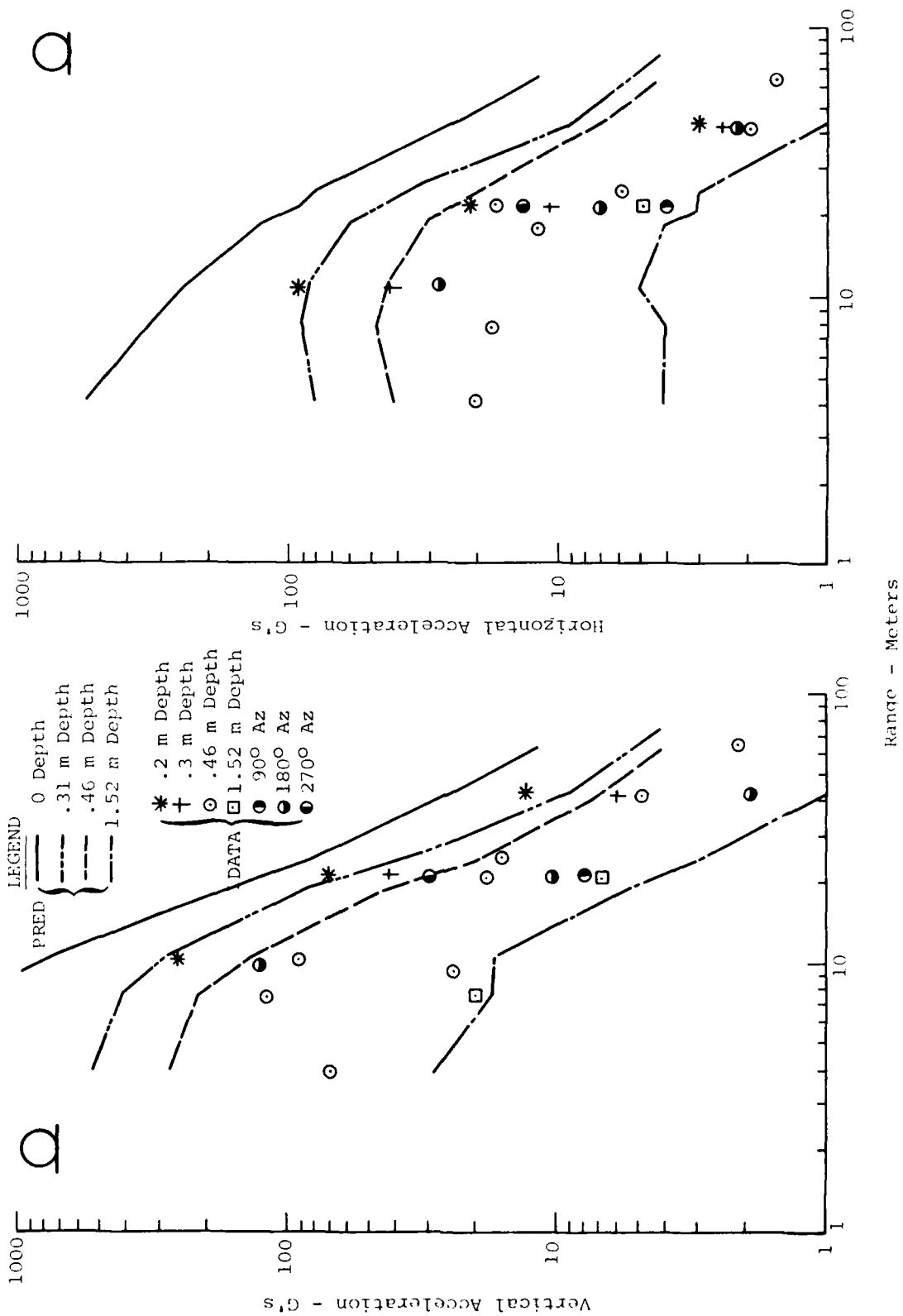


Figure 43. Comparison of Measured and Predicted Peak Values of Airblast Induced Acceleration for the Top 1.52 m of the Test Bed - MBI-2.

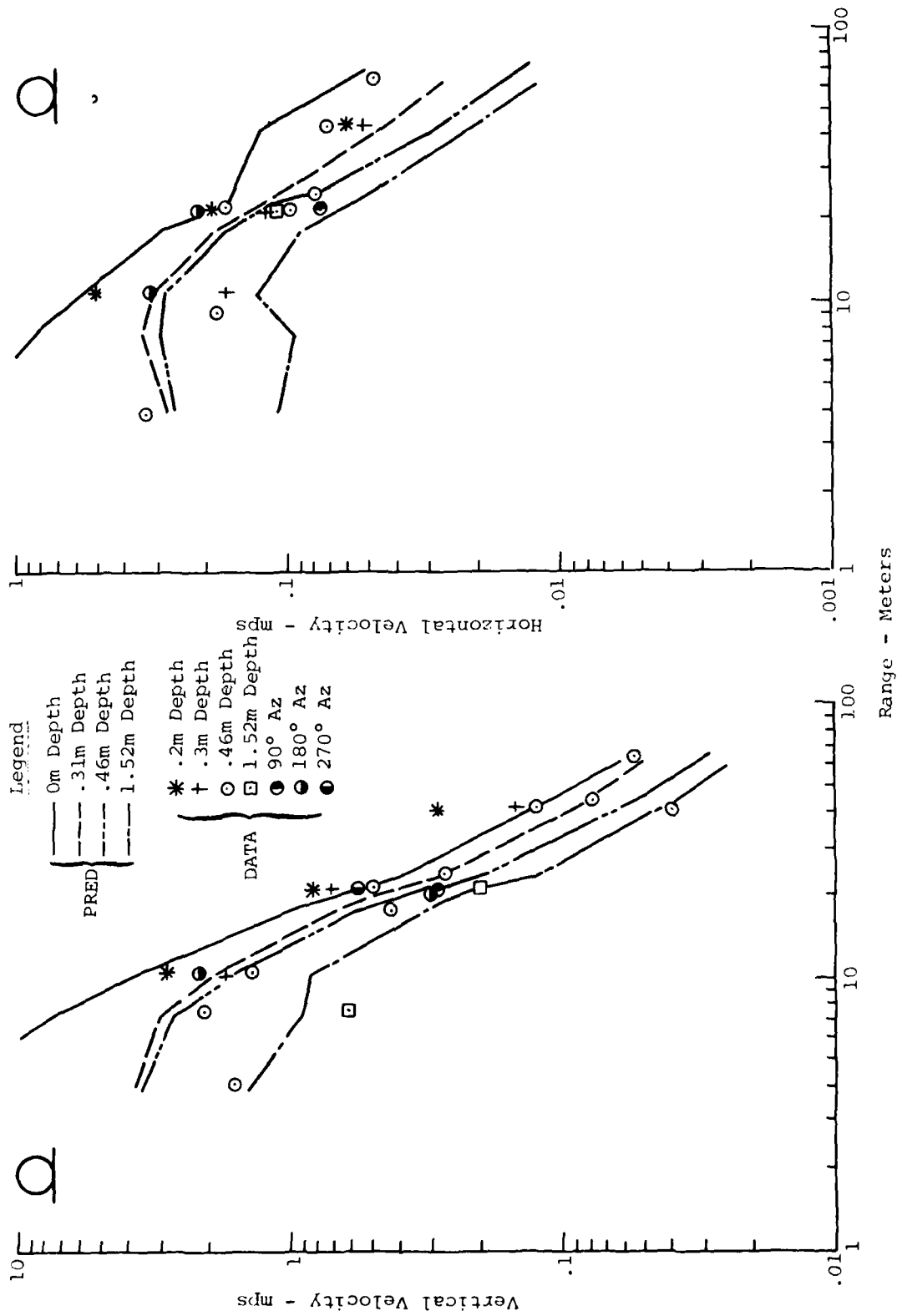


Figure 44. Comparison of Measured and Predicted Peak Values of Air Blast Induced Velocity for the Top 1.52m of the Test Bed - MBI-2

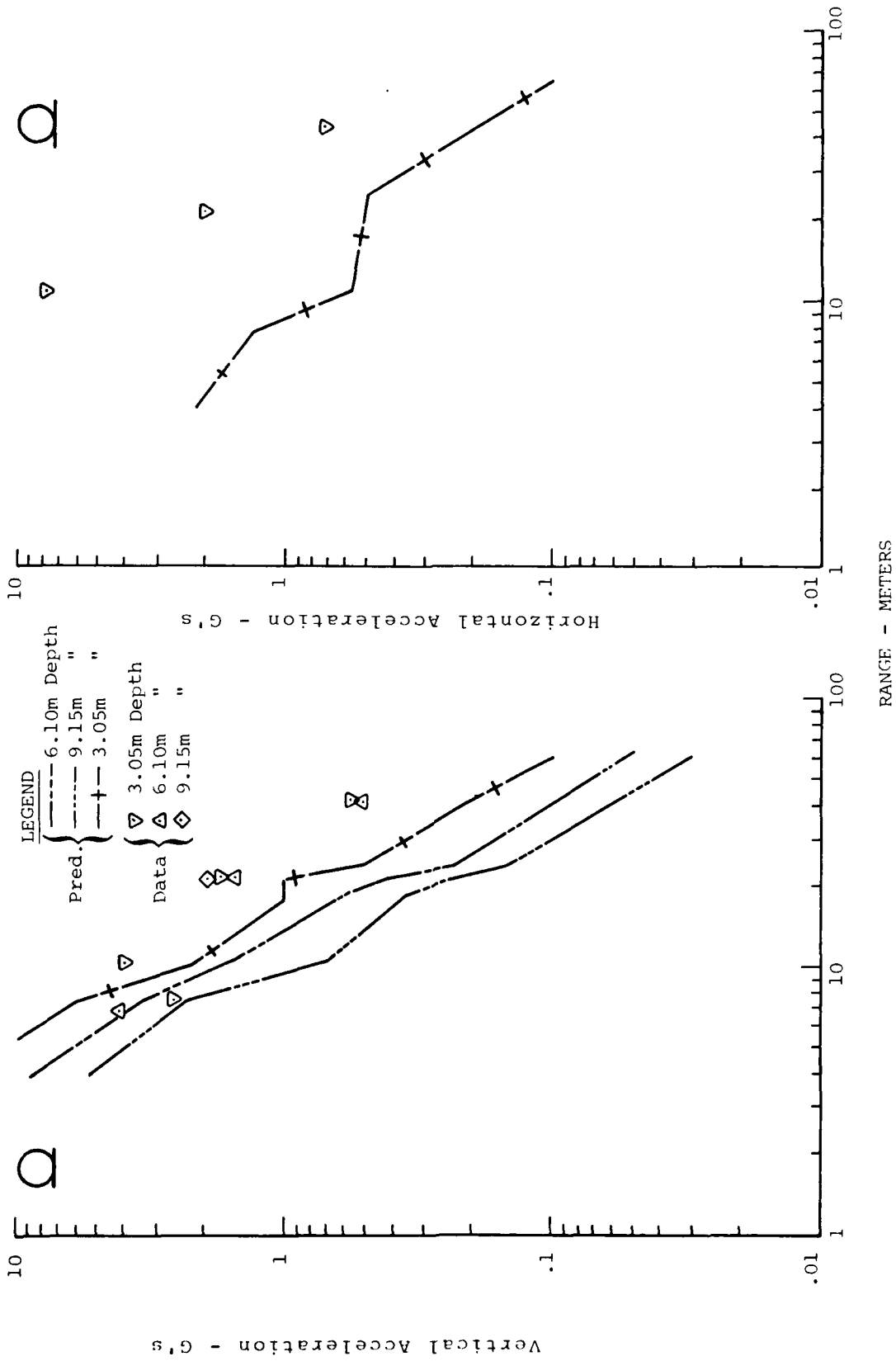


Figure 45: Comparison of Measured and Predicted Peak Values of Airblast Induced Acceleration Below the 1.52m Depth - MBI-2

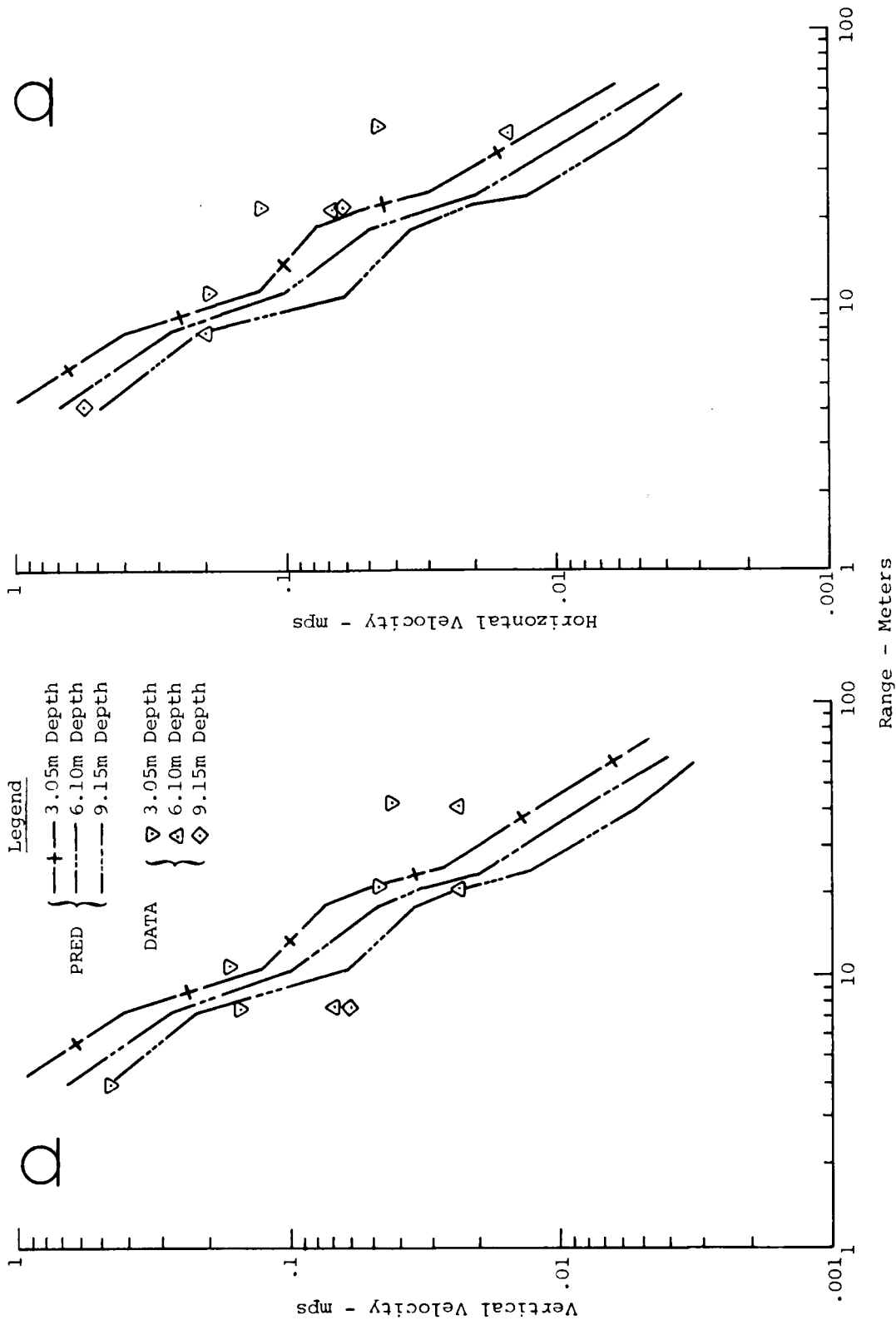


Figure 46. Comparison of Measured and Predicted Peak Values of Airblast Induced Velocity Below the 1.52m Depth - MBI-2

Figure 43 presents the peak vertical and horizontal accelerations for the top 1.52 m of the test bed. The air slap component of vertical acceleration was, in general, successfully predicted for this region. Although there were only three data points at each of the two shallowest depths (0.2 m and 0.31 m), the recorded magnitudes fell within the predicted regions. An "eyeball" fit to these data yield an attenuation rate of approximately two, which is about the same as the predicted rate of attenuation. Most data was taken at the 0.46 m depth. The magnitude of these data are bracketed within the predicted region and also attenuate at about the predicted rate. The maximum scatter of these data occurs at the 21.35 m range and is approximately a factor of four bottom to top. Data at the 1.52 m depth is extremely limited, but is slightly higher than the predicted values.

Horizontal motions, at first glance, do not appear to have been as well predicted as the vertical motions for this region. This is especially obvious at the two shallowest depths (0.2 m and 0.31 m). However, if the data scatter at the 0.46 m depth is examined, it is seen that the maximum scatter for horizontal motion is the same as seen in the vertical motions (i.e. a factor of 4 at the 21.35 m range). Assuming a maximum scatter to the 0.2 m and .31 m deep gages, and assuming the recorded values are centered within the scatter, the "bands" created are partially within the regions predicted for them. The other depths on this figure fall within the predicted regions for magnitudes, and for all depths shown the attenuation rate of the data is greater than the predicted rate.

Figure 44 presents the peak vertical and horizontal velocities for the top 1.52 m of the test bed. Vertical velocities at the 0.46 m depth were well predicted in both magnitude and attenuation. Data scatter at this depth was approximately a factor of two at the 21.35 m range. However, for these data the maximum scatter was approximately a factor of three at the 42.7 m range. The scatter was not bracketed by the predicted region, but the "eyeball" fit to the data

falls within the region. The 0.2 m depth was slightly underpredicted even when the data scatter of the 0.46 m depth was applied as described above. The 0.31 m and 1.52 m depths were well predicted in both magnitude and attenuation with range.

The horizontal velocities were not as well predicted as the vertical velocities. Magnitudes were adequately predicted, and, in general fell within predicted regions; however, the attenuation rate of the data was faster than that predicted. This is probably a result of the effect of the rather strong shear wave exhibited by the data which was not accounted for in the predictions. This will be discussed in more detail in a later section. The maximum data scatter at the 0.46 m depth was approximately three at the 21.35 m range.

The accelerations and velocities for depths greater than 1.52 m are presented in Figures 45 and 46. In general, both horizontal and vertical acceleration and velocity were underpredicted. Horizontal magnitudes were significantly underpredicted and the predicted attenuation rates generally were too slow. The discrepancy between data and predictions at these depths is due primarily to the difficulty in isolating the air slap component from other phenomena occurring at about the same time. This is especially true at the greater ranges. In fact, we were not able to pick an unaffected air slap horizontal component below the 3.05 m depth.

2 Half Buried Configuration. Three experiments were conducted at this configuration (MBI-1, MBI-3, MBI-7). Peak values of vertical and horizontal accelerations and velocities are presented in this section.

Figure 47 presents the peak values of vertical and horizontal acceleration for Event 1. Vertical motions were well predicted for all depths. Data points at 0.2 m and 0.31 m were limited but appear to be within the predicted regions. The data recorded at the 0.46 m depth was successfully predicted in magnitude and attenuation rate. Maximum scatter at this depth occurred at the 36.6 m range and was approximately a factor of 1.25.

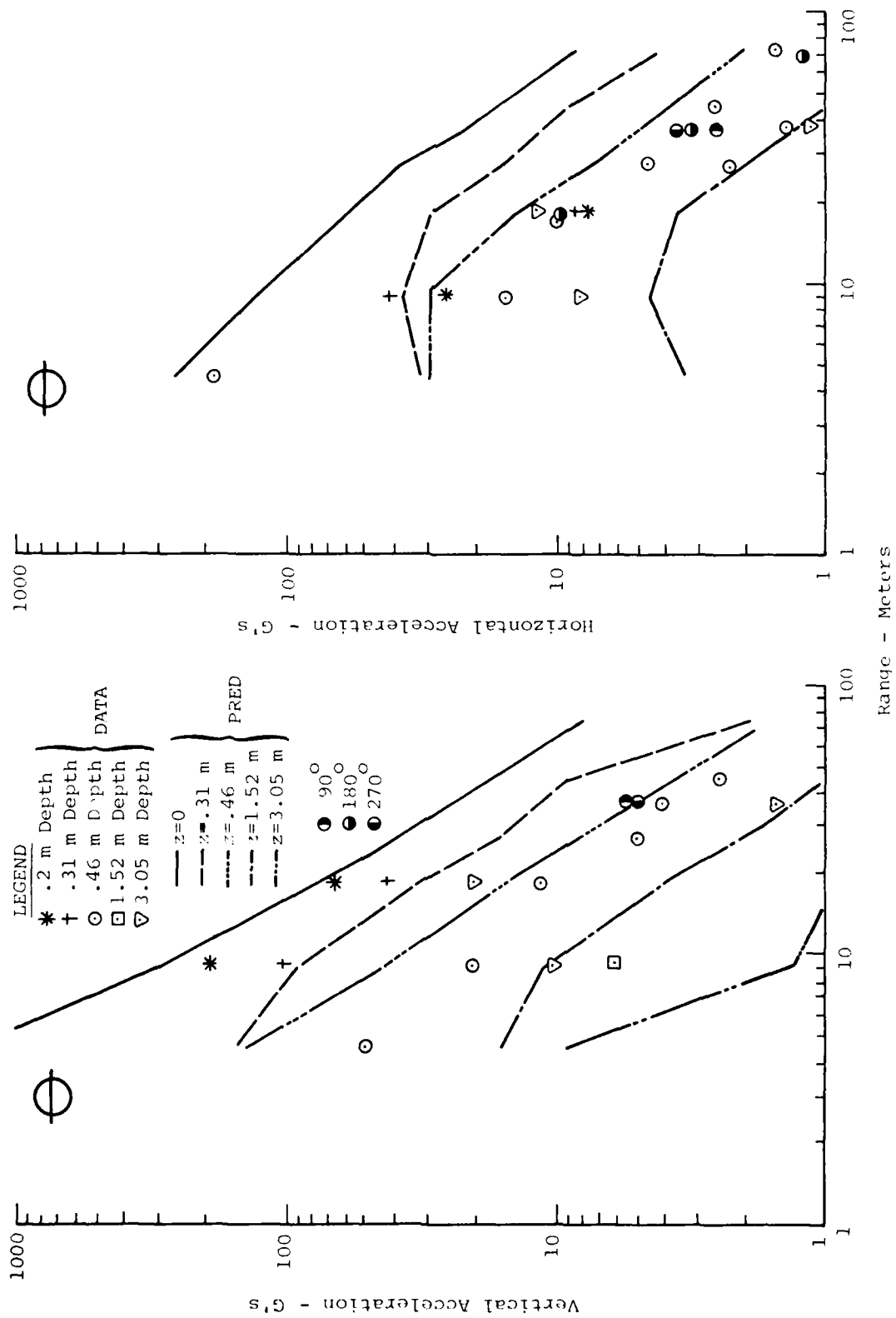


Figure 47. Comparison of Measured and Predicted Peak Values of Air Blast Induced Acceleration for MBI-1.

Horizontal motions were not as successfully predicted as the vertical motion. The data at the 0.2 m and 0.31 m depths were well below predicted levels. Prediction of the magnitudes and attenuation rate was more successful at the 0.46 m depth.

Both horizontal and vertical motions predicted for the 1.52 m and 3.05 m depths appear to be low. This is probably in part, due to the difficulty of isolating the air slap component at these depths.

Both Event 1 and Event 3 were 2.09×10^{-3} terrajoule experiments. The primary purpose of Event 3 was to measure the event to event data scatter. Figure 48 is a comparison of vertical and horizontal accelerations from both experiments. In general, the data scatter of Event 3 defines both the upper and lower bound of the data bands for both horizontal and vertical motions. Data scatter for vertical acceleration is approximately a factor of three bottom to top for all ranges and for horizontal acceleration it is about a factor of two for all ranges. The reproducibility of these experiments was good.

Event 7 utilized a 5.35×10^{-4} terrajoule charge. Peak vertical and horizontal accelerations are shown in figure 49.

In general, attenuation rates were very successfully predicted for vertical motions. Magnitudes were well predicted also.

Horizontal motions were not as well predicted. Predicted magnitudes at the 0.28 m depth appear low, especially at the larger ranges. Predicted magnitudes at the 1.52 m depth were high; however, predicted attenuation rates at both depths were approximately that exhibited by the data.

Figure 50 presents the peak vertical and horizontal velocities produced in Event 1. Vertical velocities at the 0.46 m depth were reasonably well predicted at ranges greater than 18.3 m. Magnitudes and the attenuation rate were substantially below the predicted

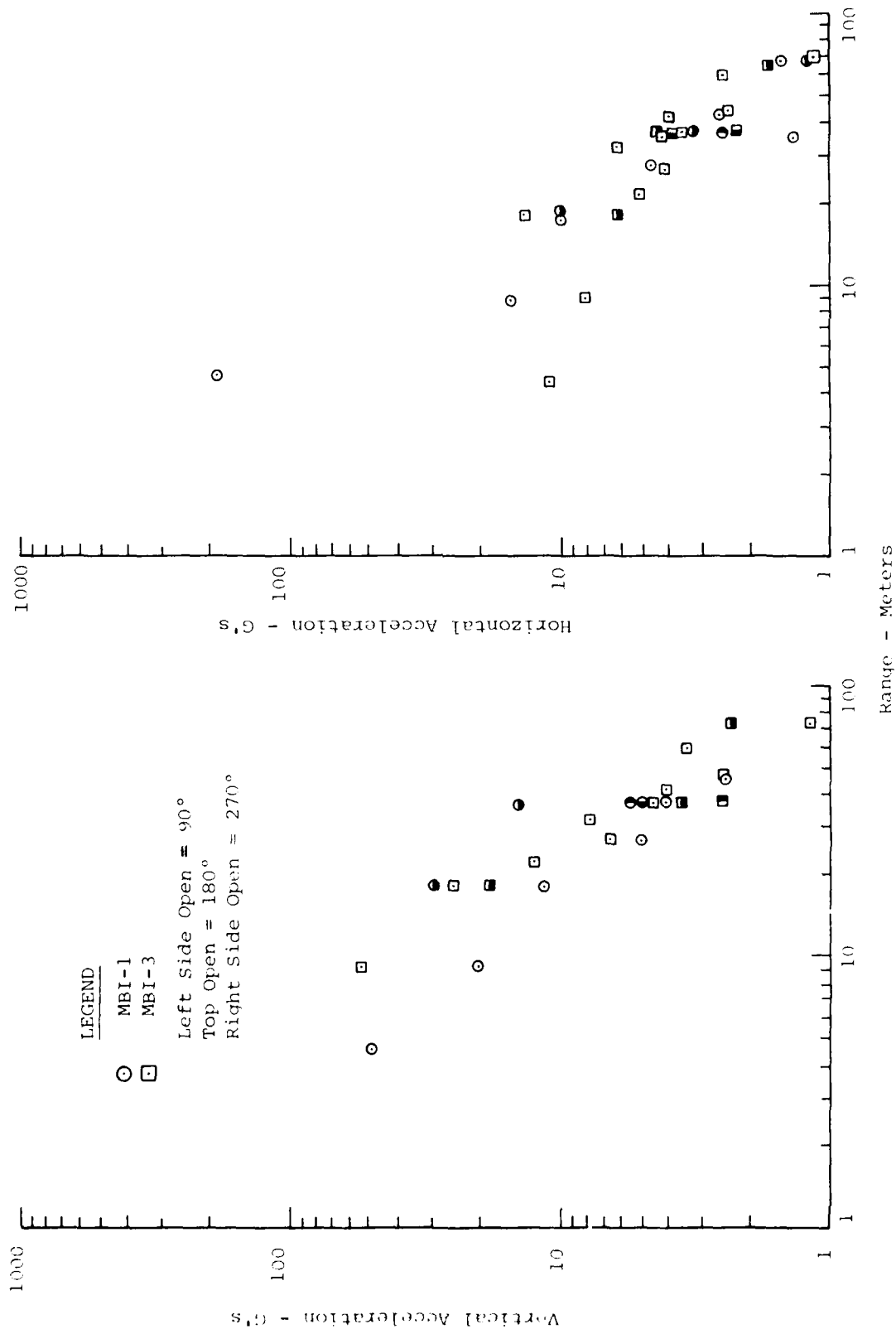


Figure 48. Comparison of Measured Peak Values of Airblast Induced Acceleration from MBI-1 and MBI-3. (At the .46 m Depth)

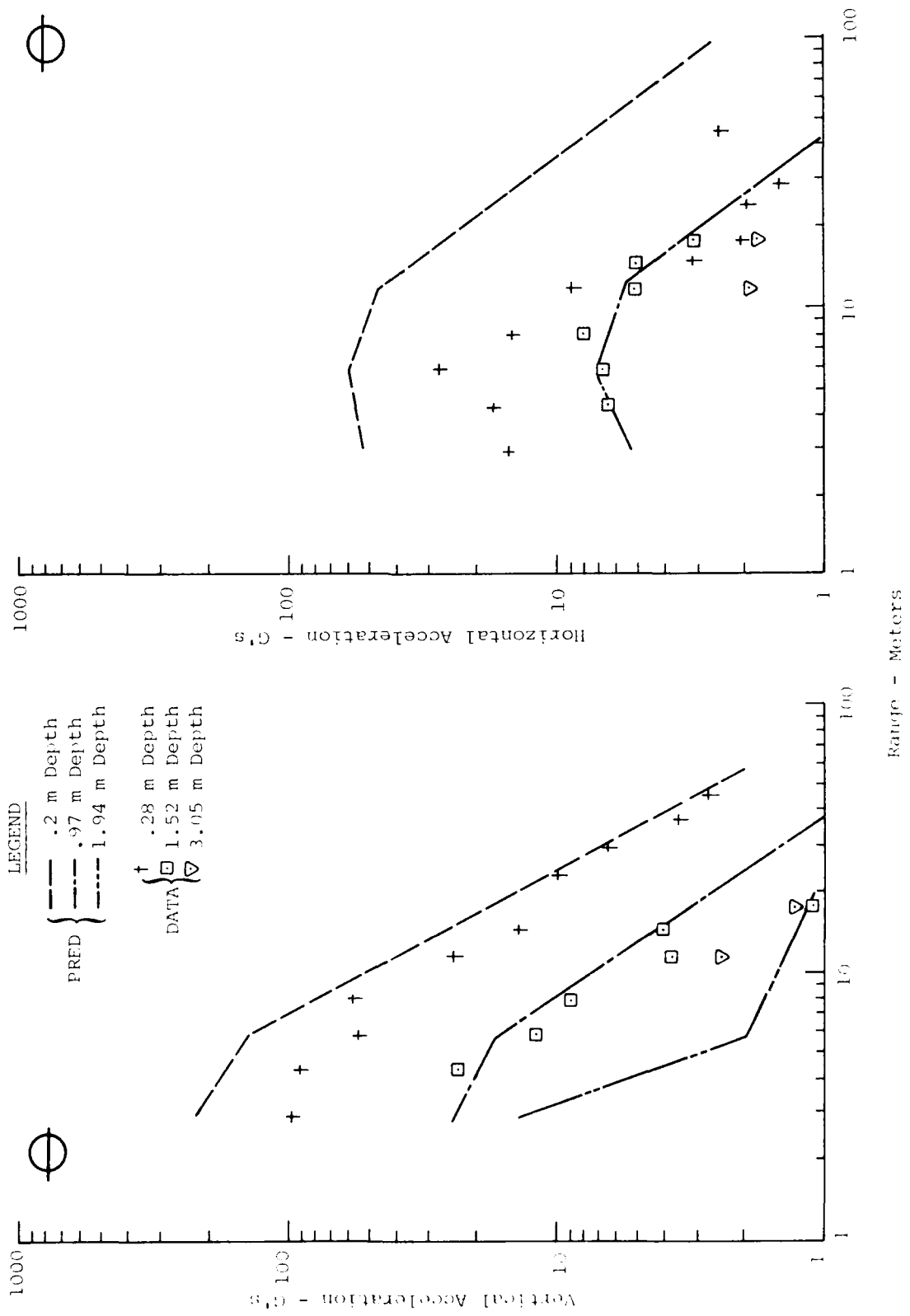


Figure 49. Comparison of Measured and Predicted Peak Values of Airblast Induced Acceleration for MBI-7.

AD-A085 726

CIVIL SYSTEMS INC ALBUQUERQUE NM
MISERS BLUFF PHASE I SINGLE BURST EXPERIMENTS. GROUND SHOCK ANA--ETC(U)
MAR 78 J L BRATTON, J S PHILLIPS

F/G 18/3

DNA001-77-C-0301

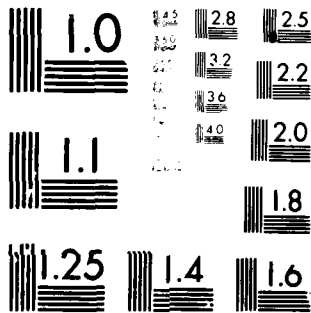
UNCLASSIFIED

DNA-5004Z

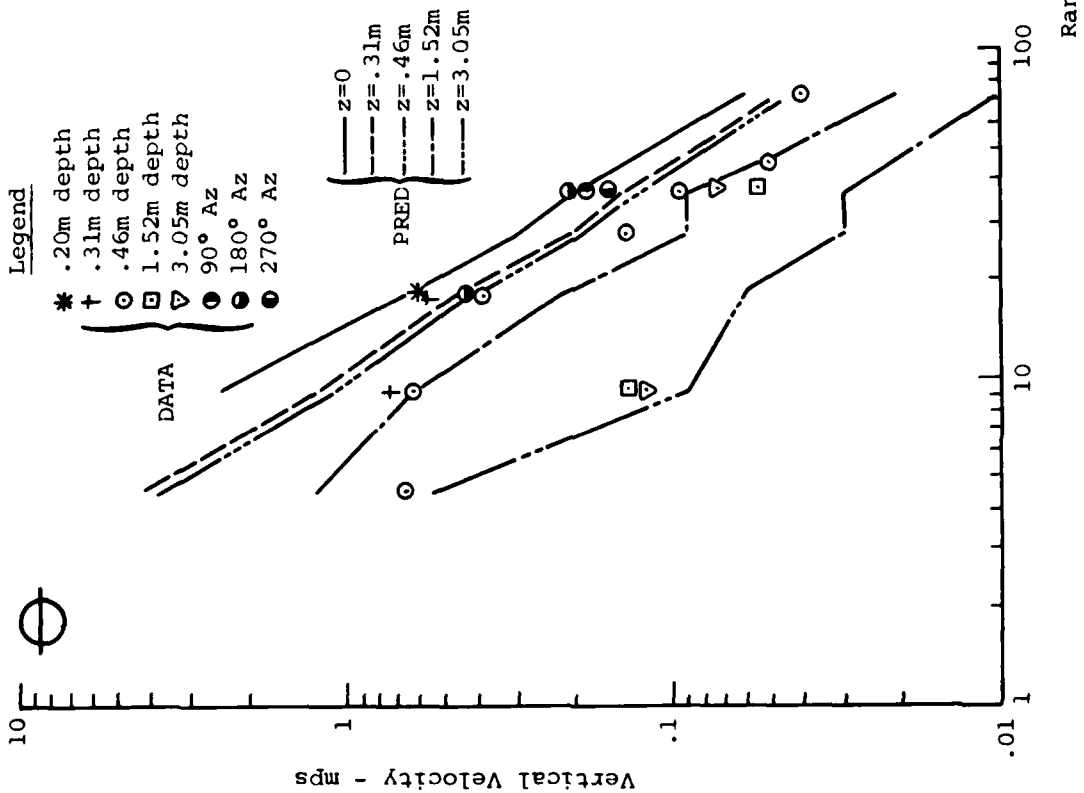
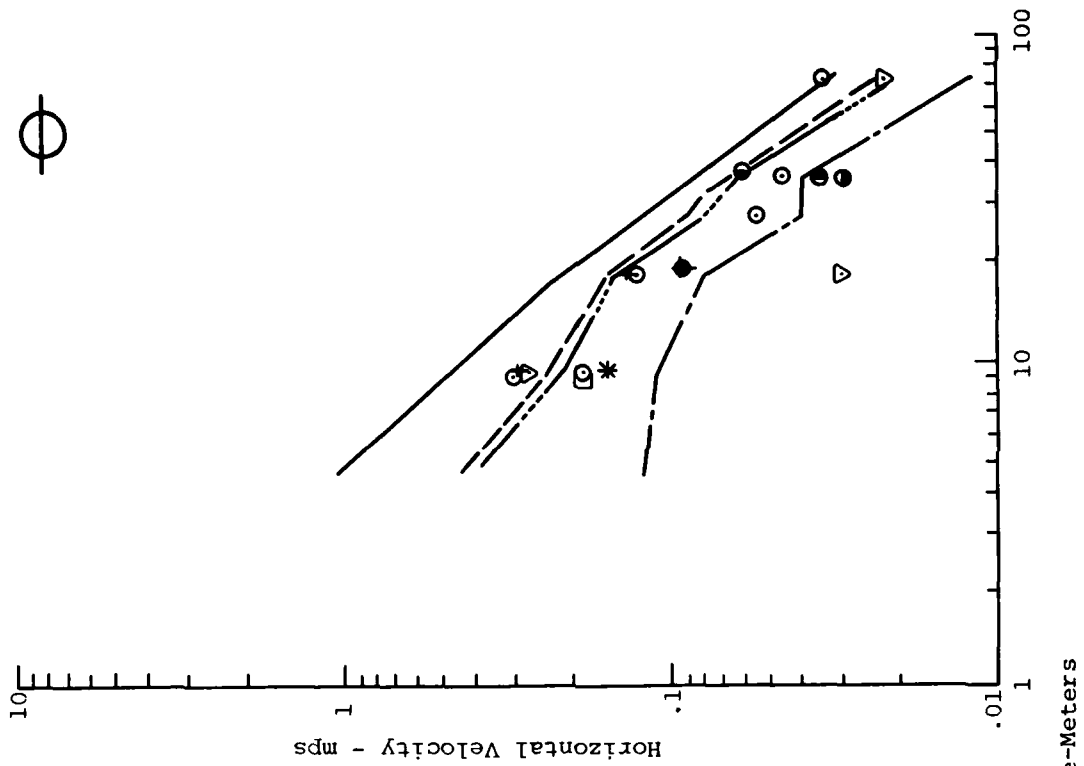
NL

2 of 2
AD
ADMIN

END
DATE
FILMED
4-80
DTIC



MICROCOPY RESOLUTION TEST CHART
NATIONAL BUREAU OF STANDARDS-1963-A



Legend

- * .20m depth
- + .31m depth
- .46m depth
- 1.52m depth
- ▽ 3.05m depth
- 90° Az
- 180° Az
- 270° Az

DATA

- z=0
- - z=.31m
- · - z=.46m
- · - z=1.52m
- · - z=3.05m

PRED

Figure 50. Comparison of Measured and Predicted Peak Values of Air Blast Induced Velocity for MBI-1

values at ranges less than 18.3 m. This also seems to be the case at the 0.31 m depth, although data is limited. Data scatter is a maximum of a factor of three at the 36.6 m range for the 0.46 m depth. Predictions at the greater depths appear high, but as pointed out before, the air slap component is difficult to isolate at depth. The broader pulse associated with the particle velocity complicates this even further. In fact, the arrival time plots (Section 3.2.2) indicate that upstream signals will arrive before the velocity peaks at most ranges and depths. Below about 3 m the upstream signals are predominantly horizontal.

Horizontal motions at the 0.46 m depth were, in general, within the predicted region for magnitudes and the predicted attenuation rate approximated the actual rate. Data scatter was a maximum of a factor of two at the 36.6 m range. Predictions at the 0.31 m depth were also very good. Predictions at other depths suffer from the same problem discussed above.

Figure 51 is a comparison plot of Events 1 and 3. As can be seen on the plot of vertical velocity, the reproducibility of the experiments is very good. Maximum data scatter in vertical motion occurs at 36.6 m range where the most data were taken and has a value of a factor of 2.5. Horizontal motions are not as tightly packed as vertical motions; however, the reproducibility is still good. Maximum scatter for the horizontal data is approximately a factor of three at the 36.6 m range.

Peak vertical and horizontal velocities for the 5.35×10^{-4} terrajoule experiment are presented in figure 52. Vertical motion at the 0.28 m depth was generally less than predicted between the 2.90 m and 7.93 m ranges. Between the 7.93 m and 17.4 m ranges, peak values are, as predicted. At ranges greater than 23.2 m the predictions are low. In general, the predicted attenuation rate approximates the actual rate at ranges greater than 7.9m. The data

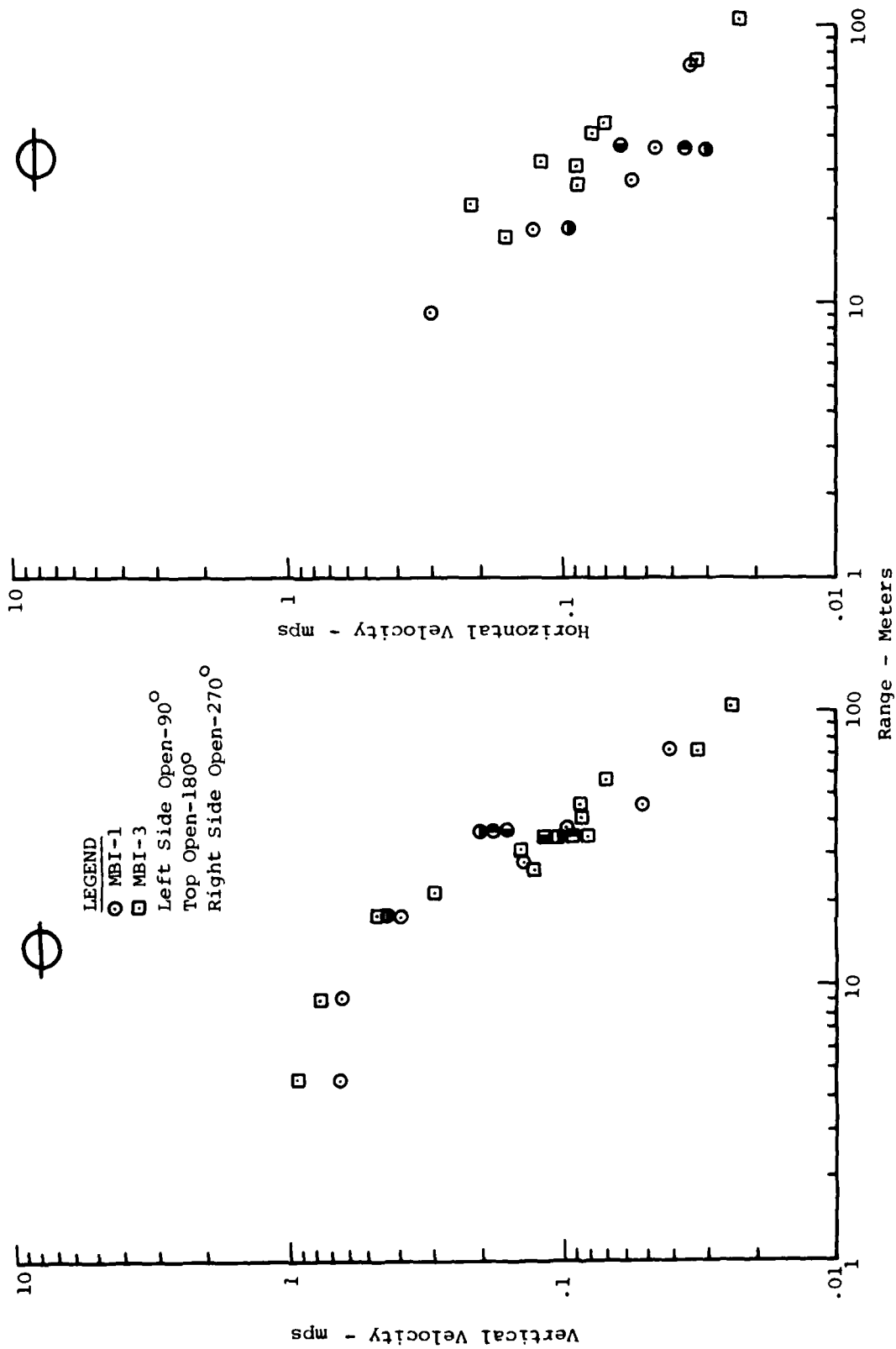


Figure 51. Comparison of Measured Peak Values of Airblast Induced Velocity from MBI-1 and MBI-3. (At the .46 m Depth)

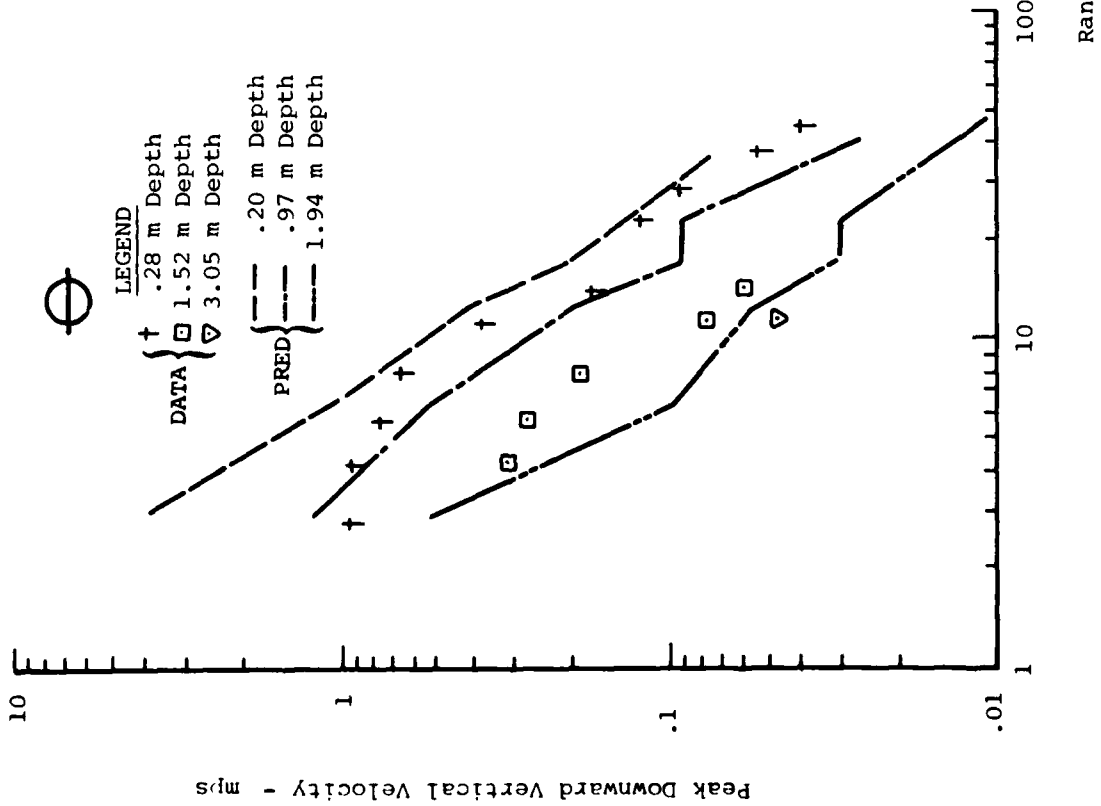
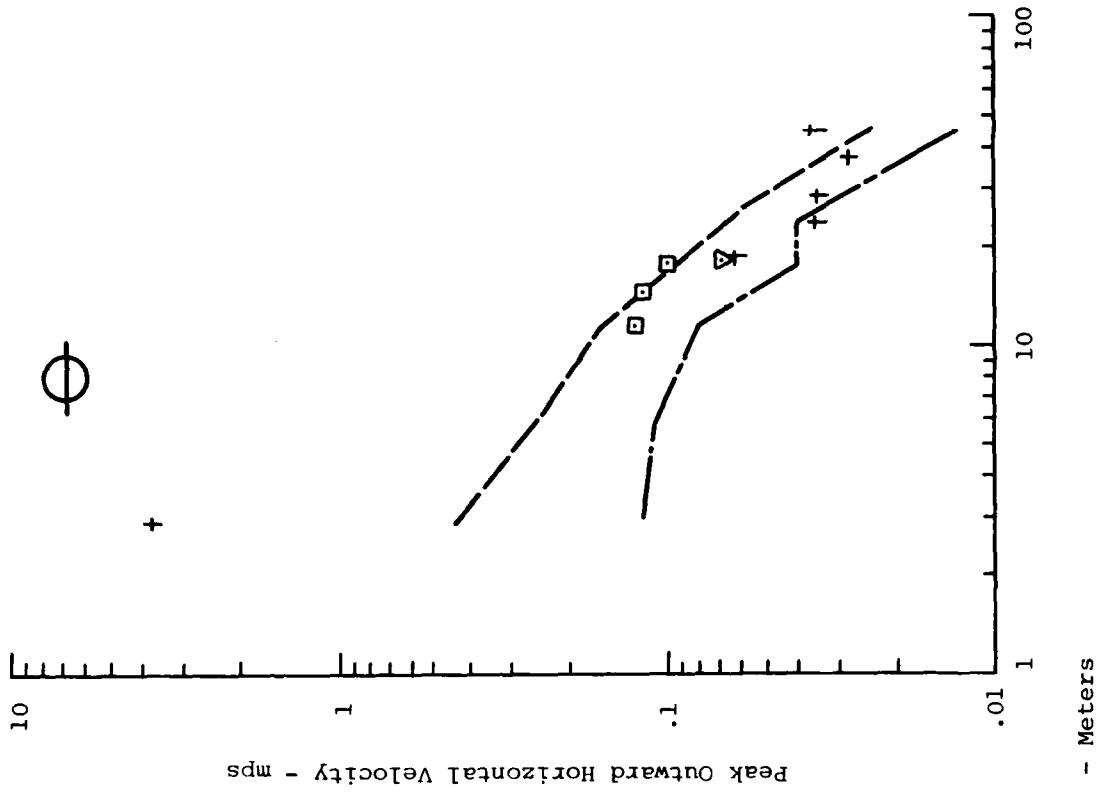


Figure 52. Comparison of Measured and Predicted Peak Values of Airblast Induced Velocity For MBI-7.

at the depth of 1.53 m falls within the predicted regions for the magnitude, and the attenuation rate is as previously described.

Horizontal motions were underpredicted and the attenuation of the data was generally slower than predicted. In addition to the underprediction, the data at the 0.46 m depth was lower in magnitude than the data recorded at the 1.52 m depth at ranges greater than 10 m. This may be due in part to the upstream signals traveling through the saturated layer and arriving about the same time as the air slap signal and thus adding to it and creating the higher magnitude.

3 Tangent Below Configuration. Peak values of vertical and horizontal accelerations are presented in Figure 53. Although there are very little airblast data, the estimations of vertical accelerations were generally good. Magnitudes were estimated well at ranges greater than 18.3 m. Data scatter for these data reached a maximum of approximately a factor of two at the 36.6 m range. The predicted attenuation rate closely approximated that shown by the data at ranges greater than 18.3 m.

Horizontal accelerations were not well predicted. Predicted magnitudes were too low. The predicted attenuation rate was too fast at ranges less than 73.2 m and too slow at ranges greater than 73.2 m. The data also exhibited a region between 45.75 and 73.2 m where there was little attenuation with range. This is probably a result of upstream signals arriving before the airblast induced motion peaks at ranges beyond about 20 m.

Peak vertical and horizontal velocities are presented in Figure 54. Vertical velocities exhibited the same general trends as the vertical accelerations. Data scatter for these data was a maximum of a factor of 1.5 at the 36.6 m range.

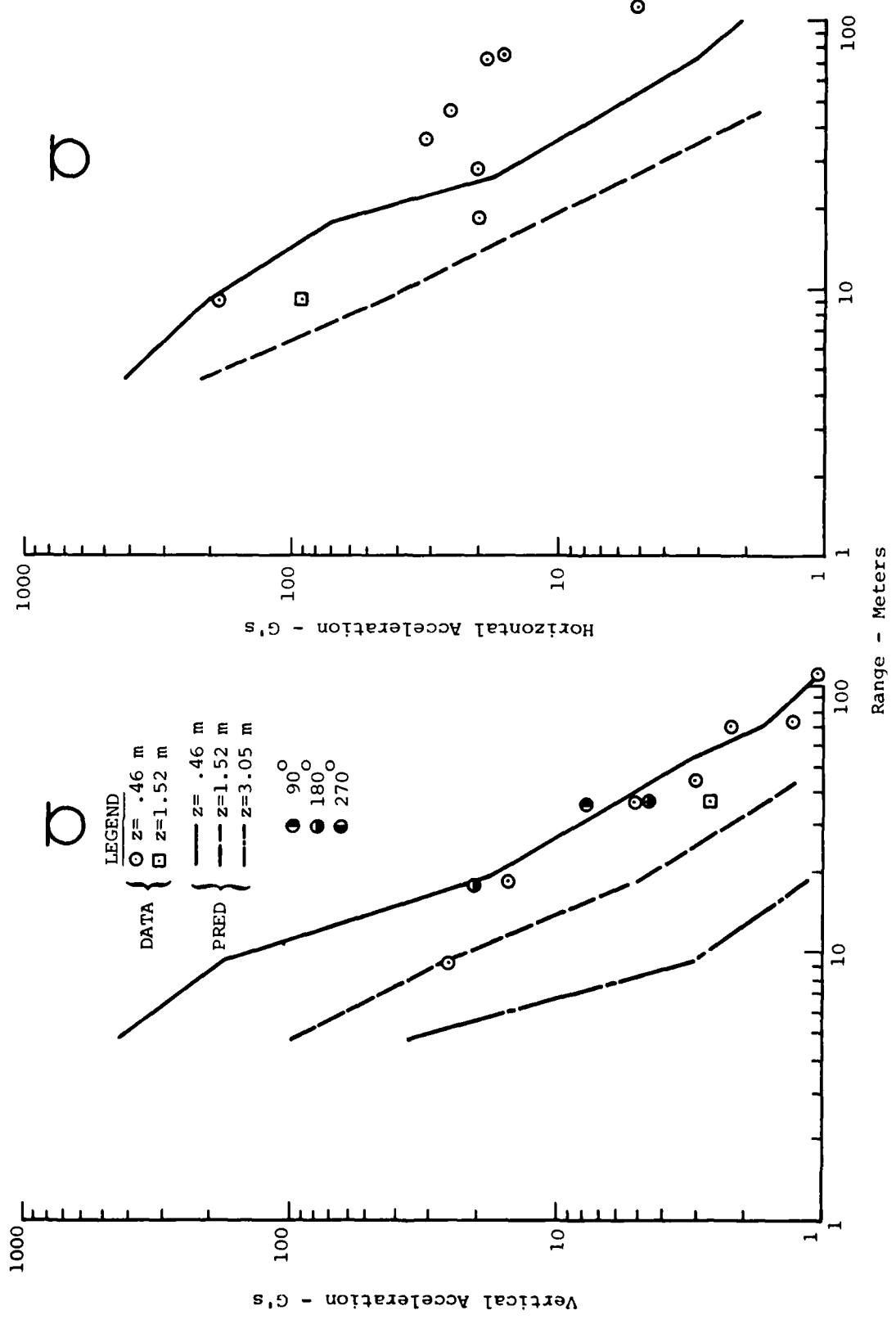


Figure 53. Comparison of Measured and Predicted Peak Values of Airblast Induced Acceleration for MBI-5.

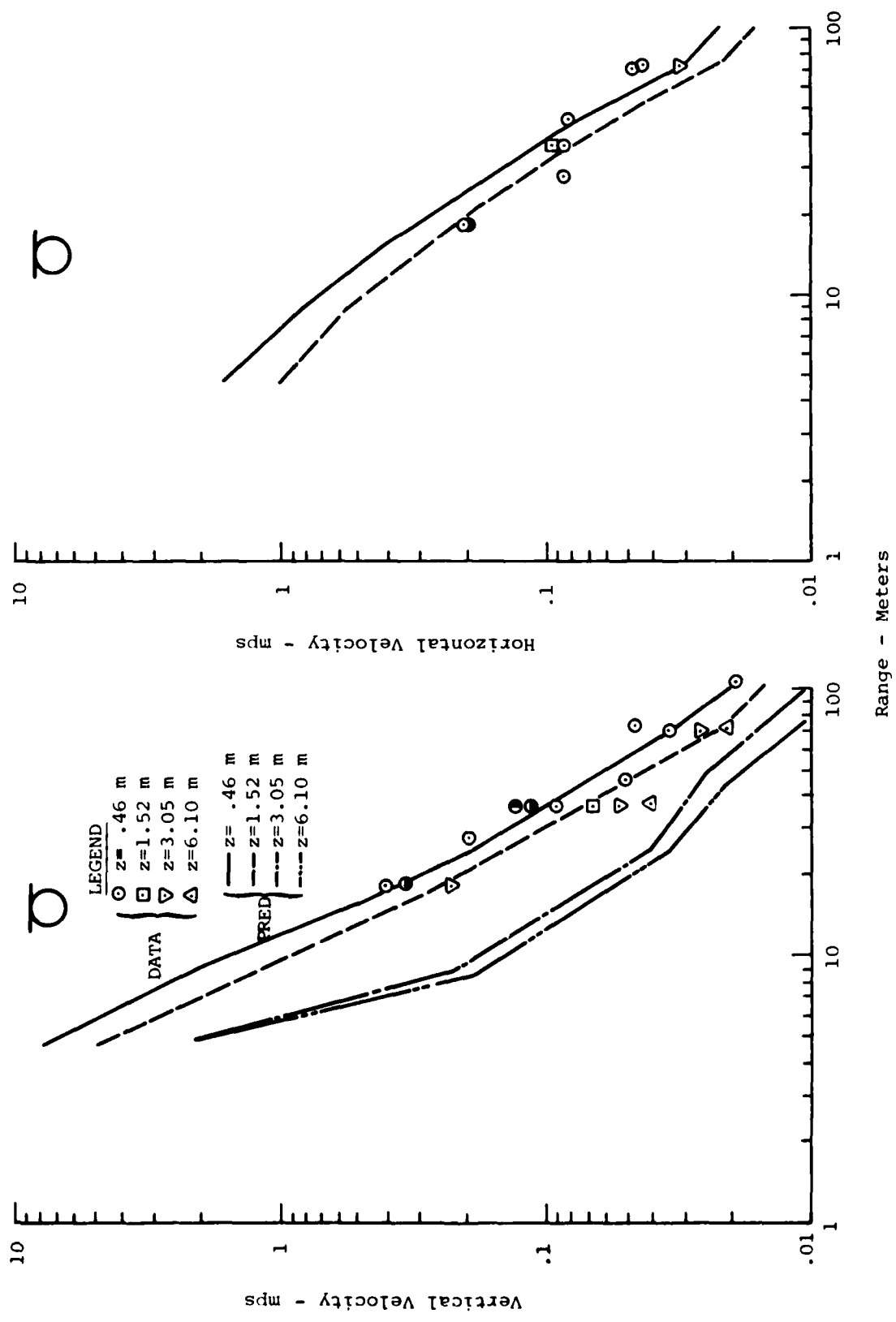


Figure 54. Comparison of Measured and Predicted Peak Values of Airblast Induced Velocity for MBI-5.

Horizontal velocities were poorly predicted. The data were below the predicted level out to the 27.45 m range, and above the predicted level at ranges greater than 45.75 m. Predicted attenuation rates were generally too slow. The region between the 27.45 m range and the 45.75 m range showed very little attenuation.

4 Height of Burst Comparison

Figure 55 presents vertical and horizontal velocities for the three heights of burst at the 0.46 m depth. Event 7 has been scaled up using cube root of the yield scaling and is shown also. Vertical velocities are about what one would expect based on the airblast comparisons. The disparities in the configurations are at the "close-in" ranges (less than 9.15 m), with peak values farther out converging to a single line. The surface tangent configuration produces the highest values, with the half buried producing the next highest. Unfortunately, the air slap component was impossible to isolate with any confidence at the "close-in" ranges for the tangent below experiment.

Horizontal velocities were not as tightly packed as verticals at the farther out ranges. However, the same general trends are observed. Vertical and horizontal velocities for the 3.05 m depth are presented in Figure 56. In general, the trends shown on this figure are the same as discussed above.

4.3.3 OSCILLATORY COMPONENT OF GROUND MOTION

a) Definition

The oscillatory component of ground motion is that portion of ground motion which has often been called outrunning or surface wave in the past. As we discussed in Section 3.2.2 we believe that this component is really composed of two parts, the outrunning signal and the surface wave. The motion peaks are associated with the surface wave portion of the signal and will be discussed below. Figures 57 and 58 are graphical definitions of this component for the three different configurations and for both vertical and horizontal velocities.

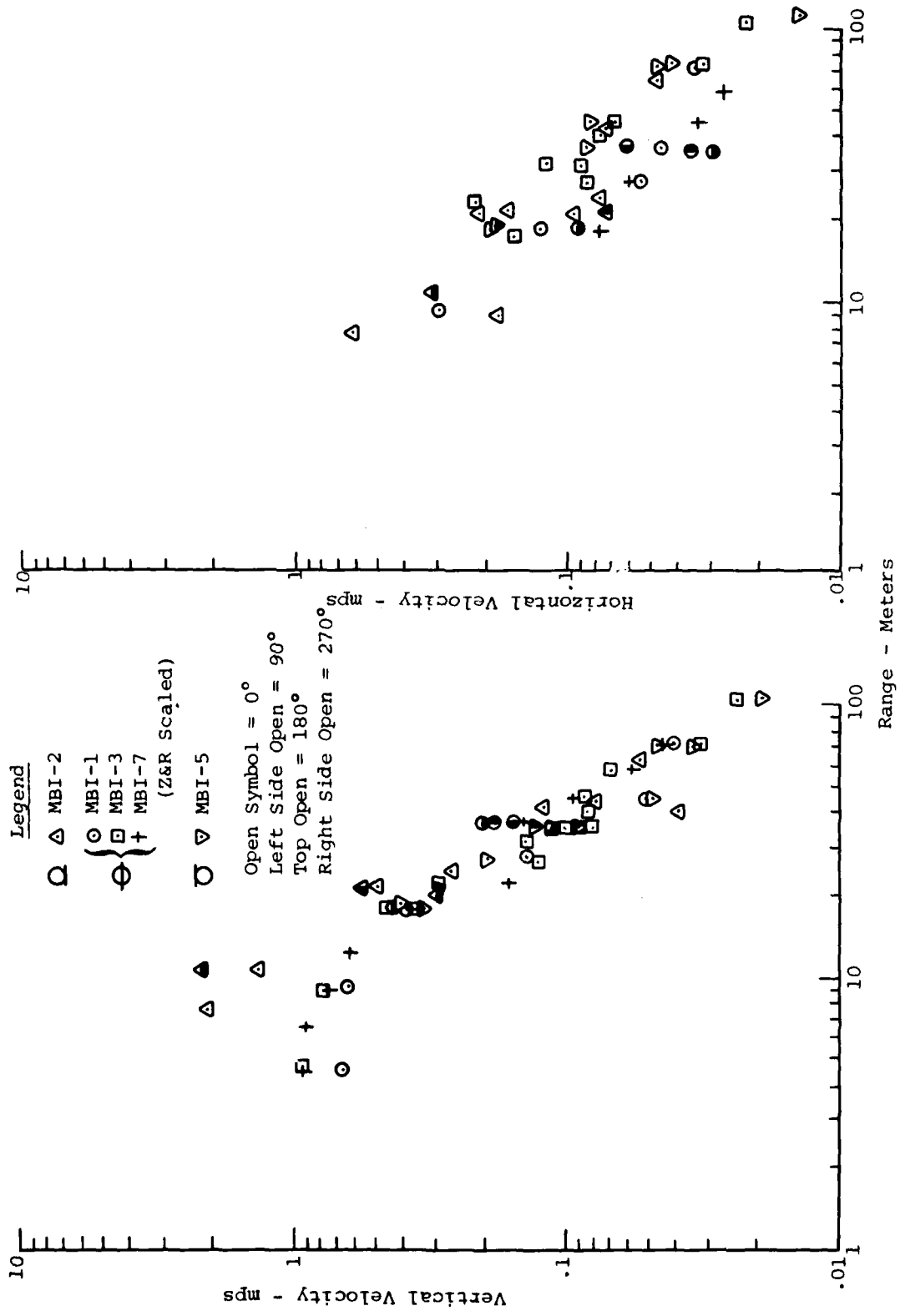


Figure 55. Height of Burst Comparison of Air Blast Induced Velocities at the .46m Depth

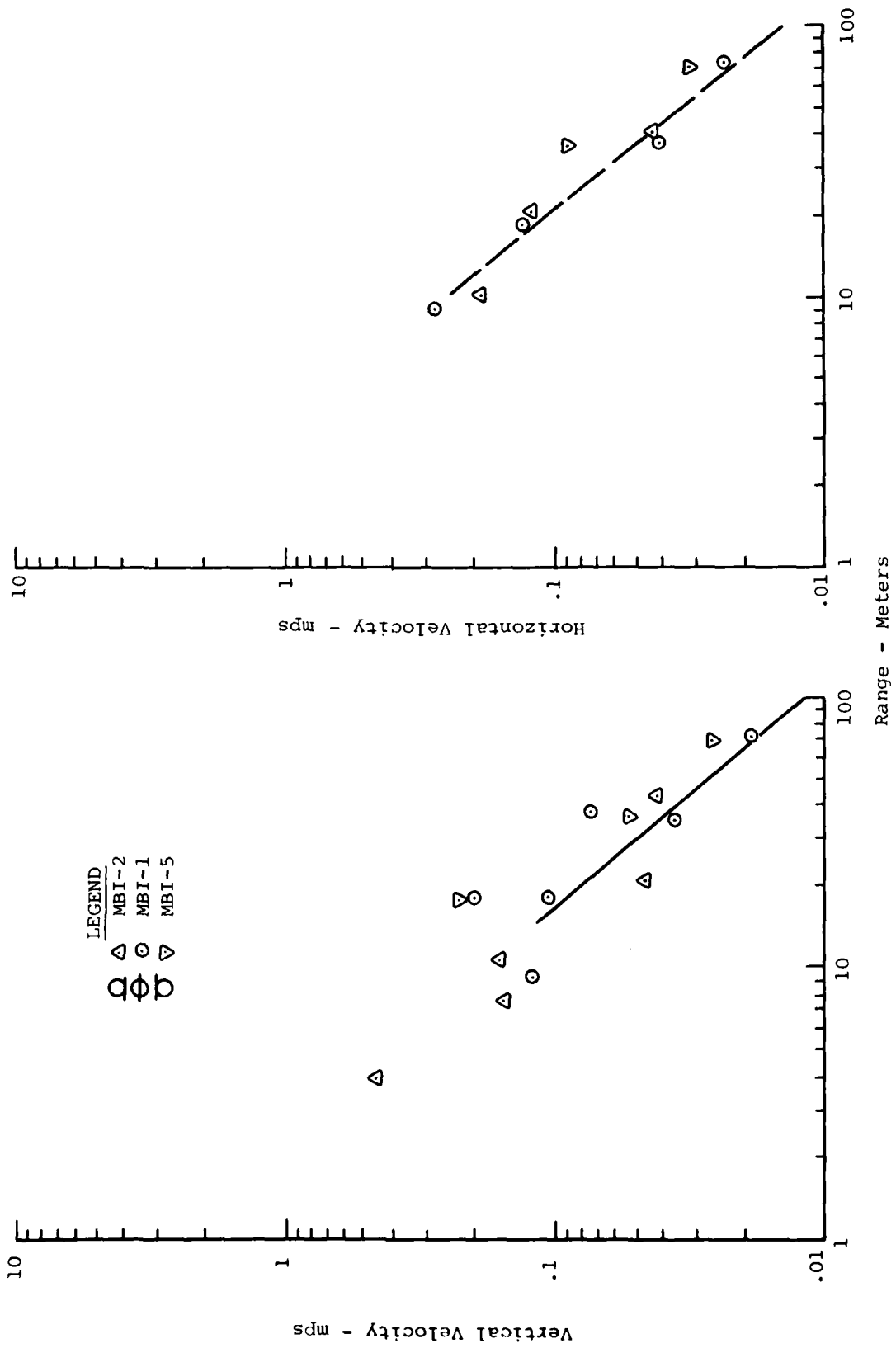


Figure 56. Height of Burst Comparison of Airblast Induced Velocities at the 3.05 m Depth.

CONFIGURATION

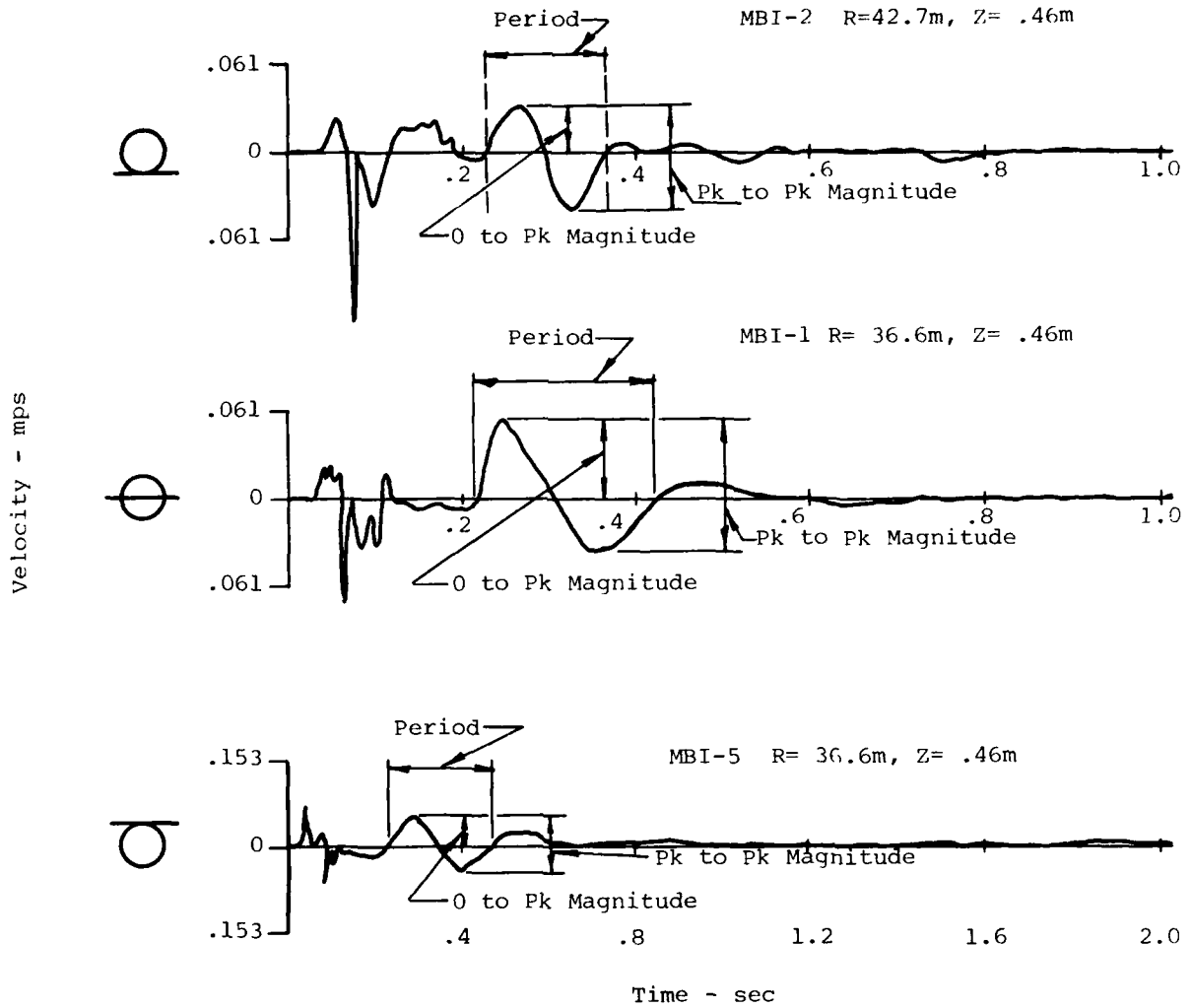


Figure 57: Definition of Oscillatory Component of Vertical Motion

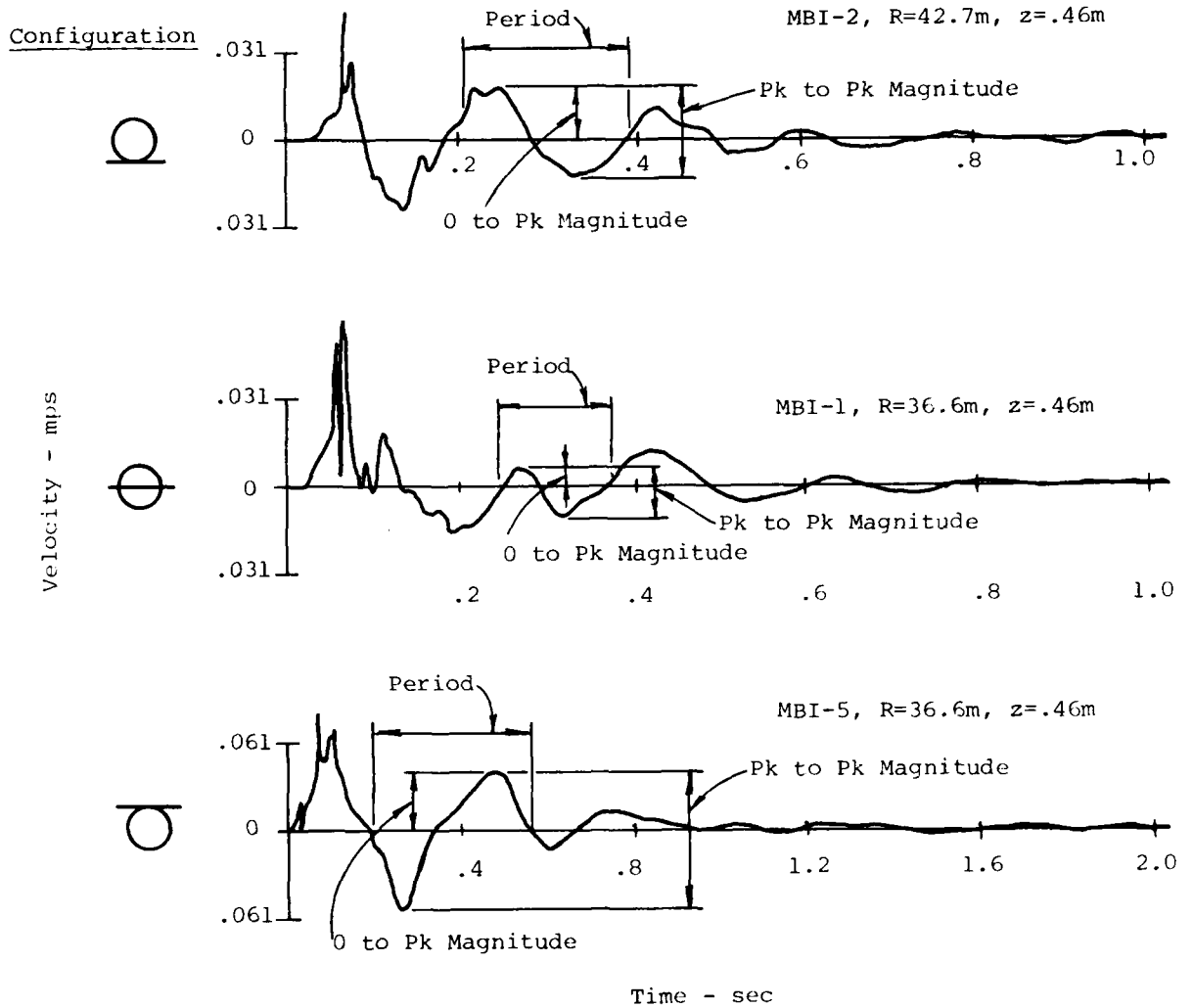


Figure 58. Definition of Oscillatory Component of Horizontal Motion

It is important to realize that although the predictions of magnitudes are in terms of zero-to-peak values, all discussions that follow (excluding those concerned with the predictions) will be in terms of peak-to-peak values. This is done because it is felt that the peak-to-peak values are less sensitive to baseline shift and thus give a more realistic picture of the phenomenology.

b) Discussion of Data

1. Surface Tangent Configuration. Figure 59 presents the prediction of the oscillatory component of motion at the 0.46 m depth compared with the zero-to-peak values of the data.

In general, magnitudes of the vertical velocity were somewhat over-predicted. The straight line fit to the data shown on the figure indicates an attenuation rate of $R^{-1.25}$ which is very close to the predicted attenuation rate of $R^{-1.2}$. The alternate fit shown on this figure results from a study of the behavior of the other experiments (which are discussed in the following sections). This fit indicates a region where the attenuation rate is $R^{-3.2}$, and intermediate region with no attenuation, and finally a region with an attenuation rate of $R^{-1.25}$.

Zero-to-peak values of horizontal velocities were also overpredicted in magnitude, however, the attenuation rate of the data and the predicted values were both approximately $R^{-1.9}$.

Peak-to-peak values of the oscillatory component are shown in Figure 60. The vertical velocities, in some respects, behave in a similar manner as did the alternate fit on Figure 59. That is, they experience an initial rapid attenuation rate of $R^{-2.3}$ at the "close-in" ranges and then a slower rate (approximately 1/2 of the original) at the remaining ranges.

Horizontal peak-to-peak values behave as did the zero-to-peak values with only a slightly higher attenuation rate of $R^{-2.3}$. Data scatter for these values was a maximum of a factor of 1.5 for the vertical velocities and about 4 for the horizontal velocities.

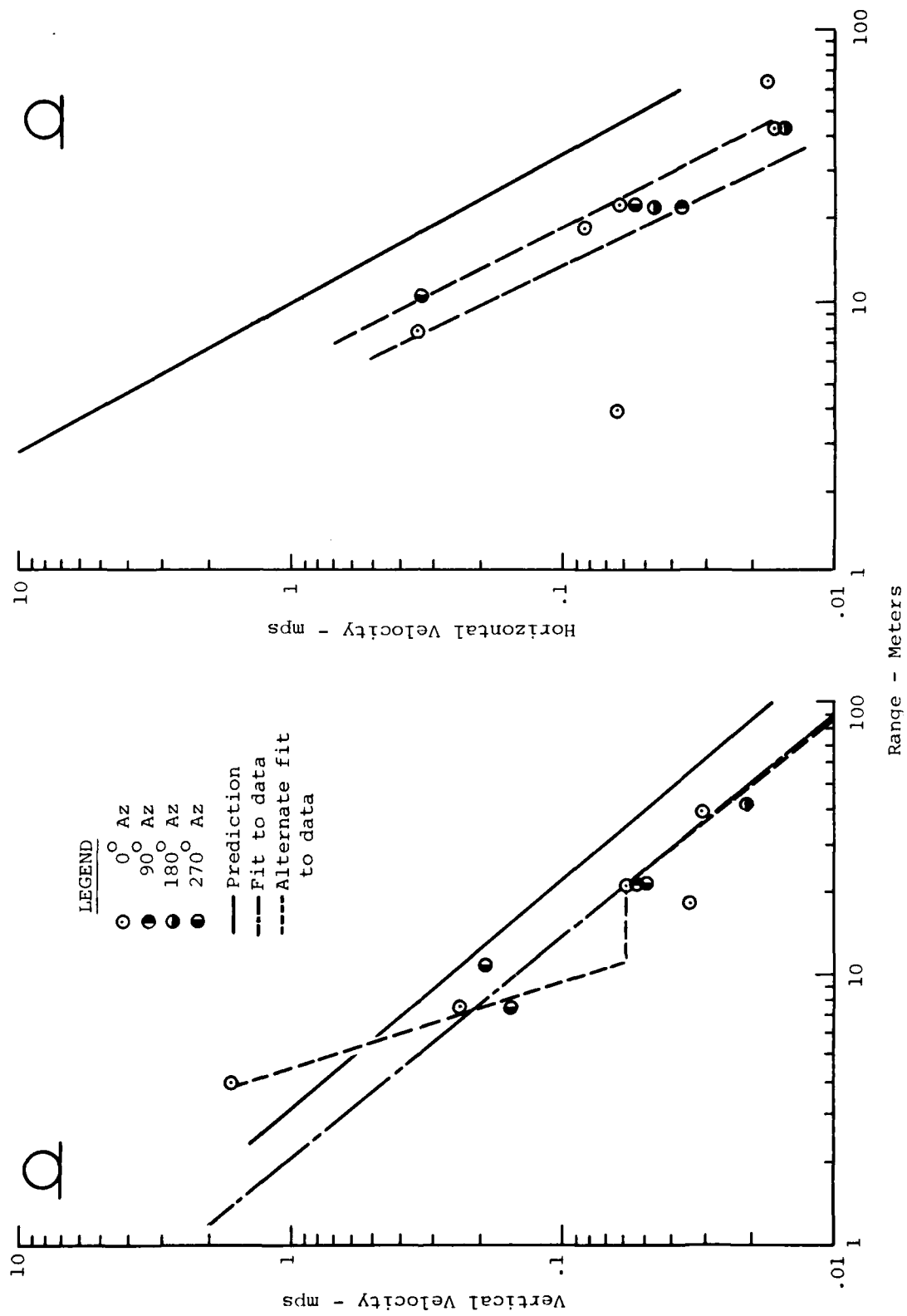
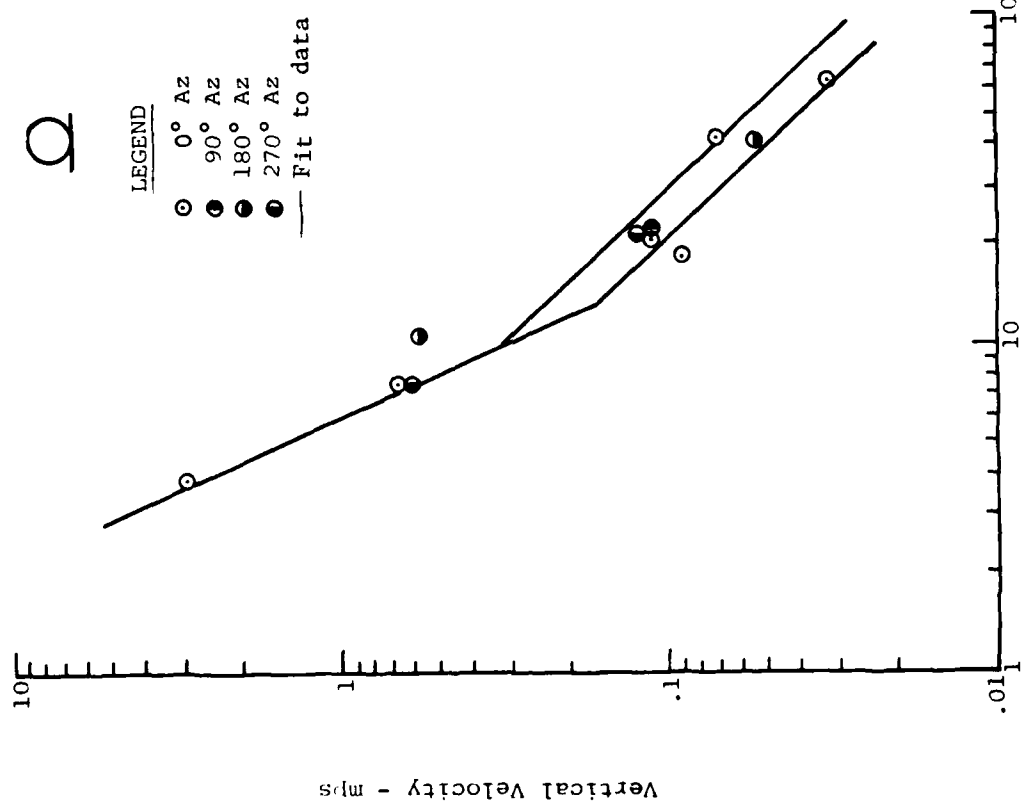
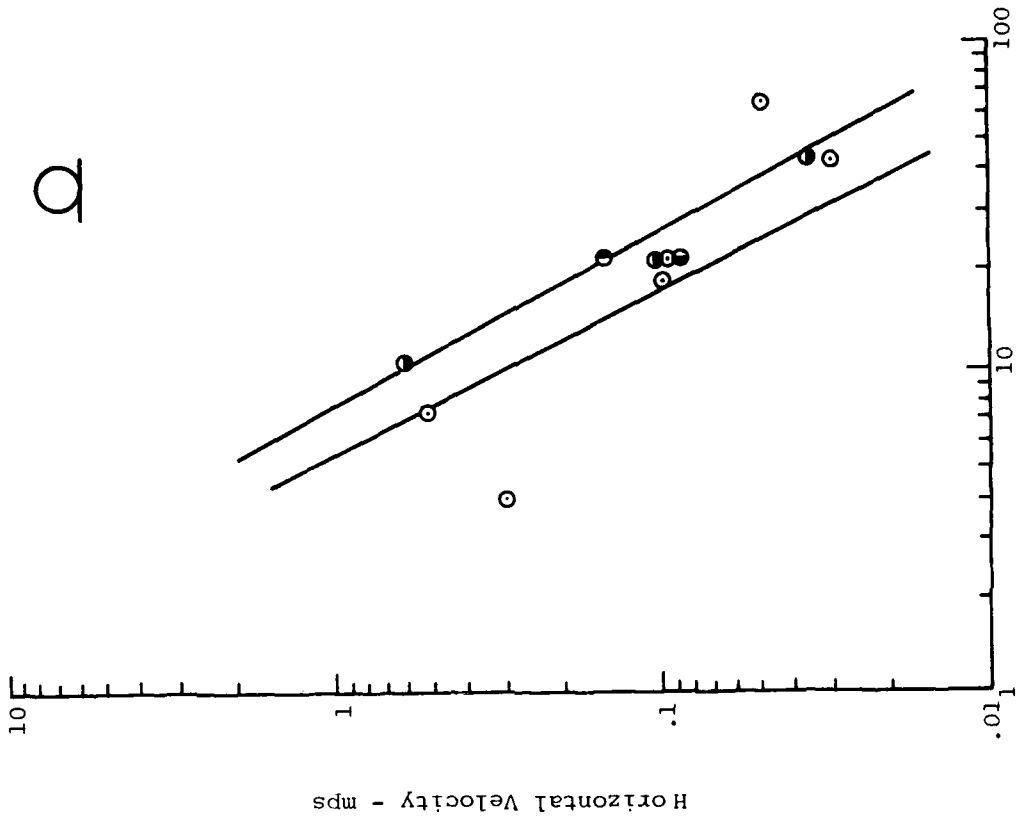


Figure 59. Comparison of Predicted and Measured Zero to Peak Values of the Oscillatory Component at the .46 m Depth for the Surface Tangent Configuration - MBI-2.



Q

Q

LEGEND

- 0° Az
- 90° Az
- 180° Az
- 270° Az
- Fit to data

Figure 60: Peak to Peak Values of the Oscillatory Component at the .46m Depth for the Surface Tangent Configuration - MBI-2

The data recorded at the greater depths are shown in Figure 61. Data is limited in these regions. In general the attenuation rate at these depths were all approximately $R^{-1.6}$. It is interesting to note that the vertical velocities at these depths are generally the same in magnitude as those at 0.46 m depth indicating there is little attenuation of this component with depth. This lack of attenuation with depth supports the hypothesis that this is a surface wave.

Horizontal velocities recorded at these greater depths seem to behave as the values at the 0.46 m depth. The attenuation rate is, however, somewhat slower at $R^{-1.6}$.

The arrival times of the oscillatory component are shown in Figure 62. As seen on the arrival time versus range plot for the 0.46 m depth, the oscillatory component is propagating away from the source at a velocity of 320 mps. The arrival time versus depth plot shows the oscillatory component is propagating upward (i.e. arriving at the greater depths first) and the velocity of propagation at depth is approximately the same as near the surface and consistent with the shear wave velocities in the upper 15 meters.

2. Half Buried Configuration. Figure 63 presents the actual and predicted zero-to-peak values of the vertical and horizontal oscillatory components for both Event 1 and Event 3 at the 0.46 m depth. The predicted vertical magnitudes were, in general, too large. A fit to the majority of the data (shown by the solid line on the figure) exhibits an attenuation rate of $R^{-0.55}$. This is somewhat "slower" than the predicted rate of $R^{-1.2}$. If the close-in point is included in the fit then a transitioning character can be seen in the data. This alternate fit shows an attenuation rate of $R^{-4.5}$ between 4 m and 11 m. At ranges greater than 11 m the attenuation rate is $R^{-0.55}$. This is termed an "alternate fit" because it places a great deal of confidence on the single data point at the 4.6 m range.

Horizontal motions were also over-predicted in magnitude. Much the same phenomena as experienced in the vertical motions is evident here. The majority of the data exhibits the attenuation

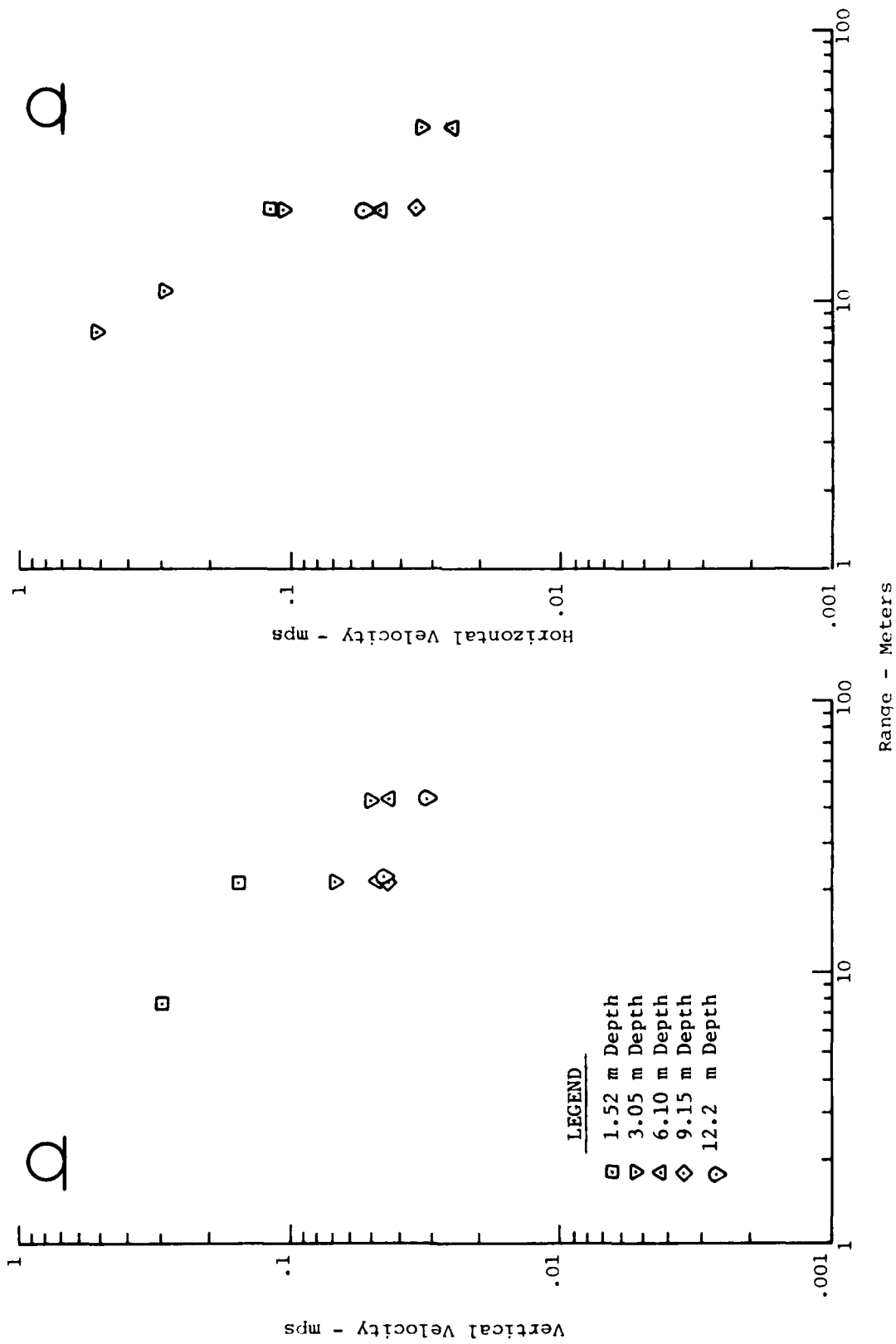
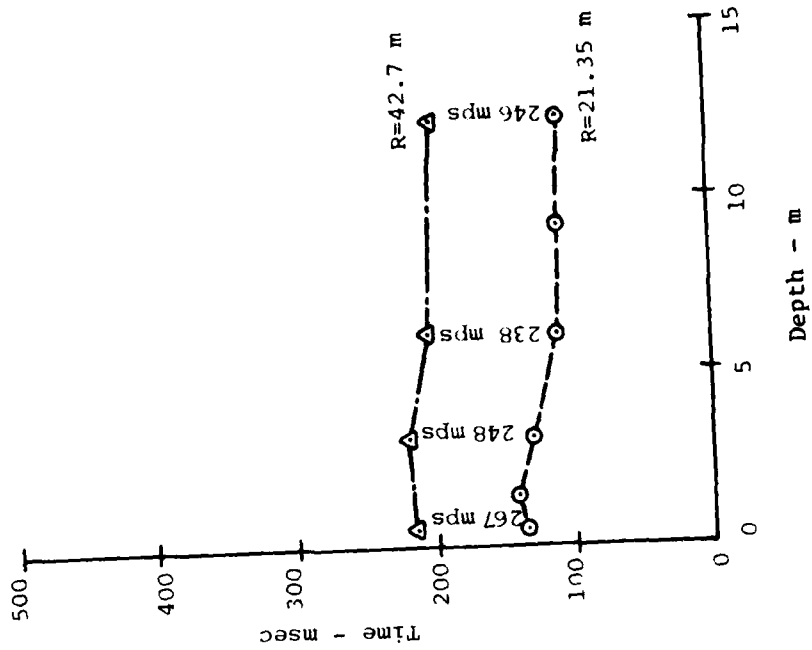


Figure 61. Peak to Peak Values of the Oscillatory Component at Greater Depths for the Surface Tangent Configuration - MBI-2.

Q



Q

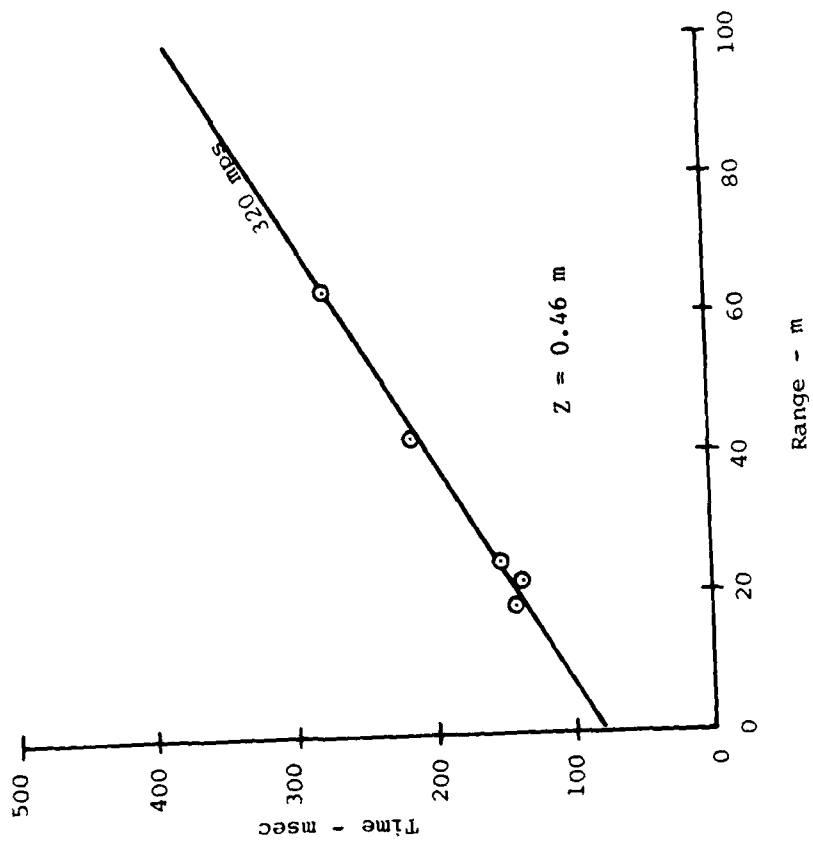


Figure 62. Arrival Time of the Oscillatory Component for the Surface Tangent Configuration - MBI-2.

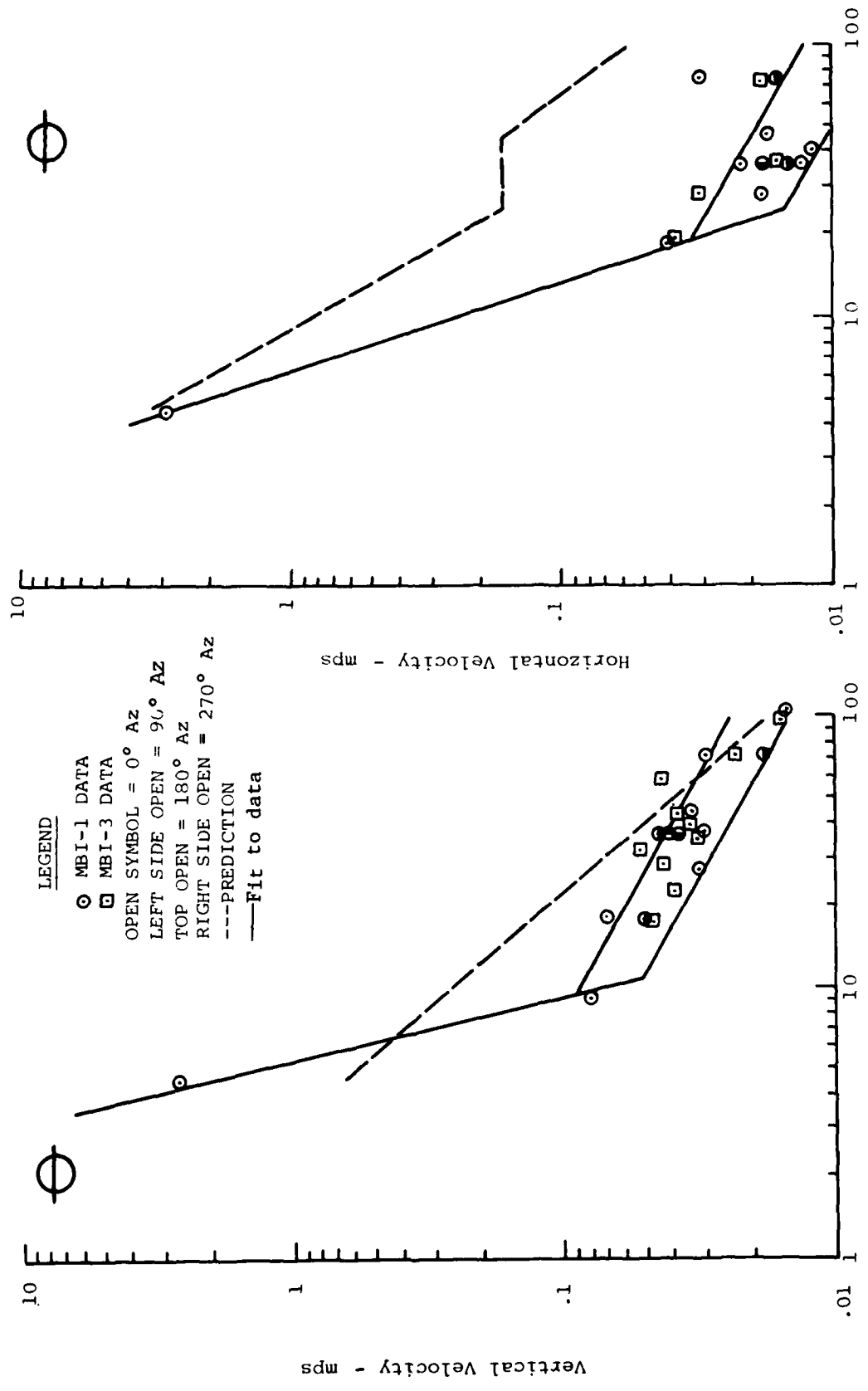


Figure 63: Comparison of Predicted and Measured Zero to Peak Values of the Oscillatory Component at the .46m Depth for the Half Buried Configuration MBI-1 and MBI-3

rate of $R^{-0.55}$. The alternate fit using the one close-in data point shows the transitioning character; i.e. rapid attenuation between the 5 m and 20 m ranges (a rate of R^{-3}) and relatively "slow" attenuation ($R^{-0.55}$) at ranges greater than 20 m.

The agreement between Events 1 and 3 is quite good in this figure. The scatter for both events is about the same. The vertical motions exhibit a maximum scatter of a factor of 1.6 with the horizontal scatter a value of 1.7.

The peak-to-peak values for these two events are shown in Figure 64. In general, both horizontal and vertical motions exhibit similar behavior to the alternate fits discussed above with the major difference being the fact that the peak-to-peak values indicated a definite transition region. This region occurs between 12 m and 50 m for the vertical motion and between 30 m and 80 m for horizontal motions. The final attenuation rates are also quite a bit "faster" for these peak-to-peak values than shown for zero-to-peak values. The final attenuation rate for vertical motion was $R^{-1.4}$.

Figure 65 presents the oscillatory component for depths greater than 0.46 m (1.5 ft). Data is limited for these depths, however, vertical motions all appear to be attenuating at the same rate of R^{-1} , while all horizontal motions attenuate at a rate of $R^{-1.9}$.

The peak-to-peak values of the third experiment (Event 7) performed in the half buried configuration are presented in Figure 66. In general the vertical motions exhibit the same trends as shown by the other two experiments. The initial rapid attenuation occurs between 4.5 m and 8 m and has a value of $R^{-3.6}$. The "transition" region extends from 8 m to 15 m. The final attenuation rate is $R^{-0.8}$.

Horizontal motions do not exhibit the behavior shown in the other experiments. The "eyeball" fit to the data is a single line and the constant attenuation rate has a value of R^{-1} .

In these three experiments the particle velocities recorded at depths greater than 0.46 m are generally about the same as those recorded at 0.46 m. This indicates that the oscillatory component is a surface wave phenomenon.

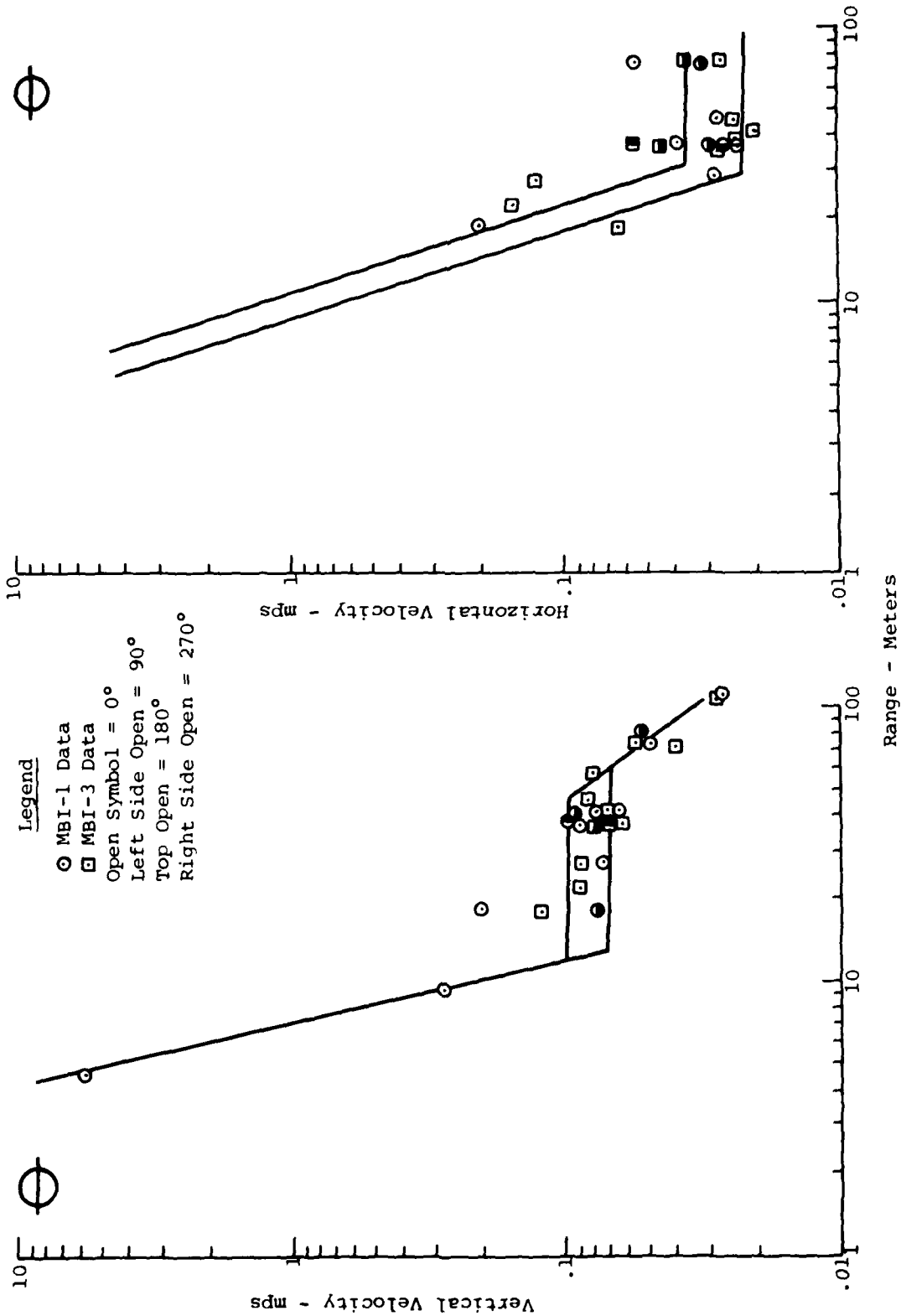


Figure 64. Peak-to-Peak Values of the Oscillatory Component at the .46m Depth for the Half Buried Configuration - MBI-1 and MBI-3

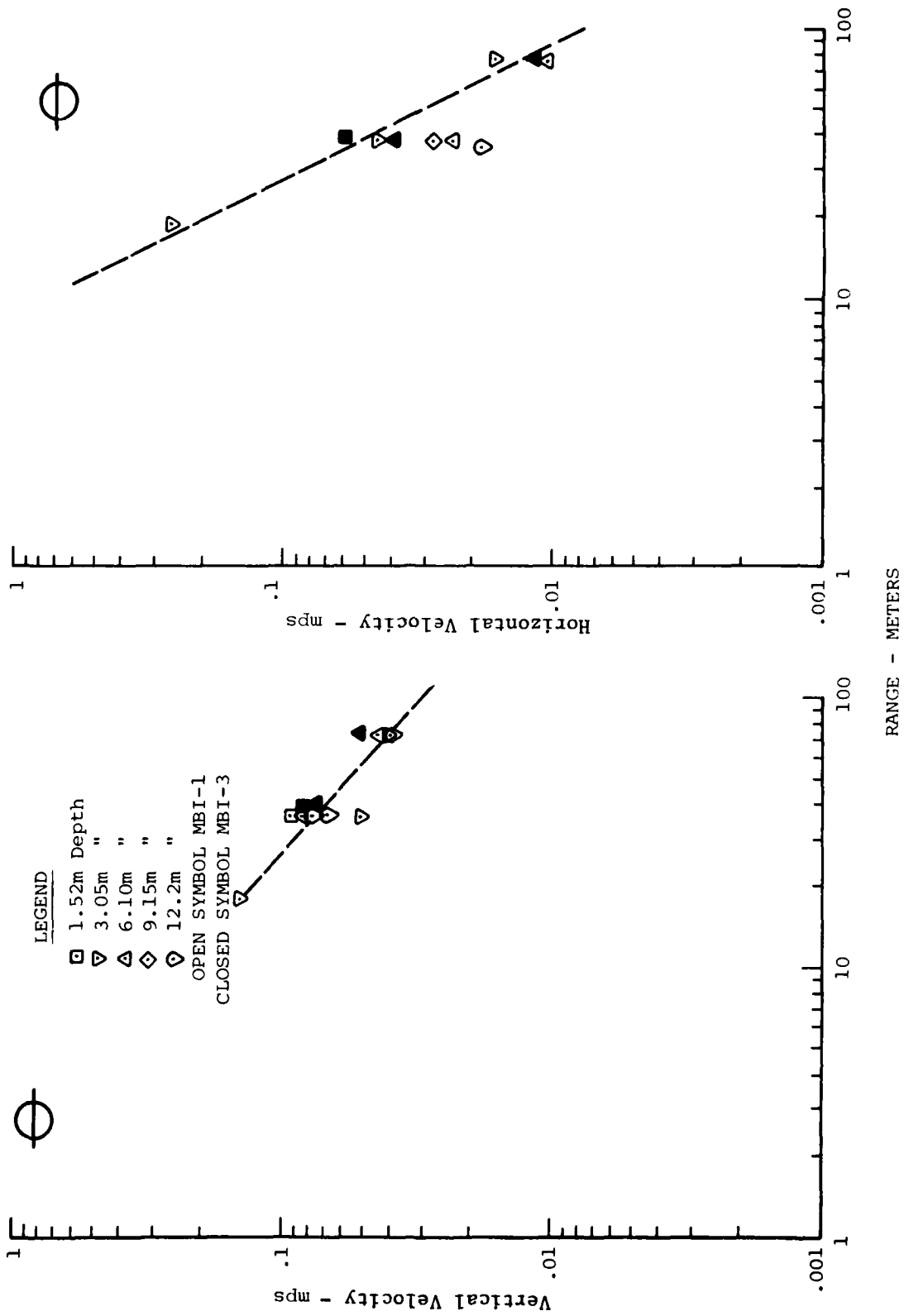


Figure 65: Peak to Peak Values of the Oscillatory Components at Greater Depths for the Half Buried Configuration MBI-1 and MBI-3

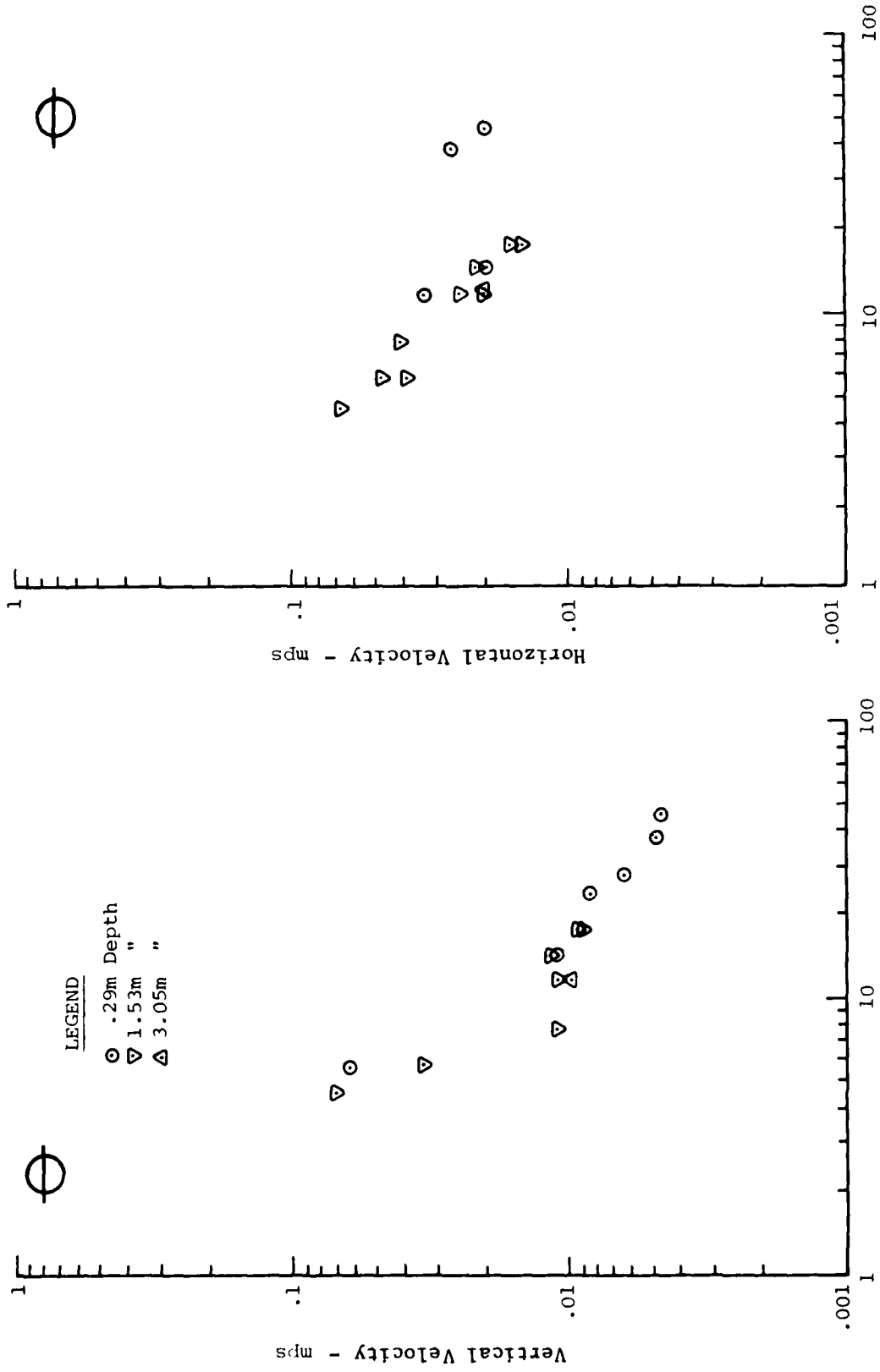


Figure 66. Peak-to-Peak Values of the Oscillatory Component for Half Buried Configuration - MBI-7.

The oscillatory component data for Event 7 scaled by the cube root of the yield are shown in Figure 67 compared to Event 1 and 3. The vertical data compare favorably to the other events. Magnitudes are within the bounds of the data and the attenuation rates are about the same. The horizontal velocities however do not compare as well. The magnitudes are similar but the attenuation rate of Event 7 is "slower" than the larger yield events and does not exhibit the transition range.

Arrival time plots for Events 1 and 3 are presented in Figure 68. These plots indicate that the oscillatory component propagates at an average velocity of 308 mps, and arrives slightly later near the ground surface. Since the wave arrives first at depths below the water table, this signal must be traveling through the saturated material. The indicated propagation velocity corresponds reasonably well to the surface tangent data and the reported shear wave velocity of the saturated materials. This also supports the contention that the oscillatory component is a surface wave.

3. Tangent Below Configuration. The zero-to-peak values for this configuration are presented in Figure 69. The prediction for the vertical velocities appears to be reasonably accurate. The predicted magnitudes and attenuation rate of $R^{-1.2}$ provide an adequate "eyeball" fit to the data, however, an argument can be made for an alternate if one considers the characteristics of the other experiments. Using this alternate fit, the initial attenuation rate would be R^{-2} . The transition region would extend from 20 m to 40 m with no attenuation and beyond 40 m the attenuation rate is $R^{-1.2}$.

The horizontal prediction does not compare as favorable with the data. The predicted values are too high and the predicted attenuation rate is too "fast".

Peak-to-peak values are presented in Figure 70 for the oscillatory component at the 0.46 m depth.

Vertical velocities are best described by a fit similar to the "alternate" fit described above. The initial attenuation rate is $R^{-2.2}$ for ranges from 10 m to 25 m. The transition region extends from 25 m to 70 m and the final attenuation rate is also $R^{-2.2}$.

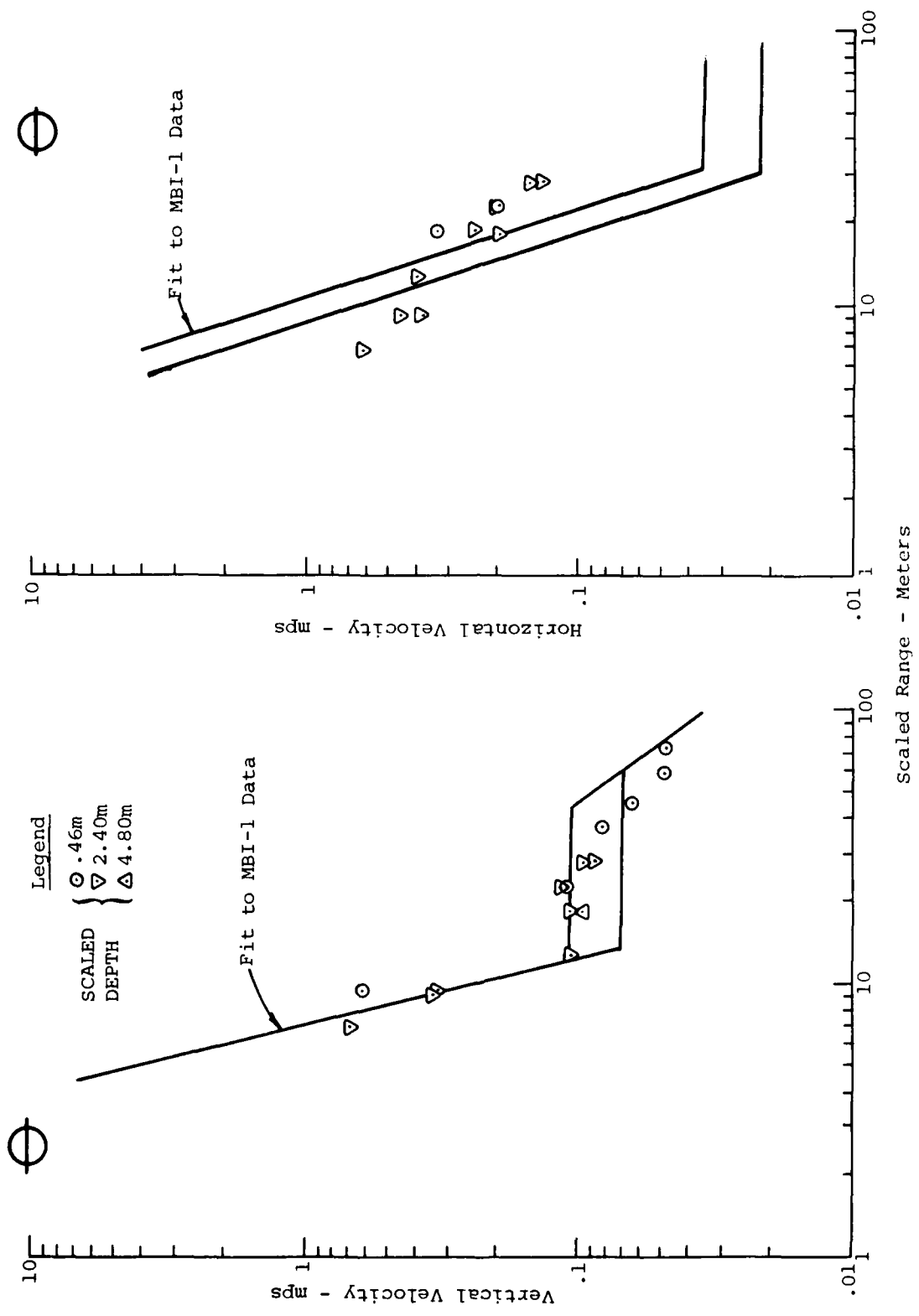


Figure 67. Oscillatory Component for MBI-1 Compared with Oscillatory Component from MBI-7

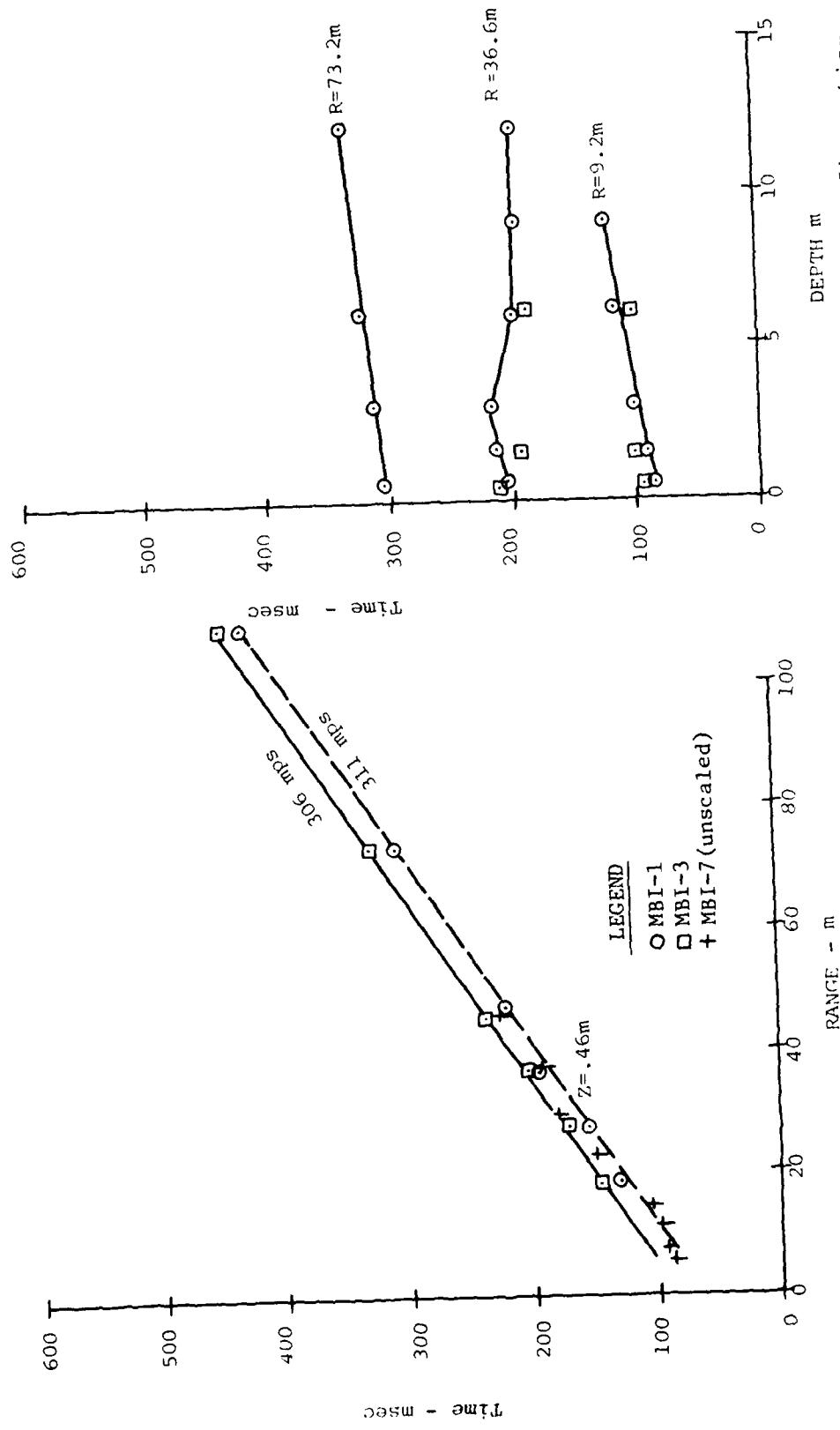
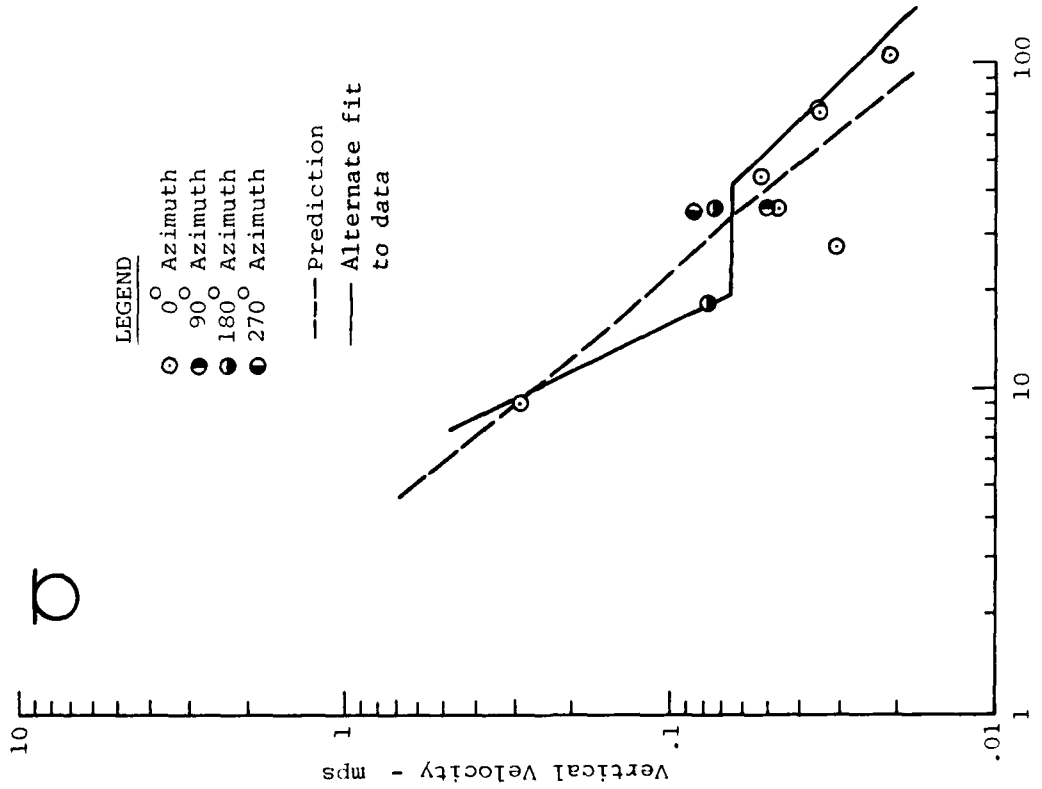
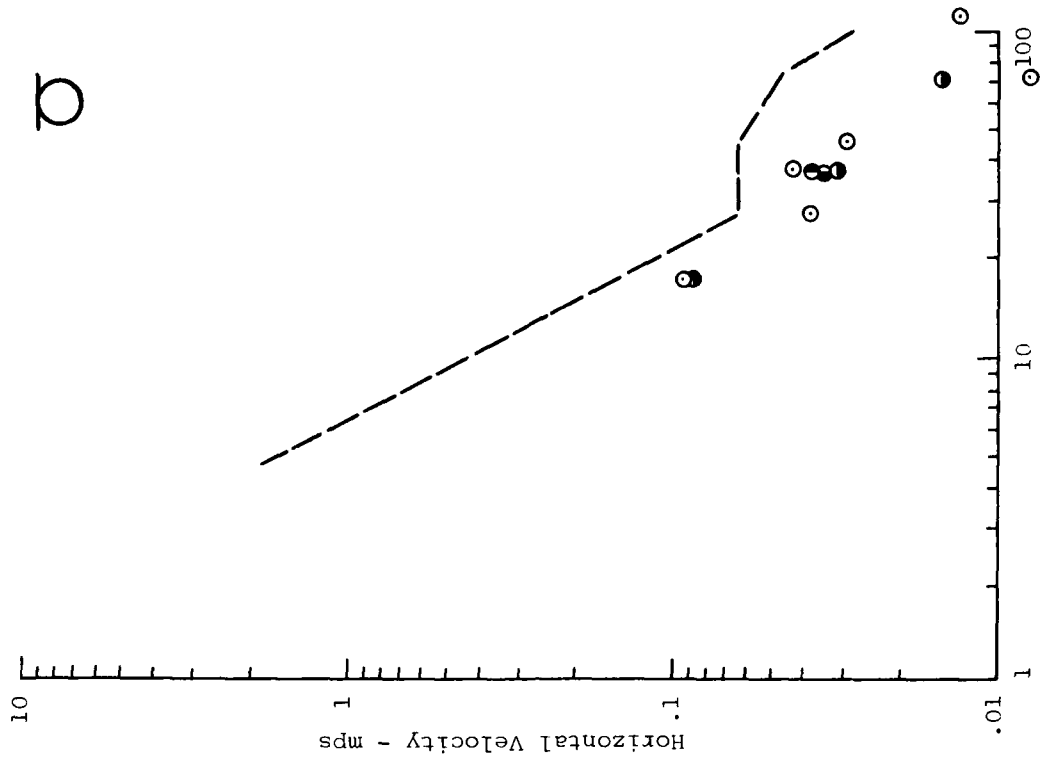


Figure 68. Arrival Time of the Oscillatory Component for the Half Buried Configuration



LEGEND

- 0° Azimuth
- 90° Azimuth
- 180° Azimuth
- 270° Azimuth

- Prediction
- Alternate fit to data

Figure 69. Comparison of Predicted and Measured Zero-to-Peak Values of the Oscillatory Component at the .46 m Depth for the Tangent Below Configuration - MBI-5.

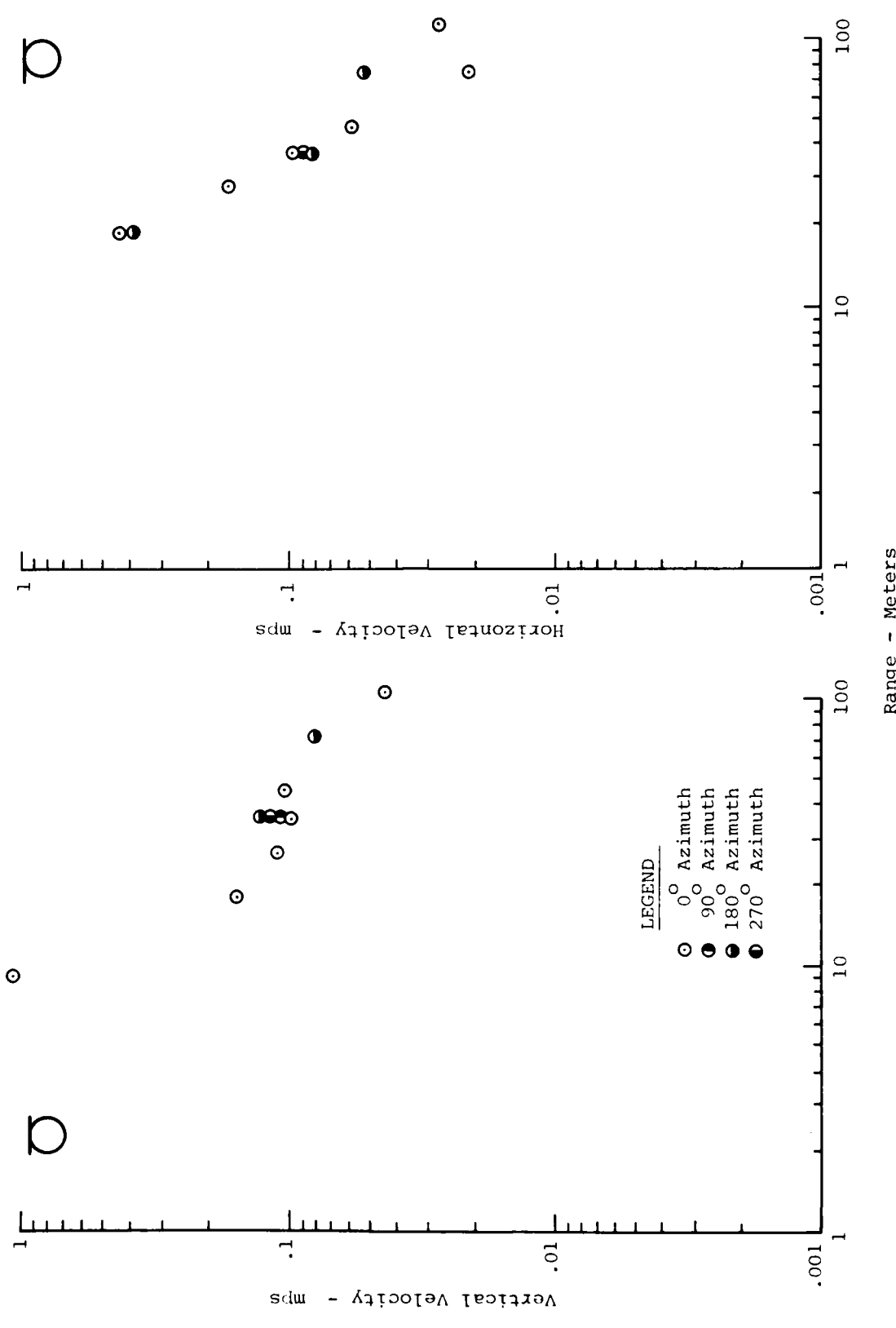


Figure 70. Peak-to-Peak Values of the Oscillatory Component at the .46 m Depth for the Tangent Below Configuration MBI-5.

The horizontal velocities are described by a single line and a constant attenuation rate of 1.9 for all ranges although there is a bit of a change in slope at the most distant ranges. The horizontal and vertical motions for depths greater than 0.46 m are presented in Figure 71. Much the same phenomena as was described for the half-buried configuration is occurring here, that is, the data recorded at the greater depths are approximately equal in magnitude to those recorded at the 0.46 m depth, indicating that there is also no attenuation of the oscillatory component with depth for this configuration.

The arrival time plots for this experiment are presented in Figure 72. The propagation velocities compare favorably with the other charge configurations; however, the oscillatory component appears to be arriving first at the shallower depths rather than the deeper depths.

4. Height of Burst Comparison. The height of burst comparison for the oscillatory components of the three different configurations are presented in Figure 73. The vertical velocities group so closely that a separate fit for the different configuration does not appear warranted. In general, there is an initial rapid attenuation rate of $R^{-3.1}$ between 4 m and 15 m. From the 15 m range to the 110 m range, the attenuation rate decreases to a value of $R^{-0.8}$. Data scatter for a fit of this nature is on the average about a factor of 1.8 or about the same as was experienced for vertical velocities on Event 2.

The horizontal motions are not as tightly grouped as the verticals, however, the fit shown on the figure appears to be adequate. This shows a constant rate of $R^{-2.3}$ for all ranges. The data scatter for these data is a factor of 4.5 which is only slightly more than the scatter for horizontal velocities on Event 2.

In general, it appears that the magnitude of the oscillatory component is not dependent to a large degree upon height of explosive source. Attenuation rates are in general the same and there

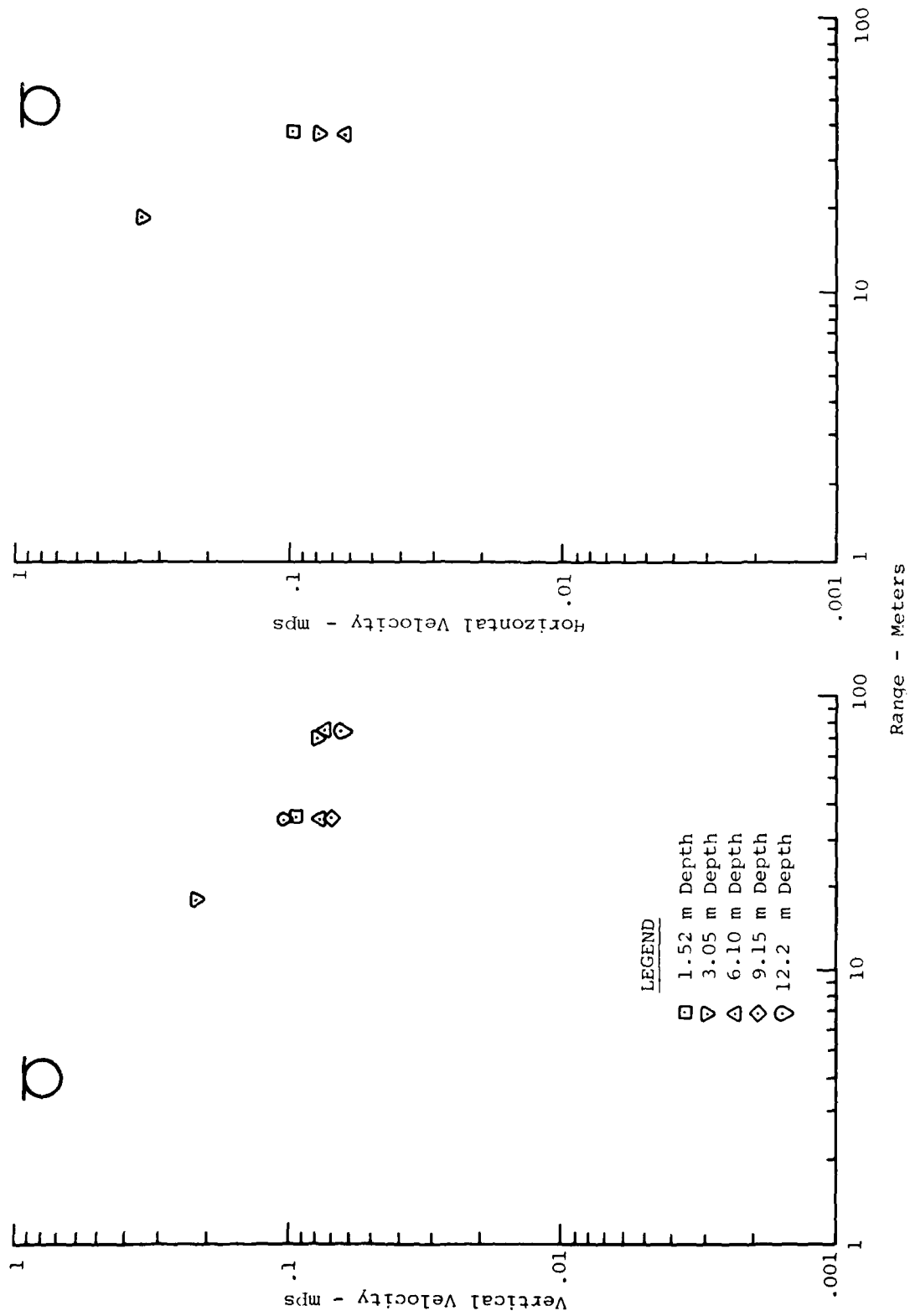


Figure 71. Peak-to-Peak Values of the Oscillatory Component at Greater Depths for the Tangent Below Configuration - MBI-5.

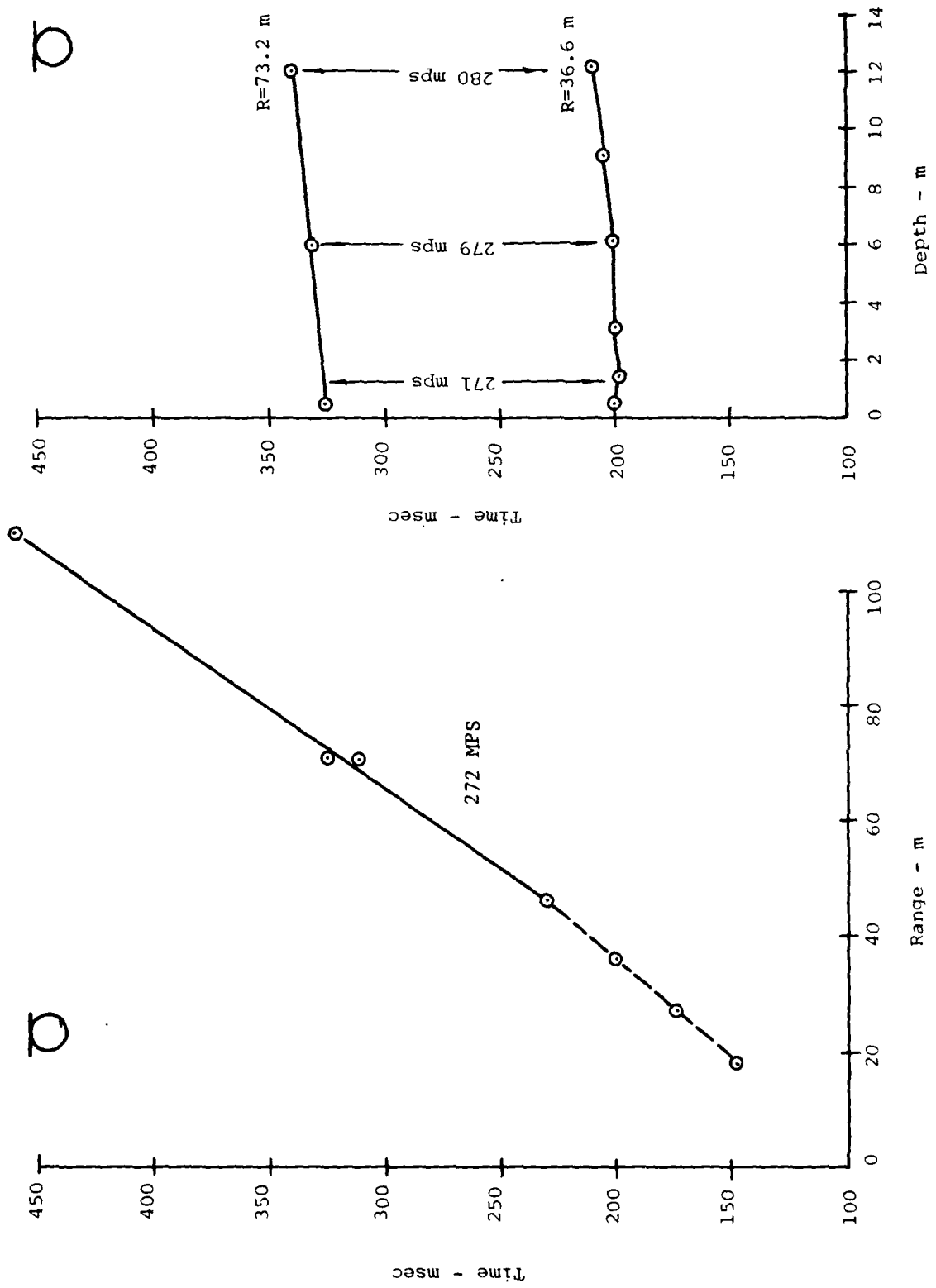


Figure 72. Arrival Time of the Oscillatory Component for the Tangent Below Configuration MBI-5.

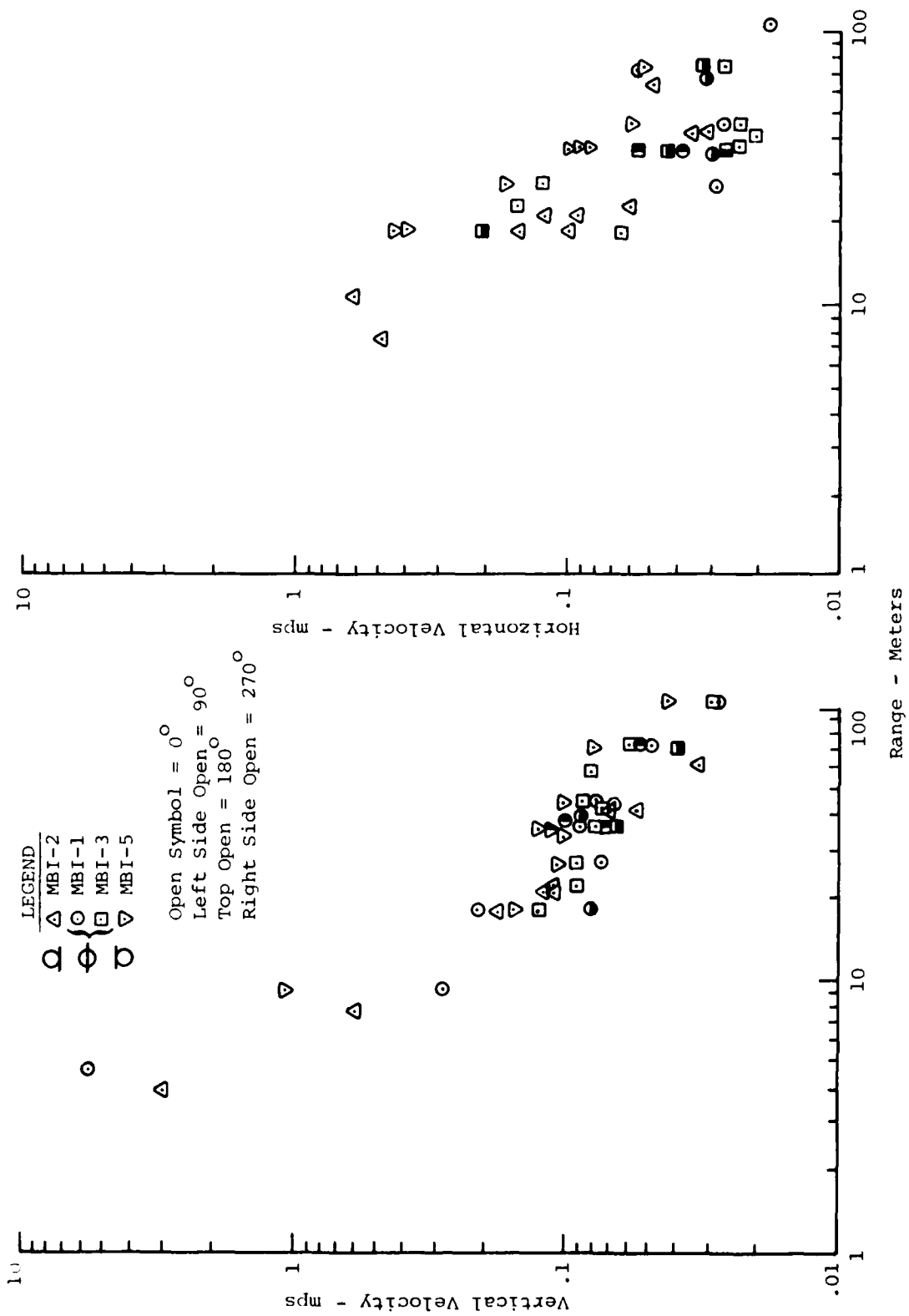


Figure 73. Height of Burst Comparison for the Oscillatory Component at .46 m Depth.

is very little attenuation with depth. The propagation velocities for the three configurations were also all approximately equal.

5. Periods of Oscillatory Motion. Figures 74 through 77 present the periods of the characteristic cycles of oscillatory motion for the vertical motions that occurred for the three different configurations. In general, the close-in ranges show a great deal of variation in periods for the different depths. This is probably a result of the interference of other signals. As range increases, the scatter in periods tends to decrease and approach a constant value. Figure 77 shows the period at the 0.46 m depth for the various charge configurations. As seen on this figure, the tangent below configuration produces periods that are longer than the other configurations. The shortest periods are produced by the surface tangent experiment with the half buried experiment falling in between. This suggests that the oscillatory component is related to the amount of energy coupled directly into the ground and that it should scale with the crater volume. Scaling of this sort met with only marginal success and is not included in this report.

The periods of the characteristic cycle of the oscillatory component for horizontal motion are presented in Figures 78 through 81. In general, the horizontal data does not lend itself to easy interpretation. The same general trend of the period converging to a single value with range is present but the periods appear to be decreasing with the increasing range. The height of burst comparison (Figure 81) generally yields the same basic results as before, that is the tangent below configuration producing the longest periods with the surface tangent experiment the lowest. The data scatter on this plot, however, is quite large.

4.3.4 Crater Related Ground Motion

a Introduction

This section contains the results of the cratering and crater related ground motion portions of the Misers Bluff experimental program. In general, the predicted crater related ground motions were

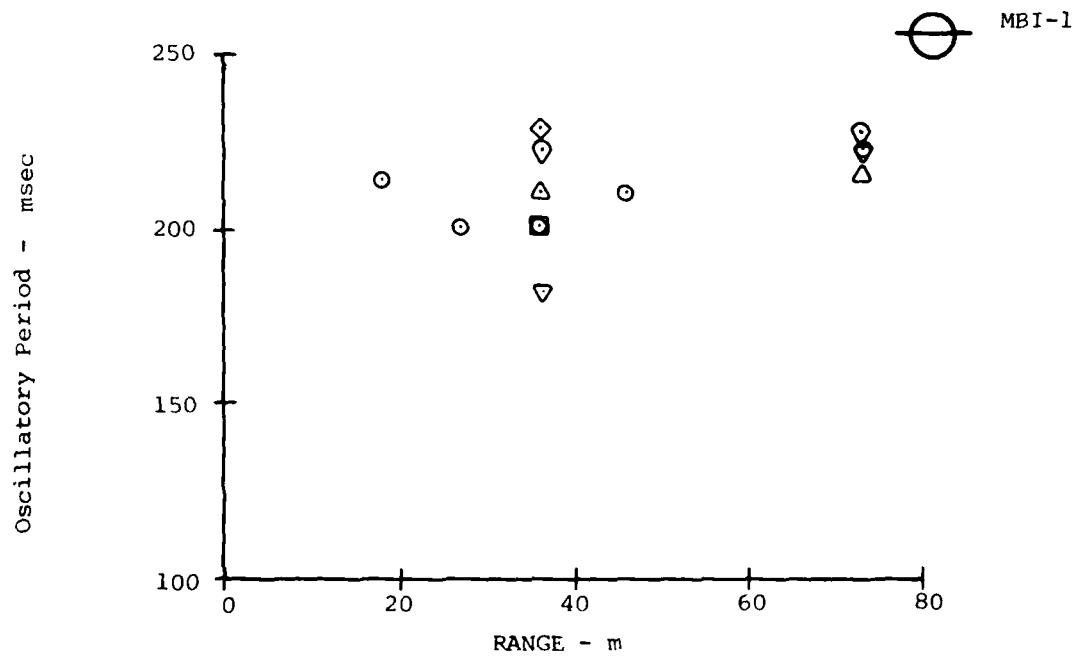
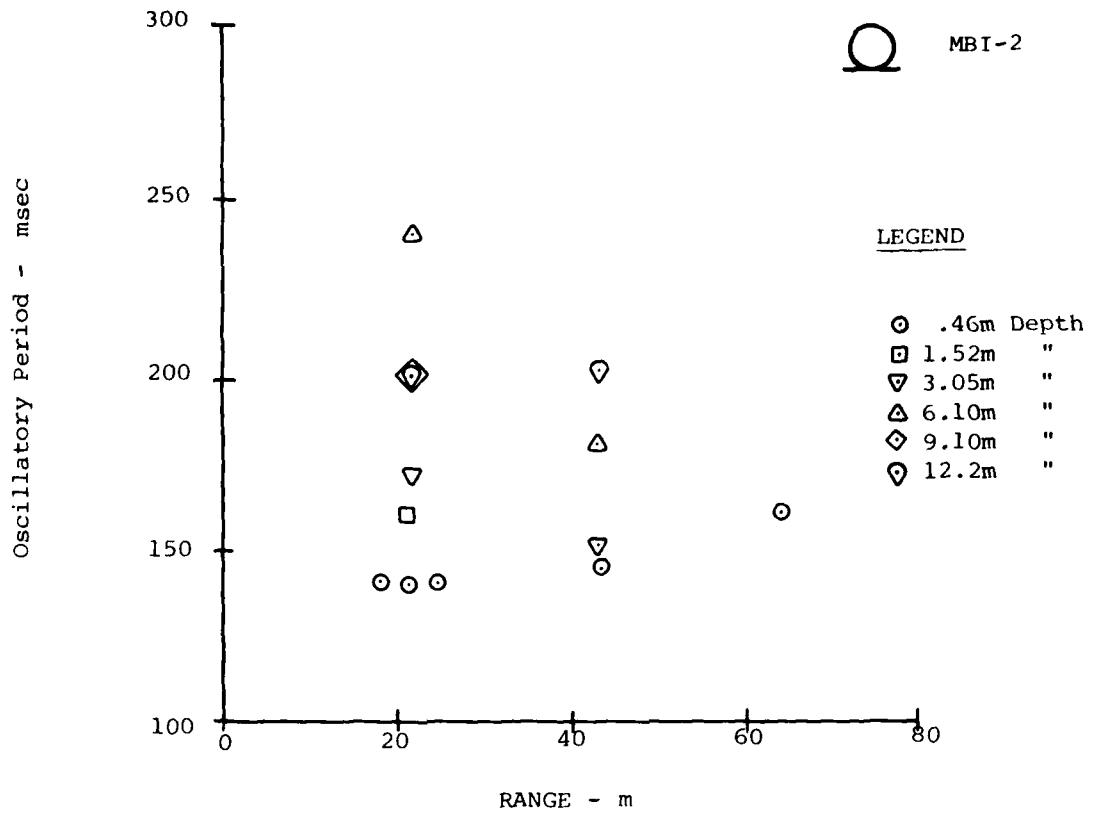


Figure 74. Periods of Oscillatory Motion for Vertical Velocity - MBI-2 and MBI-1

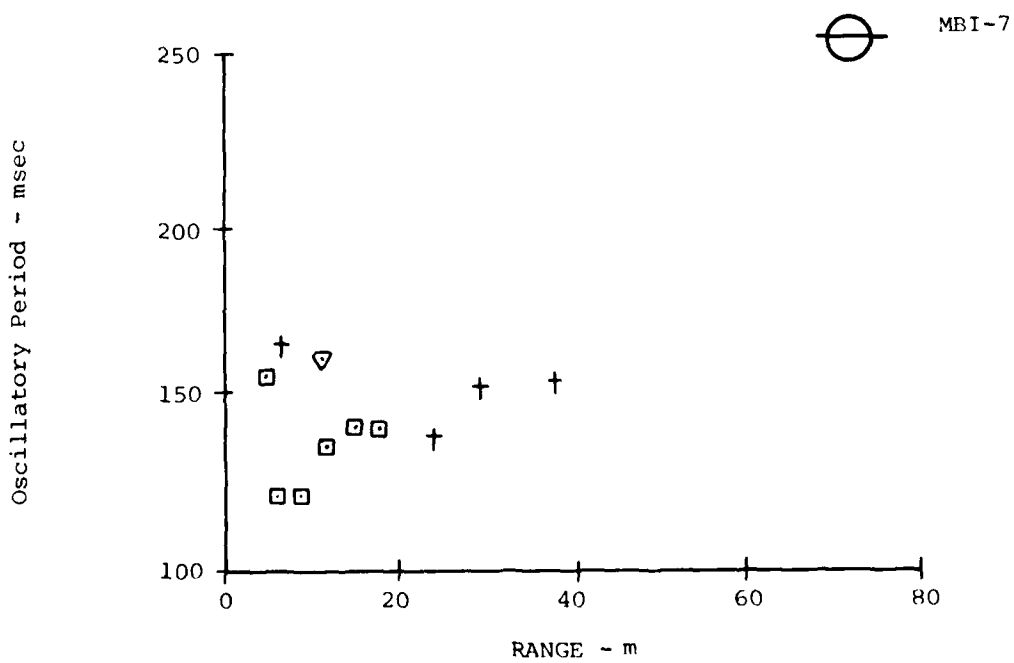
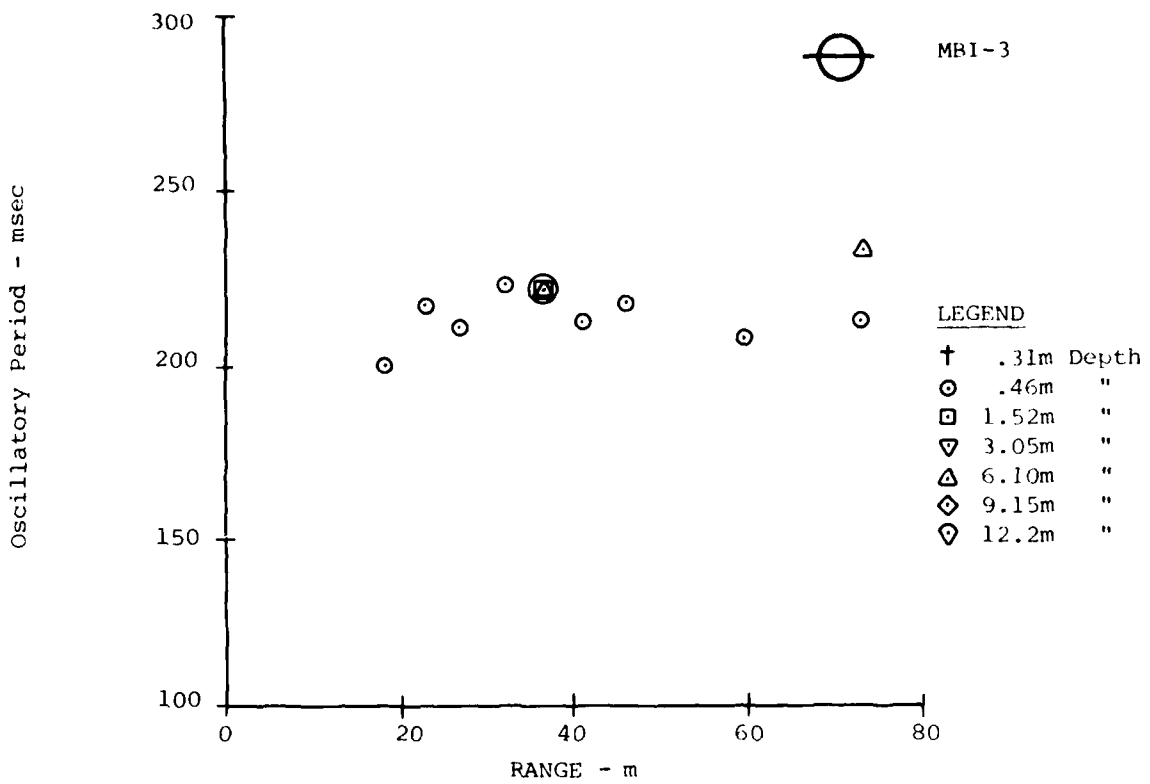


Figure 75. Periods of Oscillatory Motion for Vertical Velocity MBI-3 and MBI-7

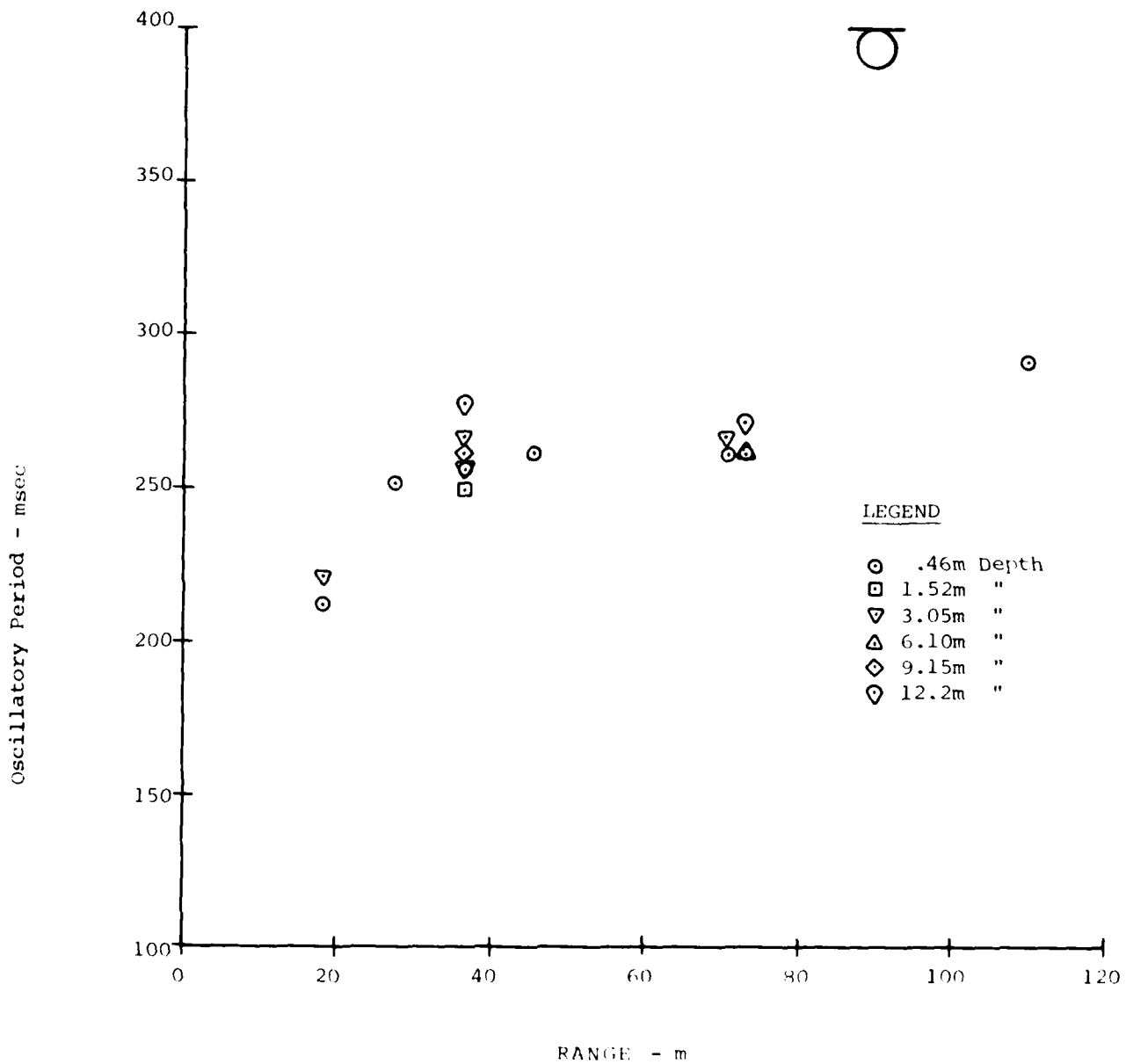


Figure 76. Periods of Oscillatory Motion for Vertical Velocity MBI-5

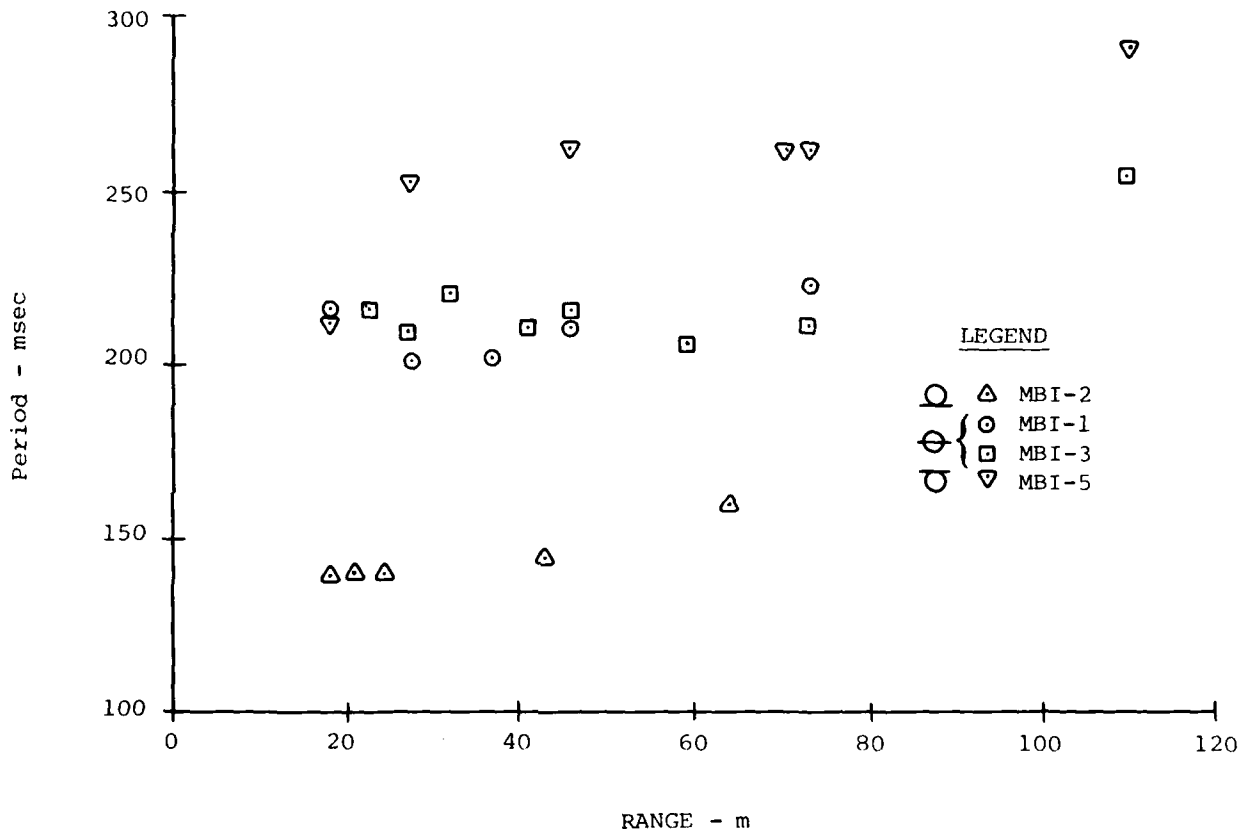


Figure 77. Periods of Oscillatory Motion for Vertical Velocity at the .46m Depth for all Events

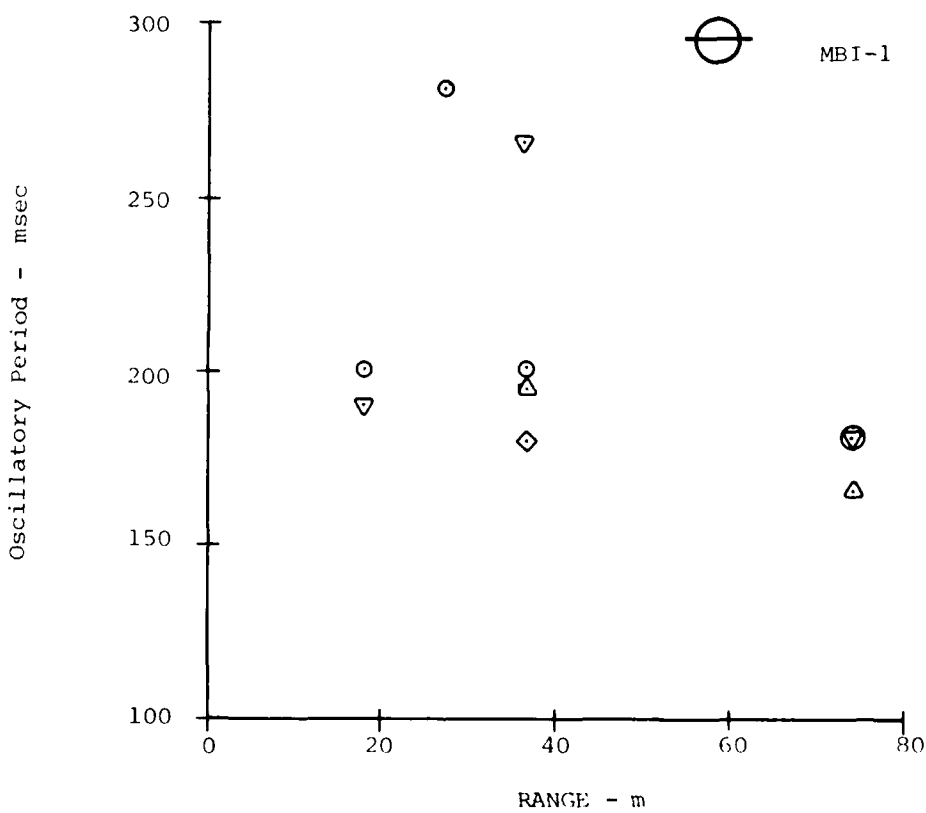
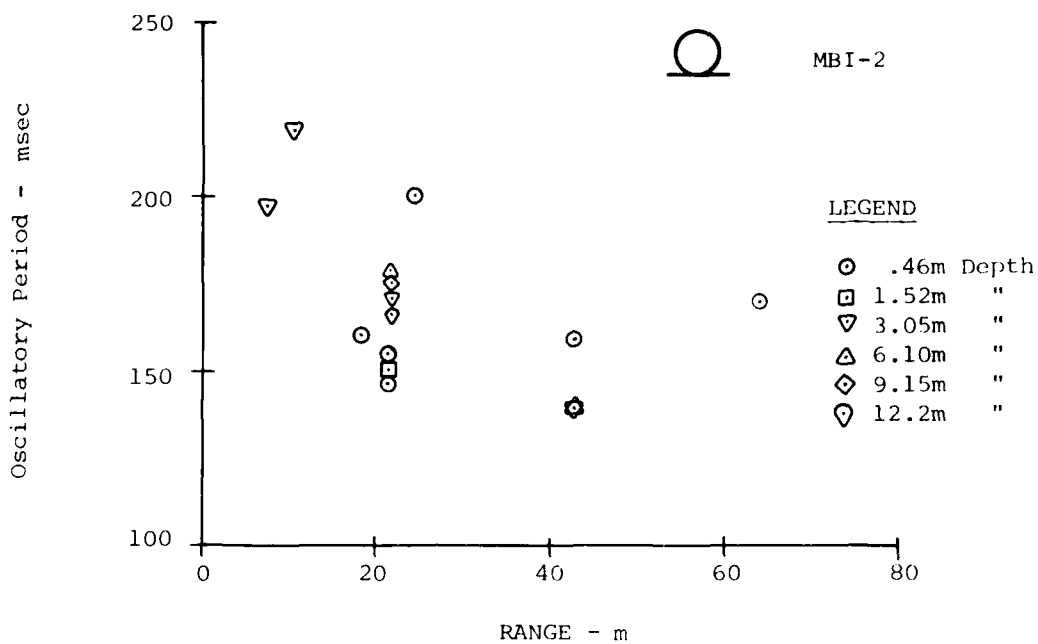


Figure 78. Periods of Oscillatory Motion for Horizontal Velocity - MBI -2 and MBI -1

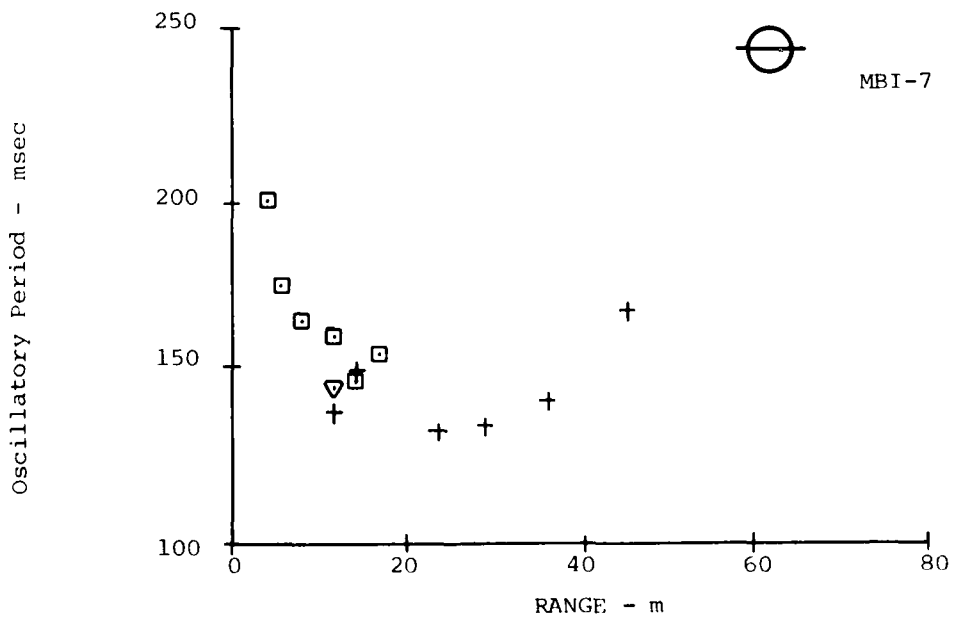
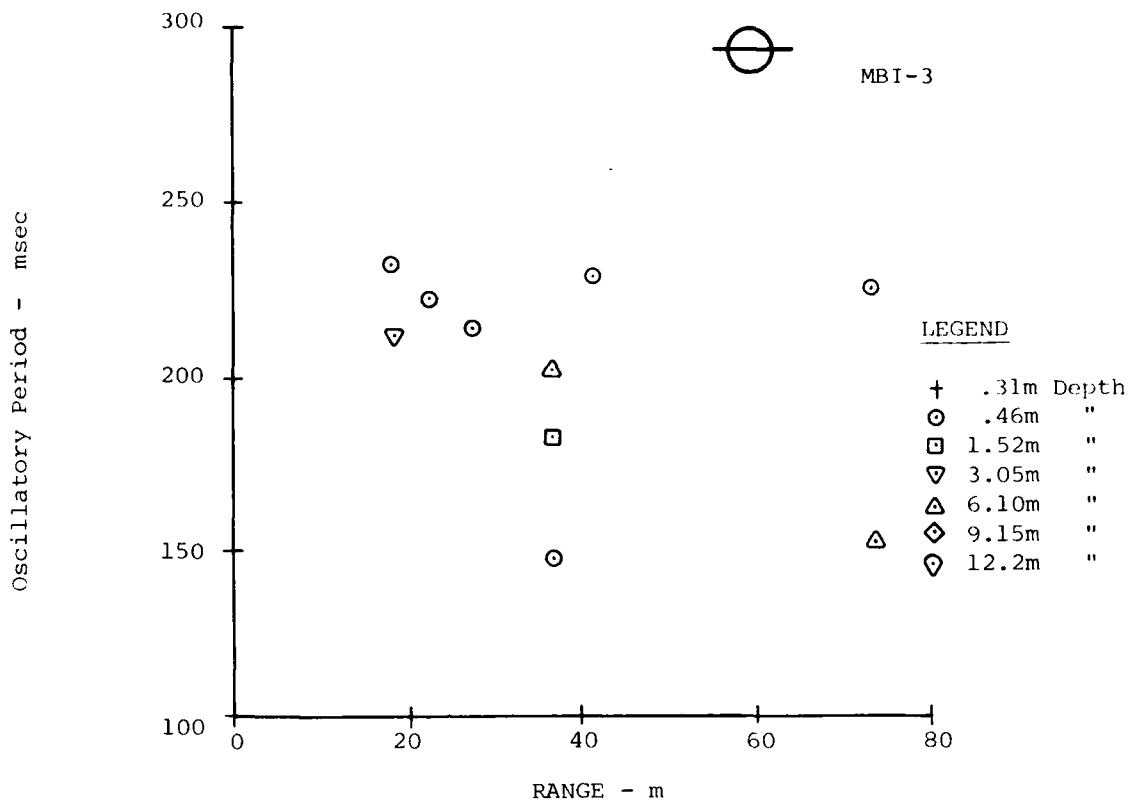


Figure 79. Periods of Oscillatory Motion for Horizontal Velocity - MBI-3 and MBI-7

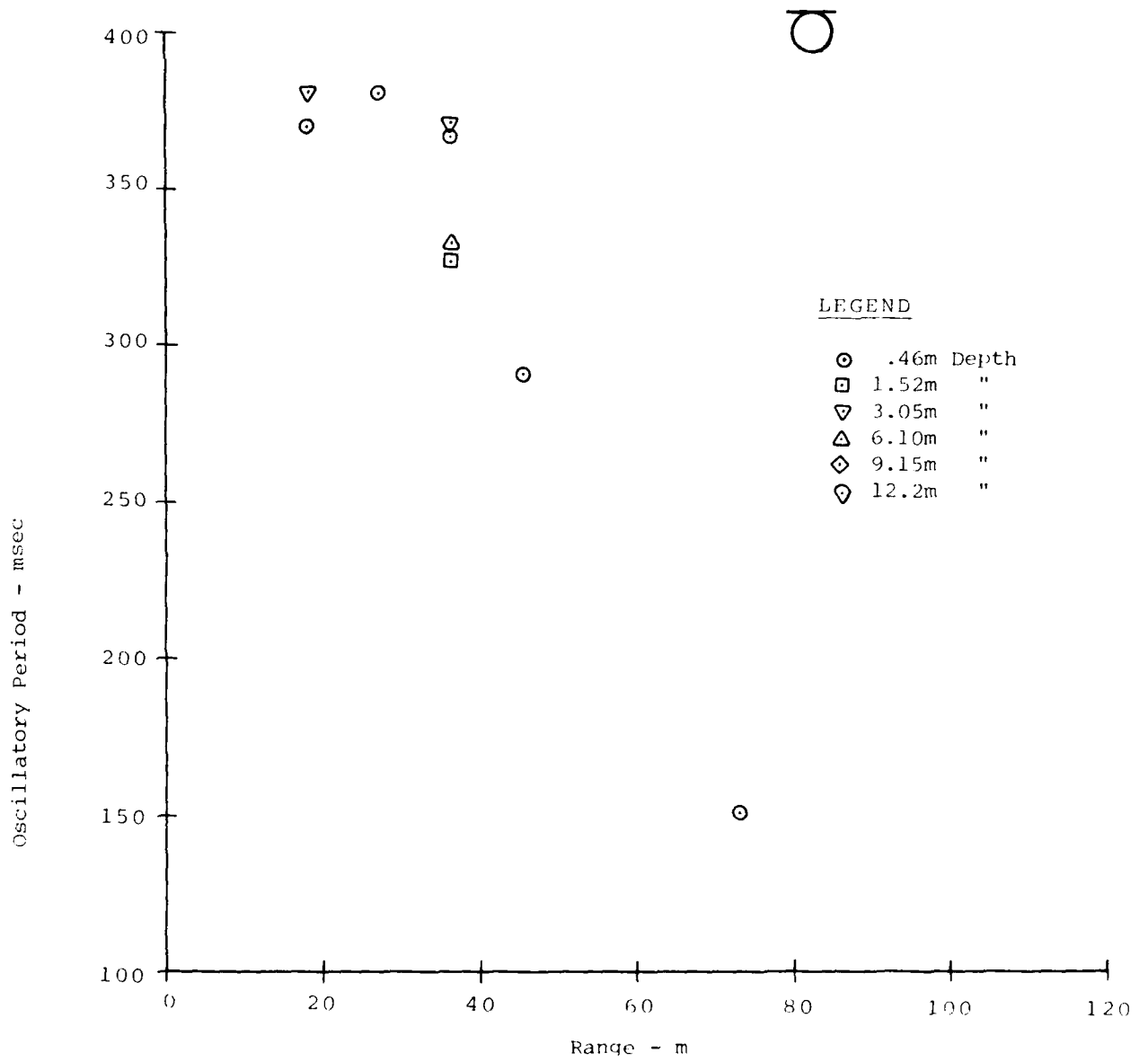


Figure 80. Periods of Oscillatory Motion for Horizontal Velocity MBI-5

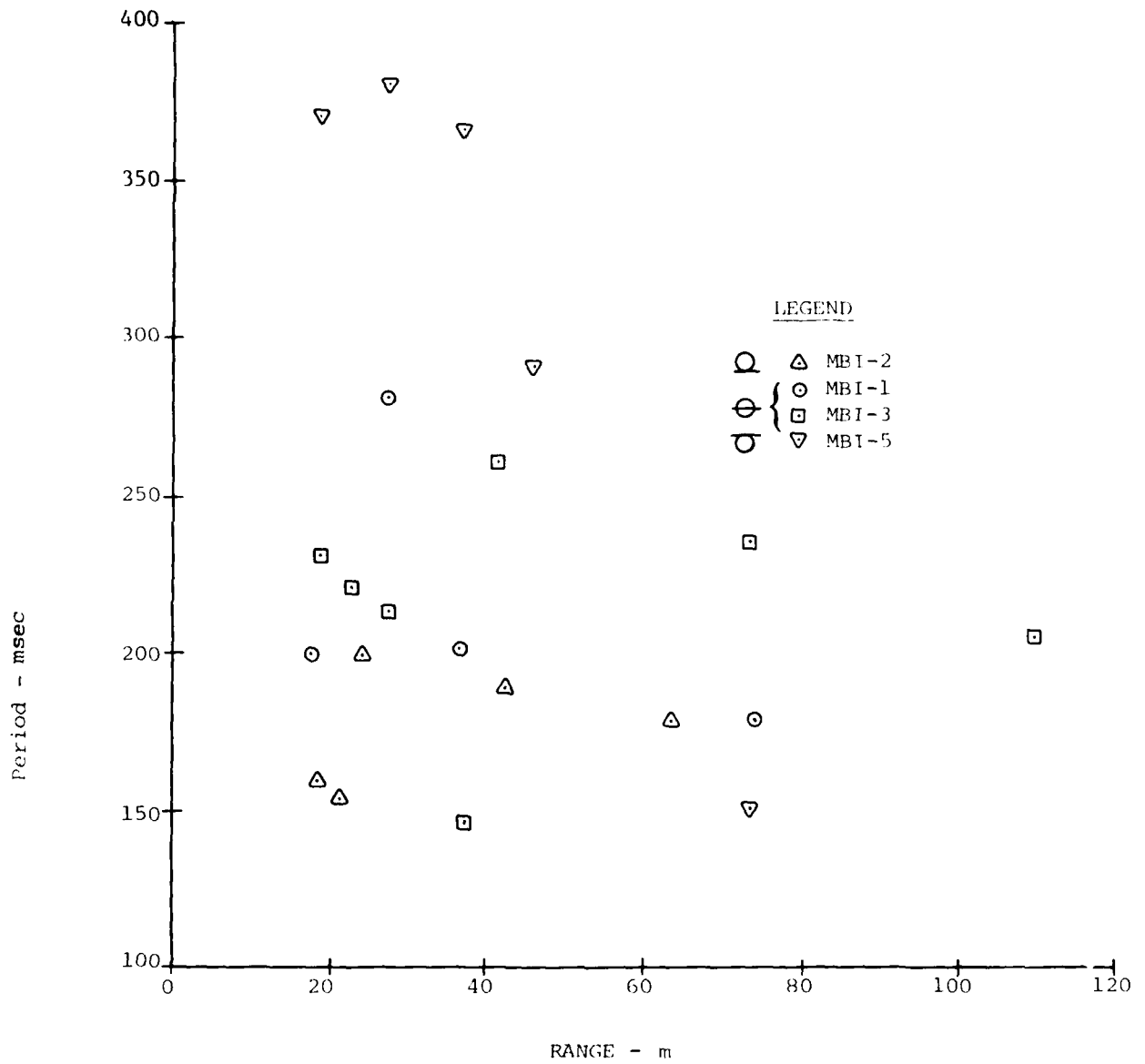


Figure 81. Periods of Oscillatory Motion for Horizontal Velocity at the .46 Depth for all Events

quite small except very near the sources. However, as one moves further away from the source, the combination of upstream airblast induced and crater induced motions are extremely difficult to differentiate. Therefore, in general, predictions are made by extrapolating the close-in effects related to the crater formation process into the outrunning region. Independent predictions are then made of the peak motions in the outrunning regions based on correlations of past data which do not differentiate the source of the observed motions.

The crater related motions are predicted based on the crater volume scaling procedure. Therefore, errors in the predicted crater volumes will be propagated directly into the crater related motion predictions and it is of interest to evaluate the crater predictions as well as the crater related motions.

b Crater

Apparent crater volumes range between 6.98 m^3 to 99.42 m^3 on this experimental program. The crater data and the pre-test predictions are summarized in Table 3. Predicted crater volumes varied from about 31 percent below the actual measured data for the tangent below experiment to about 44 percent above the measured values for the $5.35 \times 10^{-4} \text{ TJ}$ half buried experiment. Both the half buried $2.09 \times 10^{-3} \text{ TJ}$ experiment shots were predicted to be about 14 percent less than the actual measured values. This variation probably is rather typical of the error one might expect when applying current state-of-the-art crater volume prediction procedures. Examination of the predicted and measured radii and depths, however, indicates that there is a systematic trend in errors of the current prediction procedure. In all cases the radius was overpredicted and the depth underpredicted. This indicates that craters were more bowl shaped than predicted. These errors in crater volume will be propagated directly into the comparison of the crater related motion and prediction based on crater volumes. More details concerning the cratering data and ejecta distribution experiments are contained in references 17 through 21.

TABLE 3. CRATER PREDICTIONS VS DATA FOR PHASE I
SINGLE BURST EVENTS

EVENT	APPARENT CRATER VOLUME (m ³)		R _a (m)		D _a (m)	
	PREDICTED	ACTUAL	PREDICTED	ACTUAL	PREDICTED	ACTUAL
1	34.05	39.84	3.89	3.72	1.62	2.29
2	11.35	9.36	2.70	2.59	1.12	1.43
3	34.05	39.10	3.89	3.48	1.62	2.47
5	68.09	99.42	4.90	4.58	2.04	3.32
7	10.07	6.98	2.59	2.14	1.08	1.37

c Crater Related Displacements

The absolute peak upward and outward displacements have been scaled by the cube root of the crater volume and are shown in figures 82 through 87. The various depths of measurements have been broken into three groups based on depth scaled by the cube root of the crater volume. At the greater ranges it is not possible to separate the crater related and upstream airblast related contributions to the displacement peaks. The prediction curves shown on these figures are based on the predicted crater volumes, however, the actual crater volumes were so close to the predicted values that the difference in these curves is hardly noticeable.

1. Half Buried and Tangent Below Configurations. The near surface data for these events scatter about the predicted line at all ranges. At the intermediate depths the data for scaled ranges of about 10 and less are generally below the predicted near surface values but a change in attenuation rate appears to occur at about this scaled range. Beyond a scaled range of about 10 the data are generally about the near surface predicted values. At all ranges, however, the displacements are significantly greater than predicted for this depth increment. The same general trend is observed in the data for the greater depths, however, the change in slope appears to occur at a scaled range of about 7, especially for the vertical data.

Grouping the data in this way indicates an attenuation of displacement with depth, however, it is not nearly as pronounced as was predicted. The near surface and intermediate depth horizontal data actually are almost identical.

Scaling of the displacements by the cube root of the crater volume collapsed the data from the two different yields and heights of burst into one band with no trend from shot to shot. Close in, all the data follow the attenuation rate of R^{-3} predicted by the crater volume scaling relationships.

2. Surface Tangent Configuration. The data for Event I-2 are shown in figures 85 through 87. At both the near surface and intermediate depths the data are significantly greater than the predicted values. In this case also the actual and predicted crater volumes were close enough that the differences in the predicted displacements

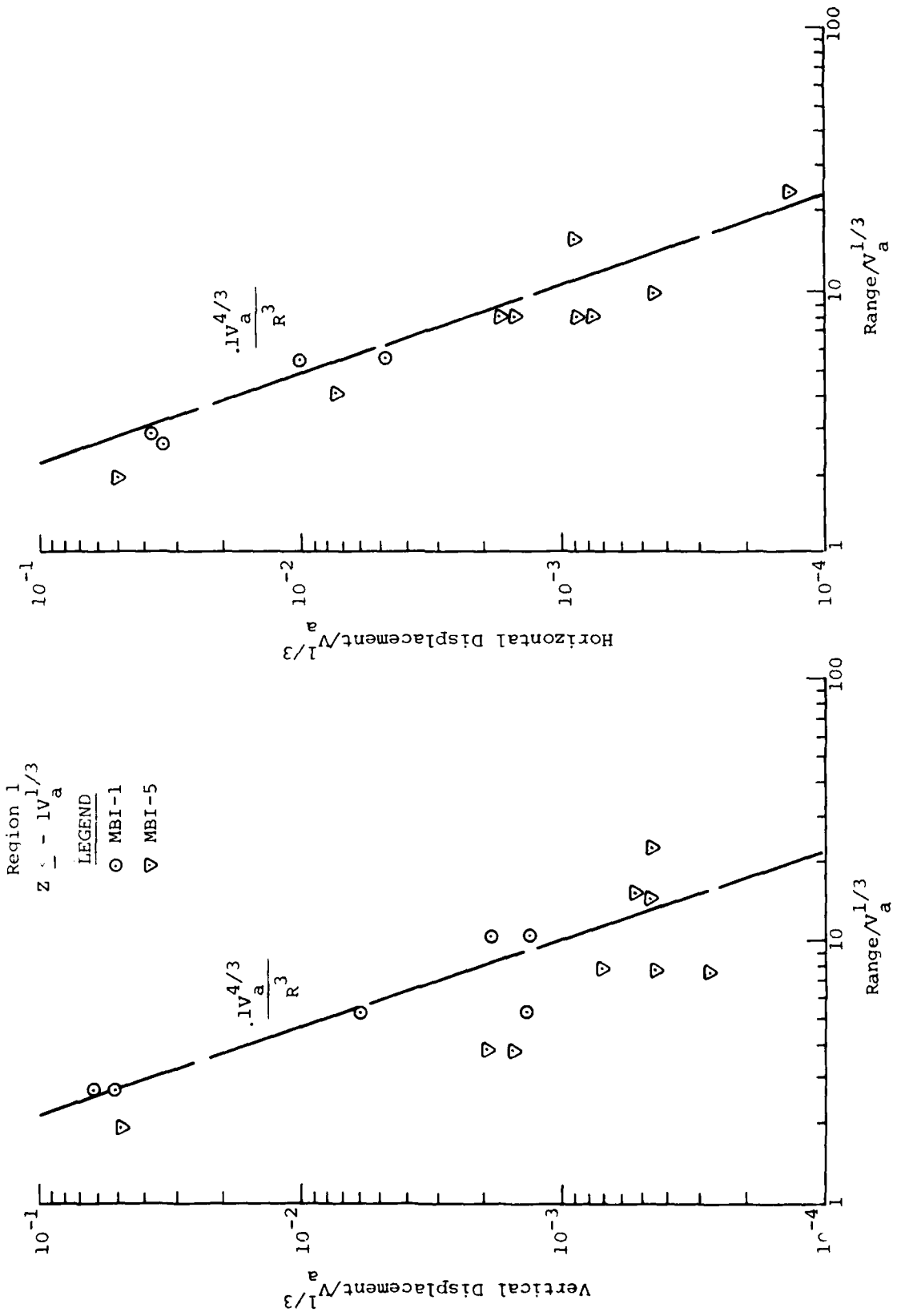


Figure 82. Crater Volume Scaled Displacements for Region 1

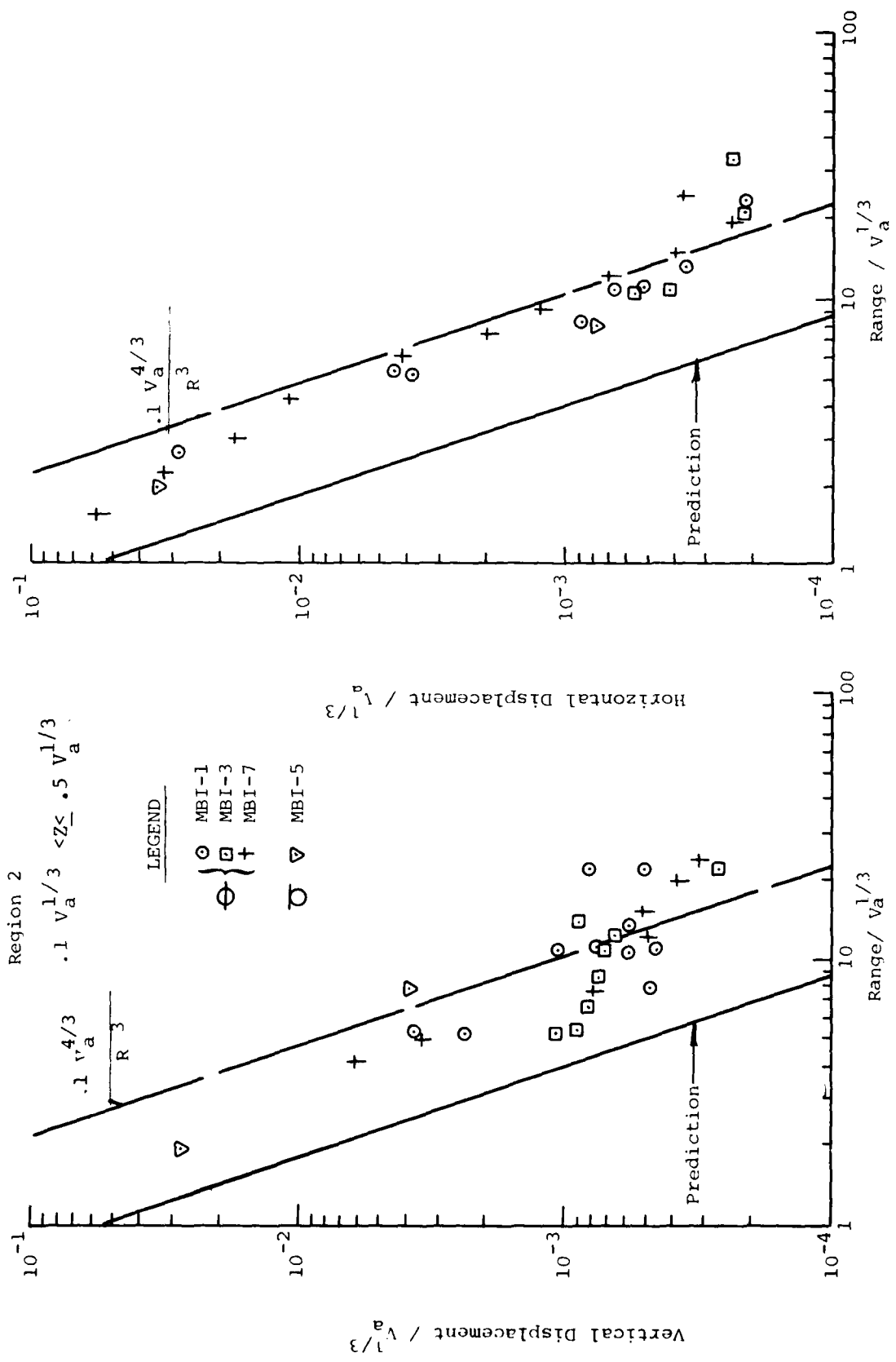


Figure 83. Crater Volume Scaled Displacements for Region 2

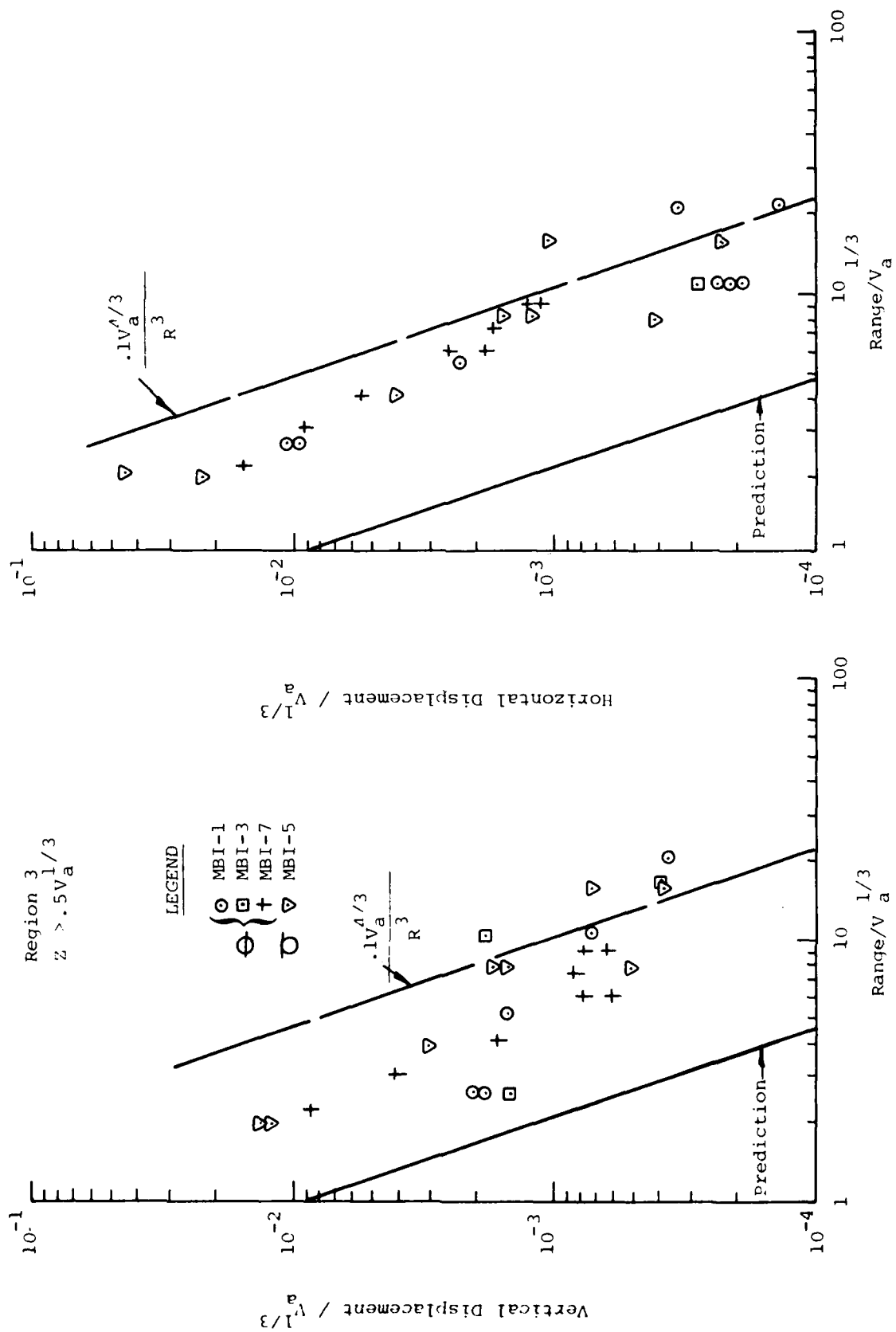


Figure 84. Crater Volume Scaled Displacements for Region 3

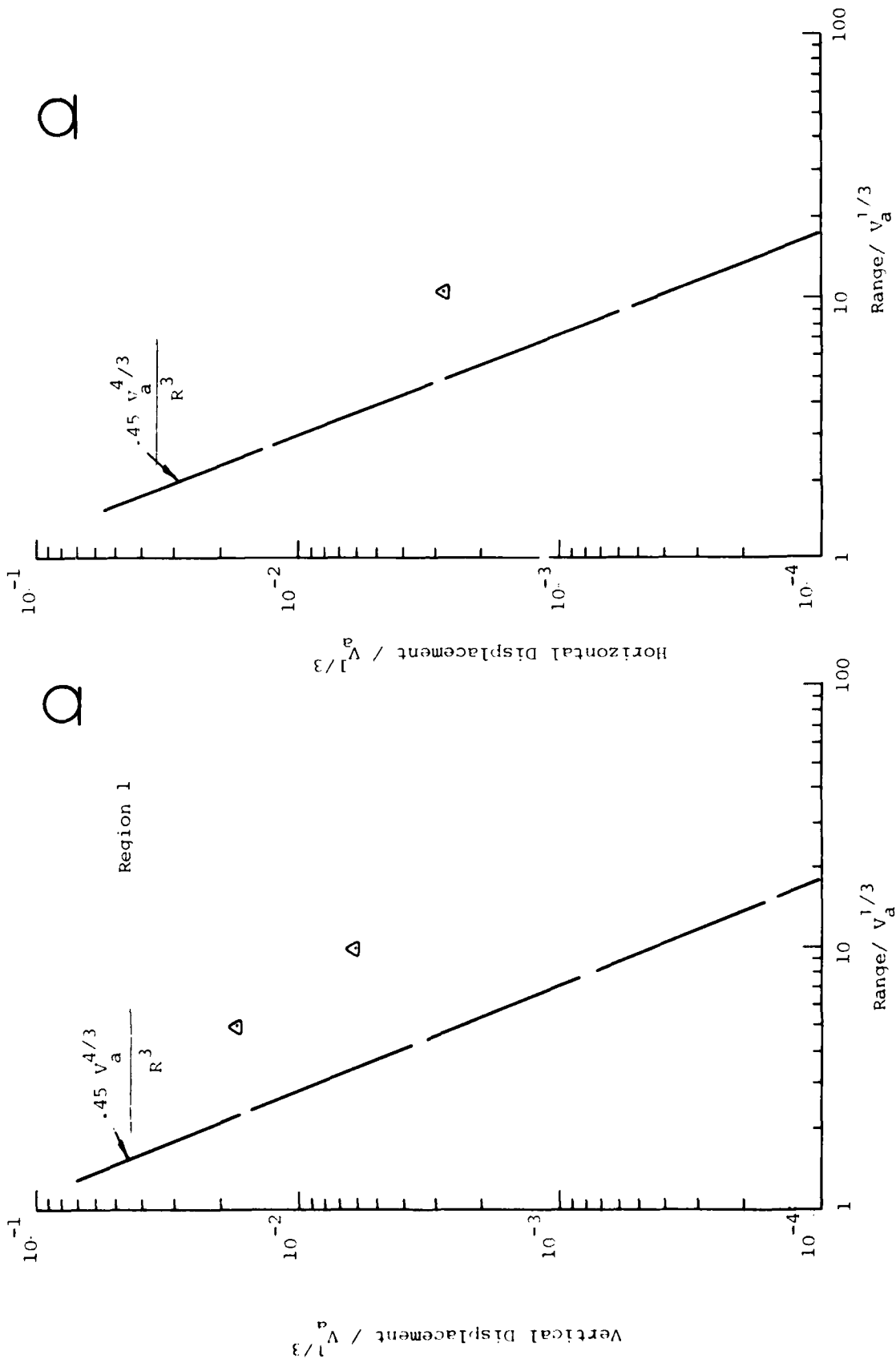


Figure 85. Crater Volume Scaled Displacements from Event 2, Surface Tangent Configuration - Region 1

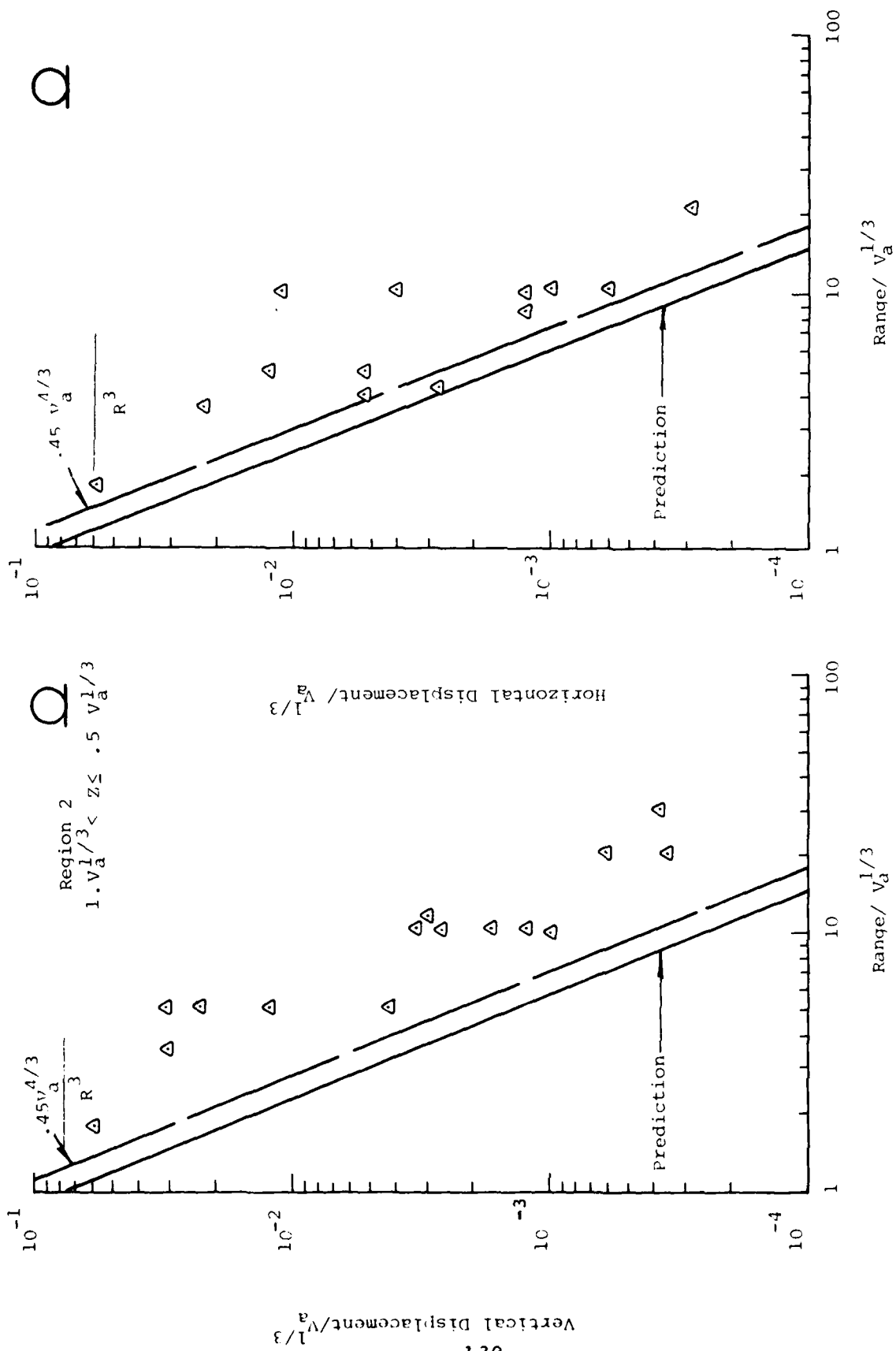


Figure 86. Crater Volume Scaled Displacements from Event 2, Surface Tangent Configuration - Region 2

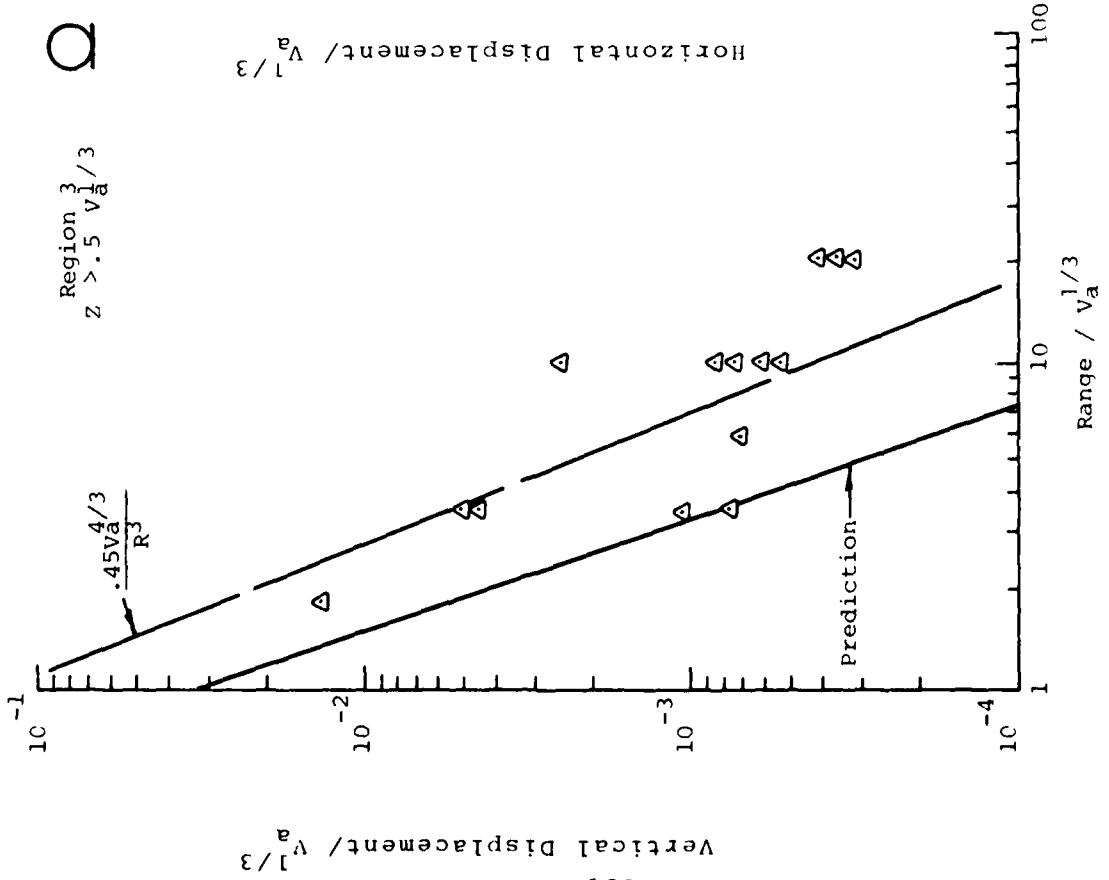
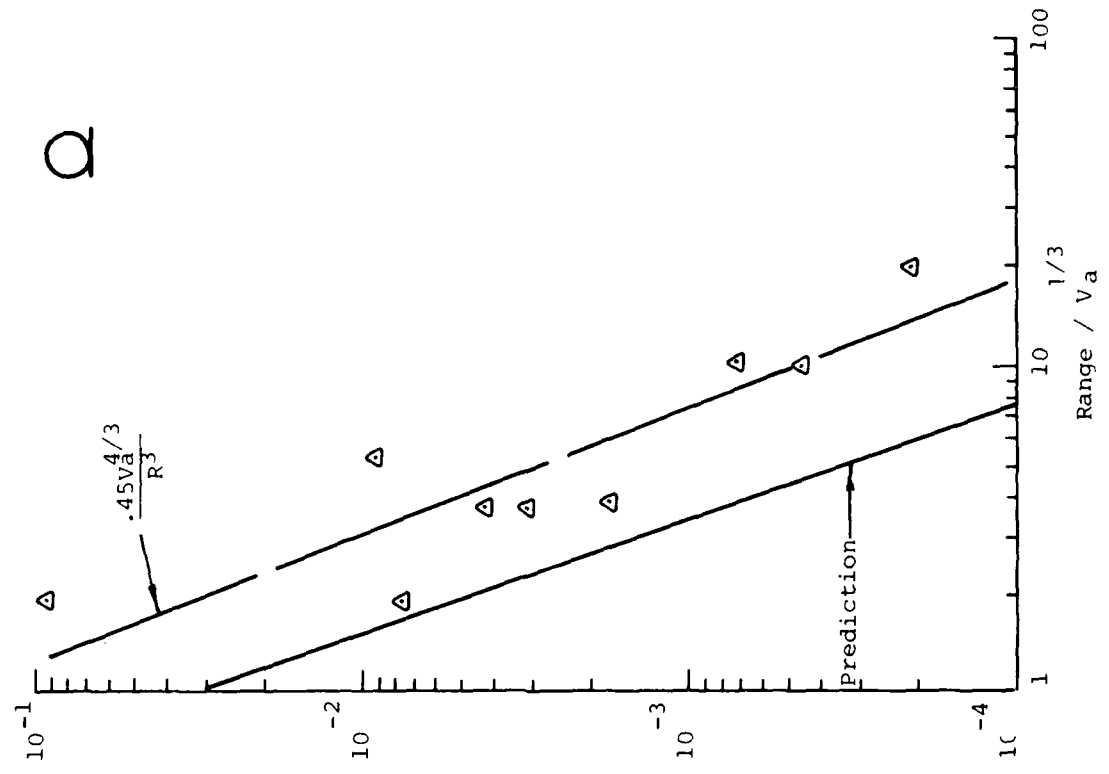


Figure 87. Crater Volume Scaled Displacements from Event 2, Surface Tangent Configuration - Region 3

are not significant. The data scatter is quite large especially for the horizontal data at the intermediate depth. The predicted attenuation with depth overestimated the actual trend and the predictions were significantly below the actual data. These data, in fact, would fall about at the upper band of all ground shock data scaled in this manner.

d Crater Related Particle Velocity

Peak particle velocities, scaled by the effective seismic velocity ($C_e = \text{Range}/\text{time of arrival of the crater related signal}$), plotted against the range scaled by the cube root of the crater volume are presented in figures 88 through 90. The depths of measurement have been divided into three groups as discussed previously.

Vertical and horizontal velocities for Region 1 ($Z \leq .1V_a^{1/3}$) are presented in figure 88. The predicted values shown on this figure were determined by the equation given in reference 10. In general, the prediction falls in the center of the data scatter for both vertical and horizontal motions and describes the motions of the tangent below and half buried experiments more accurately than the surface tangent experiment. This is due to the fact that the experiments with the greater depth of burst produce signals which have more discernable crater related motions. The surface tangent experiment was so dominated by the airblast induced motions that the values chosen were possibly a combination of the components of motion, but clearly not composed only of crater related motion.

Figures 89 and 90 present the vertical and horizontal velocities for Regions 2 ($.V_a^{1/3} < Z \leq .5V_a^{1/3}$) and ($Z > .5V_a^{1/3}$) respectively. Much the same phenomena can be seen in these figures as was described above. There is, however, a tendency of the data to collapse to the prediction line. This is due to the fact that as the depth of the measurement increases the airblast signal becomes less and less predominant making the selection of the crater related motions easier and, therefore, more accurate. The relatively less scatter in the horizontal data is also a result of the smaller airblast component in those data.

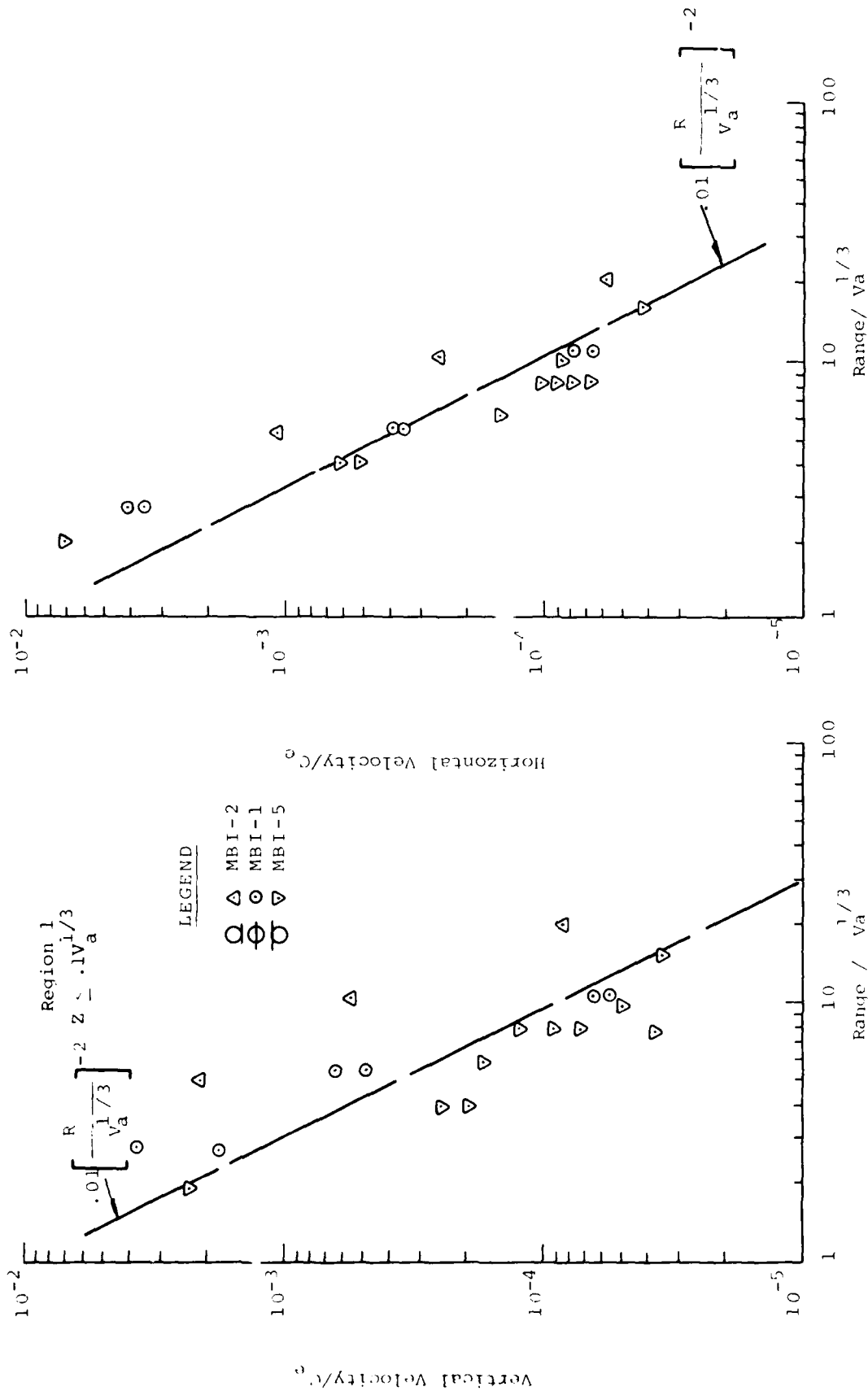


Figure 88. Crater Volume Scaled Velocities for Region 1

Region 2
 $.1 V_a^{1/3} < Z \leq .5 V_a^{1/3}$

LEGEND

- Δ MBI-2
- \square MBI-1
- \circ MBI-3
- \oplus MBI-7
- \ominus MBI-5

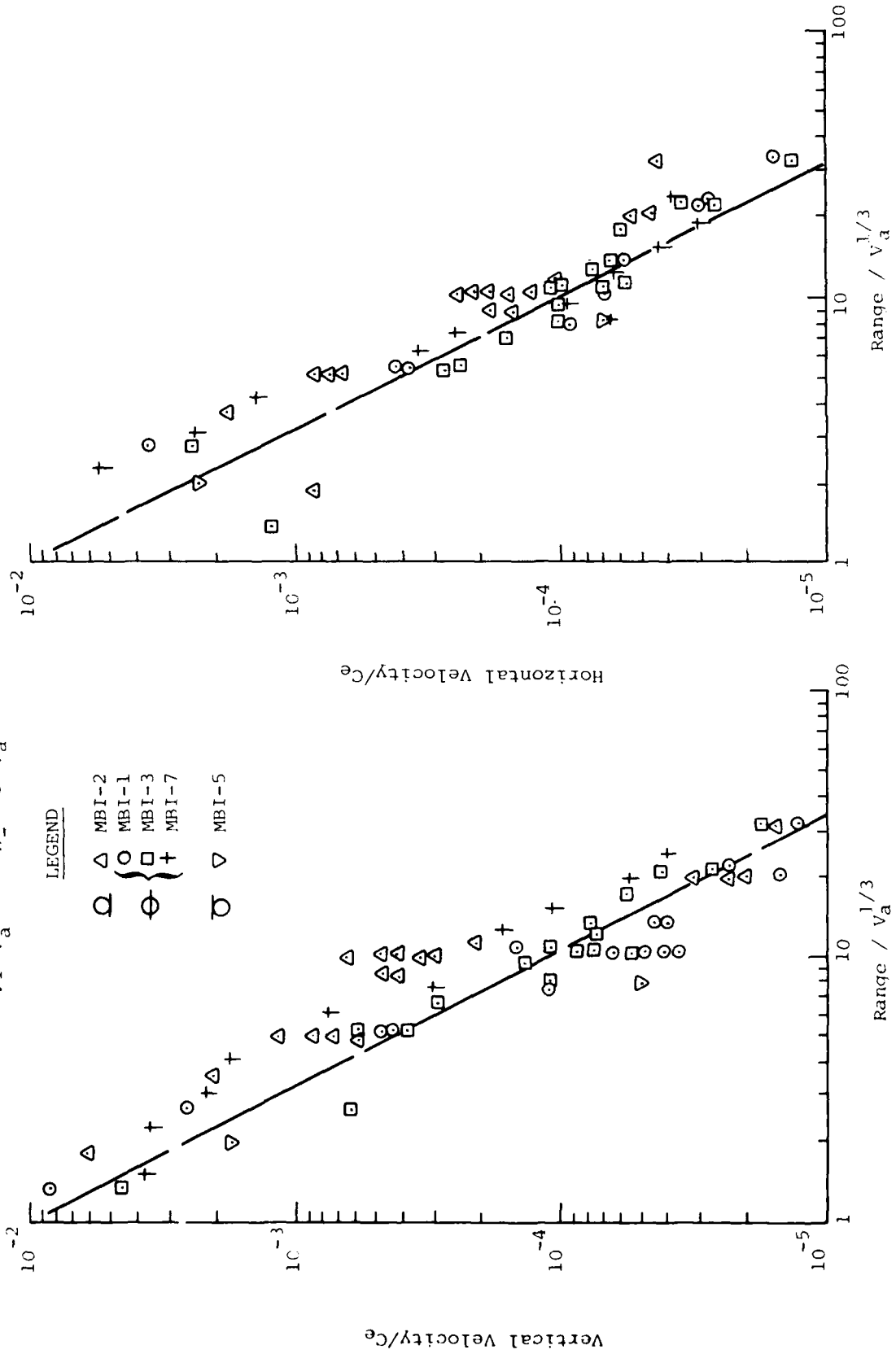


Figure 89. Crater Volume Scaled Velocities for Region 2

4.4 WAVEFORMS

4.4.1 Comparison of Measured and Predicted Waveforms

Waveforms were predicted by superimposing the various components of motion according to the predicted arrival times as discussed in Section 3.2. Waveforms were predicted for all near surface (0.46m) depths at ranges where gages were placed. Examples of the comparisons between these predictions and the data are discussed in the following sections. In general these represent some of the best and worst, as well as the more typical, comparisons.

a Surface Tangent Configuration. Figure 91 presents the predicted and measured vertical velocity waveform at the 10.68 meter range. At this range the oscillatory motion as predicted by the procedure in reference 11 is not developed, so the crater related component described in reference 10 was used for prediction of the low frequency motion. The airslap peak of the predicted waveform is about 33 percent below the measured value. The pulse width associated with this peak is about the same for both waveforms. The major upward peak of the prediction is about 50 percent above the measured waveform and the associated pulse width of the prediction is about 65 percent of the measured value. This upward peak is a combination of the reflected airblast signal and the crater related signal. The reflected airblast in the data appears to have decayed to almost zero before the crater related affects arrives. Therefore, addition is not taking place in the amplitude and the later arriving crater related pulse results in a longer duration upward pulse. The final negative half cycle of the prediction (downward crater related motion) produced a peak that is 29 percent of that measured and a pulse width 1.38 times the measured pulse width. This predicted waveform is generally good for about the first 75 msec. The major shortcoming in this waveform is the inadequacy of the prediction of the low frequency motion, which appears to be related primarily to the incorrect predicted arrival time of the crater related motions.

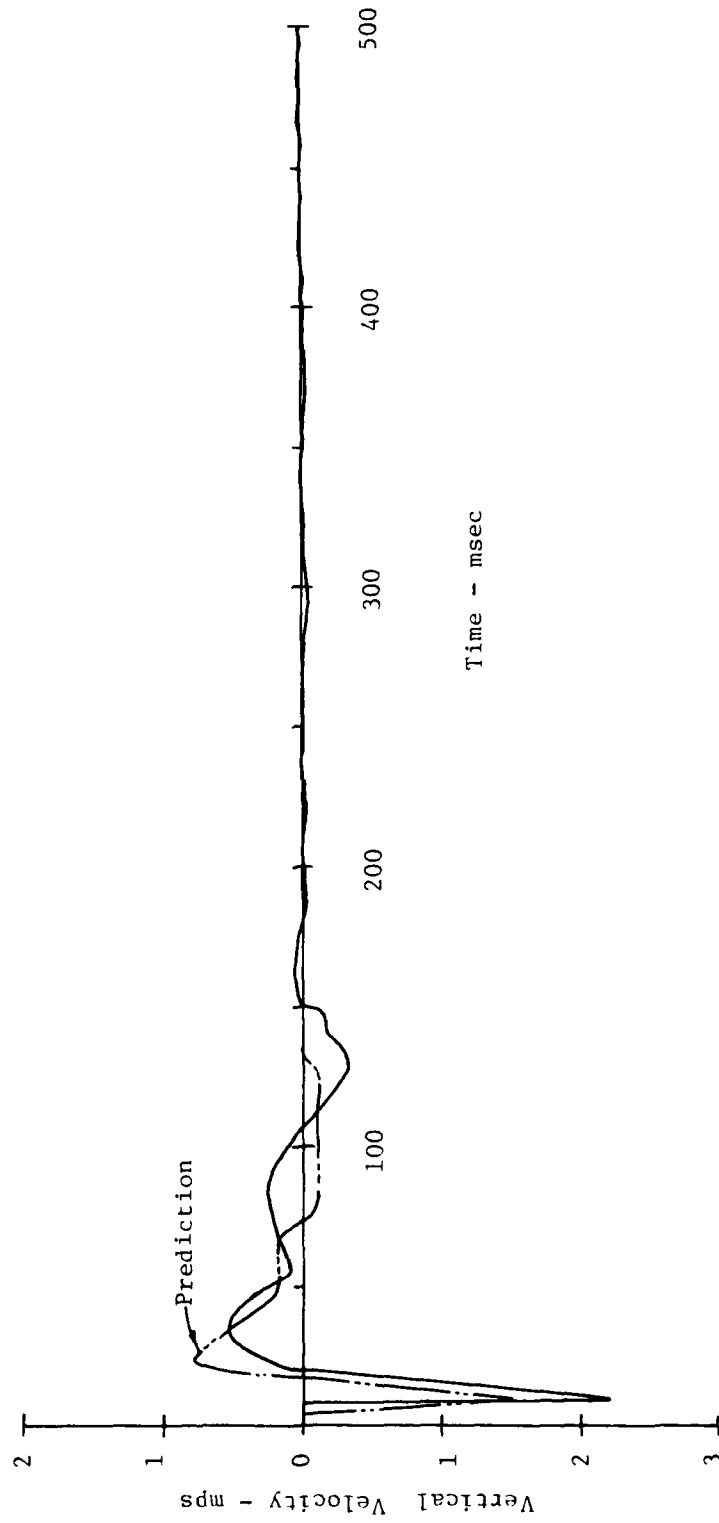


Figure 91. Comparison of Measured and Predicted Vertical Waveforms at The 10.68m Range and .46m Depth - MBI-2

The horizontal waveforms for the 10.68m range are shown in Figure 92. The low frequency motion was predicted for this waveform as mentioned above. The predicted pulse width of this signal is about 1.5 times that of the actual waveform. The prediction of the airslap motion did not include an airslap generated shear wave. This wave was present in all the near surface data and especially evident on the horizontal records. Its effect is to reverse the outward motion resulting in a shorter outward pulse and in many cases a strong inward pulse. The next major outward peak is about 76 percent of the actual value and the total pulse width of the predicted positive motion (arrival time to first negative motion) is about 93 percent of the actual. The effects of the early predicted arrival time of the crater related signal is evident here also. However, in the case of the horizontals the amplitudes of the crater related pulse is under-predicted. This prediction is generally quite good to about 80 msec. The primary discrepancy results from an incorrect prediction of the arrival time of the crater related motions and an incorrect crater related waveform after the first outward peak.

Figure 93 presents the measured and predicted waveforms at the 21.35 meter range. At this range the oscillatory component is developed enough to make use of the prediction methods in reference 11. The amplitudes of this waveform are generally well predicted. The airslap component of the prediction was within the data scatter and the pulse widths were quite similar. The low frequency motions are generally the same in magnitude, although the first positive half cycle was about 50 percent of the value exhibited by the data. The frequency of the predicted oscillatory component is about 1.5 Hz less than the data and the predicted oscillatory component arrives about 20 msec later.

The horizontal motions at the 21.35 meter range are shown in Figure 94. Again initial airslap related peak of this waveform was well predicted but the airslap related shear wave is very evident in the data. The 20-25 msec shift noted for the oscillatory component in the vertical comparison results in significant differences in the

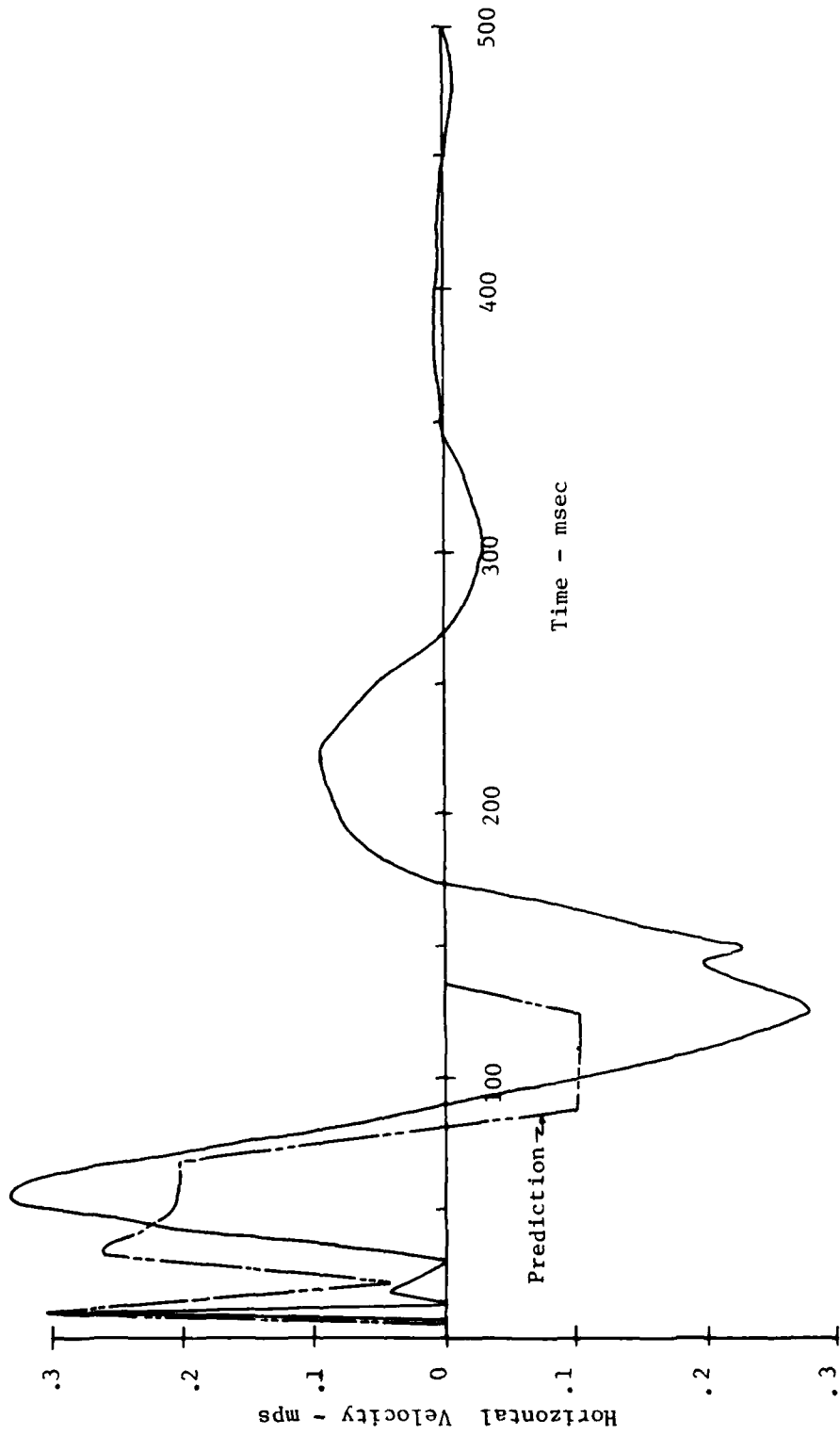


Figure 92. Comparison of Measured & Predicted Horizontal Waveforms at the 10.68m Range and the .46m Depth - MB I-2

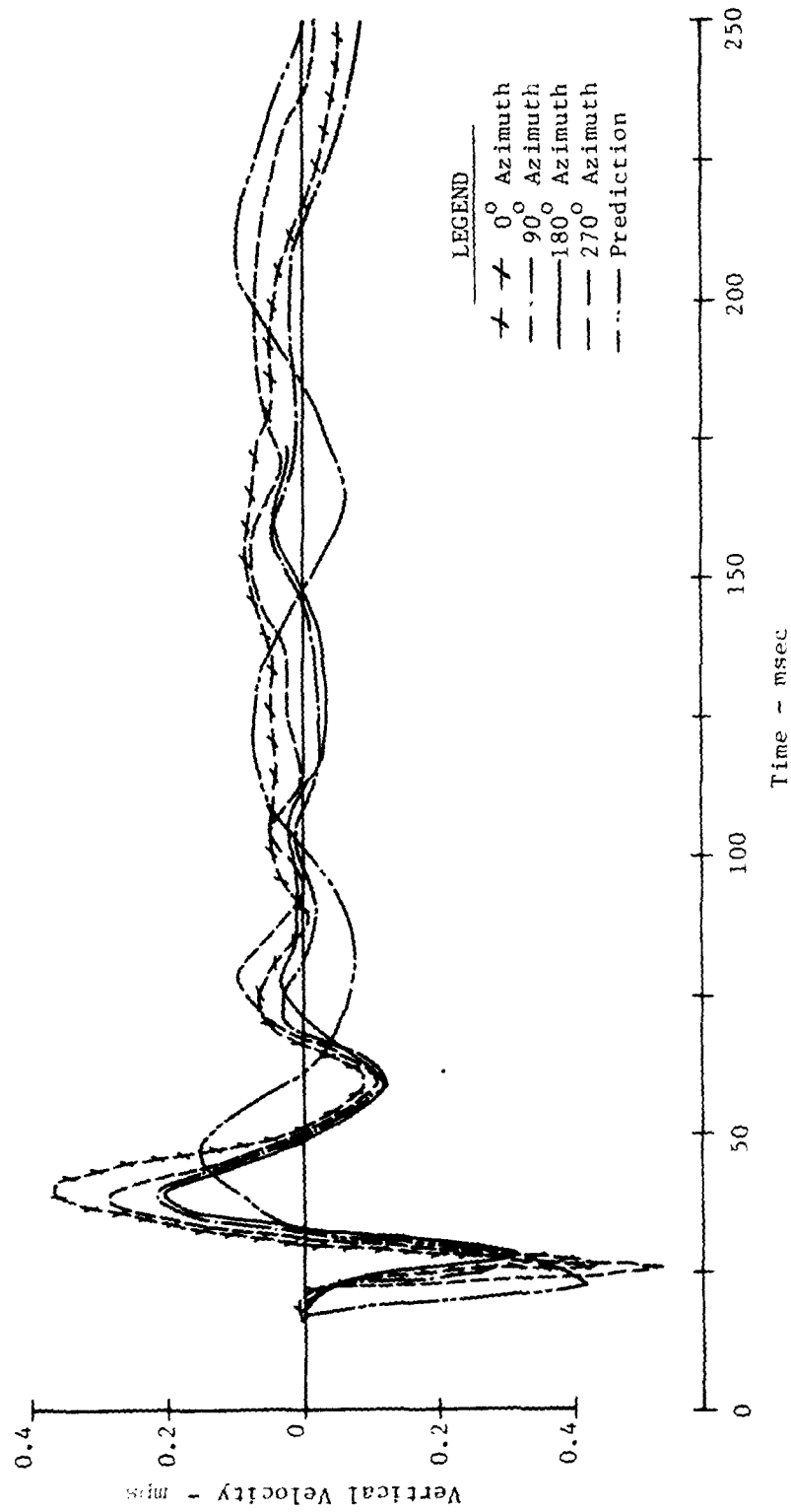


Figure 93. Comparison of Measured and Predicted Vertical Waveform at the 21.35m Range and 0.46m Depth - MBI-2

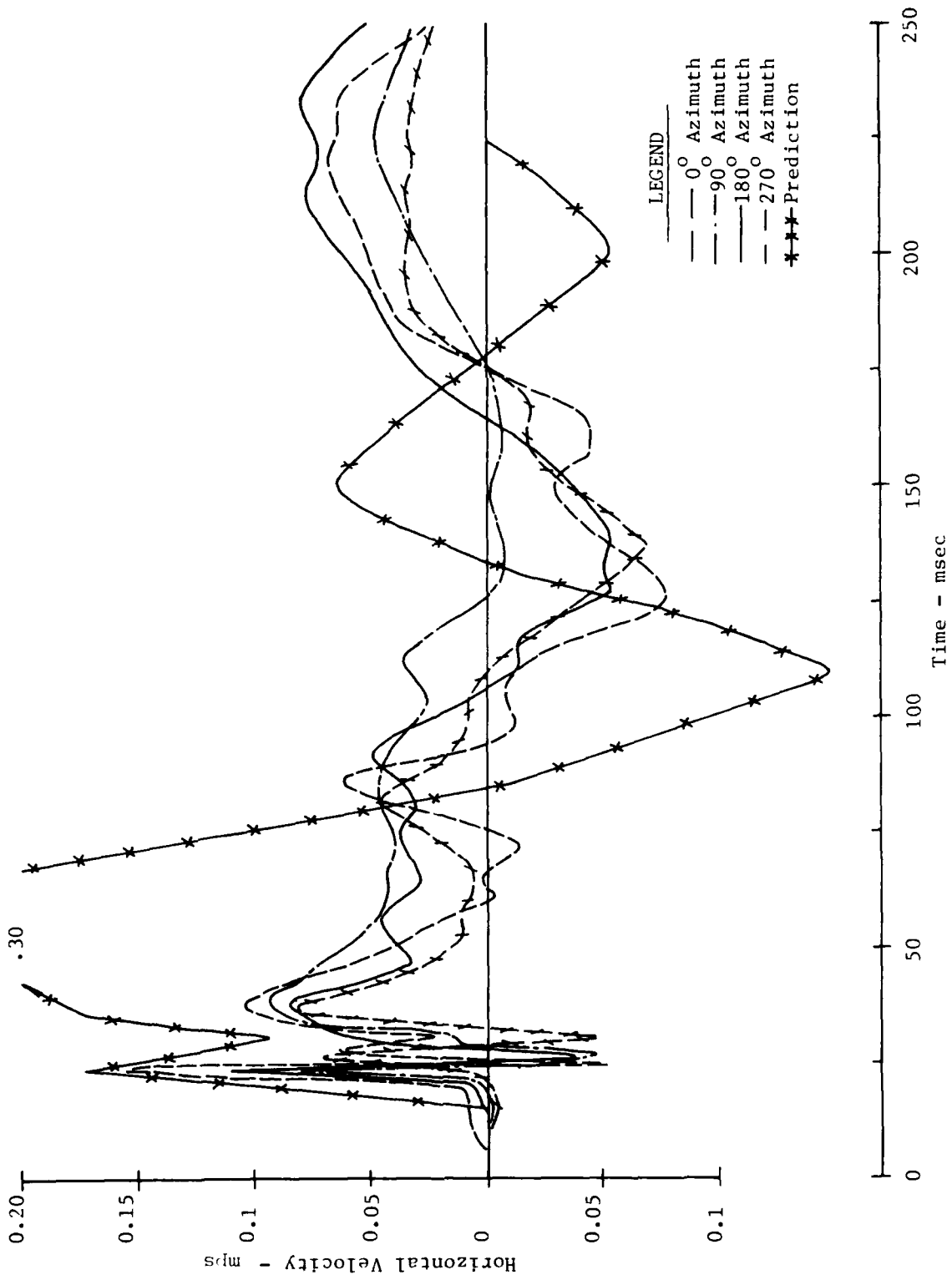


Figure 94. Comparison of Measured and Predicted Horizontal Waveforms at the 21.35m Range and .46m Depth - MBI-2.

horizontal motions. In general, the frequency of the predicted oscillatory component is about 3.7 Hz greater than the frequency of the data, and the peak values are as much as a factor of 6 greater. Had the airslap related shear wave been included in the prediction the discrepancy in amplitudes would have been much less.

b Half Buried Configuration. Figure 95 presents the vertical waveforms for the 18.3 meter range. As in the previous paragraphs, the airslap component of the predicted waveform is reasonably accurate, however, the oscillatory motion in this case is almost exactly 180° out of phase with the data. The magnitudes and frequencies of the predicted oscillatory motion are in good agreement with the data.

The horizontal waveforms for the 18.3 meter range are shown in Figure 96. The prediction produced an airslap peak which was about 1.15 times the actual value. The data showed the high frequency signal associated with the airslap shear wave which was not included in the prediction. The total pulse widths of the positive motion for both prediction and data are about the same. It appears, however, that the predicted oscillatory component arrives about 25 msec too early. The negative half cycle of the prediction is about 50 percent of the data and the pulse width is about 73 percent of the data. The prediction appears valid to about 125 msec but after this point the prediction badly underestimates the data. This same problem was noted in the 10.68m range for the surface tangent configuration. In that case the oscillatory component was the crater related pulse whereas here it was the close-in oscillatory pulse predicted by reference 11. Both procedures apparently are deficient in predicting the close-in, late time, horizontal response.

The vertical waveforms for the 36.6 meter range are shown in Figure 97. The initial p-head wave of the outrunning signal is well predicted as is the amplitude of the airslap signal. The downward airslap pulse appears to be terminated earlier than the prediction. This could be an effect of a shear head wave or perhaps the airslap related shear wave. The predicted oscillatory component is approximately 180° out of phase when compared to the data, however, the

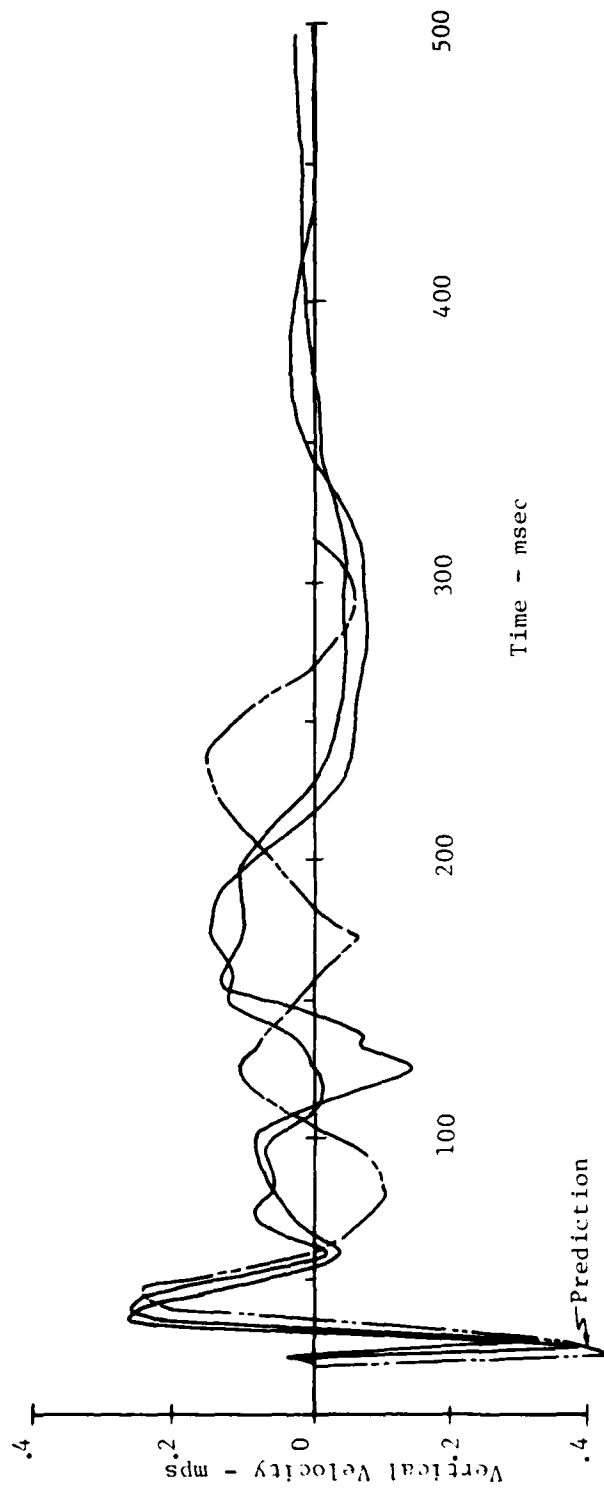


Figure 95. Comparison of Measured and Predicted Vertical Velocity Waveforms at the 18.3m Range and .46m Depth - MBI-1

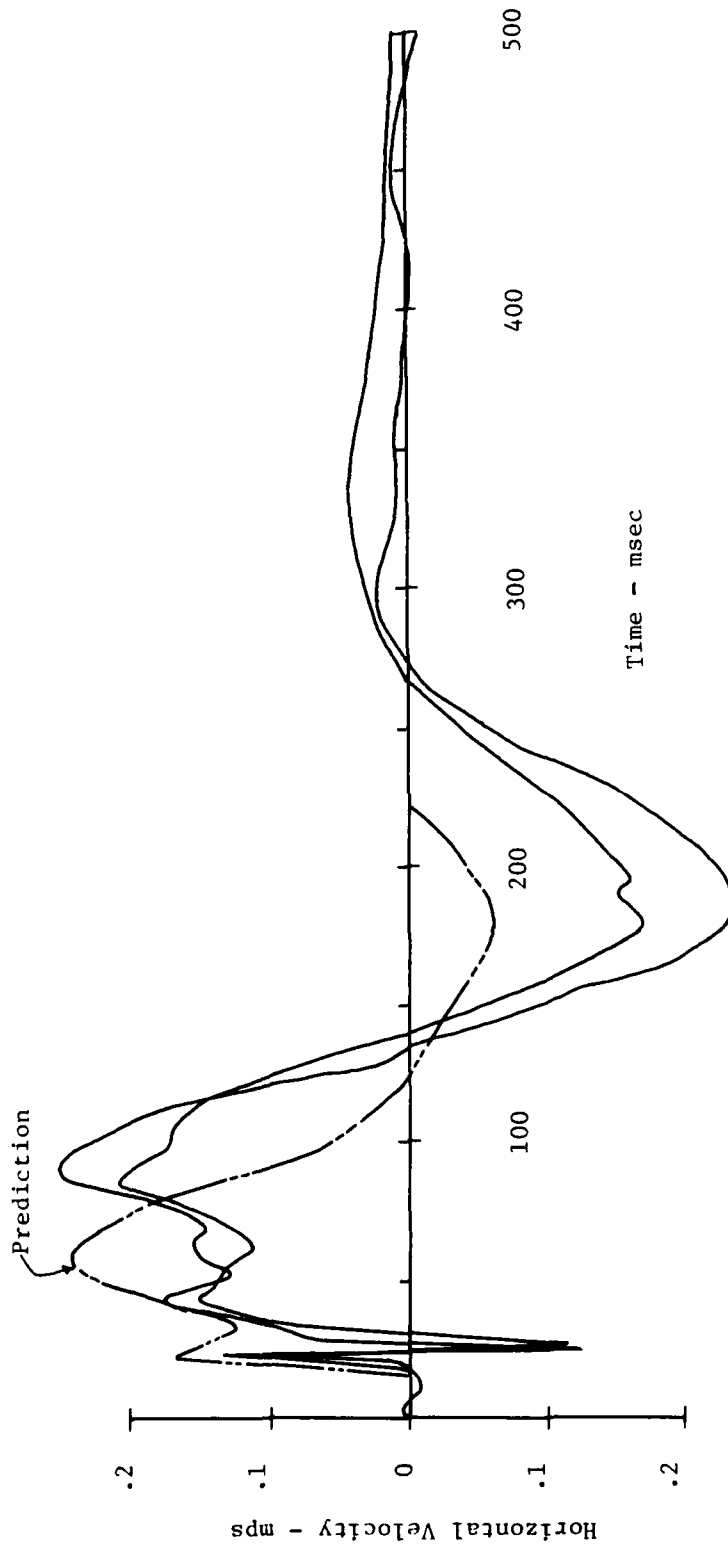


Figure 96. Comparison of Measured and Predicted Horizontal Waveforms at the 18.3m Range and .46m Depth - MBI-1

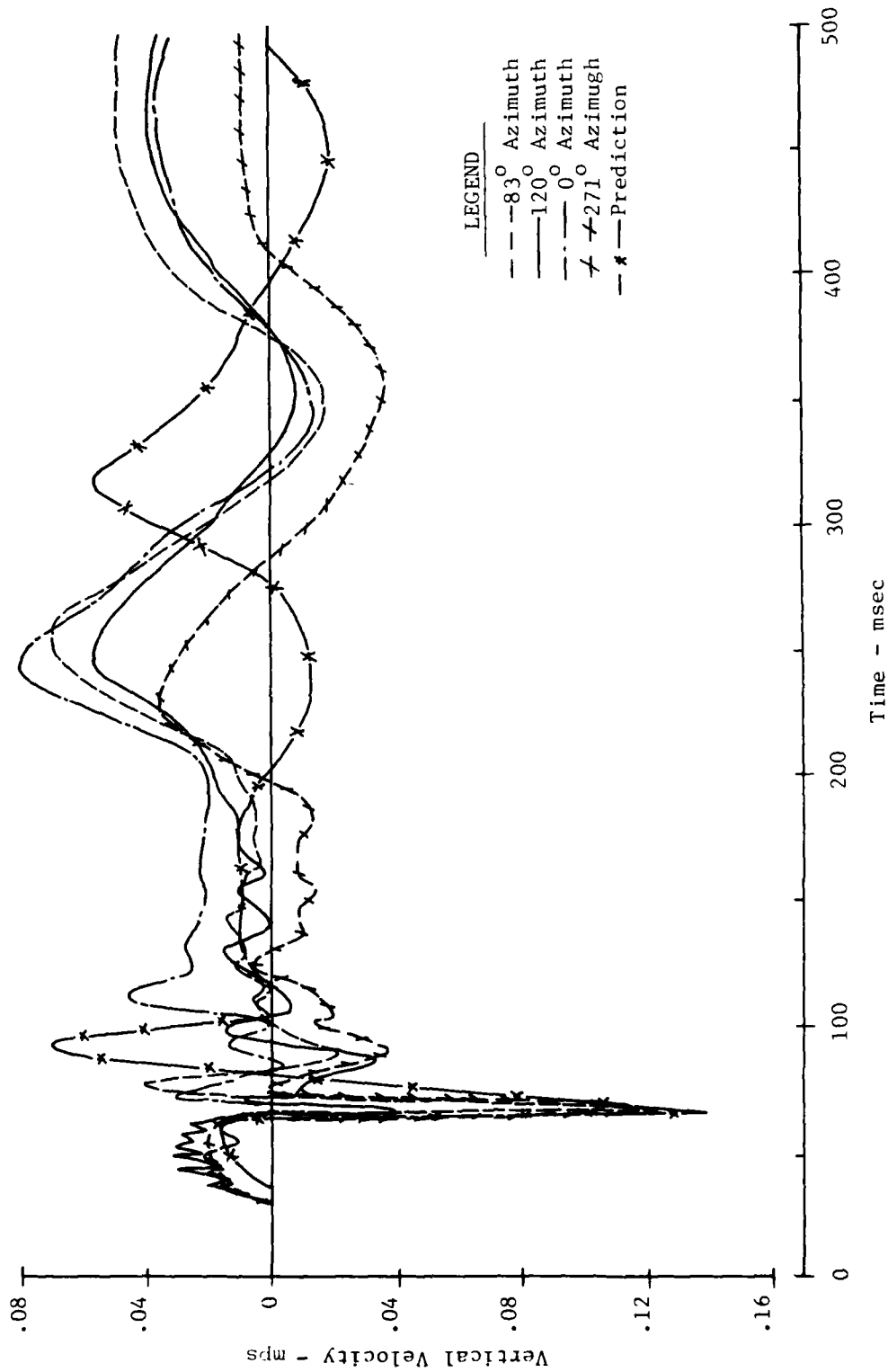


Figure 97. Comparison of Measured and Predicted Vertical Waveforms at the 36.6m Range and .46m Depth - MBI-1

structure of the waveform agrees fairly well and the peaks are within the data scatter.

Figure 98 shows the horizontal waveforms at the 36.6 meter range. The prediction overestimates the magnitudes by as much as a factor of 3 and the frequency of the prediction is about 3.4 Hz greater than the data.

c Tangent Below Configuration. The vertical waveforms for the 36.6 meter range is presented in Figure 99. As was pointed out in earlier sections this configuration was the most difficult to predict. As can be seen from the figure, success was quite limited. The arrival times and phasing for the first 200 msec were in considerable error.

Figure 100 shows the horizontal waveforms at the 36.6 meter range and similar problems are evident.

4.4.2 Event-to-Event Waveform Comparisons for the Half Buried Configurations

Vertical and horizontal velocity waveform comparisons for the three half buried experiments are presented in Figures 101 and 102. Two of the reasons for conducting the three experiments at this configuration was to check event-to-event data scatter in experiments with the same yield and to establish data for scaling between 5.35×10^{-4} TJ and the 2.09×10^{-3} TJ yields.

Examination of Figure 101 and 102 show that reproducibility of MBI-1 and MBI-3 was quite good. In general, the waveforms are as nearly identical as physically possible with respect to frequencies. Differences in magnitudes can possibly be attributed to different baseline shifts for the two events.

The third waveforms shown on these figures are from the 5.35×10^{-4} TJ yield experiment (MBI-7). These waveforms were scaled by yield scaling (reference 10) of range, depth, and time. As can be seen, the scaling generally produces satisfactory results. Frequencies and magnitudes are within the scatter usually seen from azimuth to azimuth in one experiment.

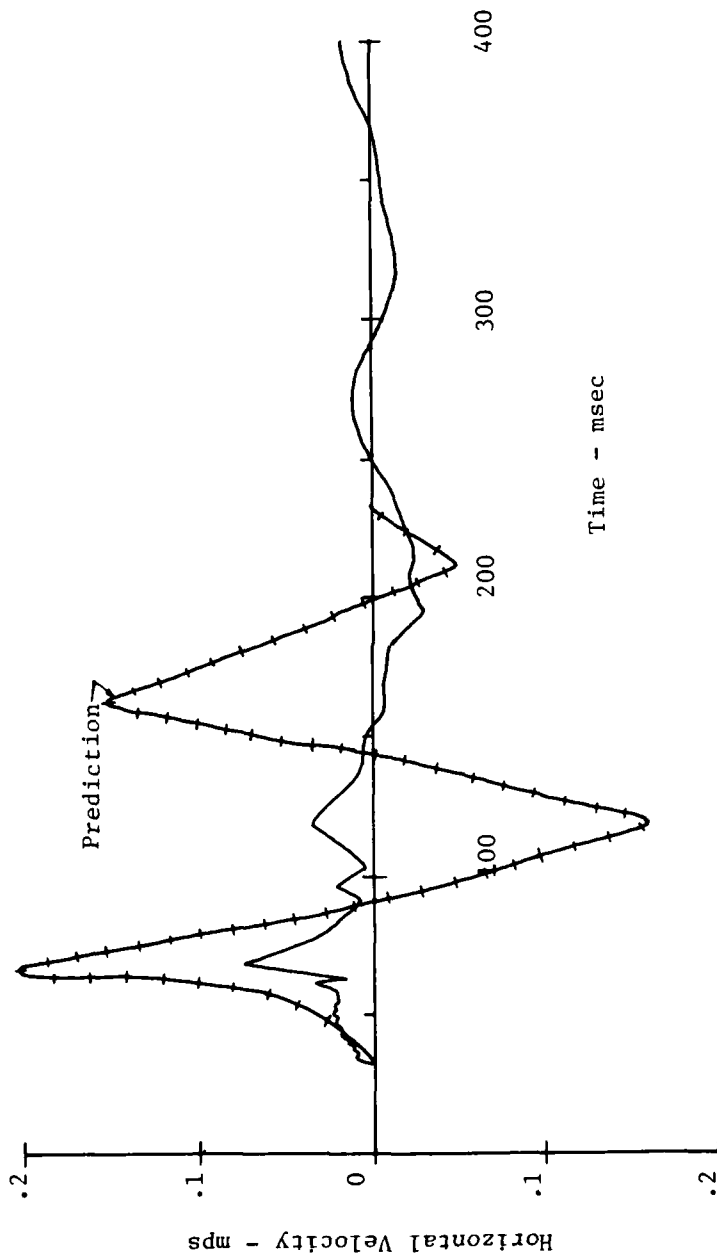


Figure 98. Comparison of Measured and Predicted Horizontal Waveforms at the 36.6m Range & the .46m Depth - MBI-1

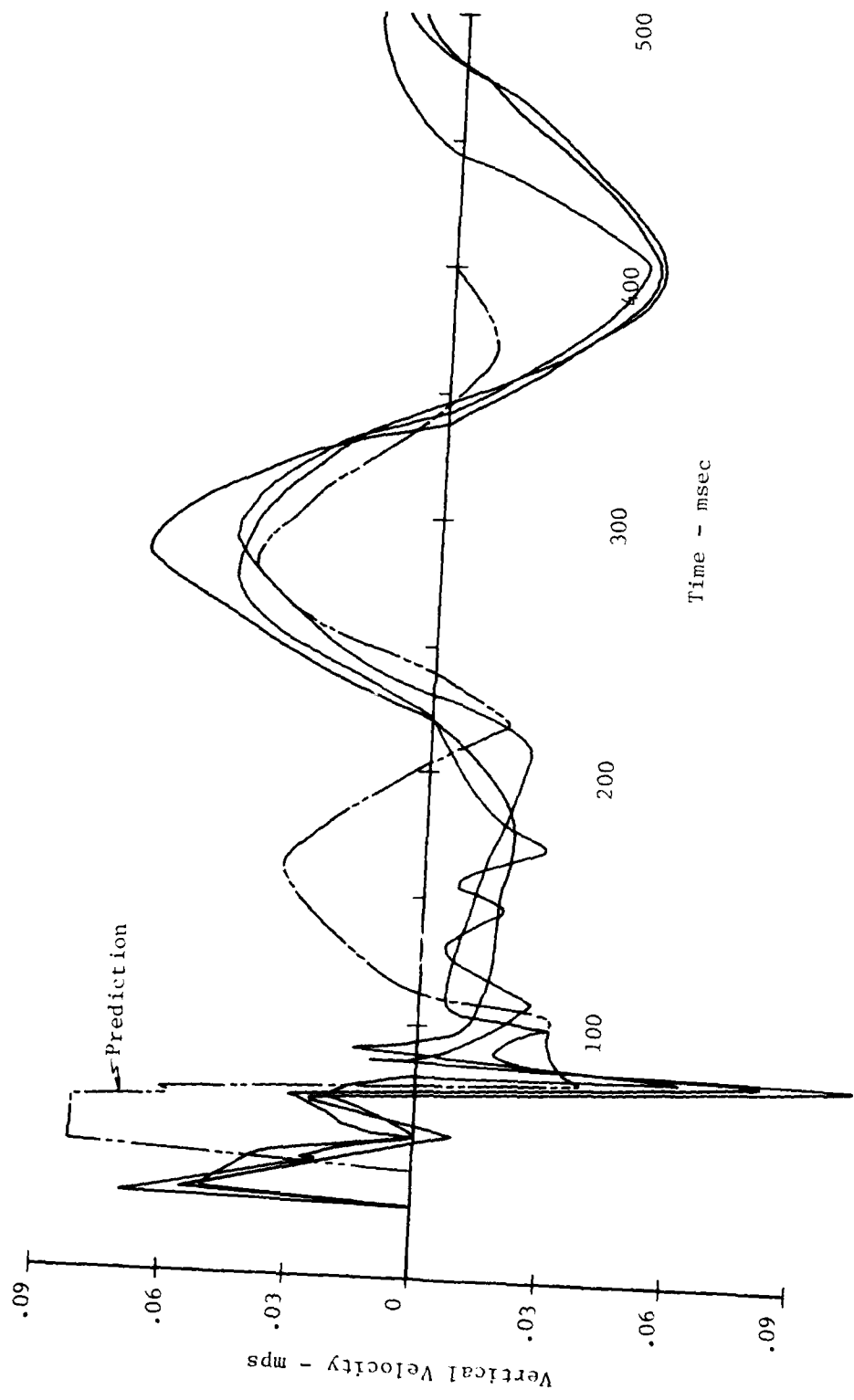


Figure 99. Comparison of Measured and Predicted Vertical Waveforms at the 36.6m Range and .46m Depth - MBI-5

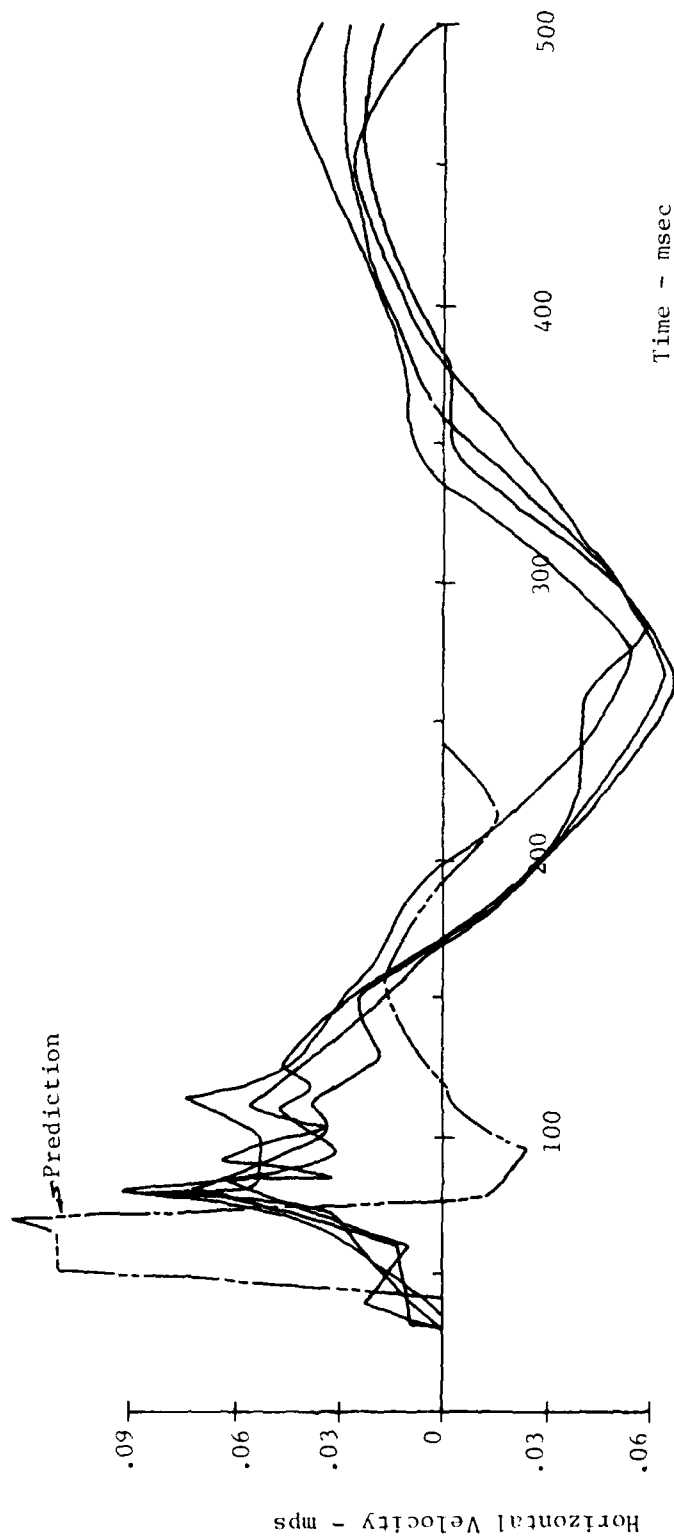


Figure 100. Comparison of Measured and Predicted Horizontal Waveforms at the 36.6m Range and .46m Depth - MBI-5

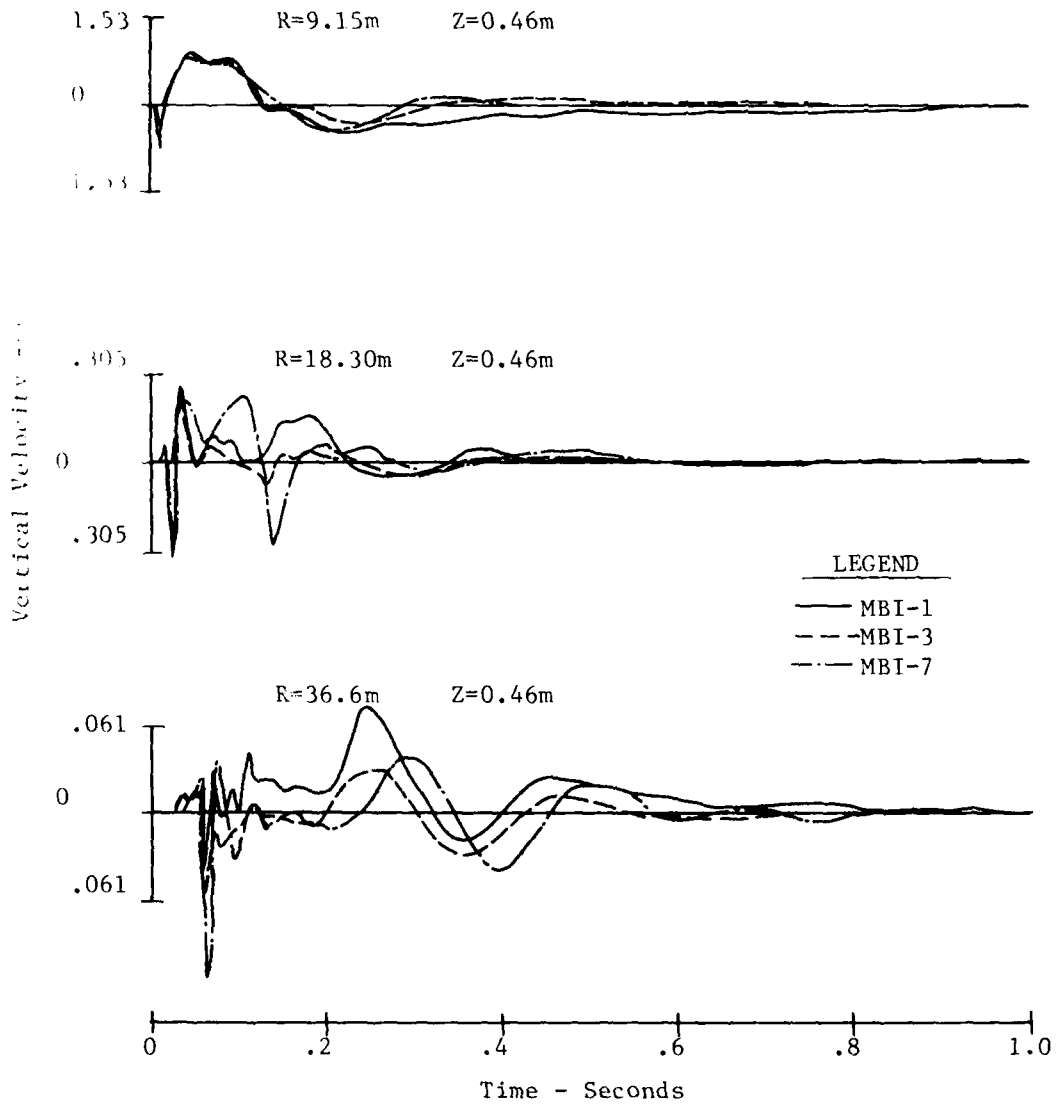


Figure 101. Event-to-Event Vertical Waveform Comparison for the Half Buried Configuration

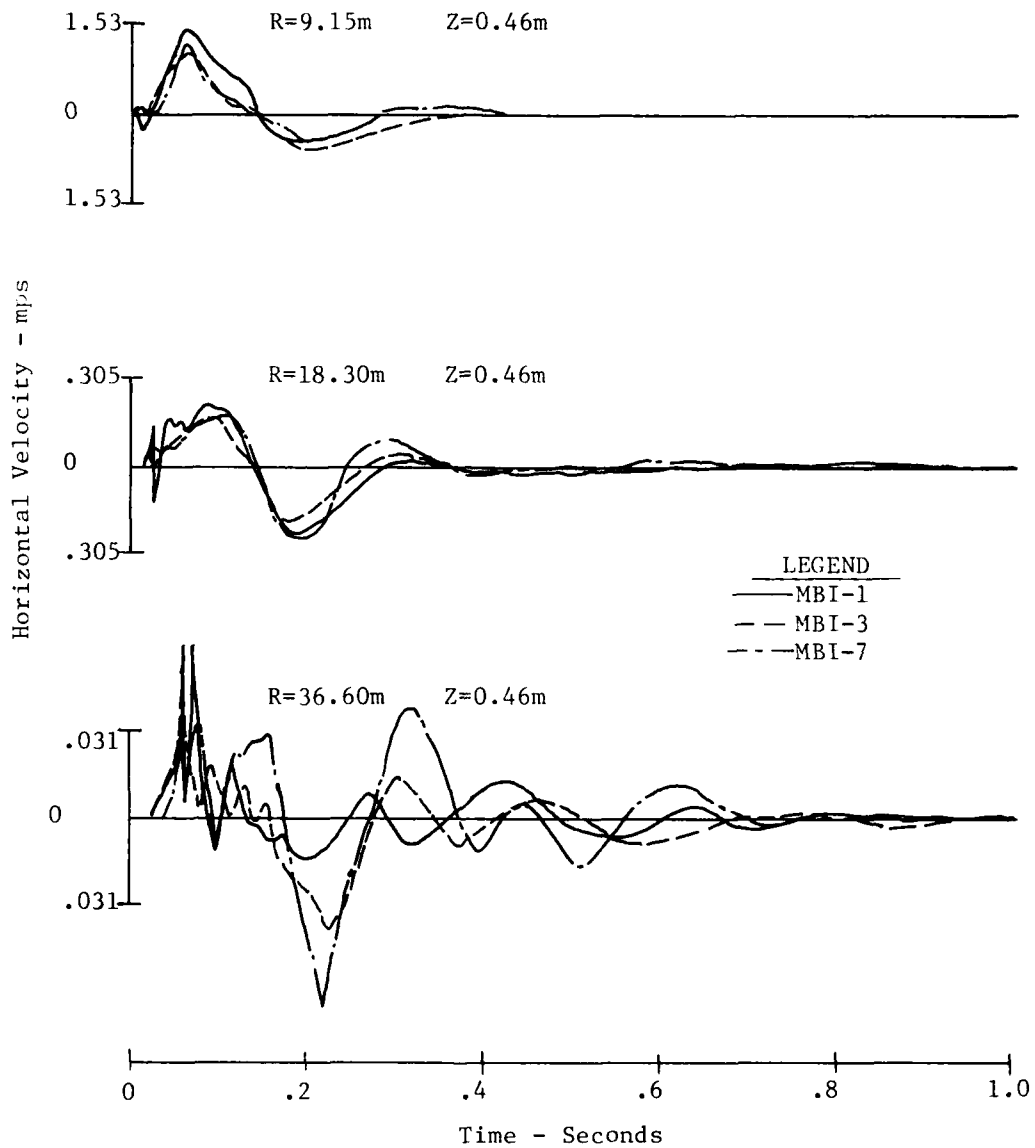


Figure 102. Event-to-Event Horizontal Waveform Comparison for the Half Buried Configuration

4.5 COMPARISON OF INTEGRATED ACCELEROMETER AND VELOCITY GAGES

Figures 103 through 106 present the comparisons of waveforms obtained from integration of acceleration waveforms and those obtained directly by velocity gages for MBI-1 and MBI-2. Figure 107 is a plot showing the maximum peak outward velocities and maximum peak upward velocities vs range for MBI-1 and MBI-2. These plots are presented here as being characteristic of this type of data received from all events. As can be seen from all these figures the agreement between the two types of gages is quite good. Frequency content is almost identical in most waveforms and most of the peaks are within acceptable data scatter.

4.6 STRESS MEASUREMENTS

A limited number of stress measurements were made on all events in Phase I. Figures 108 and 109 present some characteristic stress waveforms for the three experimental configurations used.

Vertical stress waveforms are shown in Figure 108. The surface tangent waveform is inconsistent and does not appear to contain valid data beyond the initial airslap stress. (The large amplitude noise indicates an electrical problem.) The other two waveforms are characterized by a sharp airblast related peak, followed by a large direct induced surge. As would be expected, the tangent below configuration produces the largest crater related stress but contrary to expectations it also produced the largest airslap stress.

Horizontal stress waveforms are shown in Figure 109. The three waveforms are similar, each exhibiting the sharp airblast peak and then the direct induced stress. In both the surface tangent experiment and the half buried experiment the airblast produced the highest stress. As would be expected, the direct induced signal produced the highest stress in the tangent below waveform.

Peak vertical stresses are presented in Figure 110. Neither the positive nor the negative stresses indicate any trend on an event

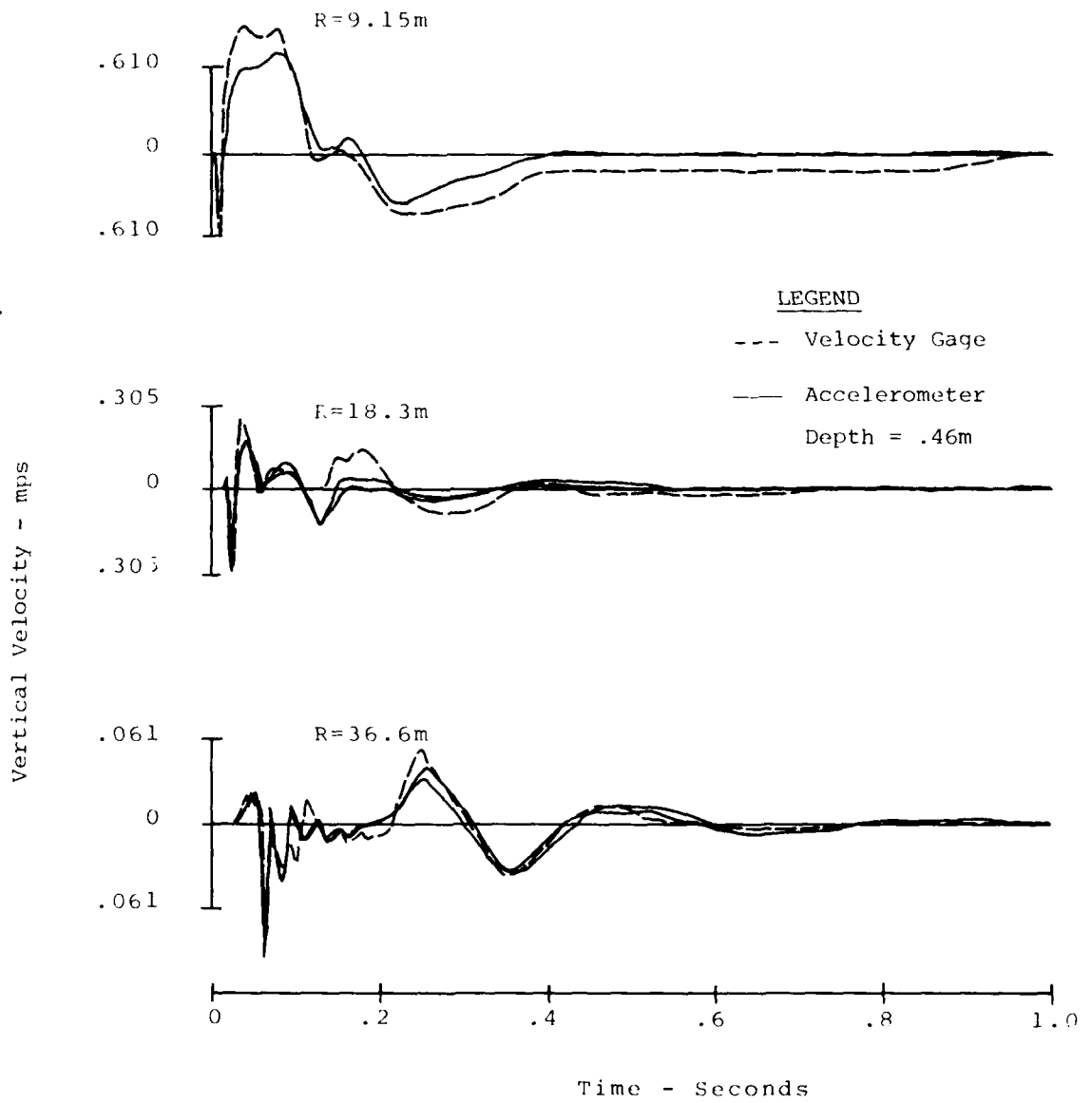


Figure 103. Comparison of Velocity Gage Waveforms and Integrated Accelerometer Waveforms MBI-1

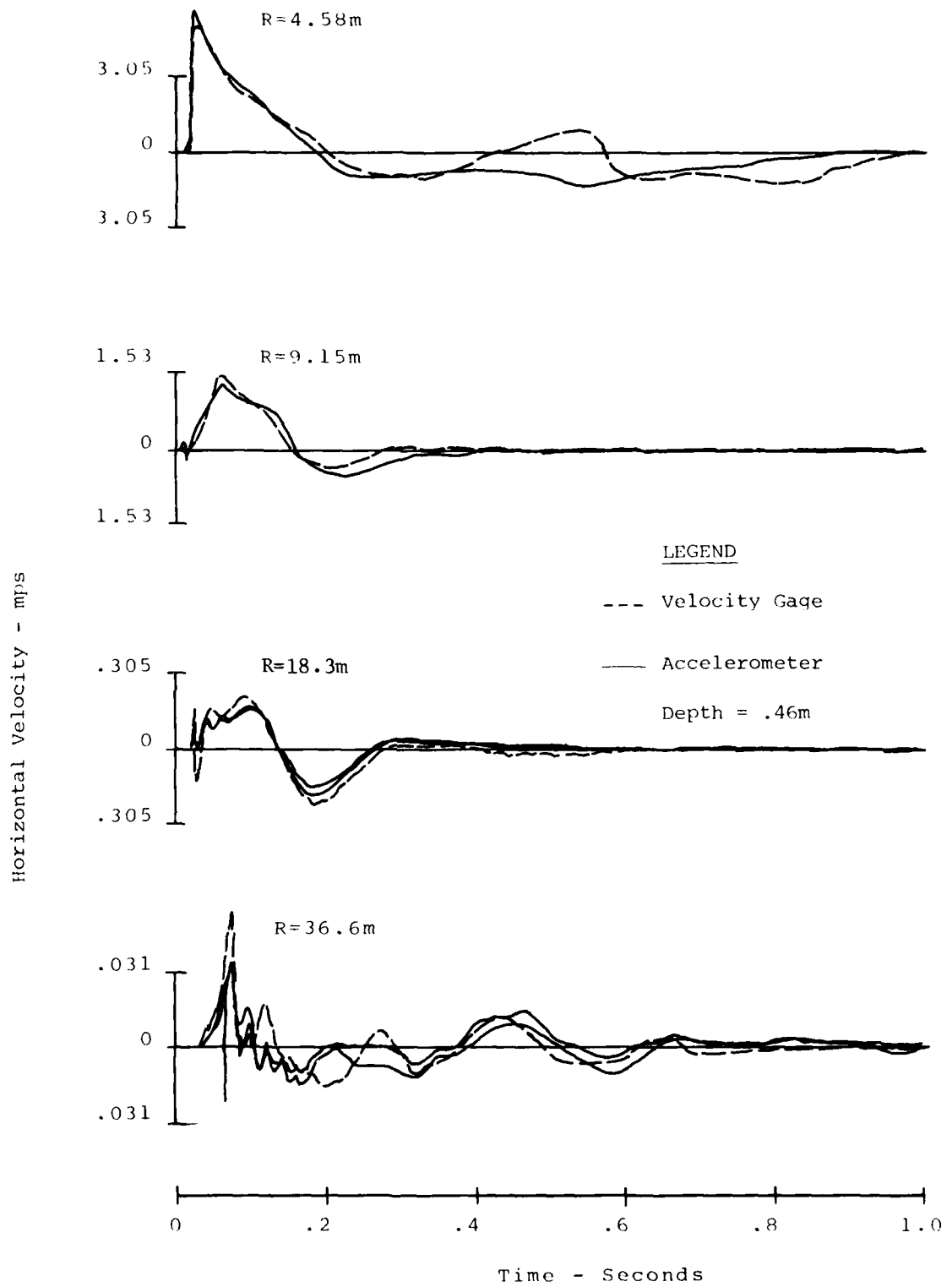


Figure 104. Comparison of Velocity Gage Waveforms and Integrated Accelerometer Waveforms MBI-1

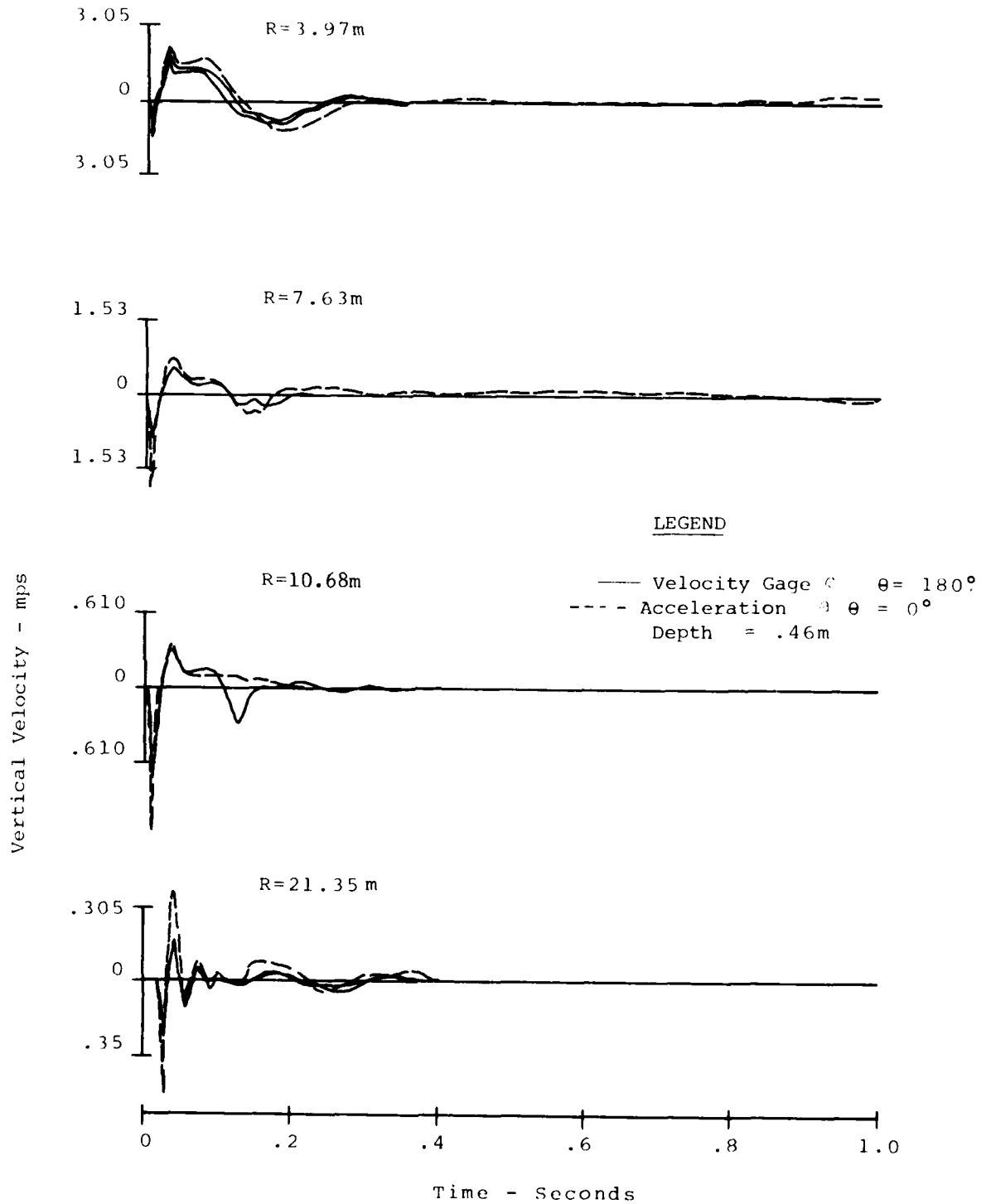


Figure 105. Comparison of Velocity Gage Waveforms and Integrated Accelerometer Waveforms for MBI-2

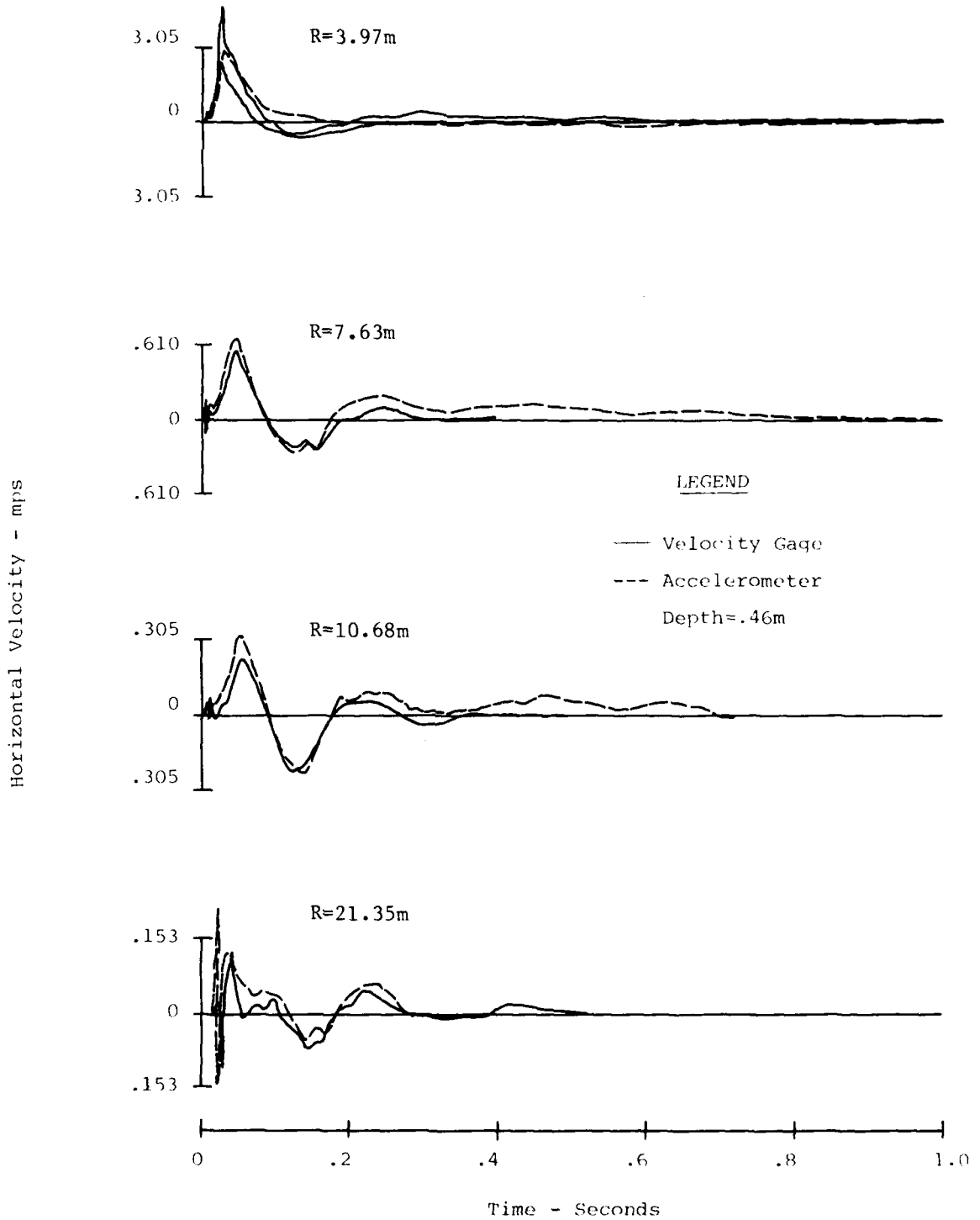


Figure 106. Comparison of Velocity Gage Waveforms and Integrated Accelerometer Waveforms MBI-2

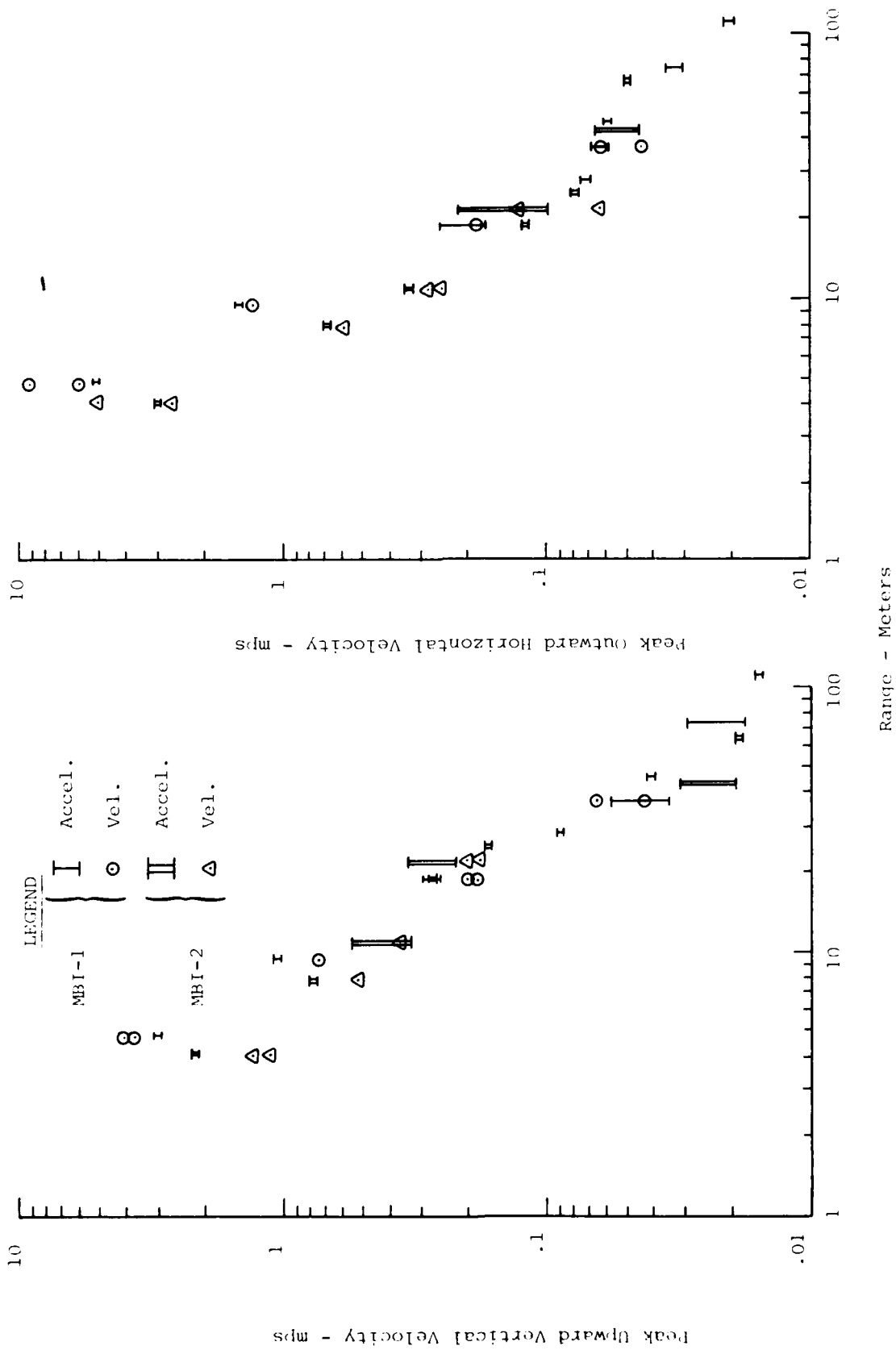


Figure 107. Comparison of Peak Values from Integrated Accelerometers and Velocity Gages

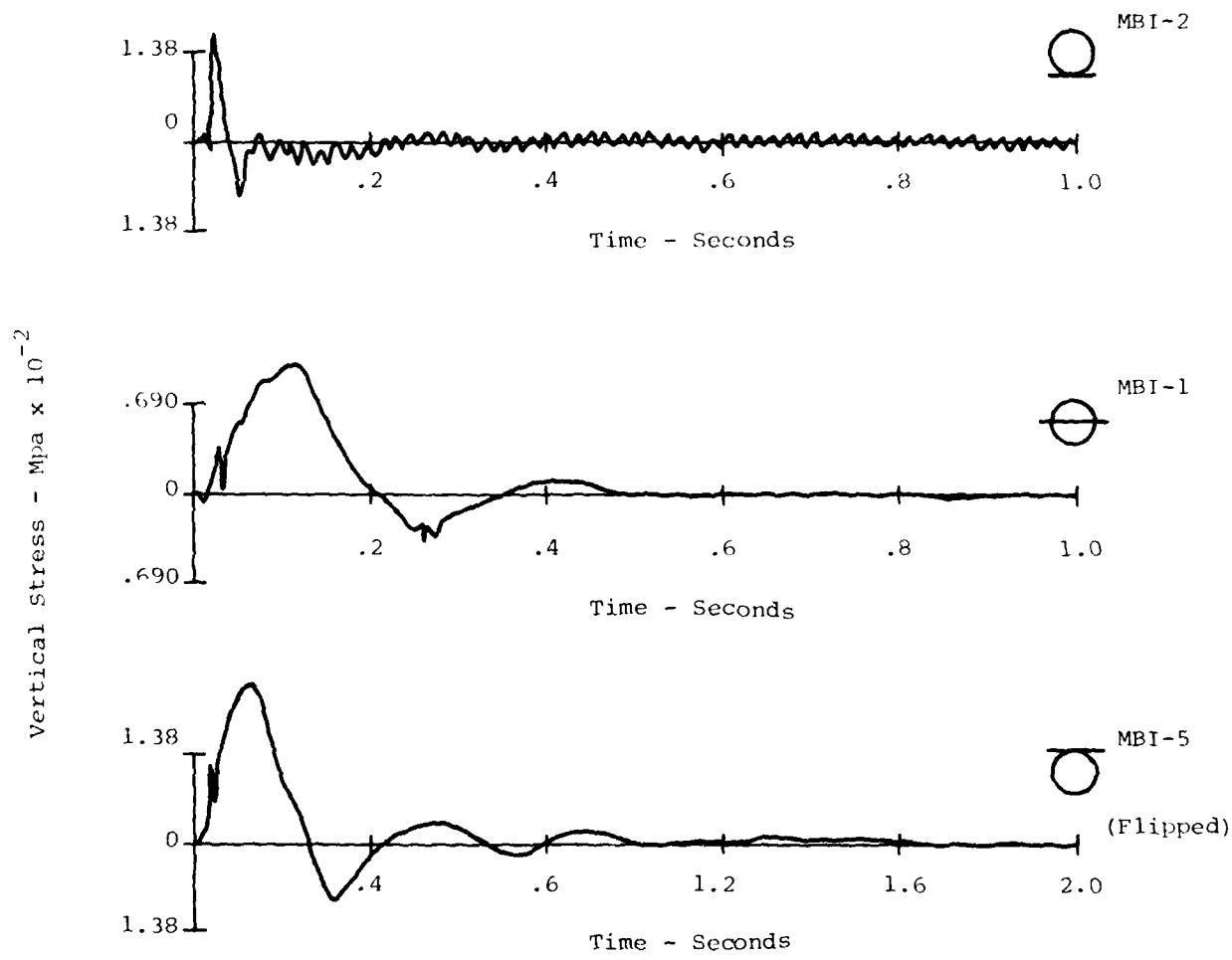


Figure 108. Vertical Stress Waveforms at R=18.3m and Z=1.5m for the Three Configurations

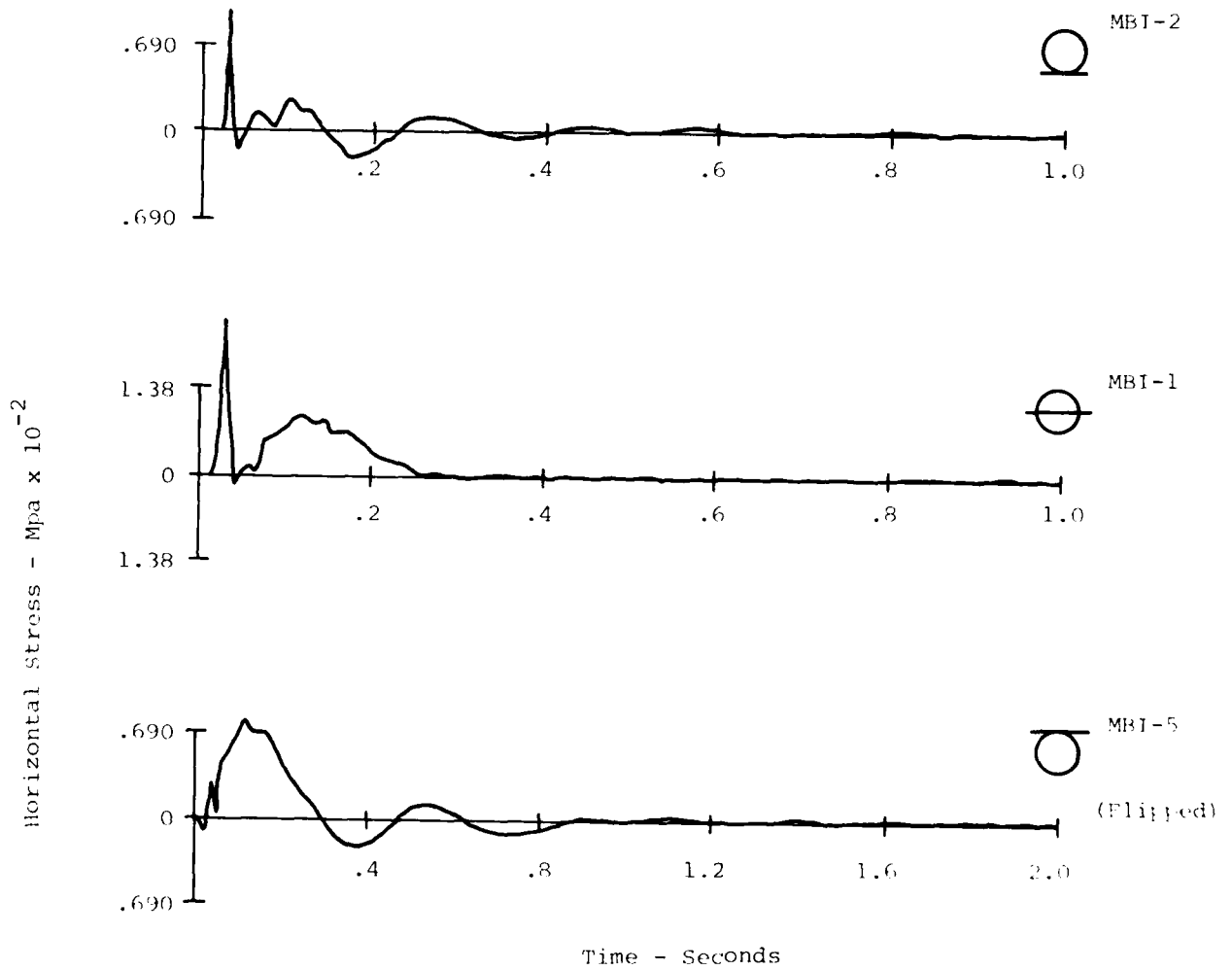


Figure 109. Horizontal Stress Waveforms at the 18.3m Range and the 1.5m Depth for the Three Configurations

by event basis. The bands shown in Figure 110 generally encompass most of the points. This makes the scatter for all events approximately a factor of 4, bottom to top with an attenuation of $R^{-2.2}$ for the positive stress. The scatter for the negative stresses is about a factor of 3.5 bottom to top and the attenuation is $R^{-1.8}$.

Peak horizontal stresses are shown in Figure 111. The data is extremely limited, but the positive stresses fall in the same bands as was used for the positive vertical stresses.

The negative peaks indicate a trend of increasing tensile stress with range.

4.7 TRANSVERSE MEASUREMENTS

A limited number of transverse measurements were made for most of the experiments in this program. If soil were truly an isotropic, homogeneous medium, and gage placement were exactly correct, these gages would provide no data. Since soil is neither isotropic or homogeneous and there are errors in aligning gages, the data received is an indirect measure of the deviation of this site, and the placement procedure from the ideal behavior.

Figure 112 presents the peak positive and negative transverse velocities for the three experimental configurations compared to the peak horizontal outward velocity from the surface tangent experiments and the tangent below experiment. Most of the data falls between .01mps and .03mps in a rather random manner indicating that these measurements are not event dependent and, therefore, more an indirect measure of the site inhomogeneties. As would be expected the transverse data is well below the horizontal data. The ratio of horizontal velocity to transverse velocity varies from about 8 at the closest range to around 4 at the farthest range.

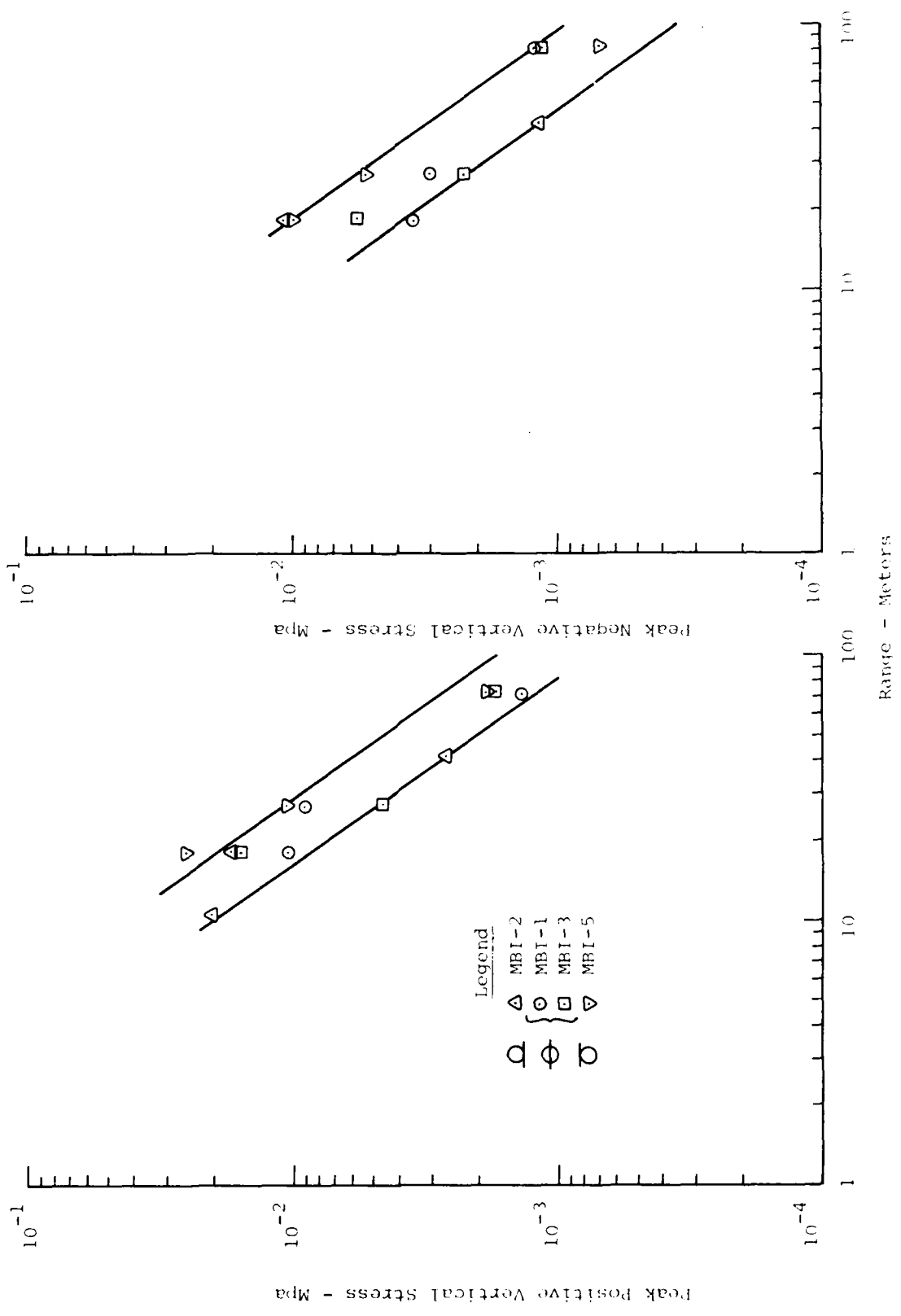


Figure 110. Vertical Stress Data from Phase I Single Burst Experiments (1.53m Depth)

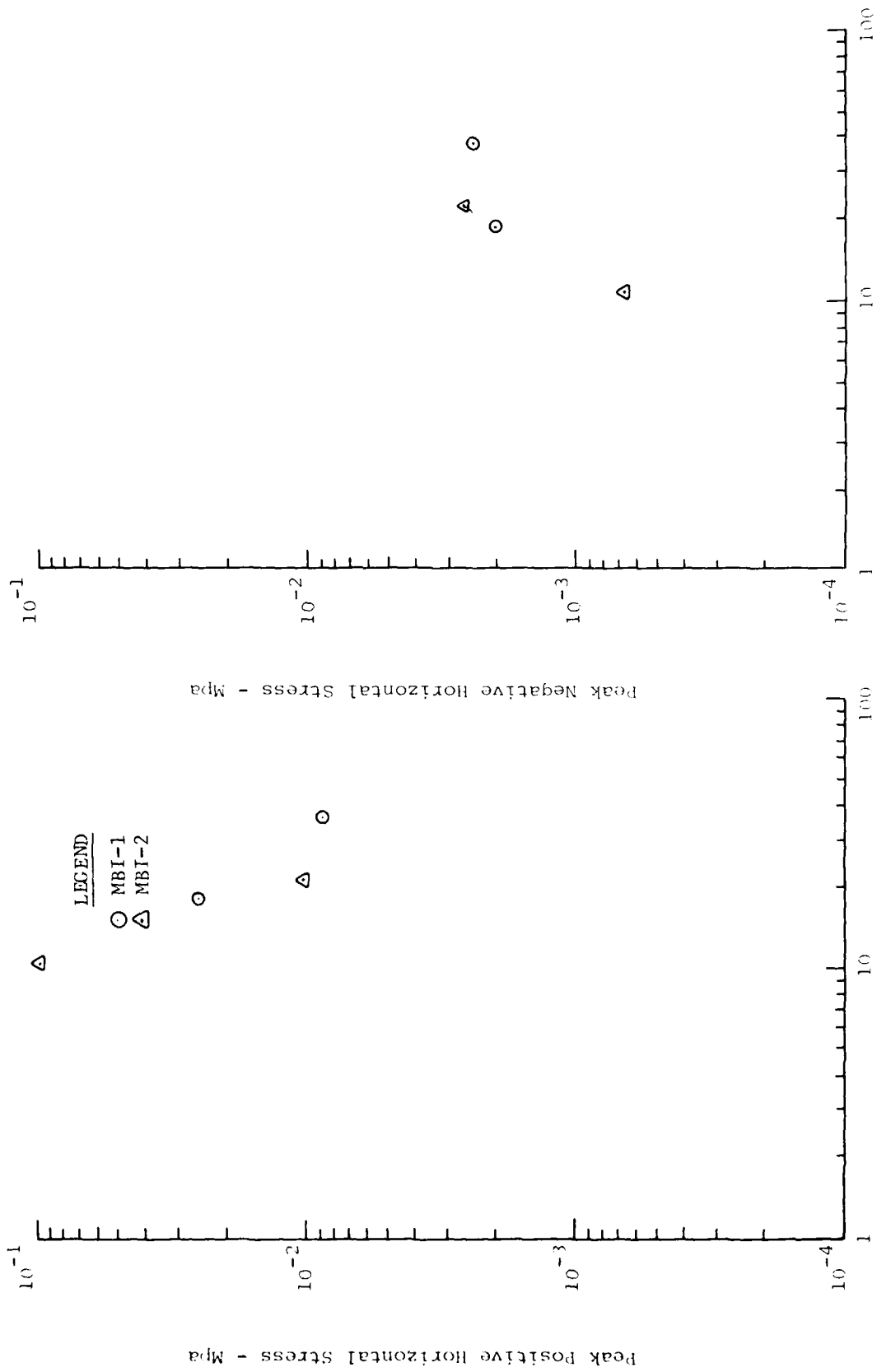


Figure 111. Horizontal Stress Data from Phase I Single Burst Experiments

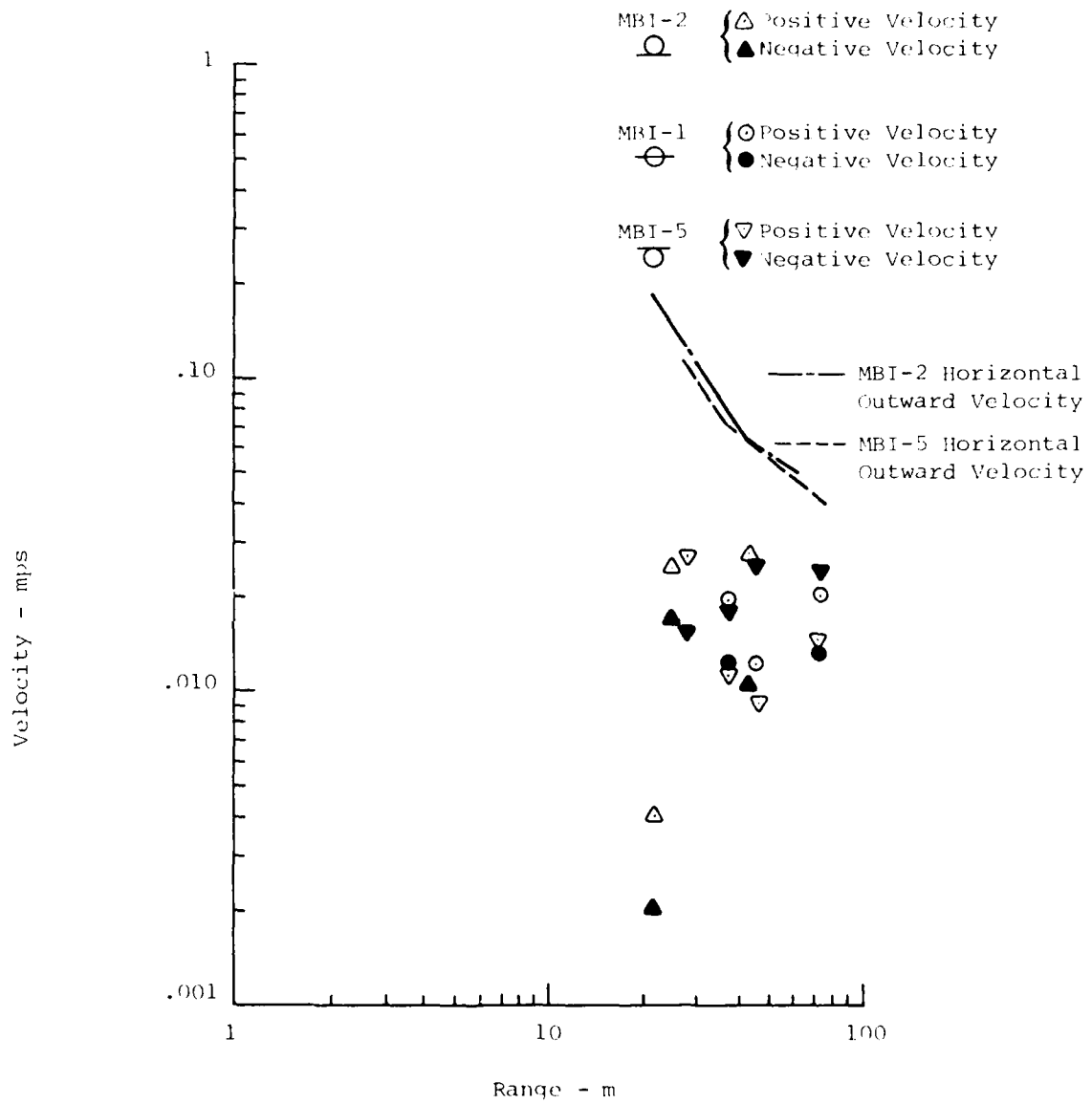


Figure 112. Tangential Data from the Three Configurations

5. SUMMARY, CONCLUSIONS, AND RECOMMENDATIONS

5.1 SUMMARY

The objectives of the single burst experiments of the Misers Bluff test program were given in Table 1. In general the purpose of these experiments was to obtain a data base for making superposition predictions for the multiburst experiments which were also conducted as part of Phase I. To better characterize this data base the program was designed to evaluate data scatter within a single experiment and from event-to-event, to investigate the scaling as a function of height-of-burst for a single yield, and to obtain data for 5.35×10^{-4} TJ to compare with data from other test sites. Since the primary purpose of these data were to provide a basis for the superposition prediction of the multiburst experiments, it is apparent that, to satisfy this objective, the phenomenology associated with the single burst experiments be well understood. Additionally, since the prediction of the nuclear multiburst ground shock environments will be based on single burst predictions which will be combined using either superposition or some other waveform synthesis methodology, it is also desirable to evaluate the accuracy and to understand the shortcomings of the single burst prediction procedure.

In order to accomplish the above objectives some 399 channels of data were studied and have been reported in previous sections.

5.1.1 Data Scatter

Evaluations of the data scatter was made by comparing peak values of airslap induced acceleration and particle velocity and the oscillatory component peak particle velocities. The data show that the higher the frequency of the component in question, the greater the data scatter observed in the experiments. The largest data scatter in peak acceleration occurred on the surface tangent experiment and the minimum on the tangent below experiment. This progression also represents the decreasing from maximum to minimum values of the observed particle accelerations. The bottom to top peak acceleration data scatter for the surface tangent experiment was about a factor of 4.

This decreased to about 3 for the half buried and 2 for the tangent below experiments. These values are reasonably consistent with previous experiments. The same trends were experienced in the airslap induced particle velocity with a factor of 3 bottom to top scatter in the surface tangent experiment, approximately 2 1/2 to 3 in the half buried experiment and about 1 1/2 in the tangent below experiment.

The oscillatory component was the lowest frequency component examined and had the least amount of data scatter; however, the scatter did not show the trend with height of burst experienced by the airslap motions. The maximum data scatter was observed on half buried experiments varied from about 1.2 to 1.6 with no real trend between horizontal and vertical components.

The above quoted factors were based on a single experiment at each height of burst; however, the experiment-to-experiment variation evidenced by events 1 and 3 is within the referenced factors. In most cases the scatter in the horizontal measurements was greater than the vertical.

5.1.2 Height of Burst

The effect of the explosive height of burst on the airslap induced ground motions was quite well predicted based on the differences in the airblast generated by the different heights of burst. Beyond a range of approximately 15 meters the height of burst effects were negligible in the particle velocities. Closer than 15 meters to the charge the higher airblast effects produced by the surface tangent experiment resulted in higher particle velocities. Slightly more height of burst dependence was observed in the horizontal particle velocities; however, even in this case it was not particularly significant. In many cases the data from a single experiment ranged from the top to the bottom of the data scatter. Given the data scatter associated with these measurements and the differences in the observed overpressure and overpressure impulse it is not surprising that the height of burst effect was as small as observed.

Even less effect of the height of burst was observed in the oscillatory component. In fact, the data scatter for the various

heights of burst overlapped. The largest apparent effect of the different heights of burst was in small changes in the arrival time of the various signals comprising the waveform and the periods of the oscillatory components. These arrival time shifts led to waveform differences, however, they did not have a significant effect on the peak values.

The periods of the oscillatory component of the tangent below event was about a factor of 2 greater than the surface tangent events.

5.1.3 Evaluation of Empirical Prediction Procedures

The prediction procedures utilized for the single burst experiments were discussed in Section 3. A summary of the comparisons of the predictions and data is contained in Table 4. These comparisons are discussed in some length in the text of the report and can be summarized as follows.

1. The airslap component was generally predicted to within the data scatter and in no case was there more than a factor of 2 difference in the vertical component. Attenuation rates of the airslap components were also predicted quite well. The differences between the predicted and measured airslap component waveforms appeared to be generally related to the differences in the predicted and actual arrival times of the various signals. Vertical motions were predicted better than horizontal motions.

2. The error in predicted arrival times of the low frequency components were as much as a factor of 3 greater than for the airslap component. This is a result of the greater distance of propagation of the oscillatory components thru the ground. The oscillatory component peak values were not predicted as well as the airslap components.

3. The discrepancies discussed above are indictive of the amount of effort which has been expended in studying the particular components. The low frequency component of motion has received very little study in the past and this is reflected in the problems associated with making those predictions and the resulting comparisons with the experimental data. The greater difference between horizontal

Table 4. SUMMARY OF PREDICTION EVALUATION

Effect	Surface Tangent $2.09 \times 10^{-3} \text{TJ}$	Half Buried $2.09 \times 10^{-3} \text{TJ}$	Tangent Below $2.09 \times 10^{-3} \text{TJ}$	Half Buried $5.35 \times 10^{-4} \text{TJ}$
Air Slap:				
TOA	-30	-30	-10	-20
V_V	WDS	WDS	WDS	0+100
A(R)	+35	WDS	WDS	0+100
V_H	WDS	WDS	-35+100	+50
A(R)	+35	WDS	-25	+20
A_V	-25+100	WDS	WDS	0+112
A(R)	+25	+10	WDS	+15
A_H	WDS+275	+65	-60,0	+450
A(R)	-10+20	-55	+50	-30
Low Frequency				
TOA	-90	-82	-75	
V_V	-55+110	-80+160	WDS	
A(R)	-60	-70+100	+5	
V_H	+400	0+750	+75	
A(R)	+30	-40+130	+75	
f_p	+100	+160	+155	

Legend

WDS - Within Data Scatter

Numbers indicate percent difference of
Prediction vs Data (Data used as Base)

A(R) = Attenuation with Range

f_p = Frequency of Major Low Frequency Motion

predictions and horizontal measurements also reflects the amount of effort which has been expended in developing prediction procedures for those components.

4. The one major discrepancy in the airslap component predictions is associated with the airblast generated shear wave. This shear wave was evident in the horizontal waveforms and led to significantly different waveforms than that predicted empirically.

5.1.4 Phenomenology

Prediction of waveforms by the methods described in Section 3 involves the superposition of a number of components which are independently predicted. This procedure assumes that the phenomenology associated with the expected motion is well understood. However, to explain the details on the experimental waveforms requires an additional level of understanding of the physics associated with each of the individual phenomena.

The airblast induced motion phenomenology is well understood even though the shear wave is not included in the prediction procedures. Inclusion of this effect would lead to much better predictions of the horizontal waveforms.

The oscillatory component is comprised of an outrunning signal which travels at p-wave speeds through the near surface layers and a surface wave which travels at shear wave speeds through deeper layers. The energy which comprises the oscillatory component comes from both upstream airblast and the directly coupled sources. Close to ground zero this component is dominated by the crater related effects. However, the surface wave portion is evident at ranges inside the outrunning radius.

The so called "transition region" in the attenuation of ground shock with range represents a change in the component of motion which contains the peak amplitude in addition to regions where the components of motion are combining in phase. In many other cases a distinct "plateau" in the attenuation occurs.

5.2 CONCLUSIONS

The analysis of the Phase I single burst experiments led to the

following conclusions about the empirical prediction procedures utilized.

1. Current empirical prediction procedures are not internally consistent when used to make a "total" prediction. Studies which have resulted in prediction relations have concentrated on a single component of motion and the total data base has never been included.

2. Air blast induced motions are reasonably well predicted with the exception of the air blast induced shear wave present in the horizontal motions. This is not treated by the current empirical prediction procedures.

3. Oscillatory motions are made up of a headwave and a surface wave component. The surface wave component dominates both the frequency and peaks of this motion. The period of the oscillatory motion is affected by both the height of burst and yield for a given geology while the amplitude appears independent of height of burst.

4. Waveform predictions are very sensitive to wave speeds and travel paths and therefore require good p- and s-wave seismic profiles.

5.3 RECOMMENDATIONS

While our ability to make empirical predictions is reasonably good in light of "normal data scatter" and unknown related to geology and weapons system performance, a number of improvements appear possible and desirable.

1. A consistent procedure should be developed for making predictions of a "total" waveform as a function of geology, height of burst and yield.

2. Prediction of surface wave portion of the oscillatory component should be based on a study of theoretical and experimental surface wave phenomenon.

3. The airblast induced shear wave should be included in horizontal airslap predictions.

4. A theoretical explanation of the transition region should

be developed and included in prediction procedures.

The accomplishment of these recommendations would result in better prediction of the details of the ground motion, in greater confidence in extrapolating the current base, and in better understanding of the relative importance in the variables involved in ground motion response of a site.

REFERENCES

1. Bratton, J.L., The Effect of Subsurface Layers on the Simulation of Shock Waves in the Ground, Fourth International Symposium on the Military Application of Blast Simulation, AWRE, Foulness, September 1974.
2. The Data Analysis Working Group, A Review of High Explosive Testing to Investigate Ground Motions Pertinent to the MX Multiple Aimpoint Systems, DAWG-TR-1, May 13, 1977.
3. Jackson, A.E. Jr., Ballard, R.F. Jr., and Curro, J.R. Jr., Material Property Investigation for Pre-Dice Throw I and II : Results from the Subsurface Exploration Programs, US Army Engineer Waterways Experiment Station, June 1976.
4. Jackson, A.E. Jr., and Peterson, R.W., Material Property Investigation for Pre-Dice Throw I and II : Results from the Laboratory Testing Programs, US Army Engineer Waterways Experiment Station, November 1976.
5. Amend, Joseph H., III, Cylindrical In-Situ Tests at Selected Nuclear and High Explosive Test Sites, AFWL-TR-76-209, Air Force Weapons Laboratory, February 1977.
6. Murrell, D.W., Misers Bluff Phase I Ground Shock and Airblast Measurements Data Report, Misc. Paper N-78-4, US Army Engineer Waterways Experiment Station, June 1978.
7. Bratton, J.L., et al, Empirical Predictions for Pre-Dice Throw II, letter report to DNA/SPSS (Maj. Todd Strong), 12 August 1975.
8. Kingery, C.N., Air Blast Parameters vs. Distance for Hemispherical TNT Surface Bursts, BRL Rpt. No. 1344, Ballistics Research Laboratory, 1964.
9. Jaramillo, E.E. and Pozega, R.E., Middle Gust Free-Field Data Analysis, AFWL-TR-73-251, Air Force Weapons Laboratory, April 1974.
10. Crawford, R.E., Higgins, C.J., and Bultmann, E.H., The Air Force Manual for Design and Analysis of Hardened Structures, AFWL-TR-74-102, Air Force Weapons Laboratory, October 1974.
11. Higgins, C.J., and Schreyer, H.L., An Analysis of Outrunning Ground Motions, AFWL-TR-74-220, Air Force Weapons Laboratory, May 1975.
12. Discussion with R.W. Henny, DES-G, Air Force Weapons Laboratory.
13. Bratton, J.L. and Cooper, H.F., Jr., "Preliminary Briefing of Middle Gust III Results", AFWL Briefing to DNA/SPSS, June 1972.
14. Proceedings of The Mixed Company/Middle Gust Results Meeting 13-15 March 1973, Volume 1, Sessions 1, 2A and 3A, DNA 3151P1, Defense Nuclear Agency, 1 May 1973.

15. Stubbs, T., Kochly, J., and Sauer, F., Middle North Series Pre-Mine Throw IV Air Blast and Ground Motion Project No. MT-301, Volumes 1 and 2, POR 6833-2, Defense Nuclear Agency, 29 October 1976.
16. Ellis, Paul A., et al, Nuclear Weapons Blast Phenomena. Volume III - Air and Subsurface Explosions, DNA Report No. DASA 1200-III. Unpublished.
17. Benson, K. and Babcock, S., Quick Look Report for Cratering and Debris Activities on MBI-1, Air Force Weapons Laboratory, September 1977.
18. Benson, K. and Babcock, S., Quick Look Report for MBI-2 Cratering and Related Effects, Air Force Weapons Laboratory, October 1977.
19. Benson, K. and Babcock, S., Quick Look Report for MBI-3 Cratering and Related Effects, Air Force Weapons Laboratory, October 1977.
20. Benson, K. and Babcock, S., Quick Look Report for MBI-5, Air Force Weapons Laboratory, October 1977.
21. Benson, K. and Babcock, S., Quick Look Report for MBI-7, Air Force Weapons Laboratory, November 1977.

DISTRIBUTION LIST

DEPARTMENT OF DEFENSE

Assistant to the Secretary of Defense
Atomic Energy
ATTN: Executive Assistant

Defense Advanced Rsch. Proj. Agency
ATTN: TIO

Defense Intelligence Agency
ATTN: RDS-3A

Defense Nuclear Agency
ATTN: SPSS, E. Sevin
ATTN: SPSS, G. Ulrich
3 cy ATTN: SPSS, J. Galloway
4 cy ATTN: TITL

Defense Technical Information Center
12 cy ATTN: DD

Field Command
Defense Nuclear Agency
ATTN: FCTMD
ATTN: FCPR

Field Command
Defense Nuclear Agency
Livermore Division
ATTN: FCPR

Joint Strat. Tgt. Planning Staff
ATTN: XPFS
ATTN: NRI-STINFO Library

Undersecretary of Defense for Rsch. & Engrg.
ATTN: Strategic & Space Systems (OS)

DEPARTMENT OF THE ARMY

BMD Advanced Technology Center
Department of the Army
ATTN: ATC-T

Chief of Engineers
Department of the Army
ATTN: DAEN-RDM
ATTN: DAEN-ASI-L
ATTN: DAEN-RDL
ATTN: DAEN-MPE-T, D. Reynolds

Harry Diamond Laboratories
Department of the Army
ATTN: DELHD-I-TL
ATTN: DELHD-N-P

U.S. Army Ballistic Research Labs.
ATTN: DRDAR-BLE, J. Keefer
ATTN: DRDAR-TSB-S

U.S. Army Cold Region Res. Engr. Lab.
ATTN: Library

U.S. Army Construction Engrg. Res. Lab.
ATTN: Library

DEPARTMENT OF THE ARMY (Continued)

U.S. Army Engineer Center
ATTN: Technical Library

U.S. Army Engr. Waterways Exper. Station
ATTN: WESSD, G. Jackson
ATTN: Library
ATTN: WESSA, W. Flathau

U.S. Army Material & Mechanics Rsch. Ctr.
ATTN: Technical Library

U.S. Army Materiel Dev. & Readiness Cmd.
ATTN: DRXAM-TL

U.S. Army Nuclear & Chemical Agency
ATTN: Library

DEPARTMENT OF THE NAVY

Naval Construction Battalion Center
ATTN: Code L08A
ATTN: Code L51, J. Crawford
ATTN: Code L53, J. Forrest

Naval Facilities Engineering Command
ATTN: Code 09M22C

Naval Postgraduate School
ATTN: G. Lindsay
ATTN: Code 0142, Library

Naval Research Laboratory
ATTN: Code 2627

Naval Surface Weapons Center
ATTN: Code F31
ATTN: Code X211

Naval Surface Weapons Center
ATTN: Tech. Library & Info Services Branch

Office of Naval Research
ATTN: Code 715

DEPARTMENT OF THE AIR FORCE

Air Force Institute of Technology
ATTN: Library

Air Force Systems Command
ATTN: DLWM

Air Force Weapons Laboratory
Air Force Systems Command
ATTN: NTES-S
ATTN: NTES-G
ATTN: SUL
ATTN: DEY
ATTN: NTE, M. Plamondon
ATTN: NTEO
ATTN: NT, D. Payton
ATTN: NTED-I
ATTN: NTED-A

DEPARTMENT OF THE AIR FORCE (Continued)

Assistant Chief of Staff
Intelligence
Department of the Air Force
ATTN: IN

Assistant Secretary of the Air Force
Research, Development & Logistics
ATTN: SAFALR/DEP for Strat. & Space Sys.

Ballistic Missile Office
Air Force Systems Command
ATTN: MNNXH, D. Gage
ATTN: MNNX, W. Crabtree

Deputy Chief of Staff
Research, Development, & Acq.
Department of the Air Force
ATTN: AFRD-M, L. Montulli
ATTN: AFRDPN
ATTN: AFRDQA
ATTN: AFRDQSM

Strategic Air Command
Department of the Air Force
ATTN: NRI-STINFO Library
ATTN: XPFS

Vela Seismology Center
ATTN: G. Ullrich

DEPARTMENT OF ENERGY CONTRACTORS

Lawrence Livermore Laboratory
ATTN: D. Glenn

Los Alamos Scientific Laboratory
ATTN: C. Keller
ATTN: R. Sanford

Sandia Laboratories
ATTN: Org. 1250, W. Brown
ATTN: A. Chabai

OTHER GOVERNMENT AGENCY

Federal Emergency Management Agency
ATTN: Hazard Eval. & Vul. Red. Div.

DEPARTMENT OF DEFENSE CONTRACTORS

Acurex Corp.
ATTN: C. Wolf
ATTN: J. Stockton
ATTN: K. Triebes

Aerospace Corp.
ATTN: Technical Information Services
ATTN: H. Mirels

Agabian Associates
ATTN: M. Agabian

Applied Theory, Inc.
ATTN: J. Trulio

Boeing Co.
ATTN: S. Strack
ATTN: Aerospace Library

DEPARTMENT OF DEFENSE CONTRACTORS (Continued)

California Research & Technology, Inc.
ATTN: Library
ATTN: M. Rosenblatt

California Research & Technology, Inc.
ATTN: D. Orphal

Civil Systems, Inc.
ATTN: J. Bratton

Civil Systems, Inc.
ATTN: S. Melzer

Eric H. Wang
Civil Engineering Rsch. Fac.
ATTN: P. Lodde
ATTN: J. Kovarna

General Electric Company—TEMPO
ATTN: DASIAC

H-Tech Labs, Inc.
ATTN: B. Hartenbaum

Higgins, Auld & Associates
ATTN: N. Higgins
ATTN: H. Auld

IIT Research Institute
ATTN: Documents Library

J. H. Wiggins Co., Inc.
ATTN: J. Collins

Merritt CASES, Inc.
ATTN: Library

Mission Research Corp.
ATTN: G. McCartor
ATTN: C. Longmire

Nathan M. Newmark Consult. Eng. Svcs.
ATTN: W. Hall
ATTN: N. Newmark

Pacific-Sierra Research Corp.
ATTN: H. Brode

Pacifica Technology
ATTN: R. Allen
ATTN: Library

Physics International Co.
ATTN: F. Sauer
ATTN: J. Thomsen
ATTN: Technical Library

R & D Associates
ATTN: J. Carpenter
ATTN: R. Port
ATTN: C. MacDonald
ATTN: J. Lewis
ATTN: Technical Information Center
ATTN: A. Kuhl

Science Applications, Inc.
ATTN: R. Schlaug
ATTN: Technical Library
ATTN: H. Wilson

DEPARTMENT OF DEFENSE CONTRACTORS (Continued)

Science Applications, Inc.
ATTN: D. Houe

Science Applications, Inc.
ATTN: B. Chambers III

SRI International
ATTN: J. Colton
ATTN: G. Abrahamson
ATTN: D. Johnson
ATTN: Library

Systems, Science & Software
ATTN: C. Needham

Systems, Science & Software, Inc.
ATTN: Library
ATTN: K. Pyatt
ATTN: C. Dismukes
ATTN: J. Barthel

Systems, Science & Software, Inc.
ATTN: J. Murphy

DEPARTMENT OF DEFENSE CONTRACTORS (Continued)

Systems, Science & Software, Inc.
ATTN: C. Hastings

Terra Tek, Inc.
ATTN: A. Abou-sayed
ATTN: Library

TRW Defense & Space Sys. Group
ATTN: N. Lipner
ATTN: Technical Information Center

TRW Defense & Space Sys. Group
ATTN: G. Hulcher

Weidlinger Assoc., Consulting Engineers
ATTN: I. Sandler

Weidlinger Assoc., Consulting Engineers
ATTN: J. Isenberg

